From Mutation to Mechanism: an Approach to Understand Photoreceptors Function

Inaugural-Dissertation
to obtain the academic degree
Doctor rerum naturalium (Dr. rer. nat.)

submitted to the Department of Biology, Chemistry, Pharmacy of Freie Universität Berlin

by

Mariafrancesca La Greca

Berlin, 2025

1st reviewer: Dr. Ramona Schlesinger

2nd reviewer: Prof. Dr. Florian Heyd

Date of defense: 06/08/2025

Declaration of Autorship

I hereby declare that I alone am responsible for the content of my doctoral dissertation and that I have only used the sources of references cited in the dissertation.

To my mother.

“To you,

who believed in my dreams

Before they even took shape,

who taught me to endure

And to fly without fear.

This goal is also yours.”

Acknowledgments

First and foremost, I would like to thank my supervisor Dr. Ramona Schlesinger and Prof. Dr. Joachim Heberle for their guidance, support and encouragement throughout my journey. Thank you for always believing in me and, most importantly, for creating an environment that felt like family.

I am also sincerely grateful to Prof. Dr. Florian Heyd for supporting this thesis as my second reviewer.

To my family, thank you for your unconditional love, patience and belief in me – even at times when I couldn´t see it myself.

A special thank you to my sister Bruna, who accompanied me on this journey from the day of my interview to the final day of submission – always listening, supporting, and encouraging me when I needed it most. To my brother Andrea, thank you for being a model of perseverance and for celebrating with me every paper, every success, and every step forward.

To my Berlin support group - Sara, Şiir, Rafael, Antreas, Anna-Maria, Eleftheria, Alexandra and Ilgın – thank you for the countless weekends spent together, the drinks, the laughs, and all the fun we shared. Your presence made everyday life in Berlin feel like home, and this journey much brighter.

To Jheng-Liang, Luiz and Federico, what began as a working relationship grew into something deeper. You became like family, and I look forward to seeing our friendship continue to grow.

To María, Aoife, Daniele, David and Severin, thanks for bringing fun and lightness to this journey.

To Kirsten and Doro, whose technical expertise and constant support were invaluable throughout this work. Their assistance greatly contributed to this research.

To my collaborators, thank you for your valuable input and stimulating discussions. In particular I would like to thank Karo, working with you enriched this research in meaningful ways.

To the students - Tim, Celine and Fenja - thank you for your dedication, curiosity and valuable contributions to this work.

List of publications

([†] equally contributed)

La Greca, M. [†]; Chen, J.-L. [†]; Schubert, L.; Berneiser, T.; Kozuch, J.; Terpitz, U.; Heberle, J.; Schlesinget, R. The photoreaction of the Proton-Pumping Rhodopsin 1 From the Maize Pathogenic Basidiomycete *Ustilago maydis*. *Front Mol Biosci.* **2022**, 9, 826990. doi:10.3389/fmolb.2022.826990.

Baserga, F.; Vorkas, A.; Crea, F.; Schubert, L.; Chen, J.-L.; Redlich, A.; **La Greca, M.**; Storm, J.; Oldemeyer, S.; Hoffmann, K.; Schlesinger, R.; Heberle, J. Membrane Protein Activity Induces Specific Molecular Changes in Nanodiscs Monitored by FTIR Difference Spectroscopy. *Front Mol Biosci.* **2022**, 9, 915328. doi: 10.3389/fmolb.2022.915328.

Oldemeyer, S.; **La Greca, M.**; Langner, P.; Lê Công, K.-L.; Schlesinger, R.; Heberle, J. Nanosecond Transient IR Spectroscopy of Halorhodopsin in Living Cells. *J Am Chem Soc.* **2024**, 146(28):19118-19127. doi: 10.1021/jacs.4c03891.

Nguyen, A. D. [†]; Michael, N. [†]; Sauthof, L. [†]; von Sass, J.; Hoang, T. O.; Schmidt, A.; **La Greca, M.**; Schlesinger, R.; Budisa, N.; Scheerer, P.; Mroginski, M. A.; Kraskov, A.; Hildebrandt, P. Hydrogen Bonding and Noncovalent Electric Field Effects in the Photoconversion of a Phytochrome. *J Phys Chem B.* **2024**, 128(47):11644-11657. doi: 10.1021/acs.jpcb.4c06419.

Asido, M. [†]; Lamm, G. H. U. [†]; Lienert, J.; **La Greca, M.**; Kaur, J.; Mayer, A.; Glaubitz, C.; Heberle, J.; Schlesinger, R.; Kovalev, K.; Wachtveitl, J. A Detailed View on the (Re)isomerization Dynamics in Microbial Rhodopsins Using Complementary Near-UV and IR Readouts. *Angew Chem Int Ed Engl.* **2025**, 64(4):e202416742. doi: 10.1002/anie.202416742.

Summary

Microbial rhodopsins and phytochromes are photoreceptors that use light to trigger biochemical processes. Upon light activation, they undergo a cyclic cascade of reactions leading to substrate transfer and/or conformational changes associated with the chromophore and protein. *Nm*HR and *Um*Rh1, two microbial rhodopsins, are a bacterial inward chloride pump and a fungal outward proton pump, respectively. While the role of *Nm*HR from a marine bacterium is similar to that of the well-known archaeal inward chloride pump halorhodopsins (*Hs*HR and *Np*HR), it shares a higher sequence homology with the bacterial outward sodium pump KR2. In addition, each rhodopsin contains a three-residue motif composed of amino acids involved in substrate transfer. The NTQ motif of *Nm*HR is quite conserved in the sodium pump KR2 (NDQ), but is represented by a neutral TSA motif in archaebacterial halorhodopsins, suggesting a divergent evolution. A comprehensive mutational and spectroscopic analysis of residues known to be important for chloride transfer in archaeal halorhodopsins and for sodium transfer in KR2 revealed that chloride release and uptake in *Nm*HR is different from that of archaeal halorhodopsins, but the architecture and residues involved in the process are more similar to KR2, despite the different charge and orientation of the transported ion.

*Um*Rh1 is a rhodopsin found in the pathogenic fungus *Ustilago maydis*, which causes corn smut disease. This fungal rhodopsin shares a high sequence similarity with the well-known archaeal outward proton pump bacteriorhodopsin (*Hs*BR), especially at residues known to be important for the proton pathway of the latter. The DTD motif of *Hs*BR is conserved in *Um*Rh1 and is represented by a DTE motif. However, extensive mutagenesis and spectroscopy revealed that the protonation dynamics of *Um*Rh1 are slightly different from those of *Hs*BR, especially in the proton uptake reaction. Furthermore, the pump activity of *Um*Rh1 is enhanced in the presence of auxins such as IAA (indole-3-acetic acid). Using time-resolved spectroscopy on *Um*Rh1 variants in the presence and absence of IAA, a potential role for auxin was elucidated. It is involved in the enhancement of the reprotonation mechanism and the proton release reaction associated with its pathogenic role.

Another aspect that has intrigued scientists over the years is the link between light and chromophore isomerization in photoreceptors, which leads to conformational changes in the

protein. How does the signal propagate in the early stages of the photocycle after photon absorption? By introducing the noncanonical amino acid p-cyano-phenylalanine in *Nm*HR and the phytochrome Agp2 into positions of conserved tryptophan residues known to be involved in conformational changes around the chromophore, preliminary results have been obtained that shed light on the protein-chromophore interaction.

Zusammenfassung

Mikrobielle Rhodopsine und Phytochrome sind Photorezeptoren, die Licht nutzen, um biochemische Prozesse auszulösen. Nach der Aktivierung durch Licht durchlaufen sie eine zyklische Reaktionskaskade, die zu einem Substrattransfer und/oder Konformationsänderungen im Zusammenhang mit dem Chromophor und dem Protein führt. Die hier untersuchten zwei mikrobiellen Rhodopsine sind *Nm*HR, eine bakterielle nach innen gerichtete Chloridpumpe, und *Um*Rh1, eine nach außen gerichtete pilzliche Protonenpumpe. Während die Rolle des aus einem Meeresbakterium stammenden *Nm*HR derjenigen der bekannten Halorhodopsine (*Hs*HR und *Np*HR) aus Archaeen ähnelt, weist es eine größere Sequenzhomologie mit der bakteriellen Natrium-Auswärtspumpe KR2 auf. Darüber hinaus enthält jedes Rhodopsin ein aus drei Aminosäuren bestehtes Motiv auf, das am Substrattransfer beteiligt ist. Das NTQ-Motiv von *Nm*HR ist in der Natriumpumpe KR2 (NDQ) weitgehend konserviert, wird aber in archaebakteriellen Halorhodopsinen durch ein neutrales TSA-Motiv repräsentiert, was auf eine divergente Evolution hindeutet. Eine umfassende Mutationsanalyse mit nachfolgender spektroskopischer Untersuchung von Aminosäureresten, die für den Chlorid-Transfer in archaealen Halorhodopsinen und für den Natrium-Transfer in KR2 bekannt sind, ergab, dass sich in *Nm*HR die Chloridfreisetzung und Aufnahme von der in archaealen Halorhodopsinen unterscheidet, dass aber die Architektur und die an dem Prozess beteiligten Aminosäuren dem KR2 ähnlicher sind, trotz der unterschiedlichen Ladung und Ausrichtung des transportierten Ions.

*Um*Rh1 ist ein Rhodopsin, welches in dem pathogenen Pilz *Ustilago maydis* vorkommt, der die Maisfleckenkrankheit verursacht. Dieses Pilzrhodopsin weist eine hohe Sequenzähnlichkeit mit der bekannten aus Archaeen stammenden Protonenpumpe Bakteriorhodopsin (*Hs*BR) auf, vor allem an Stellen, die für den Protonenweg der letzteren wichtig sind. Das DTD-Motiv von *Hs*BR ist in *Um*Rh1 konserviert und wird durch ein DTE-Motiv dargestellt. Ausführliche Mutagenese und Spektroskopie zeigten jedoch, dass sich die Protonierungsdynamik von *Um*Rh1 geringfügig von derjenigen von *Hs*BR unterscheidet, insbesondere bei der Protonenaufnahmereaktion. Außerdem ist die Pumpaktivität von *Um*Rh1 in Gegenwart von Auxinen wie IAA (Indol-3-Essigsäure) verstärkt. Durch zeitaufgelöste Spektroskopie an *Um*Rh1-Varianten in Gegenwart und Abwesenheit von IAA wurde eine mögliche Rolle von Auxin aufgedeckt. Es ist wahrscheinlich an der Verstärkung des Reprotonierungsmechanismus und der Protonenfreisetzungsreaktion im Zusammenhang mit seiner pathogenen Rolle beteiligt.

Ein weiterer Aspekt, der die Wissenschaftler im Laufe der Jahre fasziniert hat, ist die Verbindung zwischen Licht und der Isomerisierung des Chromophors in den Photorezeptoren, die zu Konformationsänderungen des Proteins führt. Wie wird das Signal in den frühen Stadien des Photozyklus nach der Photonenabsorption weitergeleitet? Durch die Einführung der nicht-kanonischen Aminosäure p-Cyano-Phenylalanin in *Nm*HR und in Phytochrom Agp2 in Positionen von konservierten Tryptophanresten, von denen bekannt ist, dass sie an Konformationsänderungen um das Chromophor herum beteiligt sind, wurden erste Ergebnisse erzielt, die Licht auf die Protein-Chromophor-Interaktion werfen.

List of abbreviations

*Nm*HR: *Nonlabens marinus* halorhodopsin

*Hs*HR: *Halobacterium salinarum* halorhodopsin

*Np*HR: *Natronomonas pharaonis* halorhodopsin

*Hs*BR: *Halobacterium salinarum* bacteriorhodopsin

KR2: *Krokinobacter eikastus* rhodopsin

*Um*Rh1: *Ustilago maydis* rhodopsin 1

Agp2: *Agrobacterium fabrum* phytochrome 2

ncAA: non-canonical amino acid

UAA: unnatural amino acid

pCNF: p-cyano-phenylalanine

SB: Schiff base

RSB: Retinal Schiff base

PSB: Protonated Schiff base

RSBH: Protonated retinal Schiff base

UV/Vis: Ultraviolet/Visible spectroscopy

FTIR: Fourier transform infrared spectroscopy

WOA: weak organic acid

IAA: indole-3-acetic acid

IPA: indole-3-propionic acid

Table of Contents

1. Introduction

1.1. Membrane proteins: rhodopsins

The word "rhodopsin" originates from the Greek words "rhodo" and "opsis", which indicate rose and sight, respectively, as cited from[1]. This class of photoreceptors are membrane proteins that sense and respond to light and are divided into microbial rhodopsins (type 1) and animal rhodopsins (type 2). Although the role of type 2 rhodopsins, a subset of GPCR receptors, is related to visual and non-visual signaling, type 1 rhodopsins use light as a trigger for energy conversion and signaling[2]. These two classes of rhodopsins share no sequence homology, although the protein architecture is conserved. The light-absorbing unit is the retinal, a derivative of vitamin A, which adopts different conformations in the ground state, all-*trans* (type 1) and 11-*cis* (type 2)[3]. Whereas some animal rhodopsins like visual rhodopsins from mammals release the retinal from the protein upon light activation (photobleaching), microbial rhodopsins undergo a cyclic reaction in which the retinal returns to its dark state configuration (photocycle) **(Figure 1)**.

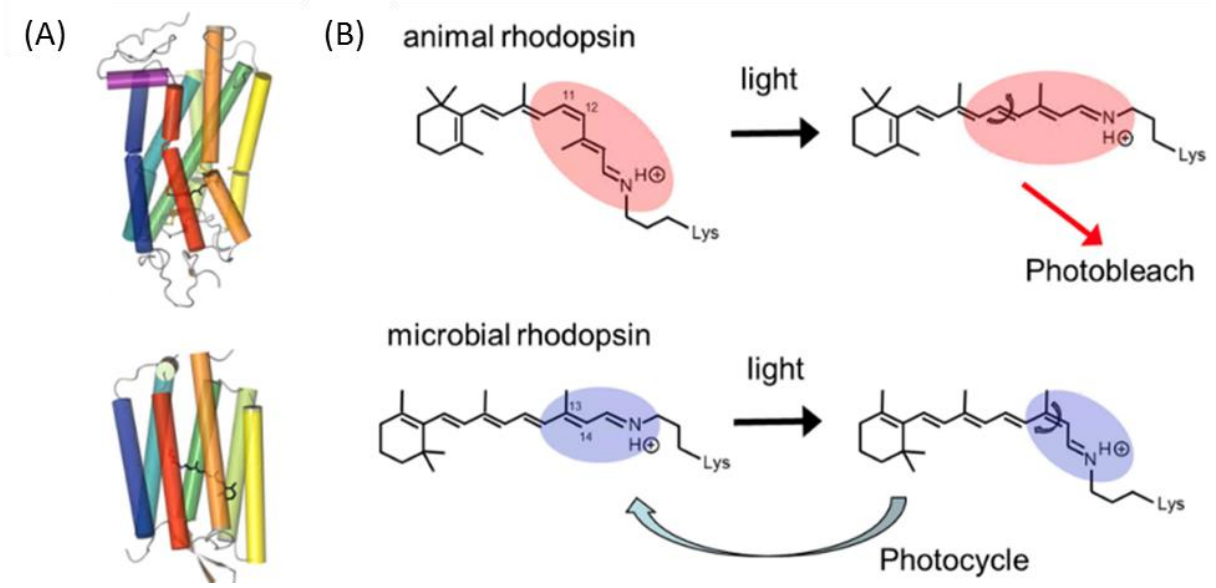

Figure 1. *Architecture of animal rhodopsins and microbial rhodopsins (A). These proteins consist of 7 transmembrane helices in which the retinal is covalently linked to a lysine residue in TM7 via a Schiff base linkage. The retinal adopts different conformations in the dark state and upon light absorption (B). Although in animal*

rhodopsins the retinal is released from the protein leading to a photobleach, microbial rhodopsins undergo a cascade of reactions called photocycle. (Figure modified from Ref.[3]).

Microbial rhodopsins have been found in all three domains of life and consist of 7 transmembrane helices in which the chromophore, retinal, is covalently bound to a lysine residue in TM7 via a protonated Schiff base, and can be further classified into pumps, channels, and sensors, the latter being coupled to a transducer **(Figure 2)**. The main difference between ion pumps and channels is related to the ion conduction pathway. While rhodopsin ion pumps require an energy input for the active unidirectional transport of the substrate, the fully connected conduction pathway in channels ensures passive ion transport[1].

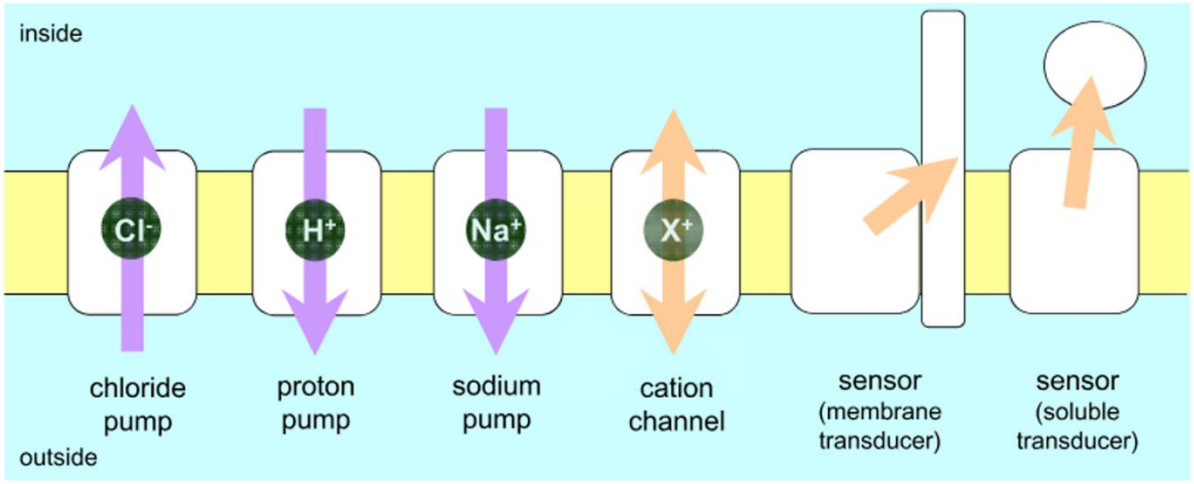

Figure 2. *Classification of microbial rhodopsins. They can be classified as ion pumps, channels and sensors. Although ion pump rhodopsins transport the substrate unidirectionally, channels have a passive ion transport mechanism. Sensors are coupled to a transducer, which can be a membrane transducer or a soluble transducer. (Figure modified from Ref.[1]).*

Upon absorption of photons via light, the retinal chromophore changes its configuration from all-*trans* to 13-*cis*, triggering a cyclic cascade of intermediates called the photocycle, resulting in protein conformational changes that lead to substrate transfer. The first rhodopsin, discovered 50 years ago, is bacteriorhodopsin (*Hs*BR), an outward proton pump from the archaeal *Halobacterium salinarum*, followed by the discovery of an inward chloride pump,

halorhodopsin (*Hs*HR) in the same organism. In addition, two other rhodopsins were identified in *Halobacterium salinarum*, named sensory rhodopsin 1 (*Hs*SRI) and 2 (*Hs*SRII), which are important for signaling and phototaxis. Initially rhodopsins were thought to be present only in archaea[4], but subsequently were also found in bacteria, algae, viruses and fungi. The well-known photoreaction of bacteriorhodopsin has since been used as a model to understand the role and function of all subsequently discovered microbial rhodopsins. The intermediates of the photocycle are J-K-L-M-N and O **(Figure 3)**. While J can only be detected by ultrafast spectroscopy due to its short lifetime, time-resolved UV/Vis spectroscopy allows to follow the rise and decay of the other intermediates of the photocycle. Retinal isomerization from all-*trans* to 13-*cis*, which occurs in 10^{-13} - 10^{-12} seconds, produces the K intermediate, where the stored energy and subsequent relaxation lead to structural changes in the protein[5]. In the next intermediate, the L state, the proton of the Schiff base is transferred to the primary acceptor, forming the M state[6]. This blue-shifted intermediate (ʎ: 410 nm) is one of the most important steps in the photocycle, in which the Schiff base is deprotonated[7], representing a crucial turning point for proton translocation. In the M to N transition, the Schiff base is reprotonated by a proton donor and returns to its original configuration. During the photocycle, the accessibility of the retinal from both sides of the membrane switches to allow vectorial transport[2]. During the photocycle, protonation events occur in the protein involving side chains of relevant amino acids and the Schiff base (SB), leading to conformational changes in the protein and are important for substrate transfer. The Schiff base is almost always protonated in the dark state and conjugated to a counterion. In bacteriorhodopsin, the counterion of the Schiff base is Asp-85, whereas in chloride pumps (as HRs), the counterion of the PSB (protonated Schiff base) is the chloride itself. The process of deprotonation of the PSB leads to the formation of the M state, while its reprotonation leads to the formation of the O state. Consequently, chloride pumps lack the M state due to the nature of the PSB counterion. The importance of this class of proteins is related to the field of optogenetics, a novel technique that uses light to control the membrane potential in neuronal cells[8] making it a potential tool for gene therapy of various diseases, such as Parkinson's disease and blindness. In fact, channelrhodopsins (ChRs), found in green algae, have been the focus of interest for optogenetic applications in the last decade[9] with promising results in mice and humans. In particular, studies on opsin-based therapies for retinal degeneration have made great progress[10].

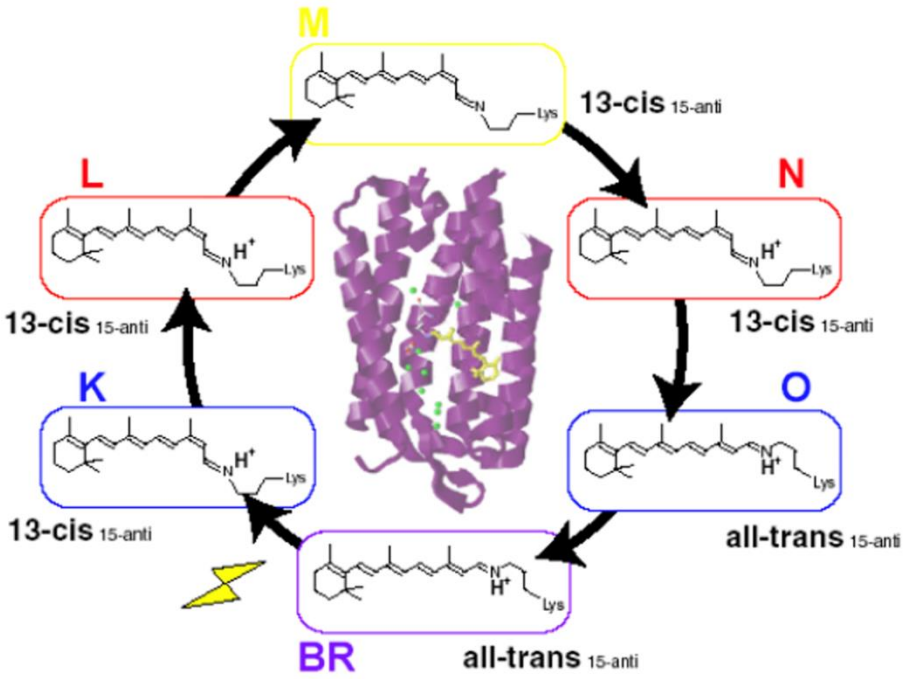

Figure 3. *Photoreaction of bacteriorhodopsin from Halobacterium salinarum. The well-known photoreaction of bacteriorhodopsin is used as a model system for all subsequently discovered rhodopsins. Upon light activation the retinal changes its configuration from all-trans to 13-cis and the stored energy and relaxation is used for the structural changes of the protein and substrate transfer. M state and O state are the most important steps where the Schiff base is deprotonated and reprotonated, respectively. (Figure modified from Ref.*[11]*).*

1.2. Light-driven chloride pumps

*Hs*HR was the first light-driven chloride pump to be discovered, and it was found in the archaeon *Halobacterium salinarum*. This organism lives in extreme conditions and the transport of chloride into the cytoplasm helps the organism to maintain the osmotic balance[12]. In the 1980s, another halorhodopsin was discovered in the organism *Natronomonas pharaonis* in a salt lake in Egypt[13] nowadays named *Np*HR. This halorhodopsin can be expressed in neuronal cells and has been studied as an optogenetic tool[14]. The sequence homology of these two functionally different rhodopsin classes (*Hs*BR versus halorhodopsins) is 34%[15], although they transport different substrates and in different directions (outward *versus* inward). As in the case of *Hs*BR, retinal photoisomerization is the trigger for ion pump activity in these rhodopsins[16]. Although the "3-letter motif", which is important to categorize ion-pumping rhodopsins, is represented by the charged DTD motif in *Hs*BR, it is replaced in halorhodopsins by a neutral TSA motif and the counterion of the protonated Schiff base, which is represented by an aspartic acid in *Hs*BR, is represented by the chloride itself in halorhodopsins. This three-letter motif is composed of residues which are located on the helix C and define the function of novel microbial rhodopsins[17]. Subsequently, from the marine environment, another class of inward chloride pumps was identified in flavobacteria, with a different motif of residues involved in ion transport (NTQ), such as *Nm*HR, FR and *aa*CIR[18]. Interestingly, these rhodopsins do not share a high sequence similarity with the archaeal halorhodopsins, thus belonging to a different phylogenetic clade. Recently, two halorhodopsins have been identified in cyanobacteria, *Mr*HR and *Sy*HR, which have a TSD motif and are therefore similar to the archaeal halorhodopsins, sharing a similar motif in which the alanine is replaced by an aspartic acid. A crystal structure of *Mr*HR was only published in 2020[19], but the majority of structural information has been reported from studies of *Hs*HR, *Np*HR and *Nm*HR **(Figure 4)**.

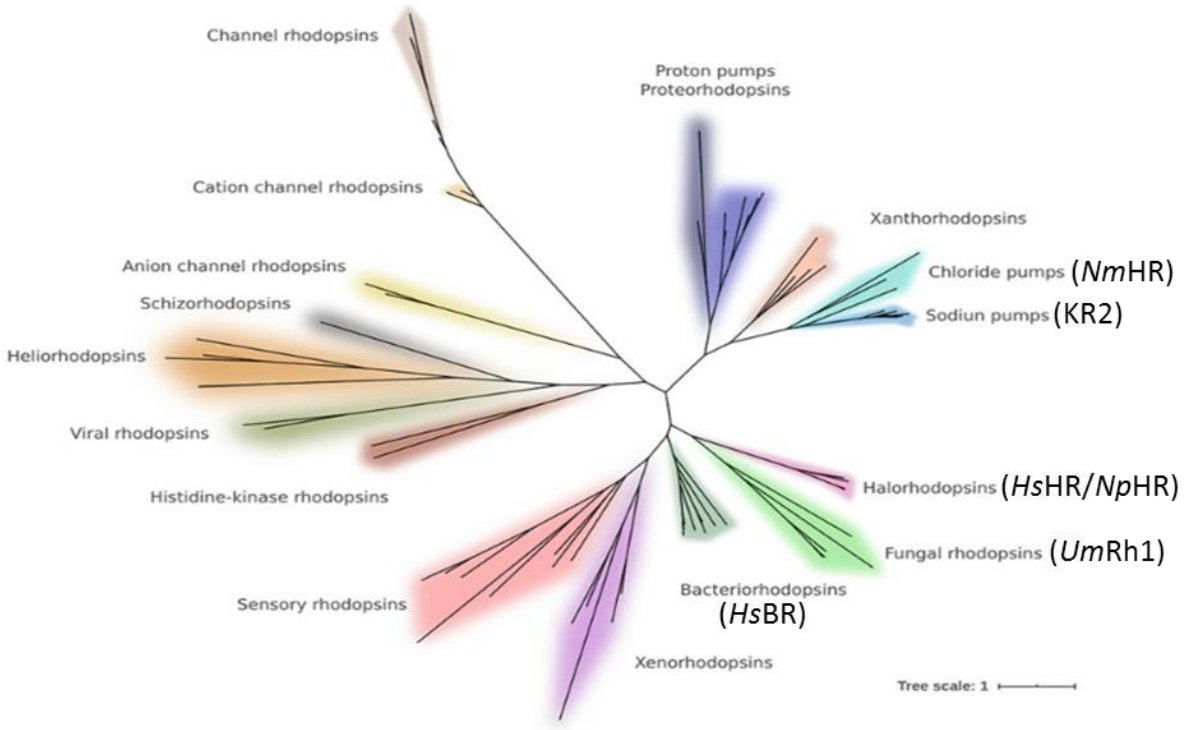

Figure 4. *Phylogenetic tree of microbial rhodopsins. Flavobacterial halorhodopsins such as NmHR belong to a different clade compared to other inward chloride pumps suggesting a divergent evolution. The rhodopsins discussed in this study are shown in brackets (Figure modified from Ref.*[20]*).*

1.3. *Nm*HR: *Nonlabens marinus* halorhodopsin

*Nm*HR, a halorhodopsin, is an inward chloride pump discovered in the marine bacterium *Nonlabens marinus*. In some literature it has been referred to as NM-R3 and CIR, but in this study and recent publications it has been referred to as *Nm*HR to use the same nomenclature as other rhodopsins (e.g. *Hs*HR, *Np*HR)[14]. Three different rhodopsins have been found in the genome of the bacterium: NM-R1, NM-R2 and NM-R3, the first with proton pumping activity, the second pumping sodium and the last pumping chloride (*Nm*HR). The chloride activity has been demonstrated and reported in previous studies, using a pH electrode and testing the active transport of chloride on light, monitoring the ΔpH[21]. Although the transported substrate is the same as that of the other two known halorhodopsins (*Hs*HR and *Np*HR), it has a higher sequence similarity with the outward sodium pump KR2 (35%) (17% for halorhodopsins)[22] and shares a similar motif of residues involved in ion transfer, NTQ for *Nm*HR and NDQ for KR2, against

the neutral motif of halorhodopsins, TSA. While in KR2 Asp-116 of the NDQ motif acts as a proton acceptor of the PSB, in *Nm*HR the counterion is represented by chloride itself, but changing Thr-102 to an aspartic acid does not convert the chloride pump to a sodium pump, suggesting that other residues may play a role in ion selectivity[23]. In addition, there are some major differences between *Nm*HR and the archael halorhodopsins that suggest divergent evolution: the first is represented by a conserved charged amino acid pair present in both rhodopsin classes (Asp-231 and Arg-95 in *Nm*HR, Asp-238 and Arg-108 in *Hs*HR) as well as in *Hs*BR and KR2. This highly conserved pair of charged amino acids is important for anion uptake and correct dark state recharging. While in halorhodopsins these two residues are indirectly bound to chloride via a water molecule, in *Nm*HR this hydrogen bonding bridge is missing and Asp-231/Arg-95 are not bound to the anion in the dark state of *Nm*HR, which may explain the lower binding affinity of chloride in *Nm*HR[24]. In addition, crystallographic studies have shown the presence of an additional α-helix at the N-terminus, which is important for the first step of chloride uptake[25] and is absent in *Hs*HR and *Np*HR. In these halorhodopsins other residues in a different region of the protein play a role in anion uptake. Interestingly, this additional structural feature is also present in KR2, suggesting a similar pattern of evolution for these two bacterial rhodopsins **(Figure 5)**.

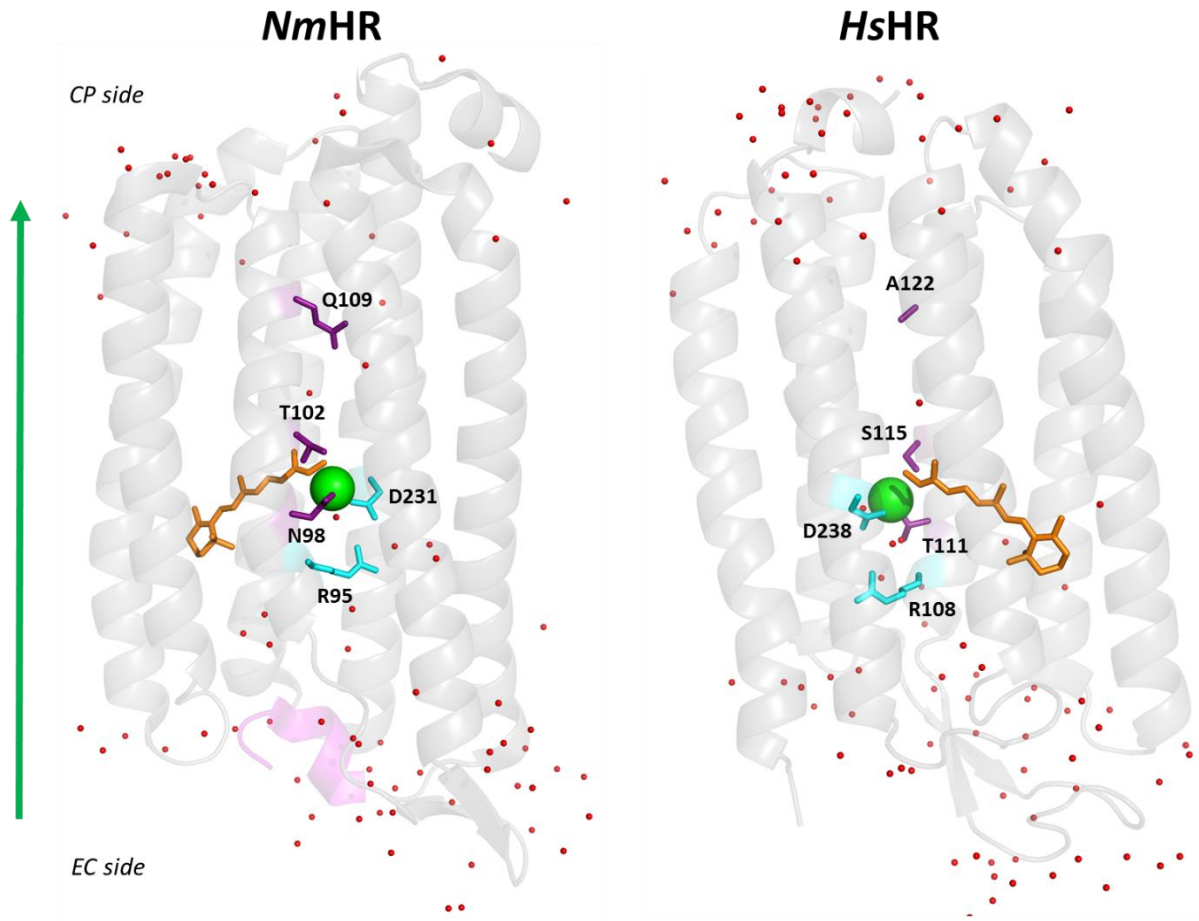

Figure 5. *Structural comparison between NmHR and HsHR. Dark state structure of NmHR (PDB: 7O8F) on the left and HsHR (PDB: 1E12) on the right. The 3 residues composing the motif are highlighted in purple. The conserved amino acid pair consisting of an aspartic acid and an arginine is highlighted in cyan. The additional α-helix at the N-terminus, in NmHR, is highlighted in magenta. The retinal and the chloride ion are shown in orange and green, respectively. The water molecules are shown as small red spheres. The green arrow indicates the direction of chloride transfer.*

1.4. Light-driven proton-pumping rhodopsins

Light-driven proton pump rhodopsins represent a substantial fraction of microbial rhodopsins; they were first discovered in archaea with the discovery of bacteriorhodopsin (*Hs*BR) in the plasma membrane of *Halobacterium salinarum* by Oesterhelt and Stoeckenius in 1971, which acts as an outward proton pump[26]. The function of this protein *in vivo* is to convert solar energy into proton motive force, and the resulting proton gradient is then used to produce ATP in cells[27]. Bacteriorhodopsin has since been used as a model system for all rhodopsins that have been discovered. Following the discovery of bacteriorhodopsin, other proton-pumping rhodopsins were identified, such as the class of proteorhodopsins (PRs) found in eubacteria[28], which are the first bacterial light-driven proton pumps[20]. Unlike bacteriorhodopsin, which can pump protons over a wide pH range, PRs are capable of pumping protons at neutral and alkaline pH[29]. Although the majority of proton-pumping rhodopsins transport the proton out of the cell, another class of proton pumps with reversed proton transfer directionality, the xenorhodopsins (XeRs), have been discovered[30], expanding the role of microbial rhodopsins in nature. Proton-pumping rhodopsins are not restricted to archaea and bacteria, but were subsequently found in eukaryotic organisms, with the discovery of the fungal LR from the fungus *Leptosphaeria maculans*[31], which exhibits a *Hs*BR-like photocycle, and then the CarO-like rhodopsins found in plant-associated fungi[32]. More recently, a new class of fungal rhodopsins was discovered in the basidiomycete *Ustilago maydis*, which resembles CarO-like rhodopsins[33] and was named *Um*Rh1, which also acts as an outward proton pump[34].

1.5. *Um*Rh1: *Ustilago maydis* rhodopsin 1

*Um*Rh1, a fungal rhodopsin, was discovered in the pathogenic basidiomycete *Ustilago maydis*, which causes smut in corn plants. Three different rhodopsins were identified in the genome of the fungus, originally named UmOps1 (*Um*Rh1), UmOps2 and UmOps3, but only the first two show proton pump activity, while UmOps3 is probably a sensor[33]. Electrophysiological experiments performed by *Dr. Ulrich Terpitz's group* showed that a positive current signal, characteristic of outward proton pumps, was detected in *Um*Rh1 (UmOps1) and UmOps2 under green light, although it was more pronounced in the former one. This higher pump activity is reflected in the localization of the GFP-tagged protein in the fungal membrane. While *Um*Rh1

is mainly localized in the plasma membrane to contribute to the proton motive force of the fungus, UmOps2 was mainly found in internal membranes[33]. The predicted structure of *Um*Rh1 shows a high similarity to the known structure of bacteriorhodopsin with conserved amino acids required for the proton pumping mechanism **(Figure 6)**. The DTD motif of bacteriorhodopsin, formed by Asp-85, Thr-89 and Asp-96, is replaced in *Um*Rh1 by a DTE motif (Asp-118, Thr-122 and Glu-129). In *Hs*BR, Asp-85 and Asp-96, located in the transmembrane helix C, act as proton acceptor and donor to the Schiff base, respectively[1]. *Um*Rh1 has a glutamate at position *Hs*BR Asp-96, which is also present in proteorhodopsins[2]. The intramembrane Asp-115 of *Hs*BR, which is highly conserved in microbial rhodopsins, is replaced by Asp-148 in *Um*Rh1. On the extracellular side of *Hs*BR, the proton-releasing group (PRG) region, a complex of amino acids including Glu-194 and Glu-204 that plays a critical role in proton release to the extracellular side of the protein[35], is replaced in *Um*Rh1 by Asp-225 and Glu-235. Another carboxylic acid residue, Asp-212, essential for proton transfer to the PRG in *Hs*BR, is conserved in *Um*Rh1 being Asp-243[36]. An interesting feature of *Um*Rh1 is its role in pathogenesis; plant auxin hormones such as indole-3-propionic acid (IPA) and indole-3-acetic acid (IAA), which are highly expressed during host infection, have a role in enhancing the pump activity of *Um*Rh1. In particular, IAA has a strong effect on accelerating the M state decay and O state rise of *Um*Rh1[34].

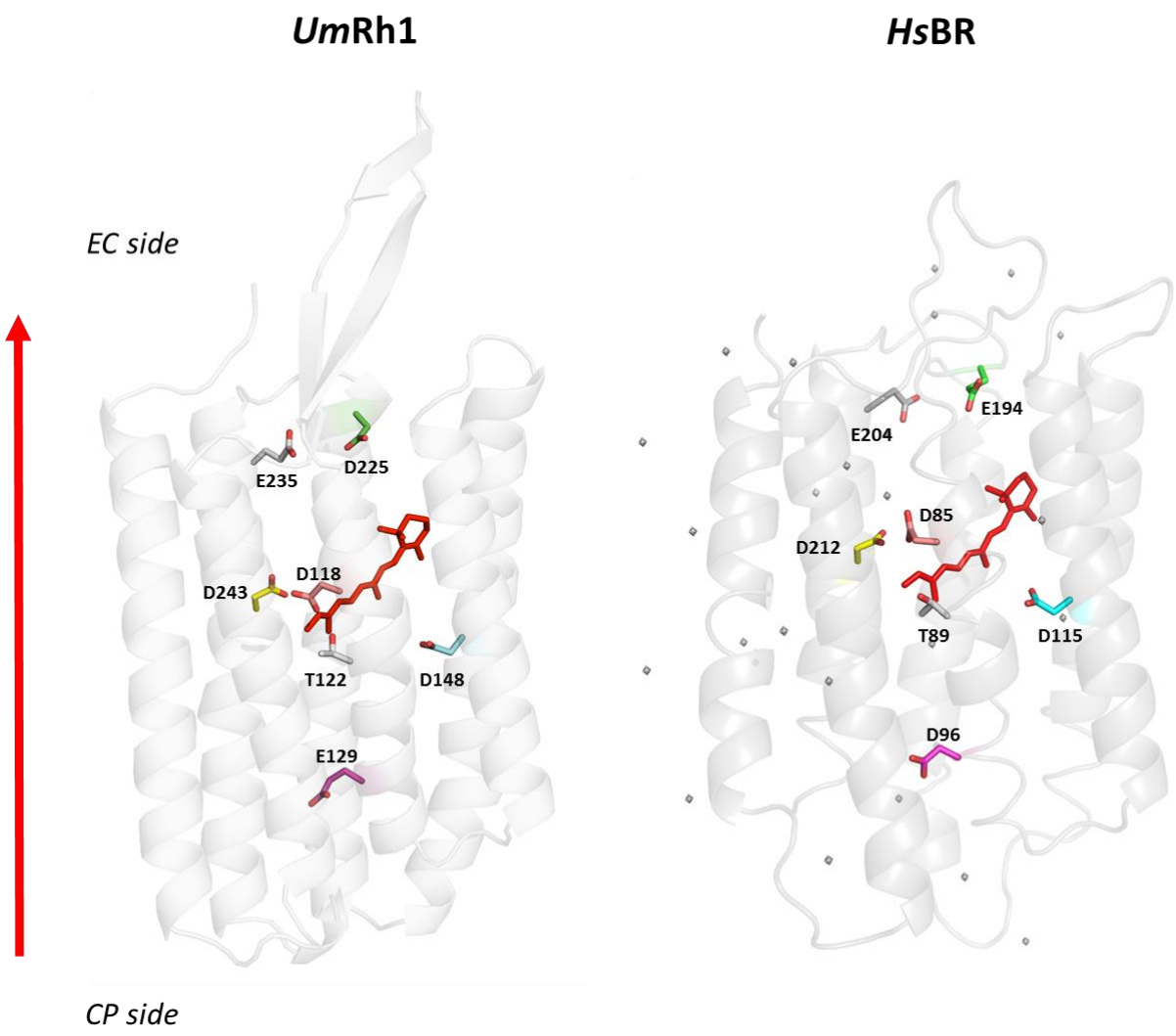

Figure 6. *Structure comparison of UmRh1 (predicted structure) on the left and HsBR (PDB: 1AP9) on the right. Conserved residues known to be important for the protonation pathway in HsBR are highlighted. The red arrow indicates the direction of proton transfer.*

1.6. Soluble proteins: phytochromes

Phytochromes are a class of photoreceptors that use red light to trigger biochemical processes. Originally thought to be unique to plants, phytochromes have been found in fungi, bacteria and algae. In plants, they are responsible for seed germination, flowering and shade avoidance, while in bacteria they have a wide range of functions from carotenoid synthesis to plant infection via tumor formation[37]. The common feature of phytochromes is the presence of a photosensory core module (PCM) at the N-terminus, which consists of three subdomains: PAS (Per Arnt Sim domain), GAF (cGMP specific phosphodiesterases, adenylyl cyclases and FhlA domain) and PHY (phytochrome specific region)[38]. This three-domain module covalently binds a tetrapyrrol chromophore that undergoes light conversion between two states, Pr (red) and Pfr (far red). In cyanobacterial phytochromes, the chromophore is represented by phycocyanobilin, whereas in prokaryotic organisms it is represented by biliverdin[39]. Bacterial phytochromes can be further subdivided into prototypical phytochromes (as Agp1), where the parent state is represented by the Pr form, and bathy phytochromes (as Agp2), where Pfr is the thermodynamically stable state[37]. While the N-terminus is the same for these two classes, the C-terminus is variable. In prototypical phytochromes it contains a histidine kinase (HK), whereas in bathy phytochromes it is assembled by a two-component system formed by a histidine kinase (HK) and a response regulator (RR). This C-terminal domain is responsible for signaling downstream gene expression[40] **(Figure 7, panel A)**.

1.7. Agp2 photocycle

The photoreaction of the bathy phytochrome Agp2, discovered in the organism *Agrobacterium fabrum*, starts with far-red irradiation ($h\nu > 700$ nm). After photoisomerization of the C-D methine bridge of biliverdin, the chromophore has a highly stretched geometry (Lumi-F), followed by thermal chromophore relaxation and proton translocation steps in the chromophore pocket leading to rearrangement of the side chains of the neighboring amino acids in Meta-F. In particular, deprotonation of the propionic acid side chain of ring C (PsC) occurs, leading to a change in the overall electrostatics of the chromophore binding pocket, which triggers a secondary structure transition in the tongue region of the PHY domain from α-helical to β-sheet, which is completed in Pr[41] **(Figure 7, panel B)**.

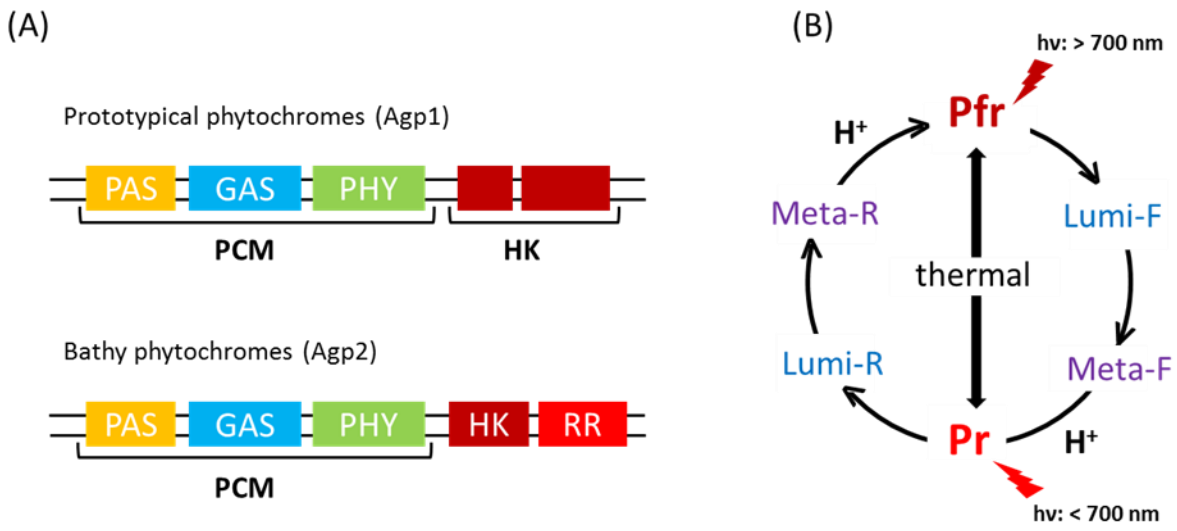

Figure 7. *Comparison of the photosensory core module (PCM) at the N-terminus and the signaling module at the C-terminus of the chromophore between Agp1 and Agp2 (A). Photocycle scheme of bacterial phytochromes. Agp2 has the Pfr form as the parent state, while Pr is the dark form of Agp1 (B).*

The transition from Meta-F to Pr is important; in this step, key residues are displaced from their original positions **(Figure 8)**. After the isomerization of the D-ring, Tyr-165 moves and induces a rotation of the side chain of Phe-192[42], which triggers the displacement of a water molecule leading to the shift of Gln-190 and Trp-440. The latter (Trp-440) is of particular interest because, together with Gln-190, it seems to be the trigger for the reorganization of the tongue domain into the β-hairpin in Pr[43]. The conformational changes in the protein structure are thought to trigger the downstream histidine kinase output module, but how the signal propagates is still an open question. In addition to the photoinduced transformations, there is a thermal pathway between the two parent states.

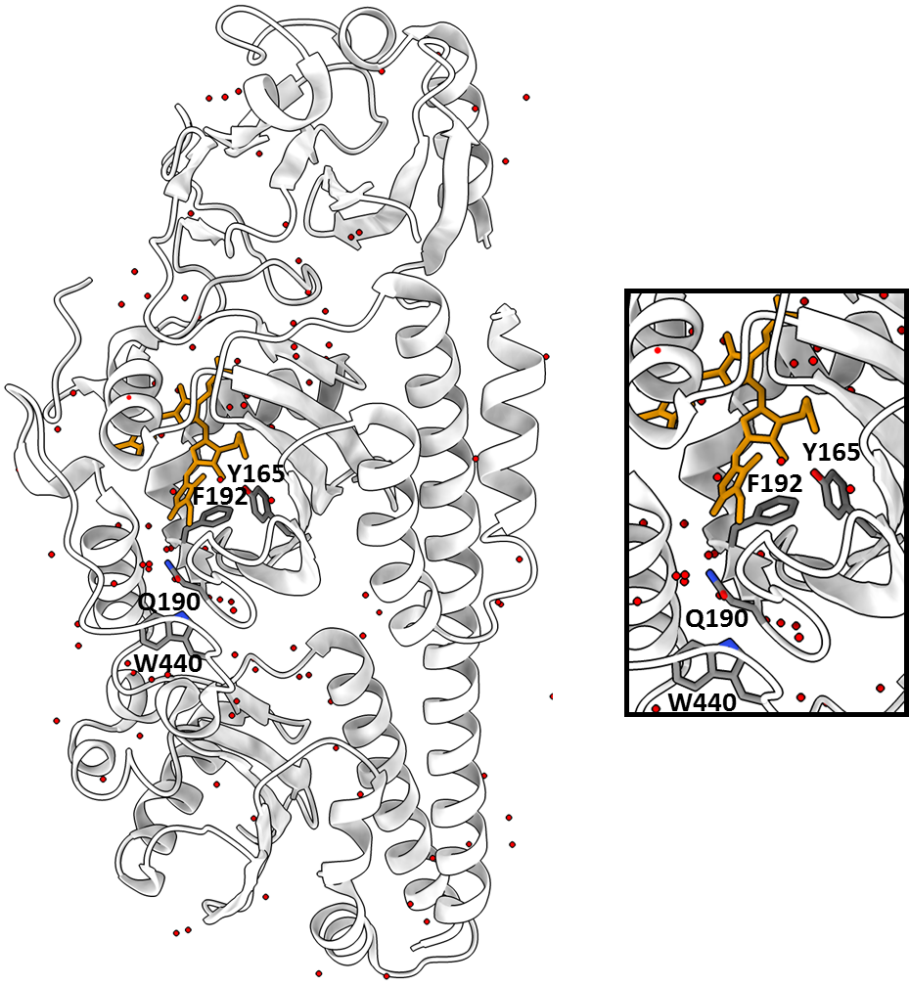

Figure 8. *Structure of the chain A of photosensory core module (PCM) of a bathy phytochrome from Agrobacterium fabrum in the Pfr state (PDB: 6G1Y). The residues involved in the secondary structure transition process are highlighted. The chromophore (biliverdin) is shown in orange and the water molecules are shown as red spheres.*

2. Motivation and strategy

In the first two parts, two microbial rhodopsins were studied (*Nm*HR and *Um*Rh1), which are an inward chloride pump and an outward proton pump, respectively, having retinal as chromophore, which under light undergo a cyclic cascade of reactions, called photocycle, which eventually lead to the transfer of substrate from one side of the protein to the other. In the third part, the bacterial phytochrome Agp2 was studied, which under red light undergoes a photoconversion between two states, Pfr and Pr. During the photocycle, biliverdin, the chromophore, undergoes a secondary structure transition from α-helix to β-sheet. For *Nm*HR and *Um*Rh1, a comparative approach has been performed to elucidate their role and protonation dynamics, using as model systems the archaeal outward proton pump *Hs*BR (for *Um*Rh1), the archaeal inward chloride pump *Hs*HR and the bacterial outward sodium pump KR2 (for *Nm*HR). The latter was chosen for comparison due to its high sequence similarity and convergent evolution. Using site-directed mutagenesis on residues known to be important for substrate transfer in *Hs*BR, *Hs*HR and KR2, and direct comparison with previously published data on these proteins, preliminary results were obtained to elucidate the role and mechanism of *Nm*HR and *Um*Rh1 and to elucidate similarities and differences. Flash photolysis and steady-state FTIR were used to study the photoreaction of *Nm*HR and *Um*Rh1, time-resolved UV/Vis spectroscopy was used to compare the photocycle of the variants with respect to the wild-type proteins, and steady-state FTIR was used to assign potential bands due to deprotonation or changes in H-bonding of conserved residues during the photocycle. In addition, a novel biophysical technique was used to study the electrostatics around the chromophore in *Nm*HR and Agp2, the insertion of the reporter group, the unnatural amino acid p-cyano-phenylalanine on conserved tryptophan residues. In the first case, two tryptophan residues close to the retinal and known to be important for the first step after retinal isomerization for chloride transfer were exchanged, and in the second case, one tryptophan residue known to be the key residue driving the secondary structure transition in Agp2 was exchanged. The preliminary results obtained with the incorporation of the unnatural amino acid will be used for further studies to elucidate the conformational changes of these two proteins related to their function. Although the thesis is structured in such a way that each protein has its own results section, similarities and differences are discussed not only with the above model systems, but also among each other.

3. Material and methods

3.1. Materials

3.2. Buffers

Name	Ingredients
Breaking buffer *Nm*HR	50 mM Tris-HCl pH 7, 150 mM NaCl
Wash buffer *Nm*HR	50 mM Tris-HCl pH 7, 150 mM NaCl, 20 mM imidazole, 0.05 % DDM (0.01 % CHS)
Elution buffer *Nm*HR	50 mM Tris-HCl pH 7, 150 mM NaCl, 400 mM imidazole, 0.05 % DDM (0.01 % CHS)
SEC buffer *Nm*HR	20 mM HEPES pH 7.5, 150 mM NaCl, 0.02 % DDM, 0.004 % CHS
Buffer A *Nm*HR	20 mM HEPES pH 7.5, 150 mM NaCl, 0.03 % DDM
Buffer B *Nm*HR	10 mM MOPS pH 7, 1 M NaCl, 0.05% DDM
Cells wash buffer Agp2	50 mM Tris pH 7.8, 400 mM NaCl, 5% glycerol
Lysis buffer Agp2	50 mM Tris pH 7.8, 50 mM NaCl, 5% glycerol

Wash buffer Agp2	50 mM Tris pH 7.7, 300 mM NaCl, 10 mM imidazole, 2% glycerol
Elution buffer Agp2	50 mM Tris pH 7.7, 400 mM NaCl, 400 mM imidazole, 2% glycerol
SEC buffer Agp2	20 mM HEPES pH 7.5, 150 mM NaCl
Breaking buffer *Um*Rh1	50 mM sodium phosphate pH 7.4, 1 mM EDTA, 5% glycerol
*Um*Rh1 buffer	20 mM HEPES pH 7.4, 100 mM NaCl
Wash buffer *Um*Rh1	20 mM HEPES pH 7.4, 100 mM NaCl, 60 mM imidazole, 0.03% DDM
Elution buffer *Um*Rh1	20 mM HEPES pH 7.4, 100 mM NaCl, 250 mM imidazole, 0.03% DDM

3.3. Plasmids

Name	Organism	Antibiotic resistance	Source
pET27b_*Nm*HR	*E. coli*	Kanamycin	Modified from pET21b_NmHR**, provided by Prof. Dr. Przemyslaw Nogly
pET21b_Agp2	*E. coli*	Ampicillin	provided by Dr. Patrick Scheerer
pPIC9K_*Um*Rh1	*E. coli* *Pichia pastoris*	Kanamycin Kanamycin/ampicillin GS418	Modified from a plasmid provided by Dr. Ulrich Terpitz
pEVOL_aaRS	*E.coli*	Chloramphenicol	provided by Dr. Johannes Von Saß

****** The DNA sequence of *Nm*HR was provided by Prof. Dr. Przemylaw Nogly and cloned into a pET27b vector. Moreover, the 6x His-tag was elongated to 10x His-tag. The T7 tag at the N-terminus was removed and the restriction sites exchanged to *Nde*I/*Bam*HI (see Appendix).

3.4. Strains

Name	Genotype	Antibiotic resistance	Manufacturer
Escherichia coli			
Top10	F- mcrA (mrr-hsdRMS-mcrBC) 80lacZ M15 lacX74 recA1 ara 139 (ara-leu)7697 galU galK rpsL (StrR) endA1 nupG		Life Technologies GmbH, Darmstadt, Germany
BL21(DE3)RP	argU (AGA, AGG), proL (CCC)	Chloramphenicol	Agilent Technologies GmbH & Co. KG, Waldbronn, Germany
MG1655 (C321ΔA(DE3))	F- lambda- ilvG- rfb-50 rph-1	Streptomycin	Addgene
Pichia pastoris			
SMD1163	Δhis4 Δpep4 Δprb1	Histidine auxotroph	Life Technologies GmbH, Darmstadt, Germany

3.5. Media

Name	Ingredients for 1 L
BHI (Brain Heart Infusion Broth)	• Brain heart infusion 6 g o Peptone 5 g • NaCl 5 g o Glucose 2 g • Na_2HPO_4 2.5 g o MQ water 1 L
BHI agar (Brain Heart Infusion Agar)	BHI components same as above plus Agar 15g
TB (Terrific Broth Medium)	o Yeast extract 24 g • Tryptone 12 g o Glycerol 4 ml • MQ water 900 ml After autoclave treatment add o 10x Phosphate buffer: 100ml 1) KH_2PO_4: 2.31 g 2) K_2HPO_4: 12.54 g 3) MQ water: 100 ml
YP (Yeast Peptone Medium)	• Yeast extract: 10 g o Peptone: 20 g • MQ water: 1 L
YPD (Yeast Peptone Dextrose Medium)	o Yeast extract: 10 g • Peptone: 20 g o Glucose: 20 g • MQ water: 1 L
YPD agar (Yeast Peptone Dextrose Agar)	o Yeast extract: 10 g • Peptone: 20 g o Glucose: 20 g • Agar: 20 g

	○ MQ water: 1 L
dYT (Double Yeast Tryptone Medium)	○ Tryptone: 16 g • Yeast extract: 10 g ○ NaCl: 5 g • MQ water: 1 L
BMGY (Buffered Glycerol-complex Medium)	○ YP: 350 mL • 500x biotin: 1 mL ○ 10x YNB: 50 mL • 1 M potassium phosphate (pH 6): 50 mL ○ 10x glycerol: 50 mL • 500 µL ampicillin (200 mg/mL) ○ 500 µL kanamycin (50 mg/mL)
BMMY (Buffered Methanol-complex Medium)	○ YP: 350 mL • 500x biotin: 1 mL ○ 10x YNB: 50 mL • 1 M potassium phosphate (pH 6): 50 mL ○ 10x methanol: 50 mL • 500 µL ampicillin (200 mg/mL) 500 kanamycin (50 mg/mL)
MD agar (Minimal Dextrose Agar)	○ Yeast Nitrogen Base: 6.7 g • Glucose: 20 g ○ Agar: 20 g • MQ water: 1 L

3.6. Chemicals

Name	Manifacturer
Gel Red (ROTI®Gelstain Red Eco)	Roth®
DDM (n-Dodecyl-β-D-Maltoside)	Sigma-Aldrich®
CHS (Cholesteryl Hemisuccinate)	Serva Electrophoresis GmbH
DNA marker (Gene Ruler 1kb)	ThermoFisher Scientific
Protein marker (Triple Color Protein Standard II)	Serva Electrophoresis GmbH
PCR cloning kit	ThermoFisher Scientific
pblunt and restriction enzymes	ThermoFisher Scientific
pCNF (p-cyano-phenylalanine)	abcr GmbH
L-Arabinose	abcr GmbH
IPTG (Isopropyl β-D-1-thiogalactopyranoside)	Roth®
All-*trans* retinal	Merck

3.7. Equipment

Name	Manifacturer
Shaker	Multitron Pro, Bottmingen Switzerland
Avanti Centrifuge J-26 XP	Beckman Coulter Life Sciences USA
Allegra X-15R	Beckman Coulter Life Sciences USA
Optima L-80 XP Ultracentrifuge	Beckman Coulter Life Sciences USA
Cells disruptor	Constants Systems®
Autoclave	Systec GmbH Linden (Germany)
Electroporator	Bio-Rad®, Micropulser™
Agarose gel electrophoresis chamber	Compact XS/S Biometra®, Jena (Germany)
SDS-Page electrophoresis chamber	Heofer® Inc, San Francisco (USA)
MicroElute® Gel Extraction kit	Omega BIO-TEK Inc, Georgia (USA)
Nucleospin® Plasmid EasyPure	Macherey-Nagel GmbH & Co. KG
Äkta	Äkta Avant 25, GE Healthcare
Affinity chromatography column	MACHEREY-NAGEL GmbH & Co. KG, Düren (Germany)
Size exclusion chromatography columns	Superdex 200, 10/300 GL, GE Healthcare HiLoad™ superdex 200 16/60 prep grade
PCR Thermocycler	MJ Mini Personal Thermal Cycler Bio-Rad®
pH-meter	Seven Compact Mettler Toledo®
UV/Vis spectrometer	Shimadzu® UV-2600i
Flash photolysis	LKS80, Applied Photophysics
FTIR spectrometer	Bruker® Vertex 80V

3.8. Biochemical Methods

3.9. *Escherichia coli* expression system

Over the last 5 decades, the expression of recombinant proteins in heterologous hosts has become a useful tool to produce larger amounts of proteins without using the original organism. The most commonly used heterologous hosts are the prokaryotic bacterium *Escherichia coli*, eukaryotic yeast, insect cells and mammalian cells, each with its own advantages and disadvantages depending on cost, expression conditions, and final protein yield. The most commonly used bacterial host today is *Escherichia coli*, a Gram-negative bacterium, due to its rapid growth, low cost and variety of culture broths, ability to achieve high cell densities, and fast and easy exogenous DNA transformation. However, there are many factors to consider when working with *Escherichia coli*, such as the inability to achieve most of the post-translational modifications, inclusion body formation and metabolic burden[44] which can lead to low recombinant protein yields. One of the factors that can overcome metabolic stress is promoter strength; lac-derived promoters induced by lactose or β-D-1-thiogalactopyranoside (IPTG) are considered strong promoters, while PBAD promoters induced by arabinose are considered medium strong promoters due to their lower expression level[45]. Therefore, strong promoters are widely used today for the expression of recombinant proteins. The T7 promoter expression system, present in pET vectors, carries the gene of interest downstream of a promoter that is recognized by the bacteriophage T7 RNA polymerase[46] and is 5 times stronger than the endogenous promoter present in *Escherichia coli*. Both the promoter and the RNA polymerase were derived from the λ prophage and integrated into an *E. coli* strain such as BL21(DE3)[47]. This system is under the control of a lacUV5 promoter that is activated by lactose or IPTG, a reagent that mimics the structure of allolactose, which binds to and inactivates the lac repressor, ensuring the transcription of the T7 RNA polymerase gene. The T7 RNA polymerase produced then binds to the T7 promoter and initiates the transcription of the gene of interest **(Figure 9 panel A)**. Other components are also present in pET vectors such as the origin of replication (ori), an antibiotic resistance gene to screen for positive recombinants, a multiple cloning site, a tag removal coding sequence, a termination signal and an affinity tag **(Figure 9 panel B)**.

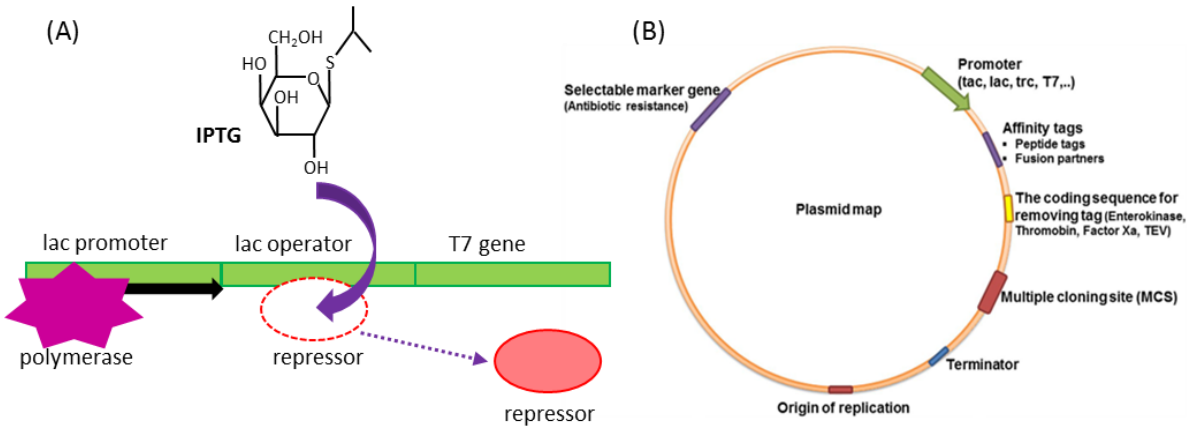

Figure 9. *T7 expression system. Scheme of IPTG induction (A), IPTG binds to and inactivates the lac repressor to promote downstream gene expression. Example of a plasmid map for protein expression in E. coli (B). Key elements are highlighted (modified from Ref.*[47]*).*

3.10. Mutagenesis

Site-directed mutagenesis (SDM) is a powerful technique for modifying DNA sequences used to study protein structure-function relationships[48]. In vitro SDM mediated by PCR (polymerase chain reaction) is currently the most effective approach to generate mutant DNA sequences[49], so over time many PCR-based methods have been developed, such as QuickChange Site-Directed Mutagenesis and Megaprimer based mutagenesis. The QuickChange Site-Directed Mutagenesis system is the simplest and most widely used method, where two complementary primers carrying the single point mutation at the desired position are introduced in a single PCR[50]. After DNA amplification and product purification, the enzyme *Dpn*I is added to the reaction mixture. *Dpn*I is a restriction enzyme that recognizes and cleaves the methylated DNA template vector, leaving the newly synthesized DNA intact. This is possible because the *in vitro* amplified DNA lacks the methylation that *Dpn*I recognizes, allowing selective removal of the template DNA **(Figure 10)**.

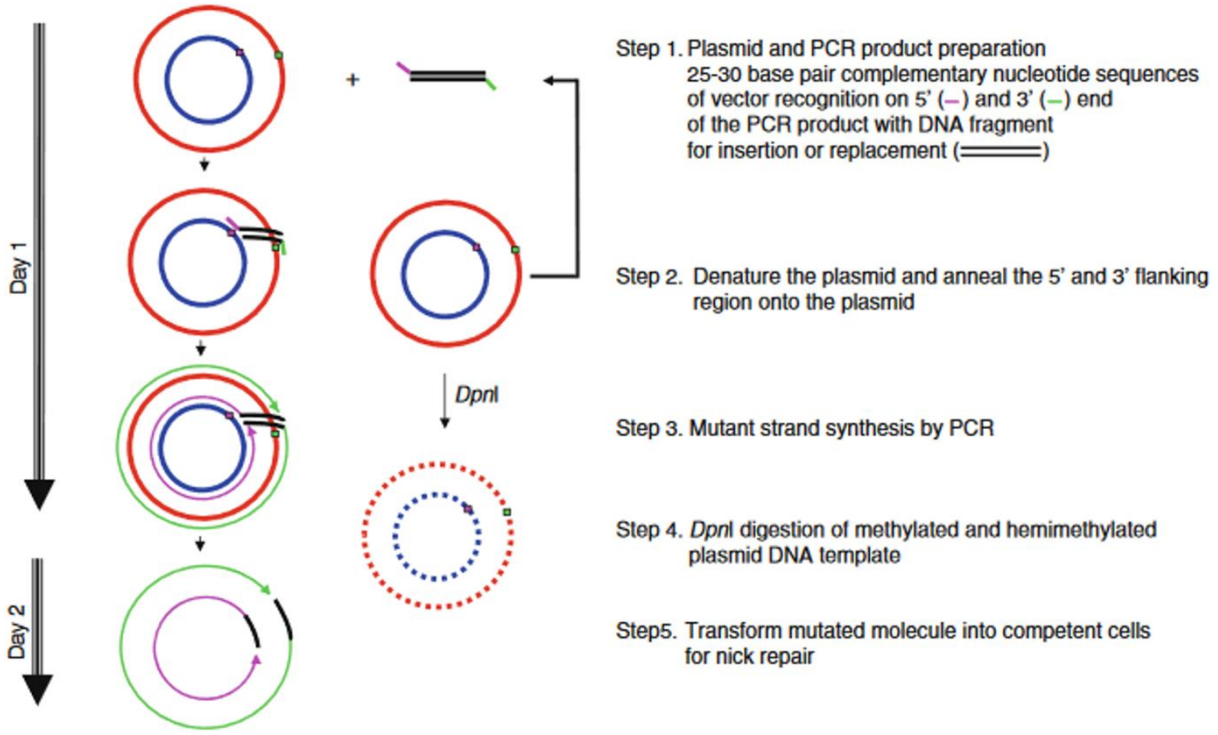

Figure 10. *Workflow of site-directed mutagenesis using a Quick Change Mutagenesis method. (Figure modified from Ref.*[51]*). Two complementary primers are used to amplify the plasmid DNA, followed by DpnI to cleave the template DNA.*

On the other hand, the Megaprimer method uses 2 flanking (external) primers and 1 or 2 mutagenesis (internal) primers carrying the desired mutation, in two rounds of PCR. In the first PCR, one of the mutagenesis primers and one of the flanking primers is used, while in the second round, the amplified DNA sequence is used as a megaprimer for the second PCR, together with the other flanking primer[52] **(Figure 11)**.

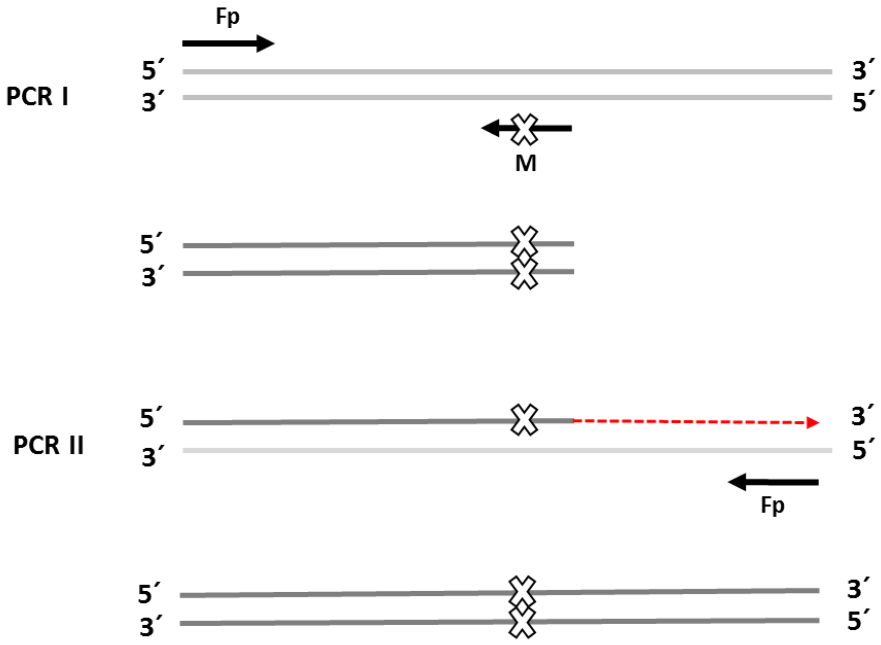

Figure 11. *Workflow of site-directed mutagenesis using a Megaprimer method. In the first round of PCR, an internal primer (M) carrying the desired mutation is used together with a flanking primer (Fp). The product of the first PCR is then used as a Megaprimer for the second round of PCR together with the other flanking primer.*

Protocols		
QuickChange Site-Directed Mutagenesis	**Megaprimer**	**Megaprimer**
	PCR I:	PCR II:
32 µl water	32 µl water	18 µl water
10 µl 5x HF Phusion Buffer	10 µl 5x HF Phusion Buffer	15 µl PCR I
2.5 µl DMSO (end concentration 5%)	2.5 µl DMSO (end concentration 5%)	10 µl 5x HF Phusion Buffer
1.5 µl Forward mutagenesis primer (100 pmol)	2 µl dNTPs (10 mM each)	2.5 µl DMSO (end concentration 5%)
1.5 µl Reverse mutagenesis primer (100 pmol)	1 µl Forward mutagenesis primer (100 pmol) + 1µl Reverse flanking primer (100 pmol) **or**	2 µl dNTPs (10 mM each)
1 µl DNA template	1 µl Reverse mutagenesis primer (100 pmol) + 1µl Forward flanking primer (100 pmol)	1 µl Forward flanking primer (100 pmol) or 1 µl Reverse flanking primer (100 pmol)
1 µl dNTPs (10 mM each)	1 µl DNA template	1 µl DNA template
0.5 µl Phusion Hot Start polymerase	0.5 µl Phusion Hot Start polymerase	0.5 µl Phusion Hot Start polymerase

Program		
QuickChange Site-Directed Mutagenesis	**Megaprimer**	**Megaprimer**
	PCR I:	PCR II:
98°C 3´ denaturation	98°C 30´´´	98°C 30´´
98°C 1´ denaturation 60°C 1´ annealing 72°C 5´ extension } x18	98°C 10´´ 68°C 15´´ 72°C 30´´ } x45	98°C 10´´ 68°C 15´´ 72°C 15´´ } x45
72°C 8´ extension	72°C 5´	72°C 5´
4°C forever	4°C	4°C

After *Dpn*I digestion, the QuickChange product is run on an agarose gel, the band corresponding to the newly synthesized DNA is excised, and the DNA is purified by a Gel Extraction kit. The plasmid is then electrotransformed into *E. coli* Top10 competent cells where the nicks are repaired. The plasmid DNA is then isolated and the plasmid containing the mutation of interest is verified by Sanger sequencing (Microsynth Seqlab). In Megaprimer mutagenesis, the product of PCR I is extracted from the agarose gel and used as a megaprimer for the subsequent PCR II. The product of PCR II is then extracted and cloned into a pBlunt vector. After Sanger sequencing (Microsynth Seqlab) to verify correct insertion of the DNA into the vector, the insert is cloned into pET27b vector for *Nm*HR and pPIC9K for *Um*Rh1 using the appropriate restriction sites. Only QuickChange site-directed mutagenesis was used to generate Agp2 variants.

Plasmid	**Restriction sites**
*Nm*HR	*Nde*I/B*am*HI
*Um*Rh1	*Eco*RI/*Not*I

3.11. Nanodiscs reconstitution

Detergent solubilization (e.g. DDM) is an easy way to extract the protein from the membrane compartment, but it does not provide a natural environment for the protein. For this reason, the use of lipid nanodiscs is becoming increasingly common, especially when the protein is insoluble or shows altered functions in the presence of detergent. Lipid nanodiscs, a modification of the human high-density lipoprotein fraction, consist of 2 copies of the amphipathic helical membrane scaffold protein (MSP) assembled into a discoidal phospholipid bilayer[53] (e.g. DMPC, DPPC, POPC), providing a native-like membrane environment for the protein **(Figure 12, panel A)**. In addition, the reconstitution of membrane proteins into lipid nanodiscs offers many advantages for biophysical studies, such as the absence of detergent, which is a major challenge in IR measurements, and the achievement of higher protein concentrations due to the increased water solubility[54].

Protocol:

Membrane protein	Scaffold proteins	Lipids
*Um*Rh1: 1	MSP1D1: 2	DMPC: 110

After mixing the membrane protein with MSP1D1 scaffold proteins and DMPC lipids in a ratio of 1:2:110, Na-cholate (20 mM) is added to the reaction and the mixture is incubated at 25°C for 1 hour, during which time the nanodiscs are assembled. The detergent (DDM) is then removed by adding Bio-Beads for 2 hours at the same temperature and then overnight at 4°C. The next day, the solution containing the protein reconstituted in the nanodiscs is aspirated with a syringe and centrifuged at maximum speed for 15 minutes, in an Eppendorf centrifuge, to remove the aggregation, and finally the sample is loaded on a size exclusion column (Äkta) to separate the fractions of nanodiscs containing the protein from the empty ones **(Figure 12, panel B)**.

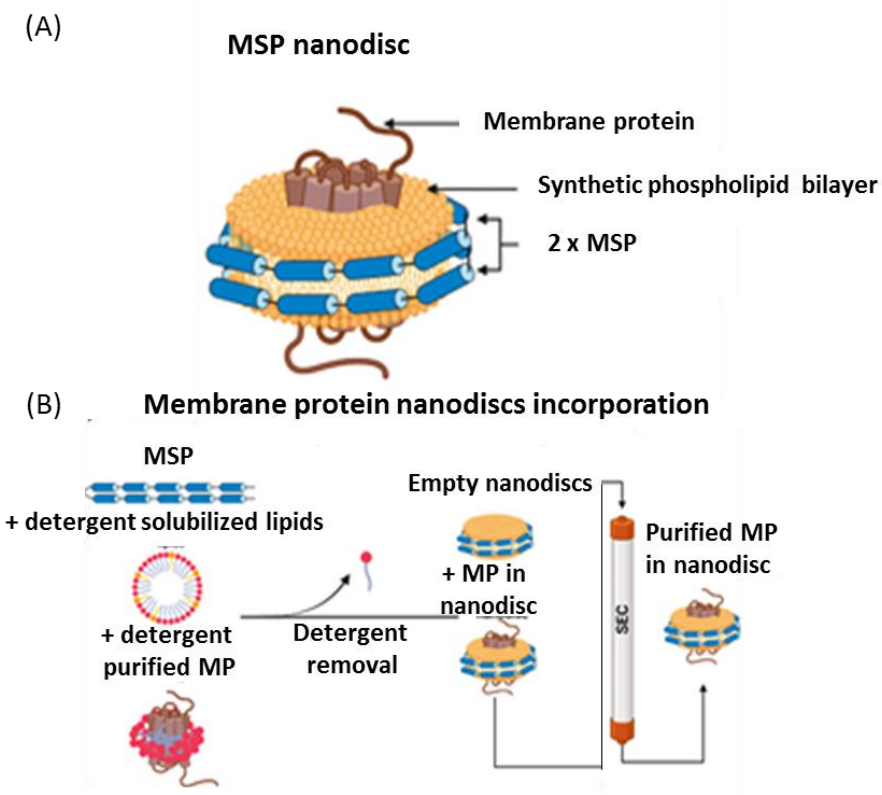

Figure 12. *Nanodiscs are composed of two scaffold proteins and a phospholipid bilayer (A). After the assembly of the membrane protein with MSP and lipids, the detergent is removed and the fraction of nanodiscs containing the protein is purified by size exclusion chromatography (B). (Figure modified from Ref.*[55]*).*

3.12. *Pichia pastoris* expression system

Eukaryotic yeasts are widely used as heterologous organisms for the production of recombinant proteins, achieving high yields. The yeast *Saccharomyces cerevisiae* has been extensively used, however it shows disadvantages regarding protein hyperglycosylation and inadequate to consume substrates such as glycerol or xylose, moreover it is sensitive to temperature and pH[56]. To overcome these challenges, other eukaryotic yeasts have been developed, such as the methylotrophic yeast *Pichia pastoris*. This organism has many advantages, such as higher cell density and protein yield[57] and proper protein folding. *Pichia pastoris* metabolizes methanol as a carbon source for energy production. While the wild type cannot be used for protein expression, the GS115 strain is the most widely used in the laboratory for the production of recombinant proteins[58]. Its genome contains two AOX genes encoding alcohol oxidase (AOX1 and AOX2). When methanol is the only carbon source used, the AOX1 promoter is highly inducible, while the AOX2 gene is controlled by a weaker promoter[59]. One of the most common *Pichia pastoris* vectors is pPIC9K, which is a secretory expression vector; a signal sequence is inserted after the promoter region[60] to ensure that the expressed protein is secreted outside the cells. After integration into the host genome, the most efficient clone must be positively screened with an antibiotic such as geneticin, as it is not possible to control the number of copies. One of the most commonly used strains for membrane protein expression is SMD1163, which has both AOX1 and AOX2 genes and is protease free[61]. The workflow for protein expression in *Pichia pastoris* is as follows: the exogenous DNA is first transformed into an *E. coli* strain such as Top10 and then after verification via Sanger sequencing is cloned into a *Pichia pastoris* expression vector using the *Eco*RI/*Not*I restriction site. The plasmid DNA is then linearized with the *Sac*I restriction enzyme and transformed into a *Pichia pastoris* expression vector such as pPIC9K. Linearization with *Sac*I is used to improve integration efficiency. The clones that grow on a MD plate are subsequently screened on plates with increasing concentrations of geneticin

and the optimal clone is tested by small scale expression prior to large scale expression as shown in **Figure 13**.

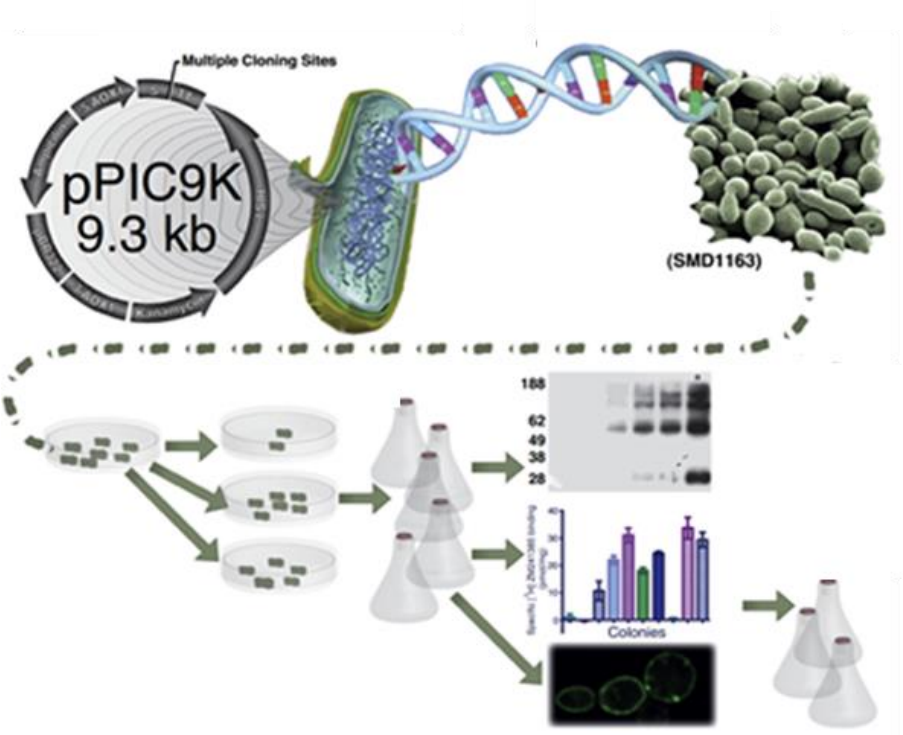

Figure 13. *Workflow of the Pichia pastoris expression system. After transformation in SMD1163 cells, the correct clone is selected on MD plates and subsequently on plate supplemented with increasing concentration of geneticin and the expression level of the optimal clone is then verified in a small scale before upscaling the expression. (Figure modified from Ref.*[61]*).*

3.13. Amber codon suppression

In vivo incorporation of unnatural amino acids (UAA) is a novel technique that allows the modification of protein properties that can be used for many applications, from spectroscopy to biology, catalysis and therapeutic approaches[62]. The mechanism of translation, the process by which the polypeptide is formed, is determined by the nucleotide sequence of the mRNA and it is a mechanism mediated by the ribosome. The loading of each amino acid is achieved by an aminoacyl synthetase - tRNA pair (aaRS), which forms an aminoacylated - tRNA (aa-tRNA) in a highly specific manner. 64 nucleotide triplets code for 20 amino acids, but 3 of these 64 codons

do not add an amino acid to the polypeptide chain. These are the 3 stop codons, called Amber (UAG), Opal (UAA) and Ochre (UGA)[63] that recruit the release factors (RF1 and RF2) to terminate synthesis and release the polypeptide from the ribosome. While tRNA anticodons are conserved among different organisms, aaRS are rather specific, i.e. they do not aminoacylate tRNAs from other species. This concept was relevant for the development of a system capable of introducing noncanonical amino acids in *E. coli in vivo*. In addition, some species do not recognize the Amber codon as a stop codon; for example, the archaeal *Metanococcus jannaschii* introduces a tyrosine at this position[63]. In addition, the aaRS in this organism has minimal interaction with its cognate tRNA, making it possible to mutate the aaRS binding pocket to accept a noncanonical amino acid (e.g. p-cyano-phenylalanine). For successful ncAA (non canonical amino acid) insertion, the *Metanococcus jannaschii* aaRS must be orthogonal to the one present in *E. coli*[64]. In 2010, *Young et al.* developed a plasmid called pEVOL containing 2 copies of the archaeal aaRS specific for the insertion of the unnatural amino acid p-cyano-phenylalanine. The aaRS gene is under the control of two promoters, one constitutive (glnS') and one arabinose-inducible (araBAD)[65]. One of the major challenges in pCNF insertion is the release factor-1, which is recruited by the UAG codon and competes with the orthogonal tRNA to stop translation at the Amber codon position. Thus, an *E. coli* strain called MG1655 (C321ΔA(DE3)), which is ΔRF1 and in which all UAG codons have been replaced by UAA, was developed. The obtained organism showed an improved success in the incorporation of the ncAA in response to the Amber codon[66]. Nevertheless, it should be pointed out that the more common *E. coli* strain BL21(DE3), also used for the introduction of UAAs, represents a good tool due to the fact that the Amber codon is the rarest in the *E. coli* genome (7%), despite the competition with the RF1 **(Figure 14)**.

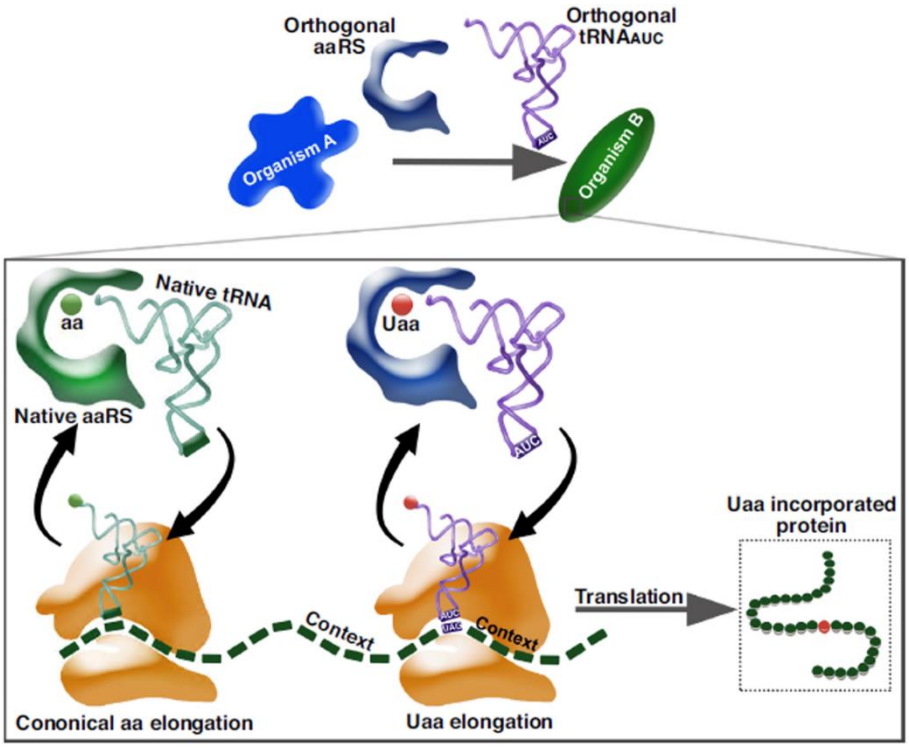

Figure 14. *Scheme of nCAA insertion in E. coli. Using an engineered tRNA/aaRS pair from the organism Methanococcus jannaschii, it is possible to introduce the unnatural amino acid pCNF at the TAG triplet (Amber codon), because this organism does not recognize it as a stop codon. (Figure modified from Ref.*[67]*).*

3.14. Expression and purification of *Nm*HR wild type and variants for spectroscopy

The gene for *Nm*HR wild type and variants was introduced into *E. coli* BL21(DE3) RP cells by electrotransformation. After 1 hour at 37°C, the cells were grown on a BHI agar plate supplemented with kanamycin (50 µg/ml). The next day, the cells were transferred to flasks containing 500 ml BHI media supplemented with 50 µg/ml kanamycin and incubated in a shaker at 37°C until OD_{600} reached 0.8 - 1.0. At this point, 0.5 mM IPTG and 12.5 µM all-*trans* retinal were added to the culture from stock solutions of 1 M and 25 mM, respectively. After 3-4 hours, the expression was harvested at 6000 rpm (rotor JLA 8.1) for 15 minutes and the pellet was stored at -80°C. The cells were then thawed and disrupted using a cell disruptor at 1.7 kbar pressure with breaking buffer *Nm*HR. After 3 rounds of disruption, a pinch of DNase and a tablet of protease inhibitor were added and the membrane fragments were centrifuged for 1 hour at 40000 rpm (rotor Ti45). The pellet was solubilized in the breaking buffer *Nm*HR containing 1.5% DDM (w/v) and stirred for 2 hours at 4°C. After another round of centrifugation, the solubilizate was applied to a Ni-NTA column and the His-tagged protein was washed and eluted with wash- and elution buffer *Nm*HR, respectively, using an imidazole gradient elution. The eluate was then concentrated using an Amicon with a 50 kDa cutoff and washed twice with buffer A.

Special cases: *Nm*HR N98D, *Nm*HR N98D/Q109D, *Nm*HR D231E and *Nm*HR D231N were disrupted and purified using 50 mM Tris-HCl (pH 8) and 1 M NaCl as published by *Tsukamoto et al.* [68]. All the other steps were the same as the above protocol.

3.15. Expression and purification of *Nm*HR wild type and variants for crystallization

Differences from the above protocol in sample preparation for crystallization are as follows. The expression was induced at lower density (OD_{600} of 0.6) with 0.5 mM IPTG and more all-*trans* retinal (50 µM), after induction the temperature was lowered to 20°C and harvested after 5.5 hours. The solubilization mixture consisted of 1% DDM, 0.2% CHS (from a stock solution of 10% DDM, 2% CHS), and 20 mM imidazole (from a stock solution of 2 M) in the

solubilization buffer. The buffers used for the Ni-NTA column had different concentrations of DDM and CHS, 0.05% DDM - 0.01% CHS. Finally, the last difference consists in an additional purification step, a size exclusion chromatography with SEC buffer, in order to obtain a higher purity. The eluate was then concentrated to ~70 mg/ml and the purity (280 nm/retinal peak (~ 546 nm) 1.7-2.2) was verified by UV/Vis spectroscopy.

3.16. Expression and purification of Agp2 and Agp2 W440F for spectroscopy

The gene for Agp2 wild type and Agp2 W440F was introduced into *E. coli* BL21(DE3) RP cells by electrotransformation. After 1 hour at 37°C the cells were grown on a BHI agar plate supplemented with ampicillin (200 µg/ml). The next day, the cells were transferred to flasks containing 500 ml of TB media supplemented with 200 µg/ml ampicillin at 37°C until OD_{600} reached 0.8 - 1.0. At this point, 0.5 mM IPTG was added to the culture from a stock solution of 1 M and the expression continued overnight at 20°C. The next day, the expression was harvested at 6000 rpm (rotor JLA 8.1) for 15 minutes and the pellet was washed twice with cells wash buffer Agp2 and once with lysis buffer Agp2 at 8.167 rpm in rotor JLA 16.250. The cells were then disrupted using a cell disruptor at a pressure of 1.7 kbar. After 3 rounds of disruption, a pinch of DNase and a tablet of protease inhibitor were added and the lysate was centrifuged at 19.678 rpm (rotor Ti45) for 20 minutes. The supernatant was then applied to a Ni-NTA column and the His-tagged protein was washed and eluted with Ni-NTA wash buffer and elution buffer. The eluate was then concentrated using an Amicon 30 kDa cutoff and applied to a size exclusion column using the SEC buffer. Absorbance at 280 nm was evaluated after size exclusion to calculate the amount of biliverdin (3 molar excess) to be added to the apoprotein overnight. The biliverdin was prepared by dissolving the powder in 0.5 ml methanol and 1.5 ml SEC buffer. The following day, the solution of protein with biliverdin was concentrated and subjected to another size exclusion to separate the protein fraction containing the biliverdin from the free chromophore. The concentration of protein was then calculated by monitoring the absorbance at ~ 750 nm.

3.17. Protocol for insertion of the unnatural aminoacid p-cyano-phenylalanine in *Nm*HR and Agp2

60 ng/µl of the expression plasmid containing the gene encoding the protein of interest, containing the TAG codon at the desired position for ncAA insertion (pET27b *Nm*HR and pET21b Agp2), was co-transformed with 60 ng/µl of the pEVOL plasmid containing two copies of the tRNA-aaRS complex of the archaea *Methanococcus jannaschii* into *E. coli* strain BL21(DE3) (for *Nm*HR W99pCNF, *Nm*HR W201pCNF and Agp2 W440pCNF) or into the *E. coli* strain C321ΔA(DE3) (for Agp2 F192pCNF). The expression was performed in TB media supplemented with kanamycin for *Nm*HR or ampicillin for Agp2 and chloramphenicol (34 µg/ml), which is the antibiotic resistance for the pEVOL plasmid. Before starting the expression, 0.2% arabinose was added to the media (from a 20% stock solution previously dissolved in MQ water) to induce the tRNA-aaRS pair on the pEVOL plasmid. The unnatural amino acid p-cyano-phenylalanine dissolved in 0.5 N NaOH (stock solution: 0.2 M) was added when the optical density of the cell culture reached OD_{600} of 0.4-0.5, to 2-4 mM pCNF final concentration. After induction with IPTG (and additional all-*trans* retinal for *Nm*HR), the expression was maintained at 20°C overnight. Subsequent cell disruption and protein purification were performed as described for the corresponding wild-type proteins.

3.18. Expression and purification of *Um*Rh1 wild type and variants for spectroscopy

50 mL of preculture containing the correct clone of *Um*Rh1 or its variants, previously screened by geneticin, sequencing, and test expression was transferred to 500 mL of BMGY medium and shaken overnight at 30°C. The next day, 100 ml were transferred to 500 ml BMMY medium and fed twice with methanol containing 500 µM all-trans retinal on that day and twice the following day. The cells were then harvested at 6000 rpm (rotor JLA 8.1) for 15 minutes and resuspended with 100 ml breaking buffer *Um*Rh1 supplemented with 100 µL PMSF (20 mg/ml) and 50 µL benzamidine (20 mg/ml) prior to cell disruption at 2.7 kbar pressure. After centrifugation at 4270 rpm (rotor SX4750), for 10 minutes, the membrane fractions were centrifuged at 40000 rpm (rotor Ti45) for 3 hours. After determining the weight of the pellets,

9x excess *Um*Rh1 buffer was used to resuspend the pellet, together with 1:1000 PMSF (20 mg/ml). The detergent DDM was then added to a final concentration of 2% and stirred overnight at 4°C. The next day, the mixture was centrifuged at 40000 rpm (rotor Ti45) for 1 hour and the solubilizate was loaded onto a Ni-NTA column and washed and eluted with wash buffer *Um*Rh1 and elution buffer *Um*Rh1, respectively. After removing the imidazole by washing the eluate in a concentrator with a 50 kDa cutoff, the concentrations and purity were checked by UV/Vis spectroscopy.

3.19. Biophysical methods

3.20. UV/Vis spectroscopy

UV/Vis spectroscopy is a powerful tool used in biochemistry and biophysics to characterize biological compounds[69]. Rhodopsins, which contain retinal as a chromophore, have a specific absorption in the UV/Vis range and therefore this technique can be used as a quantitative analysis. For liquid samples, the measurement is performed in cuvettes by first measuring the reference, usually the buffer without protein, and then the sample consisting of the protein of interest in the same buffer **(Figure 15)**. The absorbance can then be calculated using the following equation

$$A = \log_{10} I_0 / I_1$$

Where I_0 is the intensity of the light passing through the reference and I_1 is the intensity of the light passing through the sample. If $I_1 < I_0$, it means that the sample has absorbed light. The detector then converts the light to current and produces a plot of absorbance on the y-axis and wavelength on the x-axis.

The absorbance can be used to calculate the concentration of the sample using the Lambert-Beer equation

$$A = \varepsilon c l$$

Where l is the optical path length of the cuvette (cm), c is the concentration of the sample (M), and ε is the extinction coefficient of the sample (M^{-1} cm^{-1}).

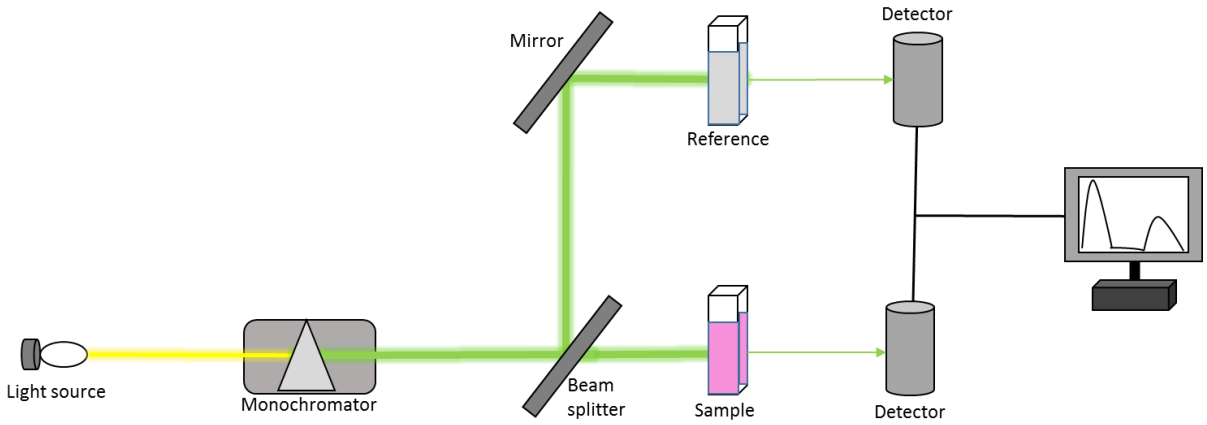

Figure 15. *Principle of UV/Vis spectroscopy. The light source is incident on the monochromator and is converged by the beam splitter and mirrors through the reference and sample. The detectors then convert the light into an electric current, producing a plot of absorbance as a function of wavelength.*

The wavelength of the chromophore absorption determines the colour of the protein in the so-called "colour tuning", which identifies each rhodopsin according to its maximum absorption of the retinal. While the tryptophans in the protein gives rise to the band at 280 nm, the retinal of microbial rhodopsins appear in a range of 400-700 nm^2. More specifically, the protonation state of the retinal Schiff base (RSB) plays a role in the UV/Vis absorption of microbial rhodopsin. The absorption is defined by the difference between the potential energy of the excited state S_1 and the ground state S_0. The electronic character of the π-electron system of the protonated retinal Schiff base changes upon emission of an electron from the energy level S_0 to the first excited state S_1 (electronic transition). In S_0, the positive charge is located on the nitrogen of the protonated retinal Schiff base (RSBH), whereas in the transition to the S_1 state, the positive charge is transferred to the β-ionone ring **(Figure 16)**[70].

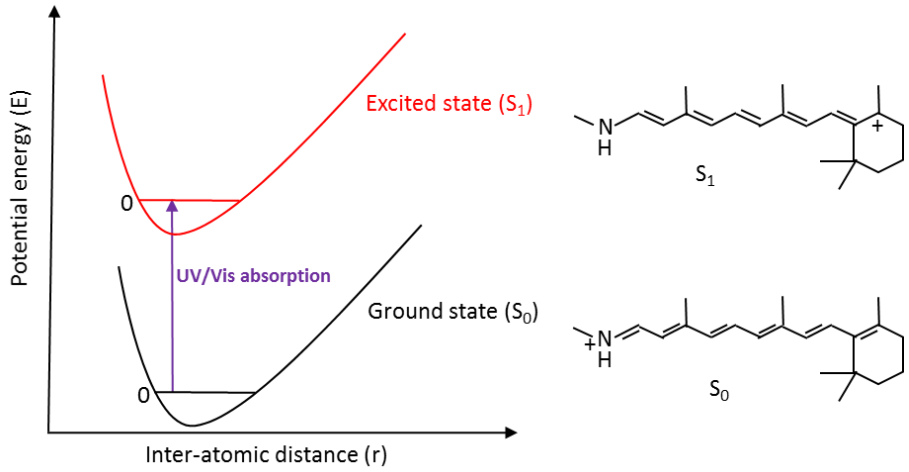

Figure 16. *Graph of UV/Vis absorption, defined as the difference in potential energy between the ground state (S_0) and the excited state (S_1).*

Upon light absorption, microbial rhodopsins undergo a cyclic cascade of reactions called photocycle. Absorption of a photon of visible light leads to a configuration change of the retinal from all-*trans* to 13-*cis* and subsequent formation of intermediate states leading to ion translocation or channel opening. The flash photolysis technique allows the spectral changes of the intermediates to be studied as a function of time. The setup is equipped with a long pulse YAG laser (532 nm) that initiates the photocycle and a xenon continuous lamp that records the absorption, combined with the use of the monochromator, the wavelength can be selected **(Figure 17)**[71].

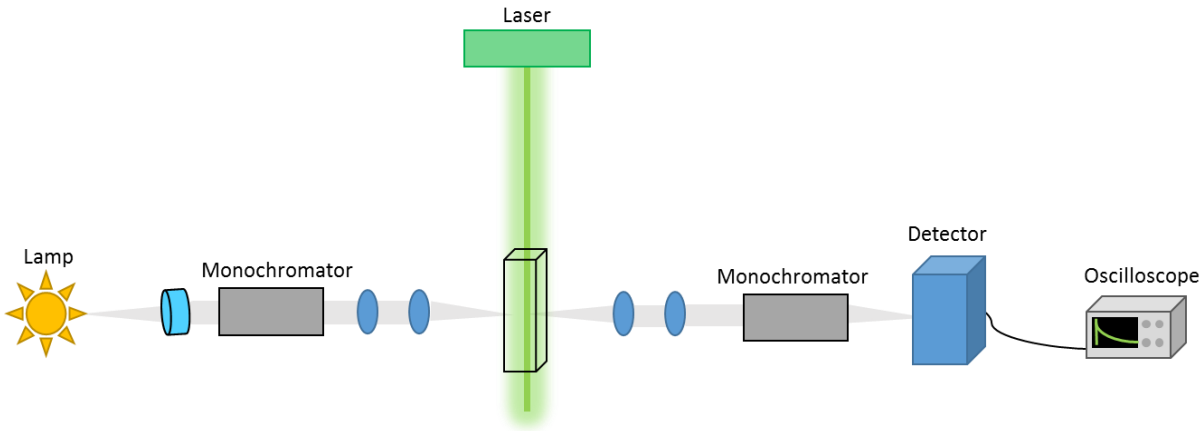

Figure 17. *Flash photolysis setup. The sample is excited by a green laser which initiates the photocycle, while the selected wavelength of the lamp records the absorption changes.*

Protocol:

The protein sample in the buffer according to the protein and the measurement is first measured in the UV/Vis spectrometer to evaluate the concentration. The optimal OD is around 0.6-0.8, at the retinal peak. Then 800 µl in a cuvette are placed in the flash photolysis setup and the wavelength range for the time-resolved experiment is 400-510 nm and 550-700 nm with 10 nm steps. Since the 520-540 nm range overlaps with the emission wavelength of the laser, this range is excluded. 10 laser shots are averaged for each wavelength to improve the signal-to-noise ratio. The data are then analyzed using Origin 2019 and MatLab 2012.

3.21. FTIR spectroscopy

Vibrational spectroscopy, such as FTIR, is used as a qualitative tool to identify the functional groups present in molecules[72]. While UV/Vis spectroscopy induces electronic transitions between the ground state and the excited state, IR spectroscopy induces vibrational transitions **(Figure 18)**. The principle of IR spectroscopy is the interaction of the IR light source with the sample resulting in a transition of vibrational energy states[73]. IR spectroscopy can be divided in near IR (12500 - 4000 cm^{-1}), mid IR (4000 - 400 cm^{-1}) (most commonly used), and far IR (400 - 10 cm^{-1}), which is rarely used.

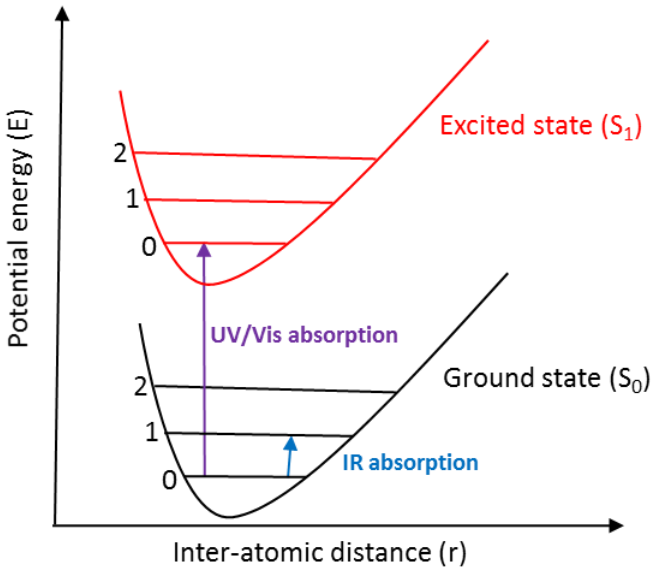

Figure 18. *Graph of infrared absorption, defined as the difference in potential energy between the vibrational states.*

The unit of IR spectroscopy is the wave number which is the inverse of the wavelength (cm^{-1}).

Eq. 1 $$\lambda = \frac{c}{\nu} = \frac{1}{\tilde{\upsilon}}$$

Vibrational spectroscopy is based on the molecular vibrations of molecules. One can imagine a chemical bond as two masses, A and B, which are connected by massless springs which are the intramolecular interactions[74]. Using Hooke's law:

Eq. 2 $$F_x = -f\Delta x$$

This equation describes that when there is a displacement Δx along the x-axis, there is a restoring force F_x and f is a constant that describes the rigidity of the string, more precisely the strength of the bond.

Applying Newton´s second law:

Eq. 3 $$F = ma \qquad a = \frac{d^2\Delta x}{dt^2}$$

Combining this equation with Hooke's law **(Eq. 2)** one obtains:

Eq. 4 $$-f\Delta x = m\,\frac{d^2\Delta x}{dt^2}$$

This equation represents the differential equation for simple harmonic motion whose result is represented by a sinusoidal motion and an angular frequency:

Eq. 5 $$\omega = \sqrt{\frac{f}{\mu}}$$

where μ is the reduced mass of the system, in order to account for the motion of both atoms in the bond: $\mu = \frac{m_A m_B}{m_A + m_B}$

To express it in wavenumbers, knowing that:

Eq. 6 $\nu = \frac{\omega}{2\pi}$ together with **Eq. 1** one obtains:

Eq. 7 $$\tilde{\upsilon} = \frac{1}{2\pi c}\sqrt{\frac{f}{\mu}}$$

Therefore, the vibrational frequency is directly proportional to the squared root of the force constant that occurs when the electron density in the bond between the two atoms increases[75] and it is inversely proportional to the squared root of the reduced mass of the system, meaning that stronger bonds absorb at higher frequencies.

The presence of functional groups in a molecule causes characteristic frequencies to appear in IR spectra. Vibrations can be classified into stretching vibrations, which increase or decrease the bond length, and bending vibrations, which cause a change in the bond angle. Bending vibrations are further subdivided into in-plane bending and out-of-plane bending; in-plane bending vibrations are subdivided into scissoring and rocking, and out-of-plane bending vibrations are subdivided into waggling and twisting[76].

The FTIR setup is based on the Michelson interferometer **(Figure 19)**, which consists of 2 mirrors, one fixed and one movable. The interferometer splits the IR beam into 2 optical paths, via a beam splitter, and recombines them to create an interference pattern and the IR light passes through the sample. The result is an interferogram, which is a plot of light versus optical retardation due to the moving mirror[77].

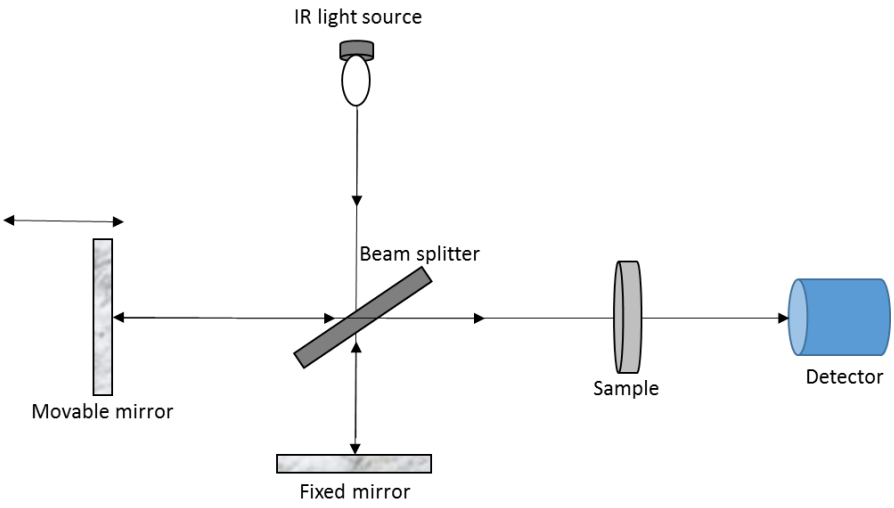

Figure 19. *Infrared spectrometer setup. IR is based on the Michelson interferometer. The beam is split into a moving mirror and a fixed mirror and then they are reconstructed creating an interference and hitting the sample which is then measured by the detector giving a plot of light versus the optical retardation of the moving mirror.*

IR is sensitive to protonation state, bond conformation such as the retinal conformation from all-*trans* to 13-*cis* which can be seen in the IR spectra. In addition, intra- and intermolecular interactions such as H-bond interaction and local electric fields can be monitored. In addition, vibrations of amino acids and protein backbone, as well as cofactors and water molecules, can be studied in IR spectroscopy[78]. One of the challenges of measuring a sample with FTIR is the detergent content of the sample and hydration. Nanodiscs can be used to overcome the use of detergents, which can cause water artifacts that overlap with the protein signal. Proteins with cofactors such as rhodopsins and phytochromes can be measured by light-induced difference spectroscopy using an LED, green for rhodopsins and red for phytochromes. The difference between the light and dark state can provide information about the side chain of amino acids (deprotonation or change of H-bonding) and chromophore conformations. For example, the 1800-1700 cm^{-1} region of IR spectra contains side chain modes of carboxylic acid residues, 1700-1600 cm^{-1} side chain of asparagine, glutamine and arginine together with amide I modes. The latter is an indication of conformational changes in the protein backbone and is usually located at about 1660 cm^{-1} [79]. The 1300-1100 cm^{-1} region is the retinal fingerprint region, where bands due to the different conformation of retinal can be found **(Figure 20).**

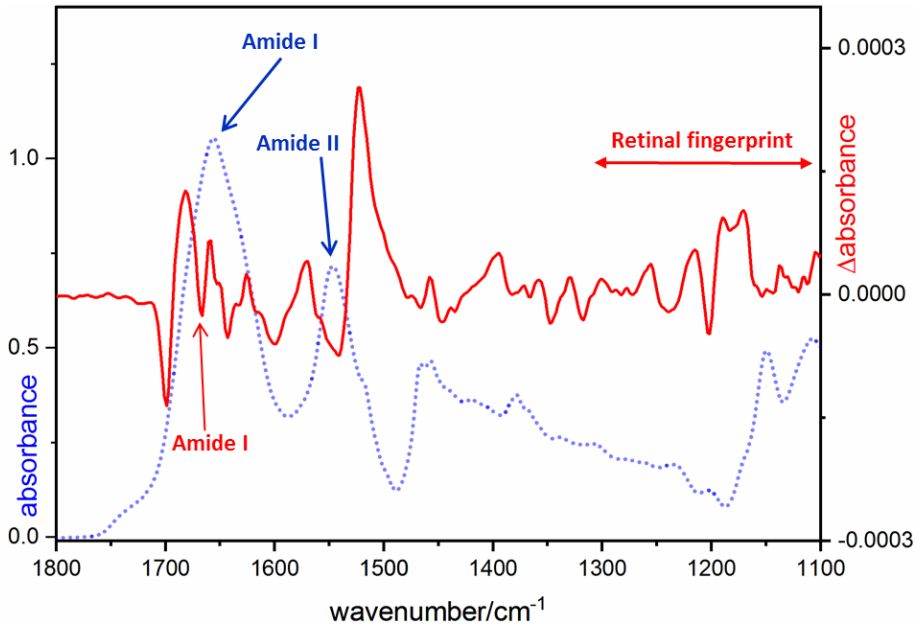

Figure 20. *IR absorption spectrum (dashed blue) versus IR difference spectrum (red) of NmHR.*

Initially thought to be limited to purified proteins, in-cell IR spectroscopy is becoming a powerful tool for studying the protein in the native environment of the cell[80].

Protocol:

The purified sample is concentrated to a concentration of 40-50 mg/ml, then placed on a BaF_2 window and allowed to dry under a stream of air, then rehydrated using a mixture of water and glycerol next to the protein sample to achieve a humidity that "rehydrates" the sample so as not to alter the functionality of the protein. After waiting approximately 1.5 hours for rehydration, the light-induced different spectra are measured, using a LED, averaging 100 scans. The spectra are then analyzed using Opus and Origin 2019 software.

4. Results

4.1. *Nm*HR: *Nonlabens marinus* halorhodopsin

In the following results section, a comparison between *Nm*HR, *Hs*HR and KR2 was performed to elucidate the role of important amino acids for the phototransduction of *Nm*HR, which are shown in **Figure 21** and listed in **Table 1**. In detail, a first elucidation of the NTQ motif (Asn-98/Thr-102/Gln-109) was performed, which is conserved in the outward sodium pump KR2 (NDQ), but is replaced by a TSA motif in *Hs*HR. This is followed by a dissection of the residues involved in chloride release and uptake and the two cysteines contained in *Nm*HR (Cys-55 and Cys-105). Finally, the insertion of the unnatural amino acid p-cyano-phenlylalanine, exchanging two tryptophan residues (Trp-99 and Trp-201), part of the binding pocket of the retinal, was studied. Some aspects of the project were carried out in collaboration with Karoline-Luisa Lê Công, Dr. Sabine Oldemeyer and Antreas Vorkas (Freie Universität, Berlin) and Dr. Marvin Asido (Goethe Universität, Frankfurt). Two master students (Celine Alisha Galander and Fenja Karin Blank) contributed significantly to the production and measurements of some of the mutants.

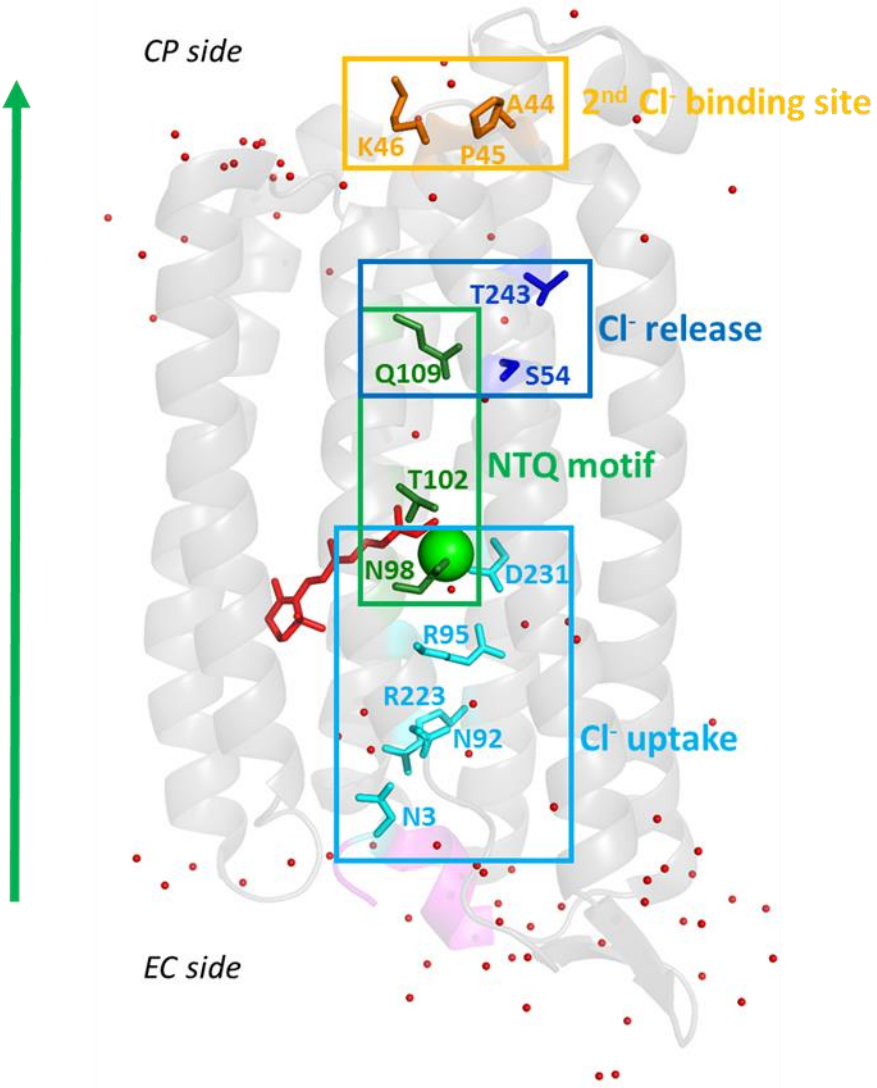

Figure 21. *Structure of the dark state NmHR (PDB: 7O8F). The NTQ motif is highlighted in green, the chloride release region in blue, the second chloride binding site on the CP side in orange and the residues involved in the chloride uptake in cyan. The additional α-helix at the N-terminus is highlighted in magenta. The direction of chloride transport is represented by the green arrow.*

	3	*55*	*92*	*95*	***98***	*99*	***102***	*105*	***109***	*201*	*223*	*231*
*Nm*HR	N	C	N	R	**N**	W	**T**	C	**Q**	W	R	D
*Hs*HR	-	-	-	R	**T**	W	**S**	M	**A**	W	L	D
KR2	N	A	N	R	**N**	W	**D**	M	**Q**	W	R	D

Table 1. *Residues important for phototransduction of NmHR. The table shows the amino acids described in this work in comparison with HsHR and KR2 (NmHR numbering). The 3-letter motif of each protein is highlighted in red.*

4.1.1. *Nm*HR chloride dependent UV/Vis spectra and its photoreaction

The UV/Vis spectra of *Nm*HR show a dependence of the absorption maxima of the retinal on the chloride concentration. When the protein is in buffer without NaCl, the maximum absorption of the chromophore is at 559 nm; this value differs slightly from that reported in the literature (568 nm)[68], probably due to different sample preparation. When the concentration is increased to 150 mM NaCl, the retinal peak is at 546 nm, and it shifts to 533 nm at 1 M salt, reaching 530 nm at 4 M salt **(Figure 22)**. This effect is due to the interaction of the counterion, the chloride anion, with the protonated Schiff base and the consequent stabilization of the ground state with respect to the excited state, resulting in a blue-shifted absorption[2,81]. To obtain a sample without NaCl, the sample with 150 mM NaCl concentration was exchanged to 400 mM Na_2SO_4 by dialysis to maintain the ionic strength (kindly provided by K.-L. Lê Công, FU, Berlin).

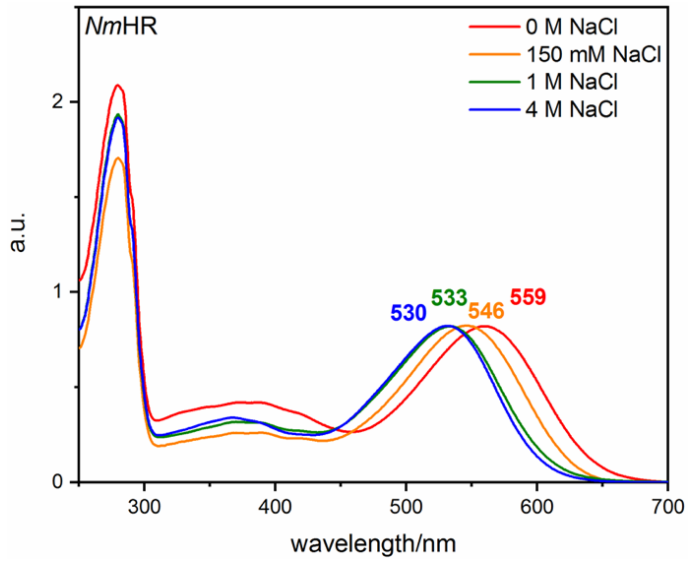

Figure 22. *UV/Vis spectra of NmHR in different salt concentrations. The salt concentrations used are: 0 M (red), 150 mM (orange), 1 M (green) and 4 M NaCl (blue). The maximum absorption of the retinal shifts from 559 nm to 530 nm with increasing salt concentration. The maximum absorptions of the retinal peaks are normalized to the sample with no NaCl.*

Upon light excitation, the retinal isomerizes from the all-*trans* to the 13-*cis* configuration, initiating a cascade of reactions. The photocycle of *Nm*HR consists of 5 intermediate states[68] **(Figure 23, panel A)**. The first state, detected by time-resolved UV/Vis spectroscopy, has a red-shifted absorption relative to the ground state, called K (580 nm), followed by a blue-shifted intermediate, called L (500 nm). During the transition between K and L, the protonated Schiff base (PSB), which is bound to the chloride in the dark state, breaks the bond with the anion and the proton of the Schiff base flips from the extracellular (EC) to the cytoplasmic (CP) side. Asn-98 and Thr-102, part of the NTQ motif **(Table 1) (Figure 21)**, help the chloride to rebind the PSB closer to the CP side of the protein (Δt: 1 µs). The anion is then released (Δt: 300 µs) at the CP side with the help of residues such as Gln-109 (also part of the NTQ motif), Ser-54 and Thr-243[25] **(Figure 21)**. Since the SB is not deprotonated during the photocycle, there is no M state and the long-lived intermediates are represented by two O states with red-shifted absorption relative to the ground state, O_1 (650 nm) and O_2 (600 nm). In the O states critical steps occur for the functionality of *Nm*HR, as chloride is released and taken up during the rise of O_1 and

decay of O_2, respectively. During the transition between the O_1 and O_2 states, structural rearrangements occur in the protein. The two O states are then followed by another intermediate with an absorption maximum similar to the ground state (530 nm), called *Nm*HR', and finally the photocycle ends. **Figure 23, panel B** shows the photoreaction of *Nm*HR measured with a flash photolysis setup in 1 M NaCl. Since the setup used does not allow measurements in the interval between 520-540 nm due to overlap with the excitation wavelength of the green laser (ʎ: 532 nm), the wavelength chosen for the ground state is 510 nm. The L state, which was assigned to 500 nm by *Tsukamoto et al.*, cannot be detected as a positive signal due to the overlap with the ground state wavelength, and was therefore omitted from the resulting figure. The two O states possessed by *Nm*HR are spectroscopically indistinguishable, being dominant at 1 ms and decaying with a time constant of 20 ms. The property of having two O states makes *Nm*HR unique; for example, the chloride pumps *Np*HR and FR contain only one O state[82] , as does the outward sodium pump KR2[83].

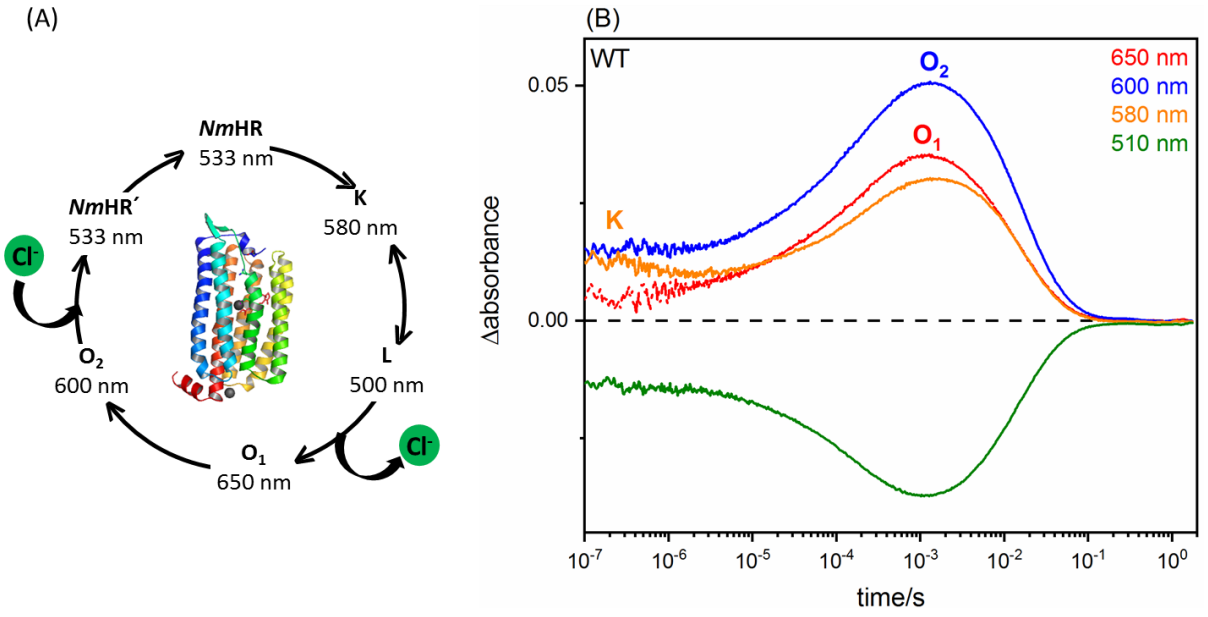

Figure 23. *Photocycle scheme of NmHR (A). The intermediate states and their maximum absorption are shown. The chloride anion is released to the CP side during the rise of O_1, and it is taken up during the decay of O_2. Photocycle of NmHR in 1 M NaCl, using a flash photolysis setup (B). The selected wavelengths are 510 nm, 580 nm, 600 nm and 650 nm which are representative of the ground state, K state, O_2 state and O_1 state respectively.*

4.1.2. Steady state light-induced difference FTIR spectroscopy on *Nm*HR

FTIR is a powerful technique for studying structural changes that occur in the protein as protonation/deprotonation events or changes in the H-bonding of individual amino acids, and rearrangements at the retinal Schiff base (RSB). When light is used as a trigger, the difference between the photoactive and dark states can be calculated[84]. The FTIR spectrum of *Nm*HR shows positive and negative bands **(Figure 24)**. The negative band at 1541 cm^{-1} refers to the C=C double bond (called ethylene stretch) of the unphotolyzed state and is shifted to 1523 cm^{-1} for the photoproduct (O state). In the 1200-1100 cm^{-1} region, specifically at 1202 cm^{-1} and 1190 cm^{-1}, the C-C single bond stretching vibration of retinal is present in the dark state and in the 13-*cis* configuration, respectively. At 1301 cm^{-1} and 1394 cm^{-1} the C-H in plane bending vibration of the Schiff base and the N-H in plane bending vibration can be observed. The negative band at 1666 cm^{-1} identifies the amide I stretching vibration, which is a marker for conformational changes in the protein backbone, while the negative band at 1642 cm^{-1} is due to the C=N-H stretching mode of the protonated Schiff base[80]. The strong negative band at 1699 cm^{-1} is indicative for side chain vibrations of asparagines or glutamines and arginines, in addition to amide I modes. It is further discussed in section **4.1.8**.

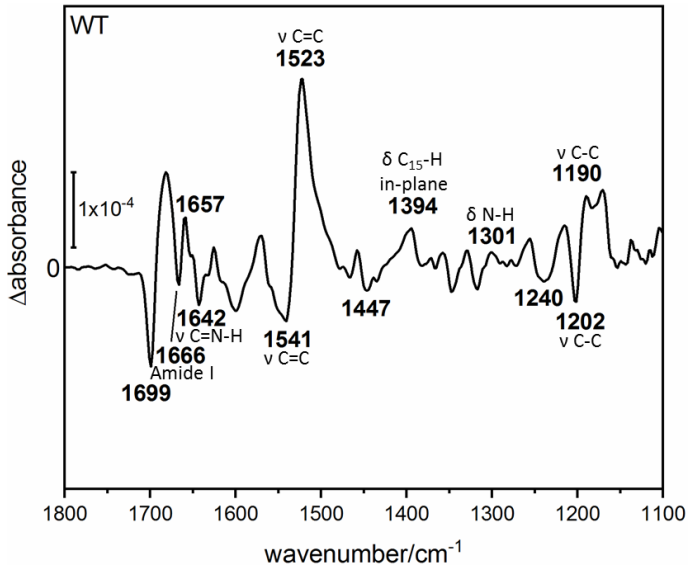

Figure 24. *Steady state light-induced difference FTIR spectrum of NmHR. The spectrum was obtained as the difference of the intermediate state minus the dark state using a green LED (λ: 525 nm). The corresponding bands are highlighted and the type of vibrations indicated.*

4.1.3. NTQ motif: Asn-98 and its role in the chloride transport of *Nm*HR

_Nm_HR N98D variant

Asn-98, together with Thr-102 (both part of the NTQ motif), is involved in the first step of chloride transfer **(Figure 25)**. In the ground state, the chloride ion is bound to the protonated Schiff base (PSB), which acts as its counterion. Upon light excitation, the retinal, which has an all-*trans* configuration in the dark state, is isomerized to 13-*cis* and loses its bond to the chloride. Within 1 µs, the Asn-98 side chain moves, pushing the chloride closer to the side chain of Thr-102, which subsequently undergoes rotameric interconversion, helping the chloride to rebind the PSB closer to the cytoplasmic side, which is subsequently released. *Sandra Mous et al.* [25] describe time-resolved crystallographic data of *Nm*HR and discuss that after the dissociation of the hydroxyl group of its side chain from the chloride, the Thr-102 side chain is then H-bonded to the side chain of Asn-98, thus preventing chloride backflow to the extracellular side.

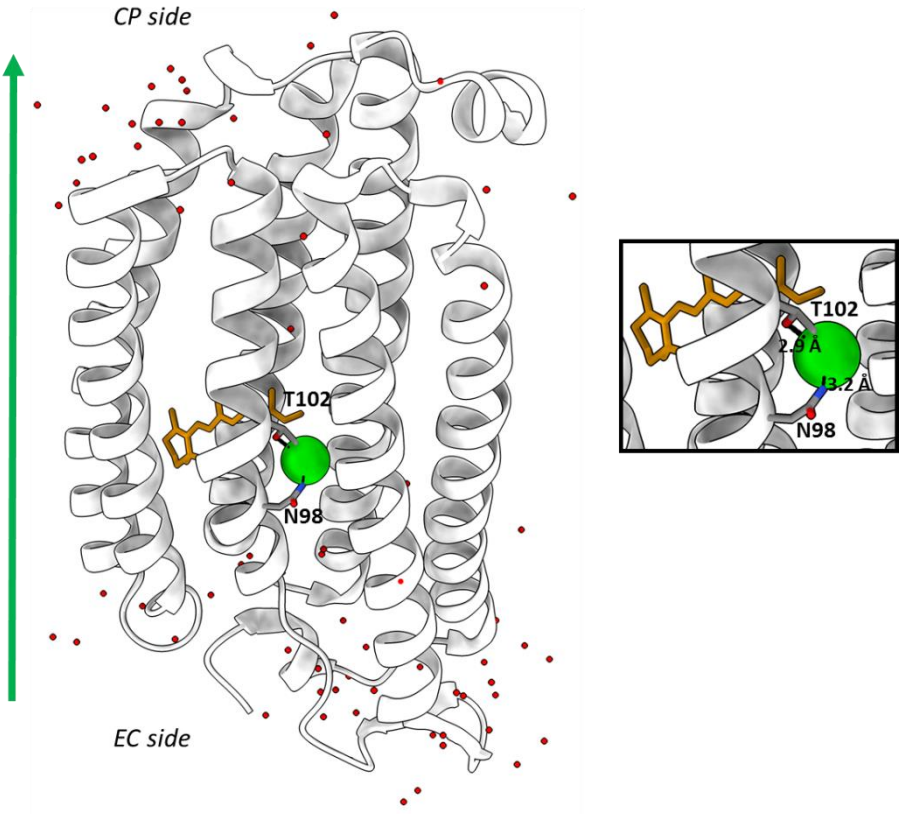

Figure 25. *Structure of the dark state NmHR (PDB: 7O8F) (left). Asn-98 and Thr-102, part of the NTQ motif, are highlighted. Retinal is shown in red and the green arrow indicates the direction of chloride transfer. Zoom of the retinal binding pocket (right). The distances between Asn-98, Thr-102 and the chloride are shown.*

To better elucidate and study the role of this residue, Asn-98 was first exchanged with a non-conservative amino acid as aspartic acid, thus introducing a negative charge at this position. The aspartic acid mutation drastically alters the photocycle of the N98D variant. **Figure 26, panel A** shows the result of the flash photolysis experiment performed on the variant in 1 M NaCl, compared to the photocycle of *Nm*HR wild type shown in **Figure 26, panel B**. On one hand, the entire photocycle is significantly slowed down (τ: 54 s), and on the other hand, while in the wild type there is no M state and the two long-lived intermediates are represented by two O states, in the N98D variant an M state is detected at 410 nm and no O state. Intuitively, the photoreaction of *Nm*HR N98D resembles the photocycle of a proton pump rather than a chloride pump, with a photoreaction more similar to that of *Hs*BR. The origin of the M state, absent in wild-type *Nm*HR but present in the variant, is due to the nature of the counterion of the Schiff base. While in wild-type *Nm*HR the counterion of the PSB is represented by the chloride itself, in the N98D variant the newly inserted aspartic acid could act as a proton acceptor replacing the chloride ion, leading to the appearance of an M state.

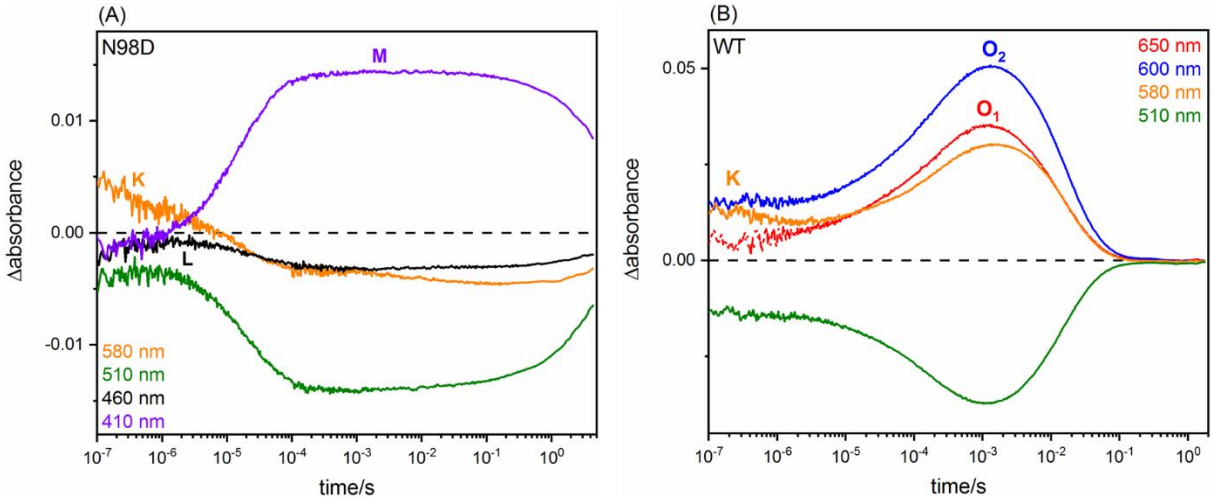

Figure 26*. Photoreaction of NmHR N98D in 1 M NaCl (A) and NmHR wild type (B) The photoreaction of the variant is more similar to a proton pump than a chloride pump with the presence of an M state, which is not existing*

in the wild-type protein, and absence of an O state,. The photocycle is significantly slowed down with a time constant of 54 s.

To understand if this hypothesis is correct, a pH titration was performed on the variant in the range of pH 9 to pH 3 and analyzed by UV/Vis spectroscopy. The pH of the sample containing 150 mM NaCl was adjusted with HCl or NaOH. The resulting spectra are shown in **Figure 27, panel A**; with decreasing pH, from 9 to 3, the maximum absorption of retinal shifts from 520 nm to 546 nm, indicating that the aspartic acid is protonated by the Schiff base, hence the origin of the M state. The resulting pKa was calculated using the Henderson-Hasselbach equation and was found to be 4.09 **(Figure 27, panel B)**.

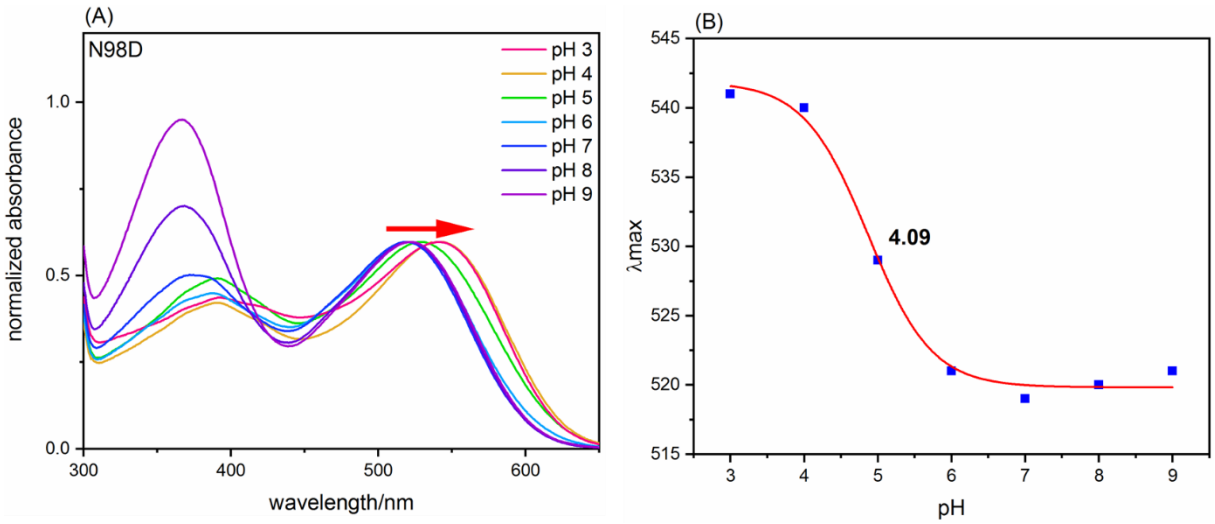

Figure 27. *pH titration of NmHR N98D in 150 mM NaCl (A). The maximum absorption of the retinal shifts to a higher wavelength when the pH is lowered, suggesting that the inserted aspartic acid is protonated. pKa of residue N98D (B) calculated using the Henderson-Hasselbach equation.*

*Nm*HR N98D was also studied using the steady-state FTIR difference technique to determine the protonation state of D98 **(Figure 28)**. The band at 1541 cm^{-1} assigned to the ground state bleaching in the wild type is at 1531 cm^{-1} due to the different maximum absorption of retinal in the UV/Vis spectra (discussed in the next paragraph), and the band at 1523 cm^{-1} assigned to the O state in the wild type spectrum is absent in the mutant, since in the latter there is no O state in

the photocycle. Interestingly, a new positive band appears in the spectrum of the mutant at 1749 cm^{-1}. This is the region of the C=O stretching vibration of carboxylic acid residues, so intuitively it can be assigned to the protonation of the inserted aspartic acid. The FTIR spectrum of the N98D variant is similar to the M state spectrum of *Hs*BR, which also contains a positive band in the carboxylic acid region corresponding to the protonated Asp-85, the proton acceptor of the Schiff base[85].

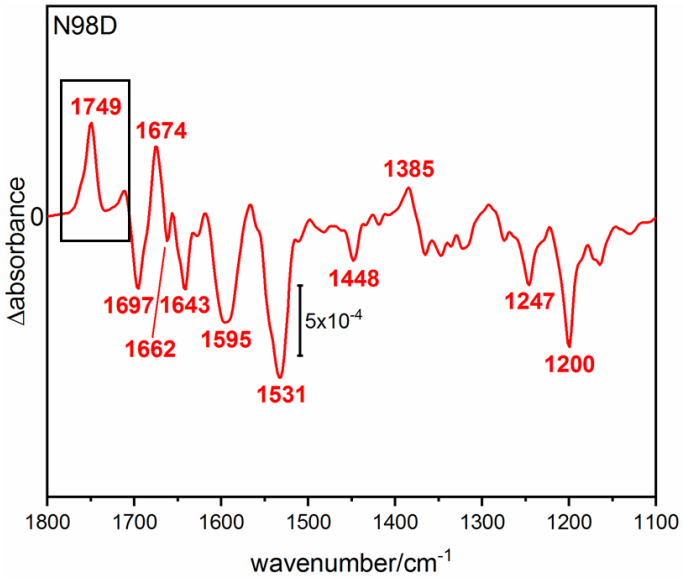

Figure 28. *Light-induced difference FTIR spectrum of NmHR N98D, using a green LED (ʎ: 525 nm). The positive peak at 1749 cm^{-1}, shown in the black rectangle, can be assigned to protonated aspartic acid during M state.*

As discussed above, Asn-98 is on homologue position of Asp-85 in *Hs*BR, so when Asn-98 was mutated with an aspartic acid, the NTQ motif of *Nm*HR was changed to DTQ. To change the motif to DTD as in *Hs*BR, and make it even more comparable to a proton pump, a double mutant N98D/Q109D was generated. The photocycle of the double mutant is the same as that of the single mutant N98D, with the presence of the M state and no detectable O state. The FTIR spectrum shows no changes between the two variants, with the presence of the positive band at 1749 cm^{-1} **(Appendix Figure S1)**. This result confirms the hypothesis that D98 is protonated, and that the proton most probably comes from the Schiff base. Gln-109 is involved in chloride release which will be discussed separately in **4.1.5**.

To clarify whether the replacement of Asn-98 by an aspartic acid converts the chloride-pumping *Nm*HR to a different ion pump, UV/Vis spectra were recorded in the presence of different chloride concentrations and other salts (the latter was performed by K.-L. Lê Công (Freie Universität, Berlin)). The maximum absorption of retinal does not shift with different chloride concentrations **(Figure 29, panel A)**, in contrast to the wild-type protein **(Figure 22)**. Furthermore, *Nm*HR N98D shows no absorption changes when tested with different salts, suggesting that it cannot bind ions **(Figure 29, panel B)** in contrast to *Nm*HR wild type which is able to pump bromide, iodide and nitrate[68].

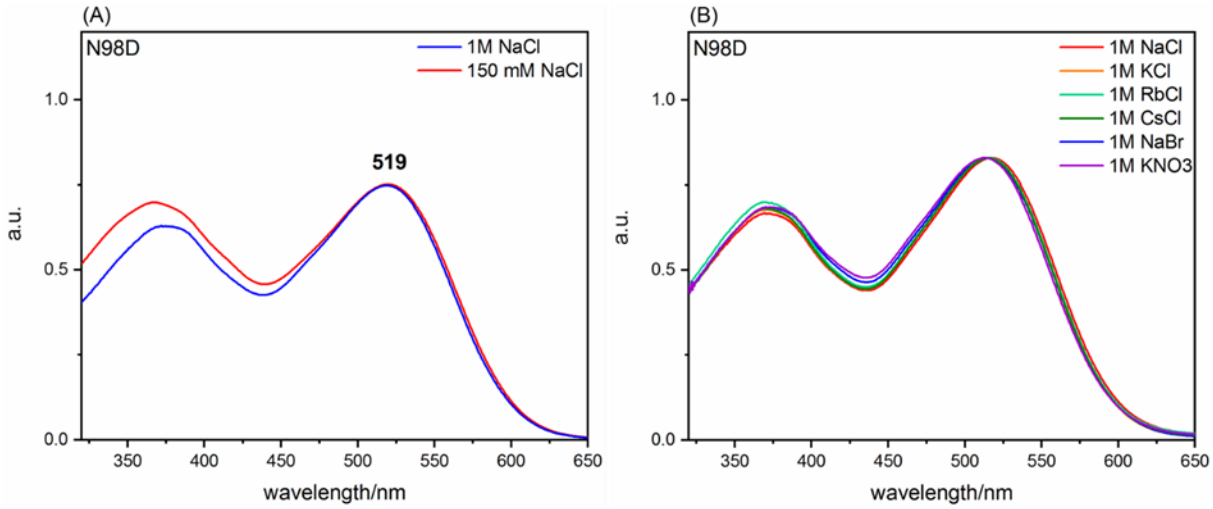

Figure 29. *UV/Vis spectra of NmHR N98D. The UV/Vis spectrum of NmHR N98D shows no shift at different concentrations of NaCl (A) or in the presence of different salts (B) (data kindly provided by K-.L. Lê Công), indicating that it cannot bind ions.*

*Nm*HR N98Q and N98A variants

To further investigate the role of Asn-98 in the photoreaction of *Nm*HR, two other mutations, a conservative substitution N98Q and non-conservative substitution N98A were examined using flash photolysis in the presence of high (1 M NaCl) and low (150 mM NaCl) salt concentrations **(Figure 30, panels A and B)**. The photocycle of *Nm*HR N98Q is significantly affected at both NaCl concentrations. At low salt, the photocycle appears to be more affected, but it is faster. This result is surprising because the side chain of glutamine is similar to that of asparagine.

However, when Asn-98 is replaced by an alanine, the photoreaction of the variant is similar to that of the wild-type *Nm*HR and the salt dependence of the O state rise is not affected.

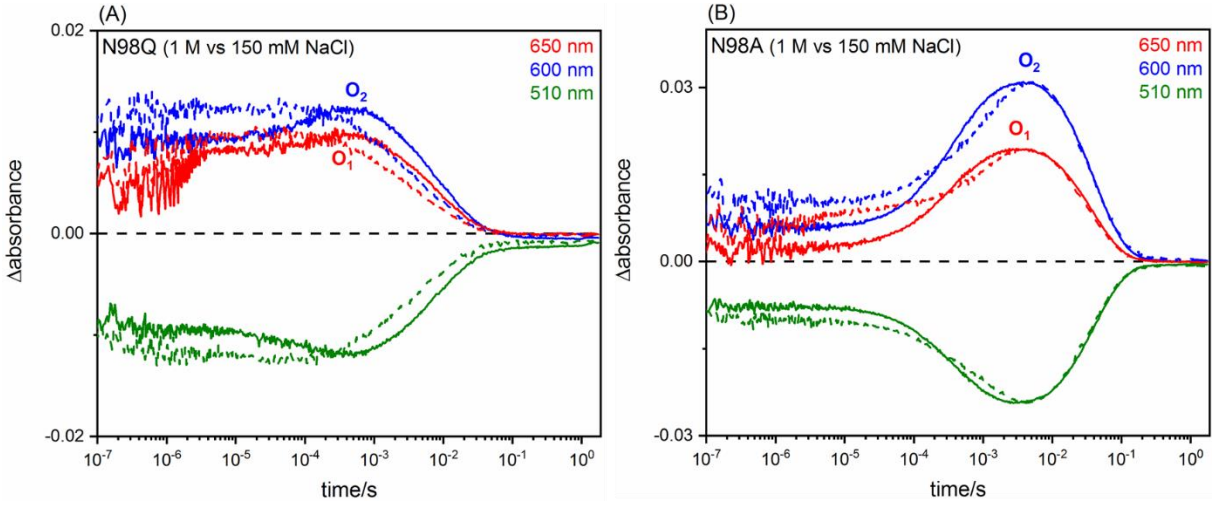

Figure 30. *Time-resolved UV/Vis spectra of NmHR N98Q (A) and NmHR N98A (B) in the presence of 1 M NaCl (solid line) and 150 mM NaCl (dashed lines). The N98Q variant shows an impaired photocycle, whereas the N98A variant shows an O state with the same chloride dependence as the wild type.*

The UV/Vis spectra of the N98Q and N98A variants show a chloride dependence of the maximum absorption of retinal on chloride concentration **(Figure 31, panels A and B)**. *Nm*HR N98Q shows a smaller shift compared to *Nm*HR wild-type, whereas *Nm*HR N98A still shows a noticeable shift at different NaCl concentrations, but both absorptions are more blue-shifted compared to the wild-type protein, suggesting a lower chloride binding affinity.

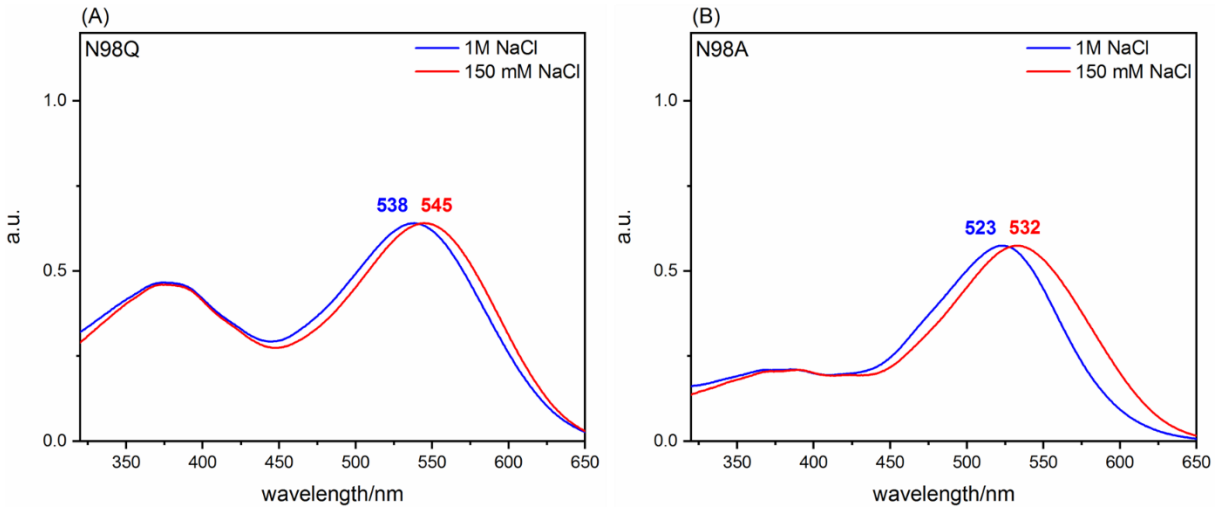

Figure 31. *UV/Vis spectra of NmHR N98Q (A) and N98A (B) in the presence of different NaCl concentrations. Both variants show a blue-shifted absorption in 1 M NaCl, but N98A shows a stronger blue-shift.*

Furthermore, the N98A variant was investigated by FTIR spectroscopy **(Figure 32)**; the light-induced difference FTIR spectrum shows that the structural changes of the protein in the O state are not affected by the alanine mutation, confirming the result of the time-resolved UV/Vis experiment.

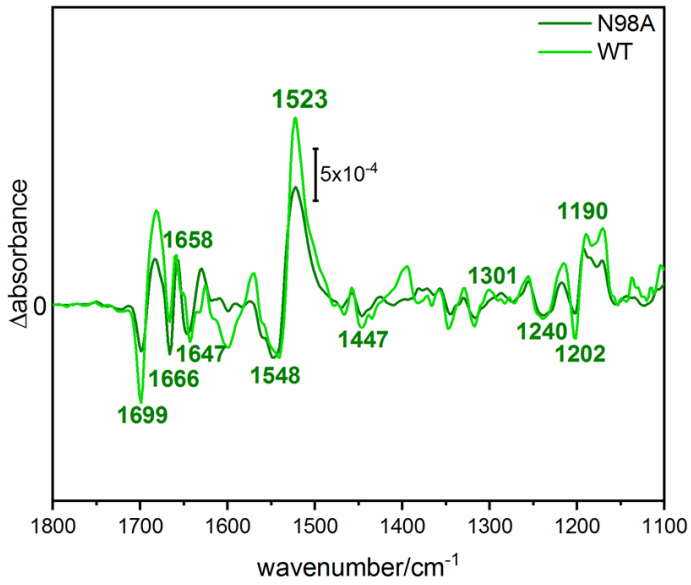

Figure 32. *Light-induced different FTIR spectra of NmHR N98A (dark green) in comparison to the wild-type NmHR (light green). Conformational changes of the protein in the O state are not affected in the variant.*

Activity test on *Nm*HR N98D and *Nm*HR N98A variants

To further validate whether *Nm*HR N98D and *Nm*HR N98A can pump chloride, the activity of the variants was tested in comparison to the wild-type protein. The samples were incorporated into the membranes of proteoliposomes loaded with lucigenin, an aromatic compound that is quenched in the presence of chloride; thus, the active transport of the anion can be observed by monitoring the fluorescence emission at 510 nm of the lucigenin. When illuminated with a green LED (ʎ: 525 nm), *Nm*HR N98D shows no changes **(Figure 33, panel B)**, as does the negative control represented by proteoliposomes without the addition of *Nm*HR **(Figure 33, panel D)**. *Nm*HR N98A, however, shows chloride transfer under light **(Figure 33, panel C)**, as does wild-type *Nm*HR **(Figure 33, panel A)**, which can be seen as a jump in fluorescence intensity upon illumination (indicated by the red arrow). The fact that both *Nm*HR N98D and the negative control show a small fluorescence jump may be due to the rupture of some of the liposomes; however, the jump is larger only in the presence of active chloride transport after illumination. The protocol and experiments were designed and performed in collaboration with Antreas Vorkas (Freie Universität, Berlin).

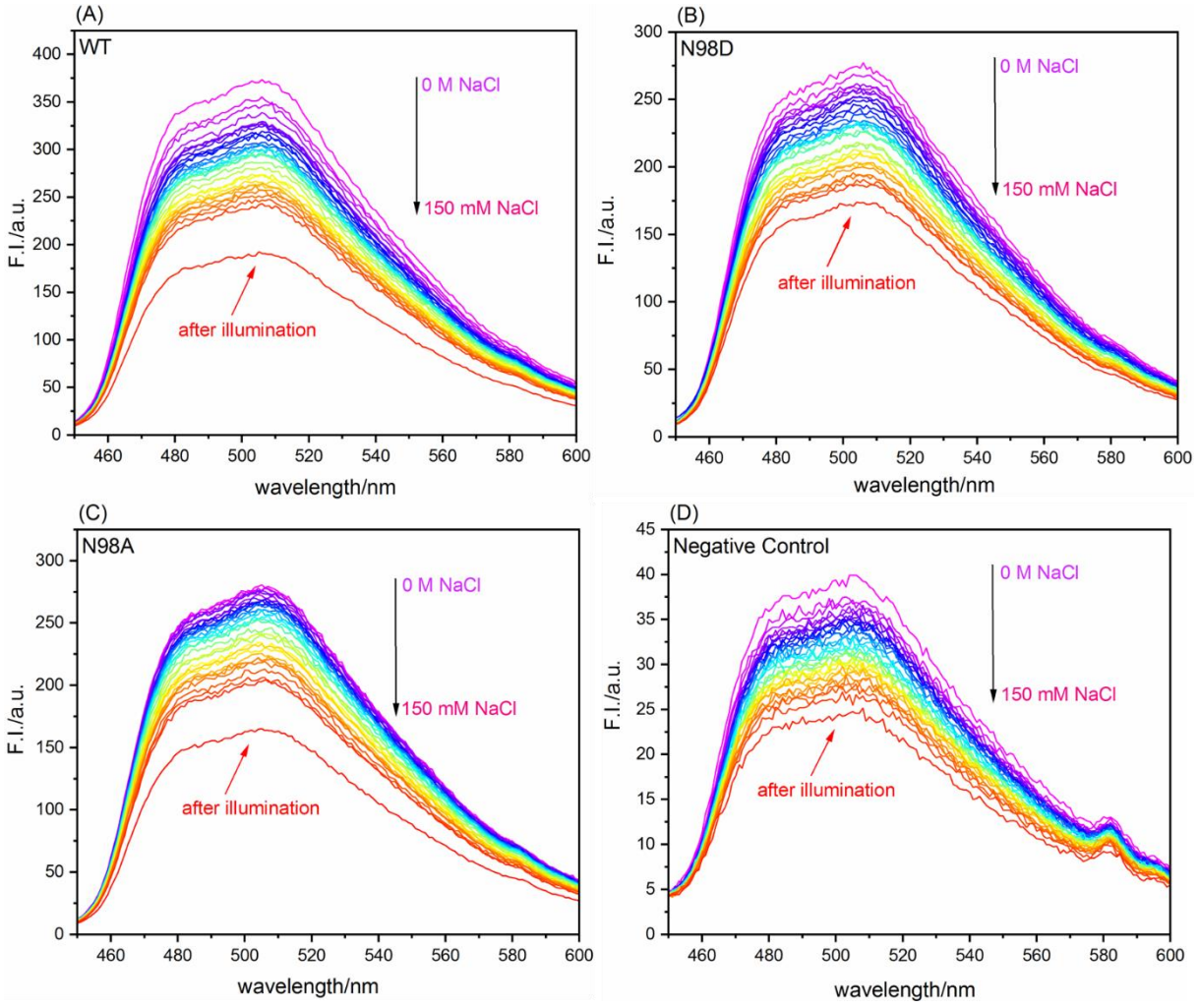

Figure 33. *Activity assay performed on NmHR wild type (A), Nm*HR *N98D (B), Nm*HR *N98A (C) and negative control without NmHR (D) proteoliposomes containing the different samples supplemented with lucigenin. The emission spectra are in the NaCl range 0-150 mM NaCl, and only the proteins capable of actively transporting chloride show a jump in fluorescence intensity upon green LED illumination. Executed by A. Vorkas*

Crystal structures of *Nm*HR N98D and *Nm*HR N98A variants

Structural studies were performed to better understand the role of these variants. The crystallization was performed by Karoline-Luisa Lê Công (Freie Universität, Berlin) **(Figure 34, panels A and B)** in a collaborative approach. In the crystal structure of *Nm*HR N98D, the chloride anion is not visible in the structure. The side chain of *Nm*HR D98 replaces the chloride as the counterion of the PSB and occupies its binding site. The structure of *Nm*HR N98D mimics

the chloride-free structure of *Nm*HR, which is consistent with the O state structure. This result supports the results of the steady-state and time-resolved UV/Vis experiments as well as the activity assay, which do not show any chloride transfer. The crystal structure of the N98A variant shows a slight bending of helix C compared to the wild type, but the chloride is in its binding site and therefore probably able to bind the PSB, as has been indicated by the spectroscopic analysis. For the N98Q variant, crystallization was not possible, although the purity of the sample was ideal (a ratio of 280 nm/545 nm < 2.0). Taken together, these results suggest that position Asn-98 may act as a key residue to maintain the kink in helix C rather than a steric valve phenomenon. The kink in helix C has been shown to be important for signal transduction in many rhodopsins, allowing for conformational changes[86]. Replacing Asn-98 with a glutamine that has a longer side chain would therefore compromise the helix C kink, preventing crystallization by changing probably the outer shape of the protein and also compromising the resulting photocycle as shown before **(Figure 30, panel A)**. *Nm*HR N98A, on the other hand, with a small amino acid, alanine, ensures a structure similar to wild-type *Nm*HR and is therefore able to crystallize under same conditions as *Nm*HR and has a similar photocycle as shown in **Figure 30, panel B**.

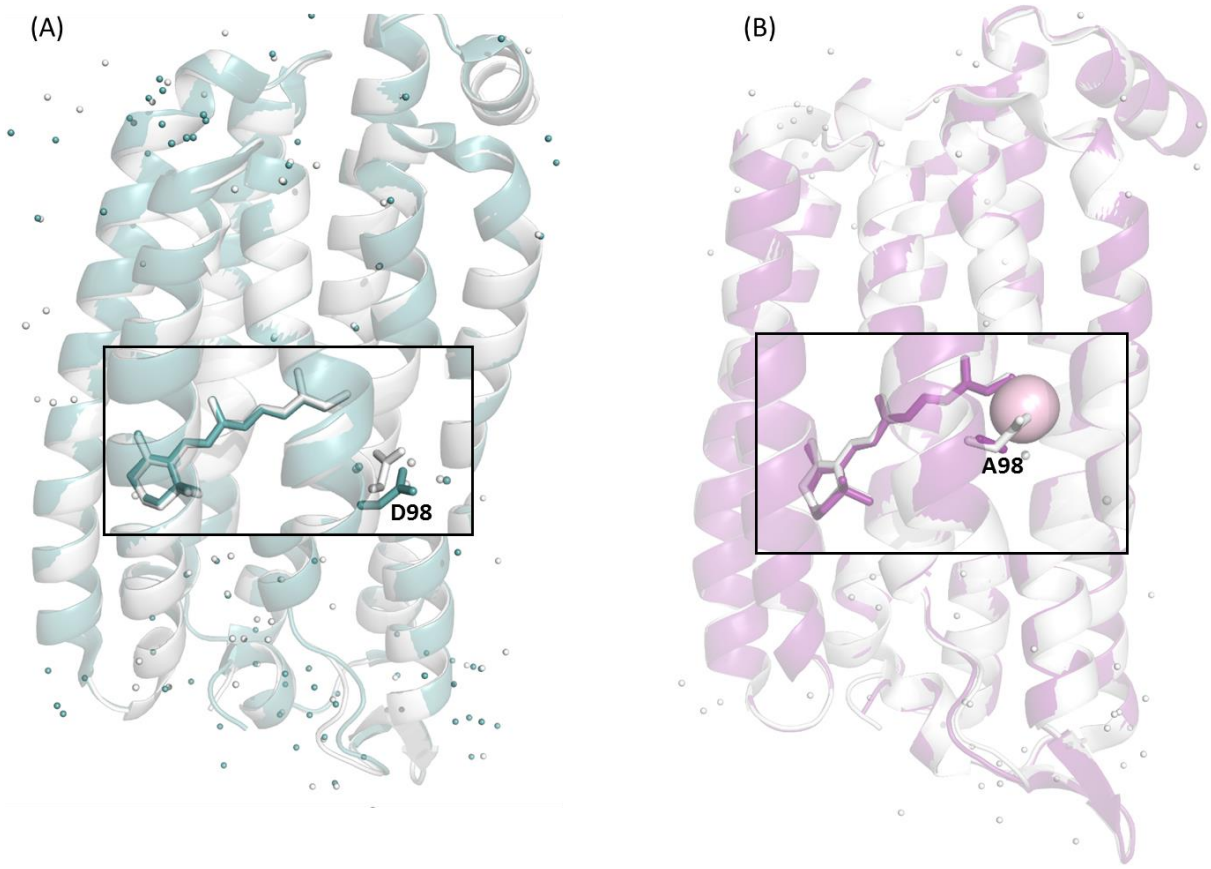

Figure 34. *Crystal structures of NmHR wild-type (PDB: 7O8F) (white) compared to NmHR N98D in green (A) and NmHR N98A in magenta (B). No chloride was found in the crystal structure of N98D and it mimics the chloride-free structure of NmHR wild type. NmHR N98A still shows the chloride anion in its binding pocket (shown as a sphere), but helix C is slightly more bent. Done by K.-L. Lê Công.*

4.1.4. NTQ motif: role of Thr-102 in *Nm*HR photoreaction

Thr-102, **(Figure 25)** is part of the NTQ motif and the rotameric interconversion of its side chain after retinal isomerization helps the chloride to bind the Schiff base on the CP side. It is conserved in the proton pump *Hs*BR, but is replaced by a serine in the halorhodopsins *Hs*HR and *Np*HR, and by an aspartic acid (Asp-116) in the sodium pump KR2, which is the counterion of the PSB. When Thr-102 is exchanged to an asparagine, the photoreaction is slowed down considerably and the release of the chloride ion, which is monitored in the rise of the O state, is delayed **(Figure 35)**. This result can be explained by the fact that it takes longer for the anion to

be transported to the PSB and then released to the CP side of the protein. It seems that the hydroxyl group of the threonine side chain is essential for the correct chloride transfer.

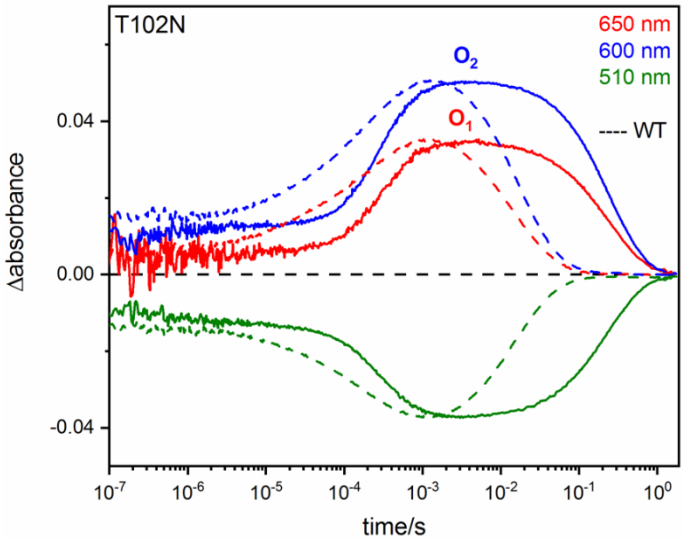

Figure 35. *Time-resolved UV/Vis spectra of NmHR T102N (solid line). The photoreaction of the variant is slowed down compared to the wild-type NmHR (dashed line), indicating that the chloride ion takes longer to be transported to the PSB.*

4.1.5. NTQ motif: role of Gln-109 in chloride release

Chloride release to the cytoplasmic side of *Nm*HR occurs during the rise of the O_1 intermediate with a Δt= 300 µs. *Sandra Mous et al.* have shown in their time-resolved structural study that the transient binding site for chloride release is formed by Gln-109, Ser-54 and Thr-243 in addition to two water molecules[25] **(Figure 36)**. Specifically, Gln-109 is the dominant amino acid for chloride transfer to the CP side. Gln-109 is part of the NTQ motif and is conserved in both *Nm*HR and KR2.

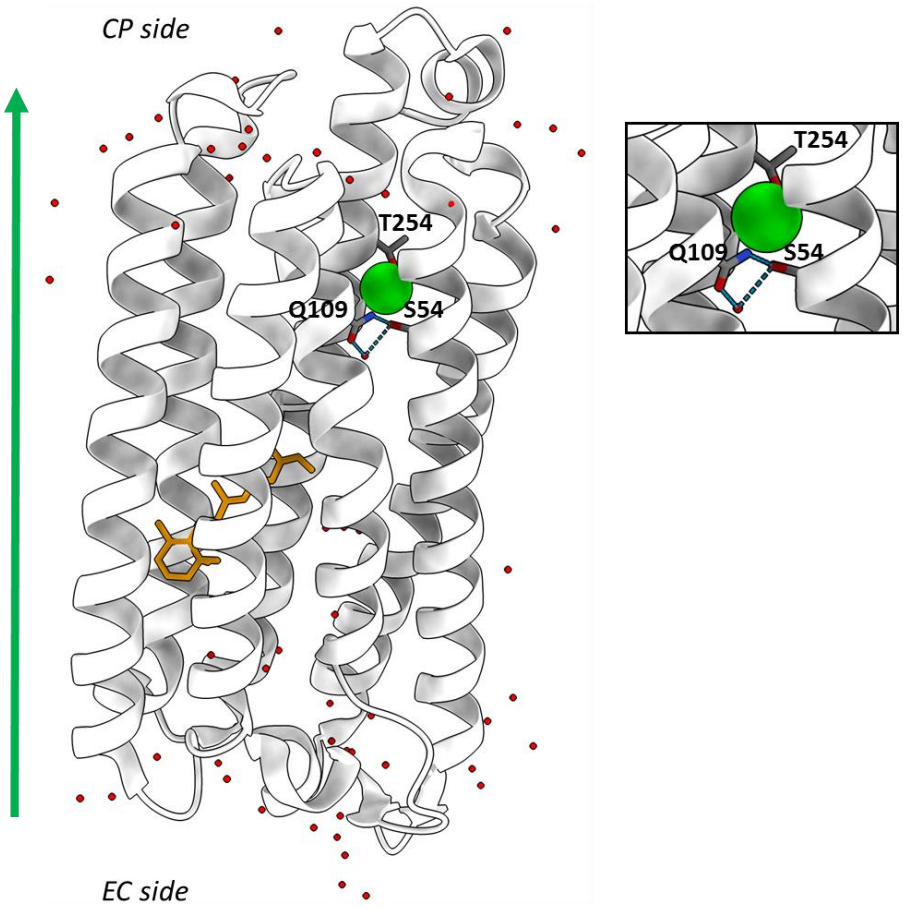

Figure 36. *Structure of NmHR at Δt: 20 µs (PDB: 7O8J). Chloride release to the CP side is achieved by Q109, S54 and T243 in addition to two water molecules.*

To investigate the role of this residue in *Nm*HR with spectroscopic methods in more detail, the Q109D variant was studied. The photoreaction of *Nm*HR Q109D shows a more pronounced K state decay compared to the wild type, and the less negative shoulder at 510 nm, corresponding to the L state, is more pronounced in the variant compared to the wild type. Interestingly, the O_1 rise is slower in *Nm*HR Q109D, whereas the decay does not seem to be affected **(Figure 37, panel A)**. Considering that during the rise of the O_1 intermediate (shown in red) in *Nm*HR, the anion is released to the CP side, one can speculate that the first part of the photocycle K-L-O_1 is slowed down in the variant because the anion takes longer to be released due to the repulsive effect of the inserted negative charge. Furthermore, the UV/Vis spectra of *Nm*HR Q109D in

different NaCl concentrations show the typical blue-shifted absorption with increasing chloride concentration, indicating that the variant is still able to bind chloride **(Figure 37, panel B)**. The sample in the absence of NaCl was kindly provided by K.-L. Lê Công (Freie Universität, Berlin).

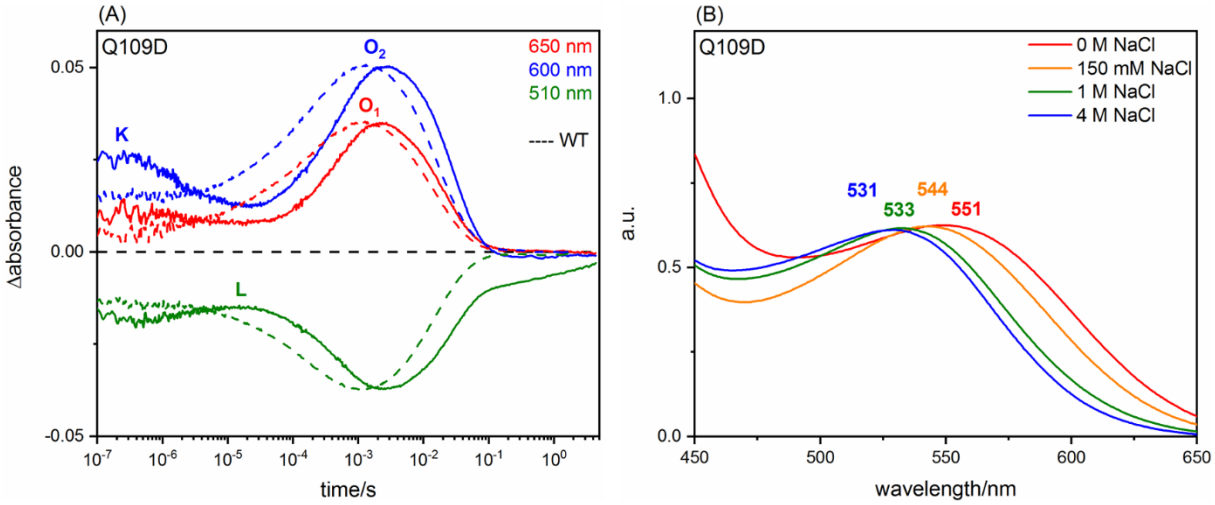

Figure 37. *Photocycle of NmHR Q109D (solid line) compared to the wild-type NmHR (dashed line) (A). O_1 rise is slowed down in the variant, indicating that the chloride release reaction is affected upon substitution of Q109. UV/Vis spectra of NmHR Q109D in different concentrations of NaCl (B). The maximum absorption of the retinal is similar to that of NmHR wild type, indicating that Q109D is still binding chloride.*

To better compare the chloride release reaction between the wild type (WT) and *Nm*HR Q109D, a chloride titration was performed in the flash photolysis setup, monitoring the O_1 rise at 650 nm **(Figure 38, panels A for WT and B for the variant)**. At chloride concentrations of 0 mM, 1 mM and 10 mM, no differences in O_1 rise were observed, whereas at chloride concentrations higher than the chloride Kd (dissociation constant: 24 mM), the Q109D variant shows a slower O_1 rise. **Figure 38, panels C and D** show the difference in the rise of the O_1 state between the samples in the presence of 10 mM NaCl and the samples in the presence of 1 M NaCl.

Taken together, these results suggest that the added negative charge at position 109 may increase the barrier for chloride transfer to the cytoplasmic side, thus delaying the O_1 rise. However, the variant is still able to pump chloride, as the maximum absorption of the retinal undergoes a blue-shifted absorption at higher NaCl concentrations. Chloride titration of *Nm*HR wild-type and Q109D was performed in collaboration with K.-L. Lê Công (Freie Universität, Berlin).

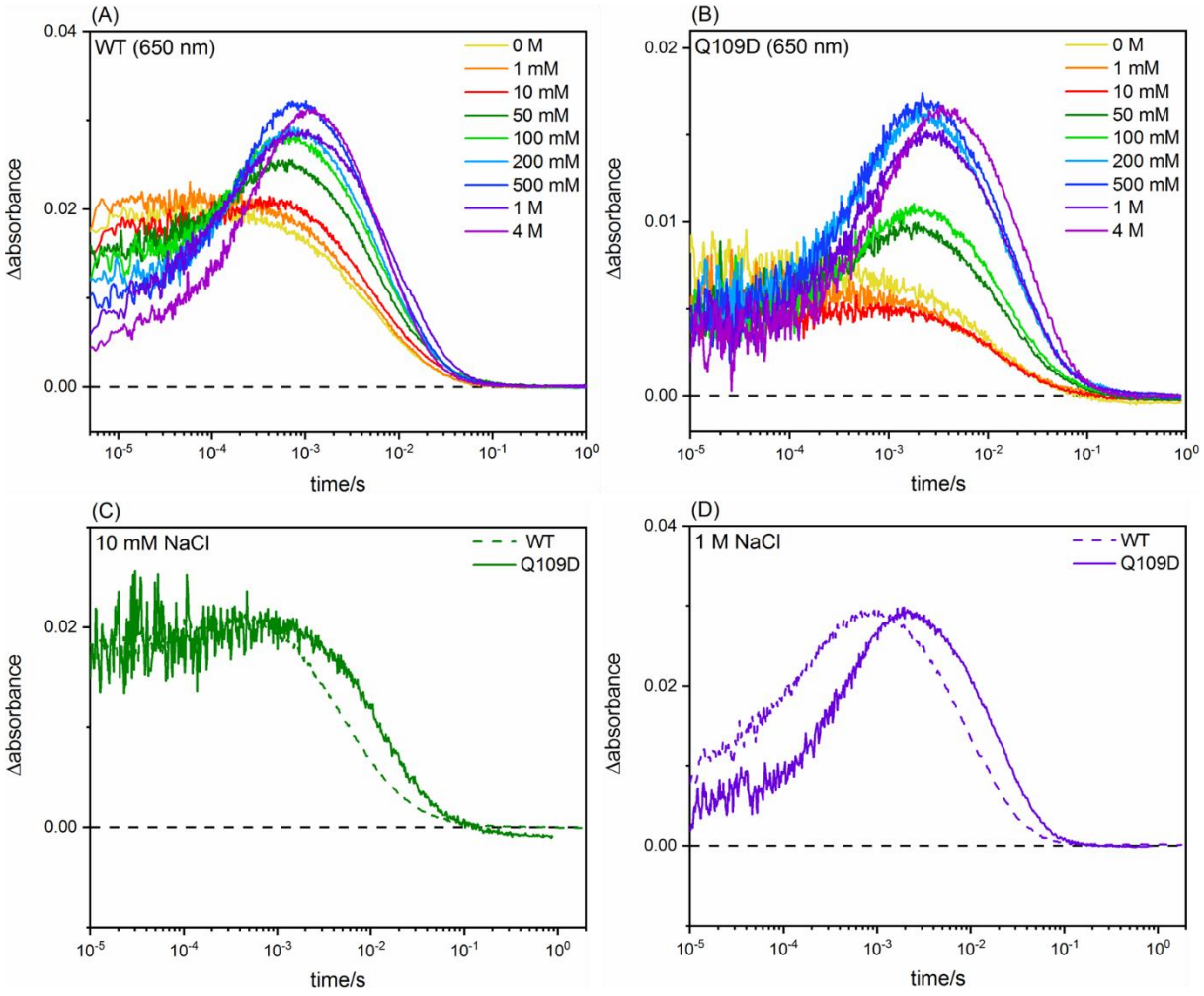

Figure 38. *Chloride titration of the O_1 state monitored at 650 nm between NmHR wild type (A) and Q109D (B). Kinetics of NmHR wild type and NmHR Q109D monitored at 650 nm in presence of 10 mM NaCl (C) and 1 M NaCl (D). At concentrations higher than 10 mM, the Q109D variants show a slower O_1 rise, indicating that chloride release to the CP side is delayed.* (*Performed in collaboration with K.-L. Lê Công)).*

4.1.6. Second chloride binding site: Ala-44, Pro-45 and Lys-46

Tsukamoto et al. have shown by X-ray crystallography the presence of a second chloride binding site on the CP loop of *Nm*HR, consisting of three amino acids, Ala-44, Pro-45, and Lys-46 **(Figure 39)**. In their study, the P45A and K46A variants were studied using a pH electrode on cells expressing the two mutant proteins to test the functionality and active transport of chloride under light[68]. Their result showed a clear functionality of both variants. To investigate whether

the photoreaction of *Nm*HR P45A and *Nm*HR K46A would show differences from the wild type, time-resolved UV/Vis spectroscopy was performed **(Appendix Figure S2).** Here it was shown that both variants do not show photocyclic changes, supporting the previous theory that these amino acids are not required for active chloride pumping. It can therefore be concluded that this second, previously unobserved chloride binding site is not essential for chloride transfer, at least under *in vitro* conditions.

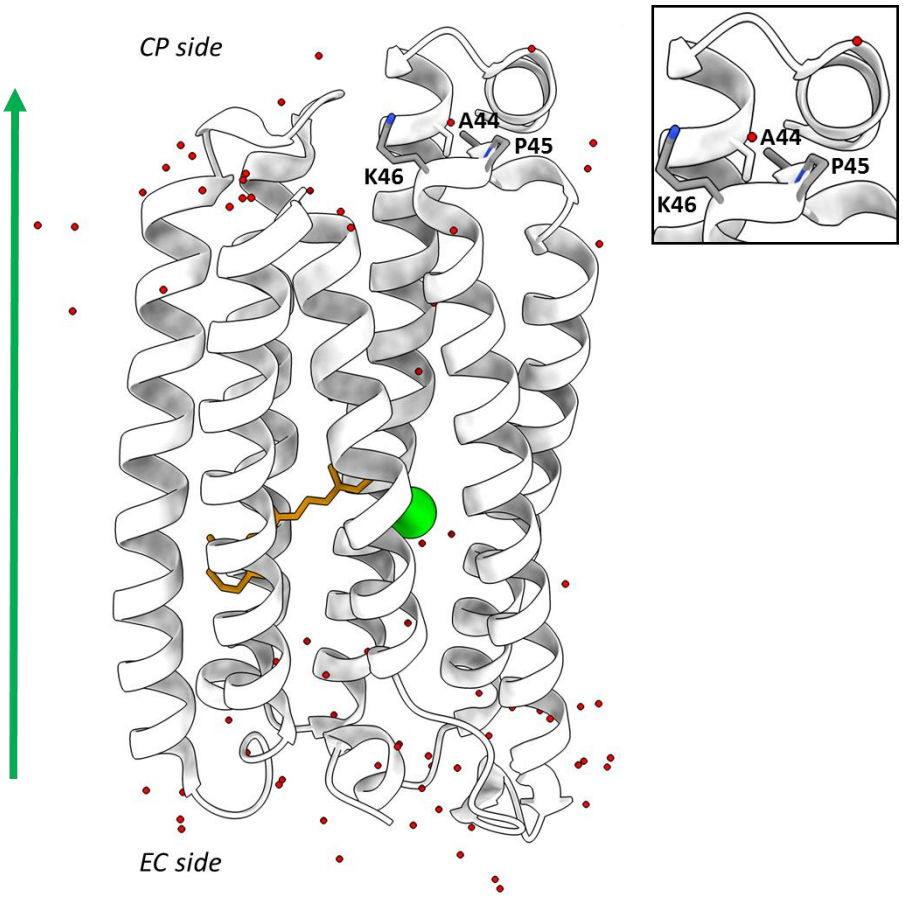

Figure 39. *Structure of the dark state NmHR (PDB: 7O8F). Residues part of the second chloride binding site are highlighted.*

4.1.7. Chloride uptake

Asn-3, Asn-92 and Arg-223 and their role in chloride uptake

At Δt= 20 µs after illumination, the chloride moves into a hole-like cavity on the EC side where positively charged residues are located, creating a positive electrostatic potential and thus facilitating the entry of the anion, during the decay of the O_2 state. Amino acids such as Arg-223, Asn-3 and Asn-92 are involved in stabilizing the chloride at this position **(Figure 40)** before the anion moves to an electrostatic site formed by Asp-231 and Arg-95 and finally recharges the dark state[25] **(Figure 43)**.

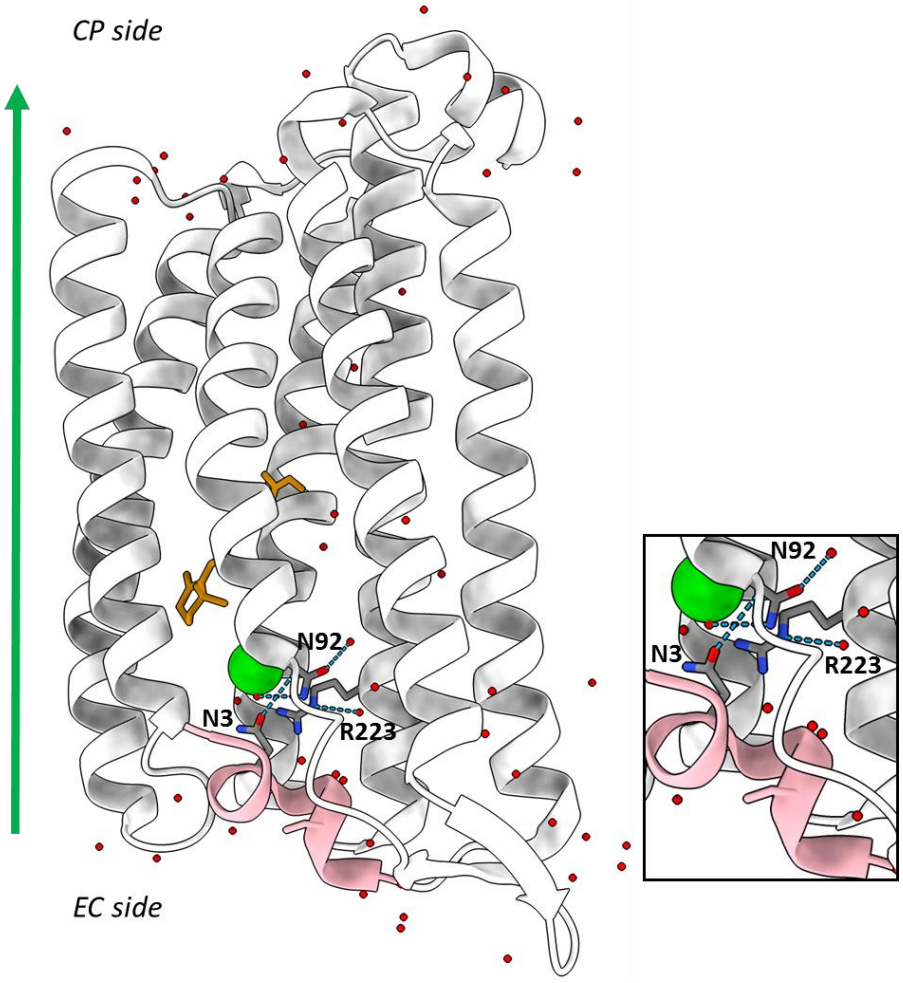

Figure 40. *Structure of NmHR at Δt: 20 µs (PDB: 7O8J), showing the residues involved in the first step of chloride uptake. These three residues are conserved in the outward sodium pump KR2, but absent in the inward chloride pumps HsHR and NpHR. The additional α-helix is highlighted in light pink.*

This hole-like structure is part of the internal cavity 1 which is conserved between *Nm*HR and KR2, but is larger and more open towards the EC side in *Nm*HR. One of the major residues here, Asn-92 is conserved in KR2 but not in *Hs*HR and *Np*HR. *Kim et al*. have shown that this residue is H-bonded to Arg-95[24], so substitutions N92Q (conservative) and N92D (non-conservative) were introduced to study the importance of this position. While the photoreaction of *Nm*HR N92Q shows only little difference from wild-type *Nm*HR **(Appendix Figure S3)**, *Nm*HR N92D shows more impressive changes, especially in the rise of the O_1 and O_2 intermediates, possibly due to the introduced negative charge **(Figure 41, panel A)**. Chloride uptake takes place during the decay of the O_2 intermediate, giving rise to *Nm*HR', which has the same absorption as the ground state (530 nm). In the photocycle of *Nm*HR N92D, there is indeed a baseline shift in the ground state, so this result indicates that the uptake of the chloride anion is delayed or impaired. In addition, *Nm*HR contains a unique feature, a short N-terminal helix, shown in light pink in **Figure 40**, which is thought to be important for structural stabilization[23]. The Asn-3 residue located on this additional α-helix has previously been shown by time-resolved X-ray crystallography to be important in the first step of chloride uptake, together with Asn-92 and the positively charged Arg-223[25]. When Asn-3 was replaced by a glutamine, the photoreaction was found to be similar to wild-type *Nm*HR **(Appendix Figure S3)** as well as *Nm*HR N92Q, but in the case of substitution by an aspartic acid **(Figure 41, panel B),** a baseline shift of the ground state was also observed. Thus, this result suggests that chloride uptake is also impaired or delayed in this case, indicating the importance of these two amino acids in chloride uptake.

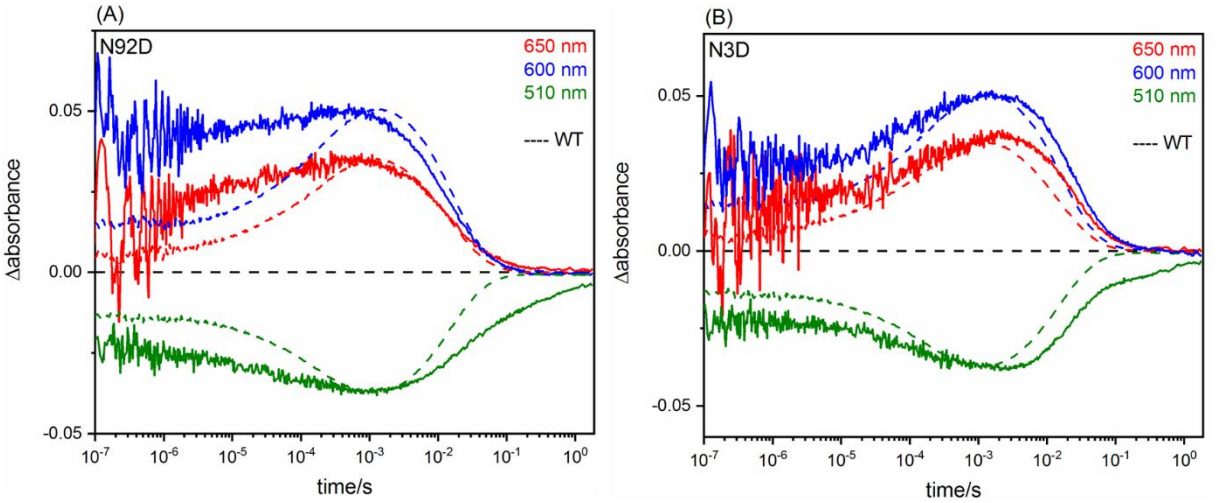

Figure 41. *Photocycle of NmHR N92D (solid line) compared to wild-type NmHR (dashed line) (A). Photocycle of NmHR N3D (solid line) compared to wild-type NmHR (dashed line) (B). Substitution of both residues by an aspartic acid leads to a delay in chloride uptake, which can be seen as a baseline shift in the ground state due to the NmHR' intermediate.*

For Arg-223, the photocycle was examined for three substitutions, R223K, R223H and R223Q **(Figure 42, panels A, B and C)**. *Nm*HR R223K and *Nm*HR R223H show a low signal-to-noise ratio, but by substitution with a glutamine the signal was found to be 10-fold lower than that of wild-type *Nm*HR, with the most striking effect on the photoreaction. Indeed, no direct comparison with the native protein could be made for the latter **(panel C)**. The lysine and histidine side chains are both positively charged, whereas the glutamine side chain is uncharged; thus, this result confirms the importance of a positive charge at position 223 in contributing to chloride uptake from the EC side.

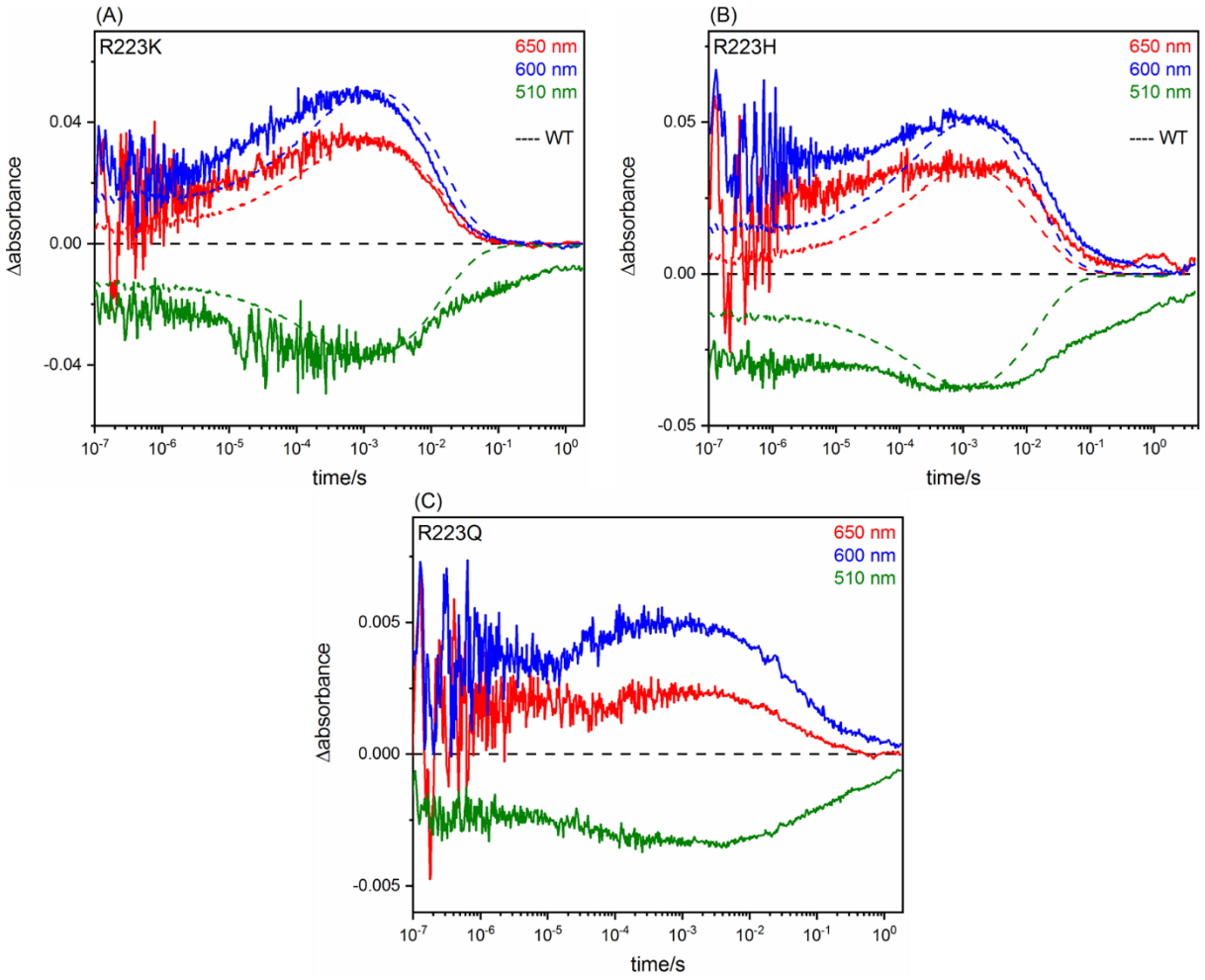

Figure 42. *Photocycle of NmHR R223K (A), R223H (B) and R223Q (C) (solid line) compared to wild-type NmHR (dashed line). The substitution of R223 has a striking effect on the photoreaction, especially in the case of NmHR R223Q, indicating that a positively charged residue is required for proper chloride uptake.*

Asp-231 and Arg-95 and their role in chloride uptake

Next, we investigated Asp-231 and Arg-95 the charged amino acid pair conserved in all ion-pumping rhodopsins for chloride uptake **(Figure 43)**[24].

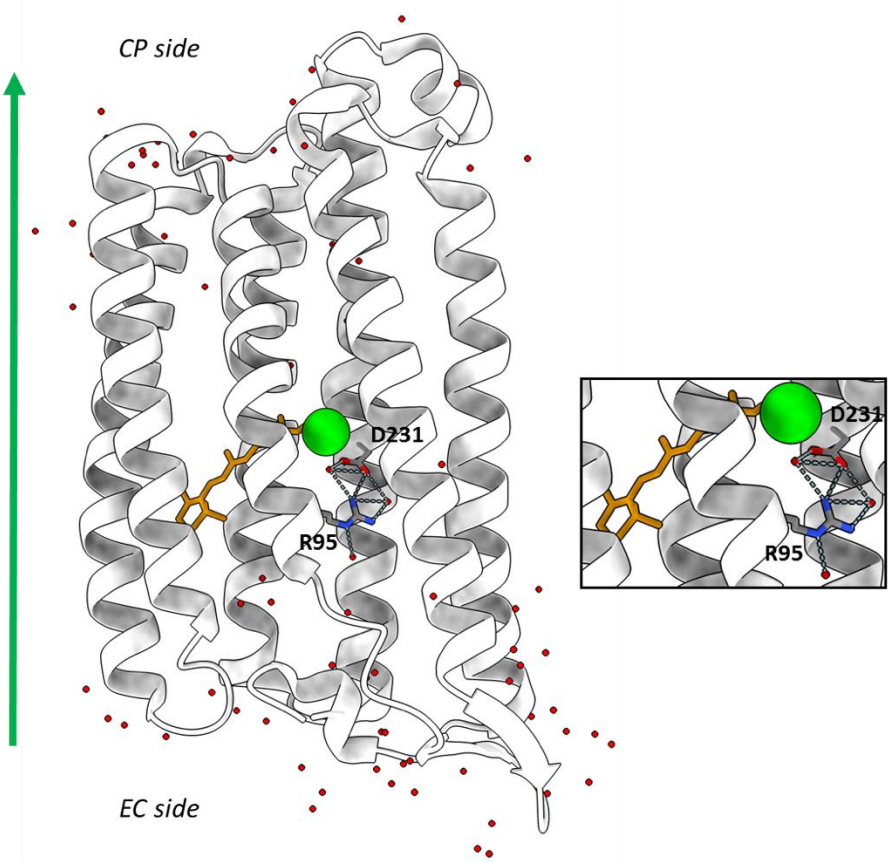

Figure 43. *Structure of the dark state NmHR (PDB: 7O8F) showing the residues involved in the last step of chloride uptake to recharge the dark state position. This charged amino acidic pair is conserved in all microbial rhodopsins.*

At Δt= 22.5 ms, the side chain of Asp-231 undergoes a large displacement to electrostatically pull the chloride to its final position, which is why mutation of Asp-231 with a conservative substitution to a glutamic acid results in a severely impaired photocycle (**Figure 44, panel A)**. The photoreaction of the D231E variant shows strong absorption only for the K and L intermediates, suggesting that the chloride can be released but not taken up. In addition, Asp-231 was exchanged with an asparagine and a cysteine, resulting in an even more impaired photoreaction, resembling the chloride-free wild-type photocycle **(Appendix Figure S4)**. However, the R95A variant also shows an impaired photocycle, with the presence of a K, L, and O_1 state suggesting that again the chloride cannot be taken up, but the strong and long absorption indicates that there is a pathway back to the K state **(Figure 44, panel B)**.

Furthermore, when comparing the maximum absorption of retinal from variants D231E, D231N, D231C and R95A **(Table 2)**, those at position D231 show a strong red-shifted absorption like the chloride-free *Nm*HR (559 nm), whereas that of *Nm*HR R95A is at 538 nm, probably retaining a modest pump activity. It can therefore be concluded that the side-chain position of Asp-231 is fundamental. The aspartic acid/arginine pair is also present in other halorhodopsins, but whereas in archael halorhodopsins this charged amino acid pair is bound to the chloride via a water molecule, in *Nm*HR there is no H-bond mediation with the chloride to the Asp-231/Arg-95 pair **(Figure 43)**.

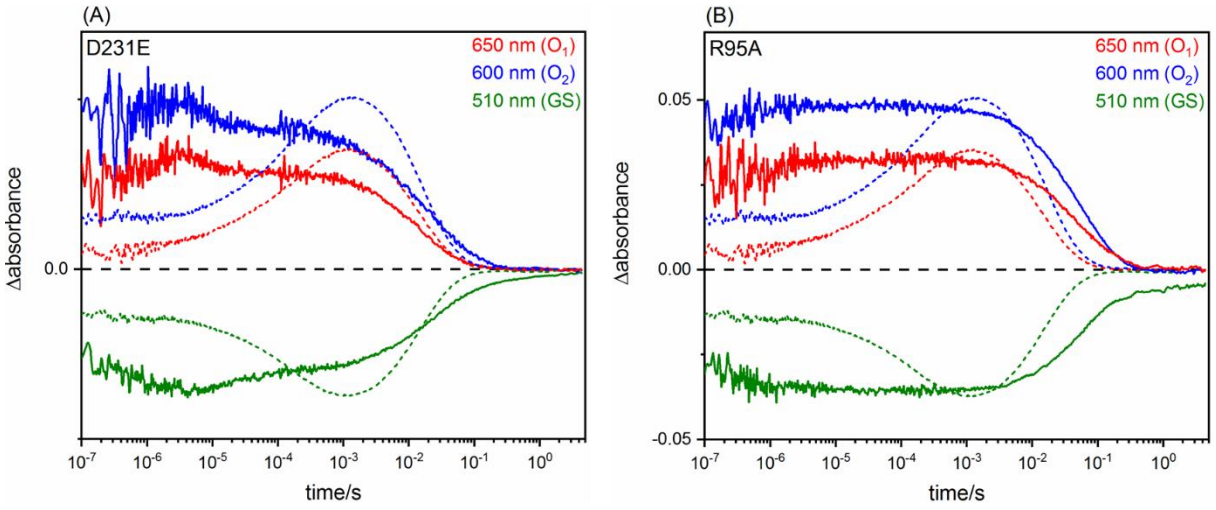

Figure 44 *Photocycle of NmHR D231E (A) and R95A (B) in comparison with the wild-type NmHR (dashed line). The substitution of D231 with a glutamic acid leads to a strongly impaired photoreaction. The R95A variant also shows an impaired photocycle, but to a lesser extent.*

	Maximum absorption (in 1 M NaCl)
***Nm*HR wild type**	533 nm (559 nm in 0 M NaCl)
***Nm*HR D231E**	550 nm
***Nm*HR D231N**	554 nm
***Nm*HR D231C**	564 nm
***Nm*HR R95A**	538 nm

Table 2. *Comparison of the maximum absorption of the retinal in the NmHR D231E, D231N, D231C and R95A variants with respect to the wild type, in presence of 1 M NaCl. D231 variants exhibit a strong red-shifted absorption which is similar to the chloride free NmHR wild type.*

4.1.8. Band assignment at 1699 cm^{-1}

The FTIR spectrum of *Nm*HR wild type shows a negative band at 1699 cm^{-1} **(see Figure 24)**; the 1700-1600 cm^{-1} region contains the side chain vibrations of asparagine, glutamine and arginine in addition to amide I modes[78]. In an approach to assign this band the *Hs*HR FTIR spectrum in the literature was studied[87] and a band was detected at 1695 cm^{-1} (-) 1688 cm^{-1} (+), which was assigned to the side chain vibration of Arg-108, which is the homologue of Arg-95 in *Nm*HR. For this reason, the R95A variant **(see also 4.1.7.)** was studied by light-induced steady-state FTIR **(Figure 45)** (in collaboration with Dr. S. Oldemeyer (FU, Berlin). Surprisingly, *Nm*HR R95A still shows the characteristic negative band, although slightly shifted (1697 cm^{-1}) indicating that the band is not due to Arg-95.

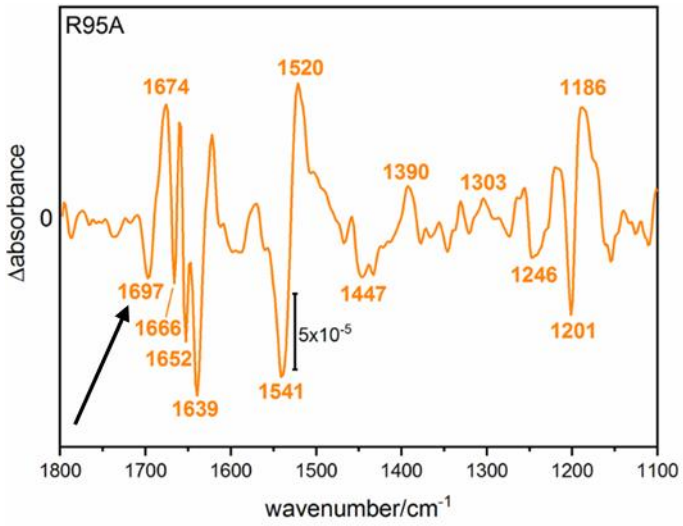

Figure 45. *Light-induced difference FTIR spectrum of NmHR R95A, illuminated by a green LED (λ:525 nm). The variant still shows the negative band at 1697 cm^{-1} (indicated with a black arrow).*

Since arginines are very sensitive to D_2O exchange, they can cause a shift of about 50 wavenumbers[78] and in general the exchange of protons with deuterium can be easily detected as

a shift in IR spectra[88]. Dr. S. Oldemeyer (Freie Universität, Berlin) personally reported that H_2O/D_2O exchange on *Nm*HR wild type results in a small shift of the band at 1699 cm^{-1} by only a few wavenumbers (1697 cm^{-1}) (*data not shown*), supporting the idea that this vibration does not originate from Arg-95 or any other arginine of *Nm*HR. The next attempt to interpret this band was to compare it with the FTIR spectrum of KR2, which shows a negative band in this region, at 1692 cm^{-1}, which has been suggested to originate from the C=O vibration of Asn-112[89]. The corresponding amino acid in *Nm*HR is Asn-98 which, when replaced by an aspartic acid, gives only the shift to 1697 cm^{-1} **(Figure 28)**. Therefore, Asn-98 could not be assigned to this band either.

In a further approach to assign or interpret the band, the following asparagine and glutamine residues which are involved in chloride uptake, were examined: Asn-3, Asn-92 and an additional residue, Gln-68, which is located near Arg-95. **Figure 46** shows the light-induced difference spectra in the 1700-1600 cm^{-1} region of the following *Nm*HR variants N3D, N3Q and N3T in **panel A**, variants N92D, N92Q and N92T in **panel B**, and Q68D in **panel D**. *Nm*HR Q68D clearly shows a negative band and is therefore not being the desired residue **(panel D)**. The interpretation of the Asn-3 and Asn-92 variants is more complicated. The variant N3Q still shows the band at 1699 cm^{-1}, but on substitution with an aspartic acid the band disappears or decreases in intensity. Interestingly, the band reappears after substitution with a threonine. This result suggests that Asn-3 is not the immediate candidate, since the threonine side chain vibration is at 1300-1100 cm^{-1} and 2500-2400 cm^{-1} at least in the case of *Hs*BR[78]. Surprisingly, the Asn-92 variants show the same behavior, also not being the direct residue to be assigned solely assigned to the band at 1699 cm^{-1}. The idea was then to generate the double mutant N3T/N92T and to compare it with the single point mutations **(Figure 46, panel C)**. The result of this experiment is inconclusive because it is difficult to assume whether the negative band has completely disappeared or has lost its intensity. Therefore, the interpretation would be that both residues contribute to the signal or, alternatively, the negative band at 1699 cm^{-1} is an amide I mode rather than due to an amino acid side chain. Its disappearance or reduced intensity would then be then interpreted as a loss of the ordered protein structure resulting from the substitutions on the EC side.

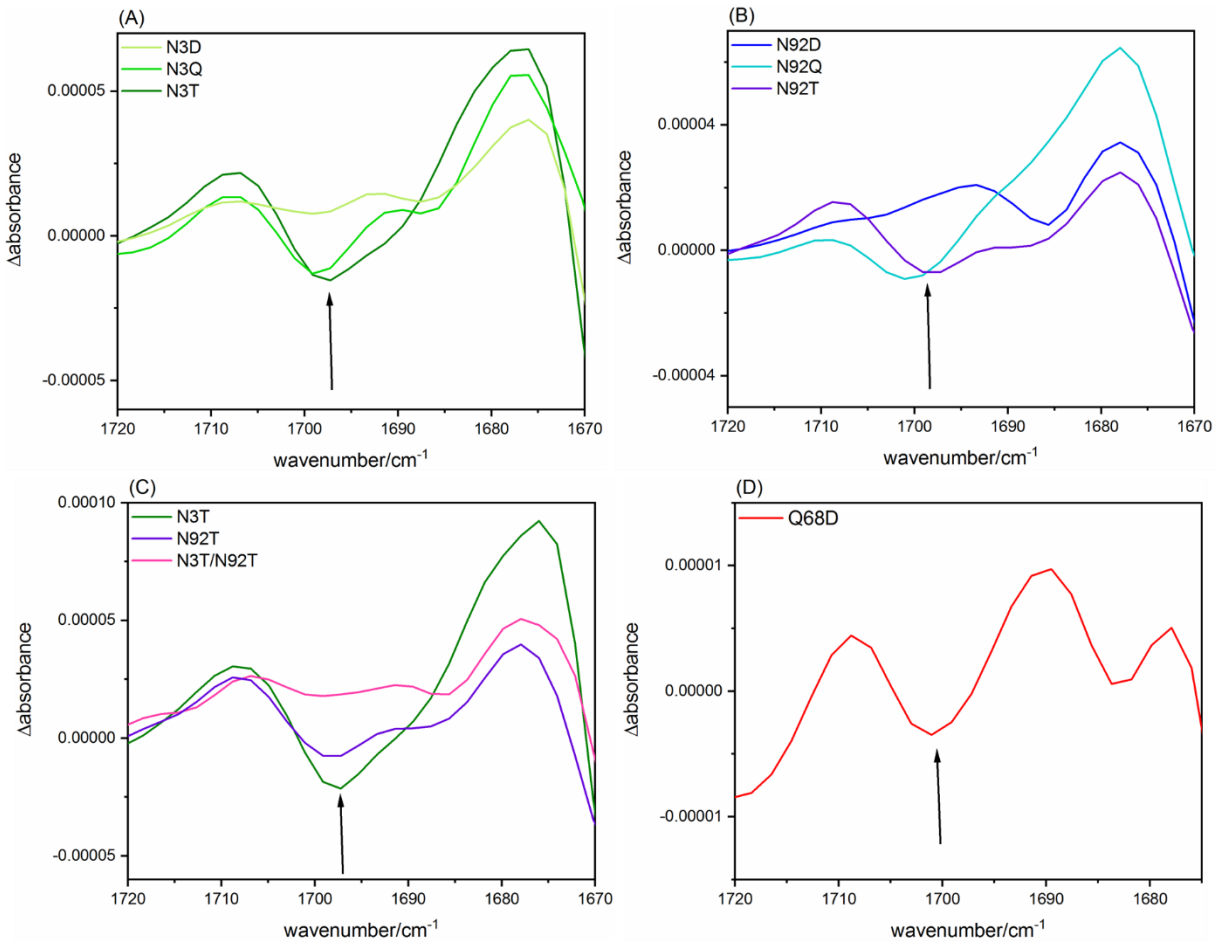

Figure 46. *Light-induced difference FTIR spectra of NmHR N3 and N92 with different substitutions (A), (B), (C) and NmHR Q68D (D), in the region of interest illuminated by a green LED (λ:525 nm). Although the latter clearly shows the band at 1699 cm^{-1}, in the case of the N3 and N92 substitutions, the assignment suggests either an H-bond interaction between N3 and N92 or an amide I mode.*

4.1.9. Cysteines in *Nm*HR: Cys-55 and Cys-105

The S-H stretching vibration of the cysteine side chain can be observed in the FTIR spectrum at about 2500 cm^{-1}[190]. The IR spectrum of *Nm*HR wild type in the 2650-2450 cm^{-1} region shows a distinct negative band at 2550 cm^{-1} with no positive counterpart **(Appendix Figure S5)**; this negative feature is due to deprotonation of a cysteine residue. *Nm*HR contains two cysteines in total: Cys-55, which is exposed to the solvent, and Cys-105, which is close to Thr-102, part of the NTQ motif of *Nm*HR close to the retinal chromophore **(Figure 47)**.

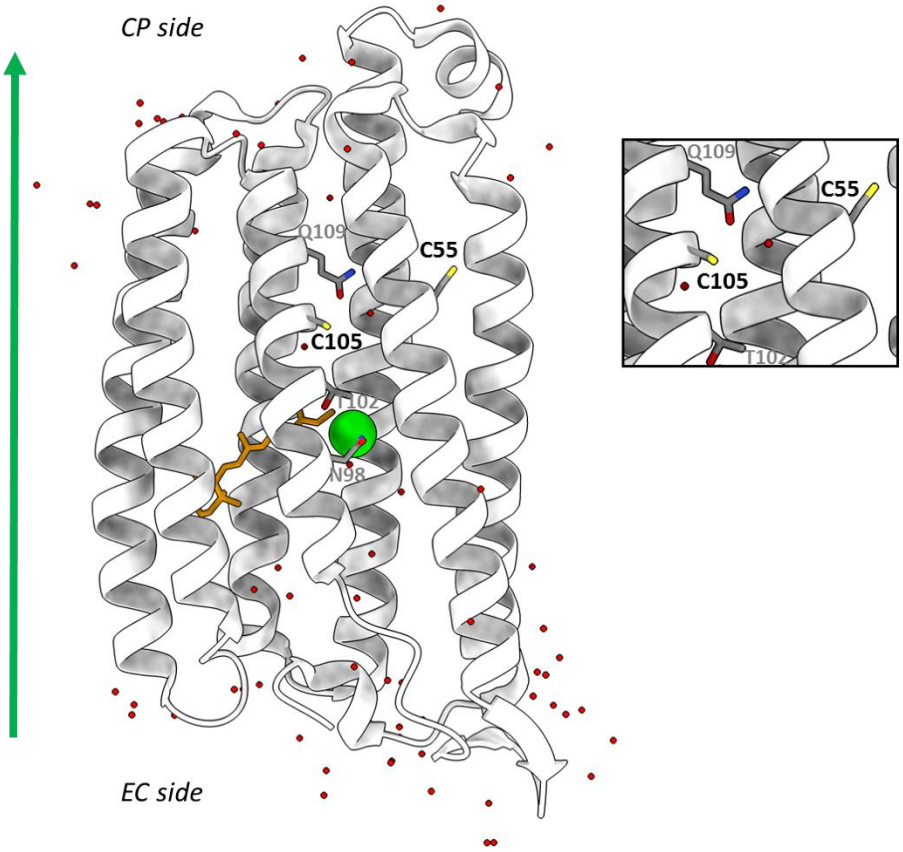

Figure 47. *Dark state structure of NmHR (PDB: 7O8F) with C55 and C105 highlighted. The C55 side chain is exposed to the solvent, whereas C105 is close to the NTQ motif (highlighted in gray) and the chromophore.*

To understand which of the two cysteines is responsible for the deprotonation signal in the IR spectrum, single point mutations were performed to conservatively replace them with a serine, resulting in variants C55S and C105S. Flash photolysis experiments performed on the variants

are shown in **Figure 48, panels A and B**. Both proteins show a functional photocycle, although the accumulation of O states was found to be slower, indicating protein conformational changes with a more pronounced effect on O_2 rise in *Nm*HR C105S[68].

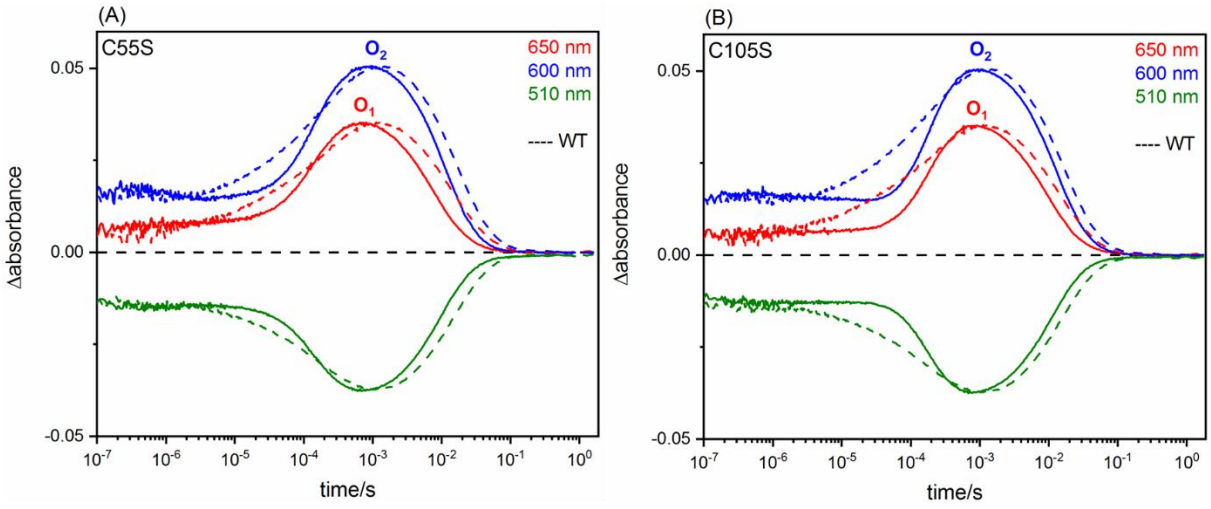

Figure 48. *Photoreaction of NmHR C55S (A) and C105S (B) (solid line) compared to wild-type NmHR (dashed line). The photoreaction of both variants shows a slower accumulation of O rise, more pronounced in the case of O_2 rise, which is a marker of protein conformational changes, more obvious in the variant C105S.*

The FTIR spectra of these two variants show the same band positions as wild-type *Nm*HR, in the region of 1800-1100 cm^{-1} (**Appendix Figure S6**). On the other hand, when the two variants were compared with the wild-type in the 2650-2450 cm^{-1} region of the S-H stretching vibration, only *Nm*HR C55S showed a negative band at 2552 cm^{-1}, whereas no deprotonation band was detected for *Nm*HR C105S **(Figure 49)**[80]. This result indicates that Cys-105 is responsible for the negative band being deprotonated during the photocycle.

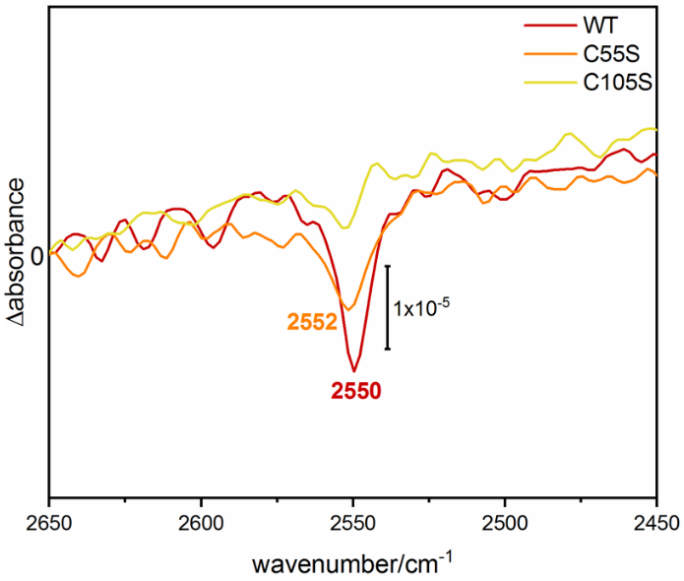

Figure 49. *Light-induced difference FTIR spectrum of NmHR wild type (dark red), NmHR C55S (orange) and NmHR C105S (yellow) illuminated with a green LED (λ:525 nm) in the region of the S-H stretching vibrations where active cysteines are visible. Although NmHR wild type and NmHR C55S clearly show a negative peak at about 2250 cm^{-1}, NmHR C105S shows no band, indicating that Cys-105 is responsible for the negative band.*

Since Cys-105 in *Nm*HR is in homologous position of a methionine in *Hs*HR, *Np*HR and KR2, variant C105M was generated and studied using time-resolved UV/Vis and FTIR techniques. **Figure 50, panel A**, shows the S-H stretching vibration region in the FTIR spectra of the variant compared to the wild-type *Nm*HR, confirming again that Cys-105 is the cause of the negative band since the band at 2550 cm^{-1} disappears in variant C105M. However, the photoreaction of the variant does not show any difference to the wild-type *Nm*HR **(Figure 50, panel B)**. This is quite surprising considering that the methionine side chain cannot be deprotonated. This observation can be interpreted in two ways, there is an alternative way to deliver a proton or the deprotonation has no strong impact on the photocycle and/or mechanism of chloride transfer.

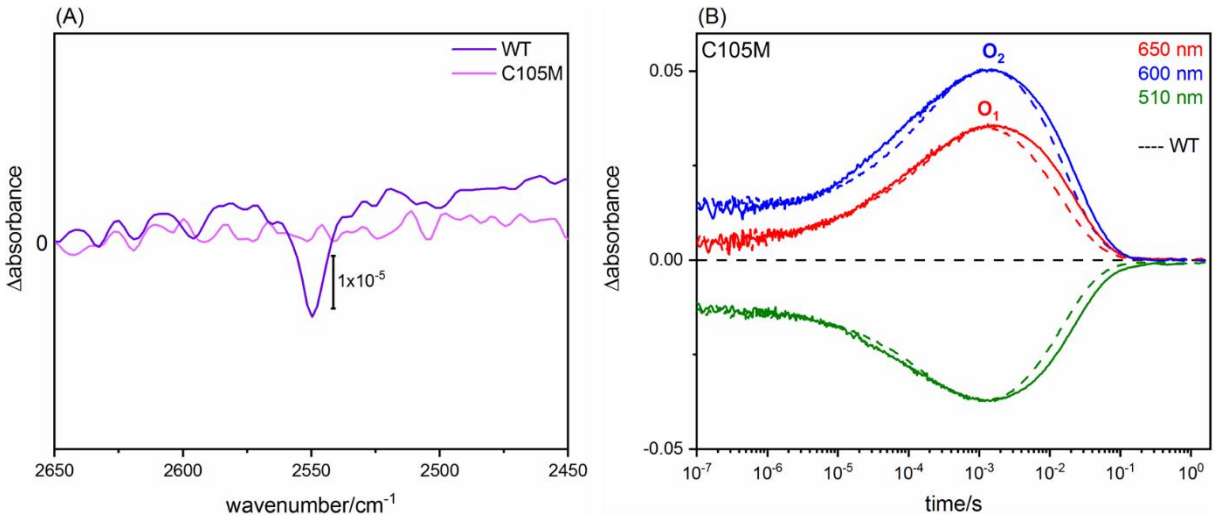

Figure 50. *Light-induced difference FTIR spectrum of NmHR wild type (purple) and NmHR C105M (pink) in the S-H stretching vibrations of cysteine side chains, illuminated with a green LED (λ:525 nm) (A). Although NmHR wild type clearly shows a negative peak at about 2250 cm^{-1}, NmHR C105M shows no band, confirming that Cys-105 is due to the deprotonation band. Photoreaction of NmHR C105M (solid line). The photoreaction of the variant shows only minor changes compared to wild-type NmHR (dashed line) (B).*

Table 3 shows the maximum absorption of the cysteine variants with respect to the *Nm*HR wild type in the presence of high and low salt. All variants show a dependence of the maximum retinal absorption on the chloride concentration, indicating chloride transport comparable to the wild-type protein.

	Maximum absorption (1 M NaCl)	**Maximum absorption (150 mM NaCl)**
***Nm*HR wild type**	533 nm	546 nm
***Nm*HR C55S**	536 nm	545 nm
***Nm*HR C105S**	535 nm	541 nm
***Nm*HR C105M**	535 nm	542 nm

Table 3. *Comparison of the maximum absorption of the retinal in the variants NmHR C55S, C105S and C105M, with respect to the wild type, in the presence of two different salt concentrations. All the variants show a chloride dependence of the retinal peak in the UV/Vis spectra.*

4.1.10. Insertion of p-cyano-phenylalanine exchanging Trp-99 and Trp-201

A common feature of many rhodopsins like *Hs*BR[91], ChRs[92], KR2[93] and *Nm*HR is the presence of two tryptophan residues on opposite sides of the retinal, that stabilize the chromophore in the excited state[94]. These conservative tryptophans play a role in photoisomerization as well as pump or channel opening. In *Nm*HR the two tryptophan residues are located at amino acid positions 99 and 201 **(Figure 51)**.

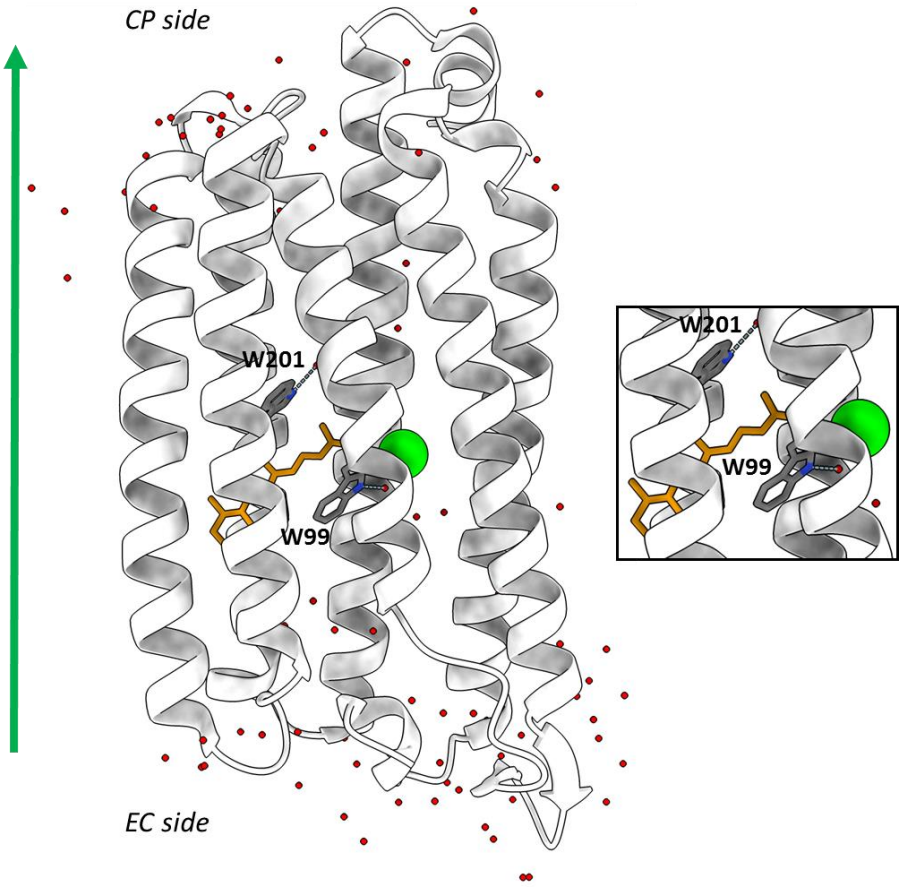

Figure 51. *Dark state structure of NmHR (PDB: 7O8F) with W99 and W201 highlighted. The side chains of these two tryptophanes are on the opposite side of the retinal, "sandwiching" the chromophore.*

Previous studies have speculated that these residues may be involved in the major conformational changes that *Nm*HR undergoes compared to *Hs*BR or KR2[95,96]. To further

investigate their role and involvement in the electrostatic environment of the retinal, ultrafast spectroscopy can be used. This technique provides information about early processes on the femtosecond to picosecond time scale that occur after retinal photoisomerization[97], that cannot be observed by time-resolved UV/Vis spectroscopy with slower time resolution (microsecond to millisecond time scale). In addition, some reporter groups are highly sensitive to electrostatic changes, such as the non-canonical amino acid p-cyano-phenylalanine (pCNF)[98], which can be co-translationally introduced into the protein via Amber stop codon suppression. In this study, pCNF was used successively used to exchange the highly conserved tryptophans Trp-99 and Trp-201. Since previous studies have shown how fundamental they are to the photoreaction of *Nm*HR, a first exchange with the canonical phenylalanine was tested to verify that the photocycle of *Nm*HR was still functional before proceeding with the pCNF variants. The maximum absorption in the UV/Vis spectrum of the retinal of the W99F and W201F variants, and wild-type *Nm*HR are shown in **Table 4**. While the shift of the absorption maxima in the W201F variant is comparable to that of the wild-type, *Nm*HR W99F has a slightly smaller shift and is more blue-shifted. This is more likely due to the fact that Trp-99 is part of the binding pocket of the retinal and is hydrogen bonded to the chloride, so substitution with a phenylalanine dramatically changes the electrostatics around the retinal. Nevertheless, both variants can be considered as active chloride pumps.

	Maximum absorption (1 M NaCl)	**Maximum absorption (150 mM NaCl)**
***Nm*HR wild type**	533 nm	546 nm
***Nm*HR W99F**	529 nm	534 nm
***Nm*HR W201F**	532 nm	543 nm

Table 4. *Comparison of the maximum absorption of retinal in the UV/Vis spectra in the NmHR W99F and NmHR W201F variants with respect to the wild type in the presence of two different salt concentrations. All variants show a chloride dependence of the retinal peak, although NmHR W99F shows a smaller shift.*

The kinetics of these two variants were also investigated by flash photolysis **(Figure 52, panels A and B)**. The entire photocycle of *Nm*HR W99F is slowed down compared to the wild-type

*Nm*HR with a ground state recovery time constant of 0.23 s (wild type: 0.02 s), while *Nm*HR W201F has a ground state recovery time constant of 0.07 s, which is more similar to the wild-type *Nm*HR. Interestingly, the O_2 rise in *Nm*HR W201F is significantly slowed down compared to the O_1 rise. During the O_2 rise, conformational changes occur in the protein[68], suggesting that Trp-201 is involved in these structural changes.

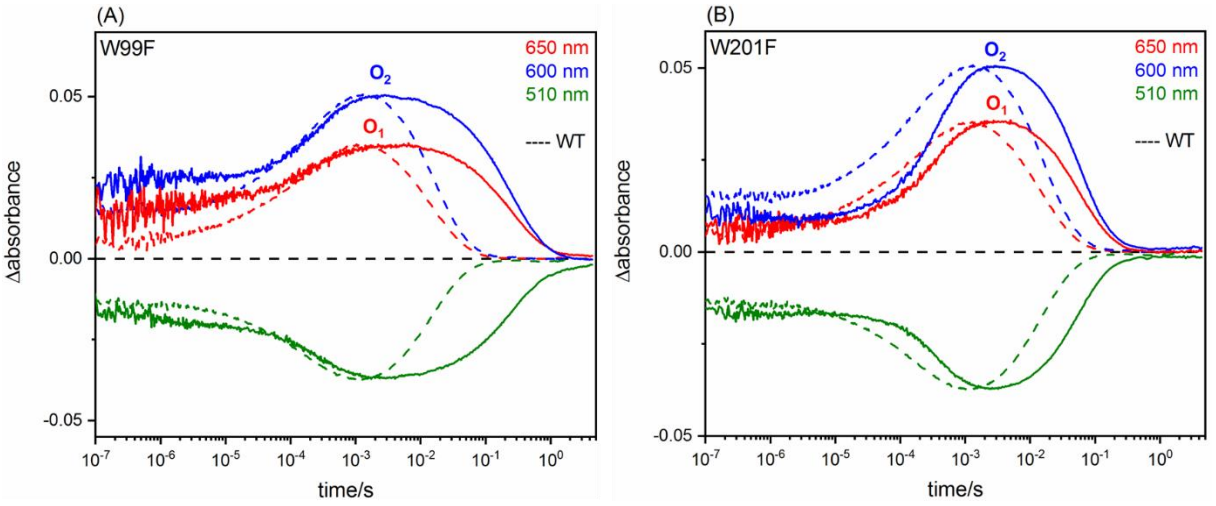

Figure 52. *Photocycle of NmHR W99F (A) and NmHR W201F (B) (solid line) compared to wild-type NmHR (dashed line). The photoreaction of both variants shows a slower photocycle, more pronounced in the case of NmHR W99F. However, the W201F variant shows a slower accumulation of O_2 rise, indicating that the substitution of Trp-201 has an effect on conformational changes in the protein structure.*

To address this point light-induced difference FTIR spectra of *Nm*HR W99F and *Nm*HR W201F were examined and displayed in **Figure 53, panels A and B**, showing that the structural changes associated with the O state are still present upon light activation.

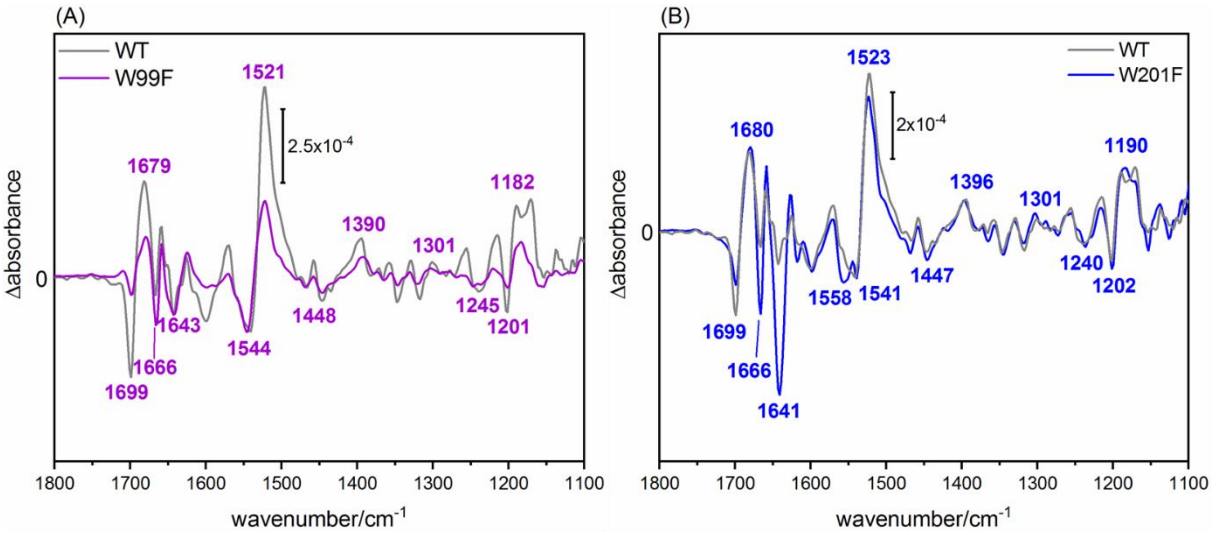

Figure 53. *Light-induced difference FTIR spectra of NmHR W99F (A) and NmHR W201F (B) compared to NmHR wild type. Both variants show structural changes associated with the O state.*

Since the exchange to phenylalanine did not result in any serious changes in activity and structural movements, the insertion of pCNF was advanced. To verify that the unnatural amino acid was successfully incorporated into the protein, 20 mL of test expression of *Nm*HR W99pCNF and *Nm*HR W201pCNF fed with pCNF were compared to cultures without the addition of pCNF (negative control). As expected, only cells fed with pCNF show a red color **(Figure 54, panels A and B)**. Unexpectedly, however, on an SDS gel *(data not shown)*, the characteristic band of *Nm*HR at approximately 31 kDa was also present in the extract from cells without pCNF, although only the truncated form of the protein was expected due to the Amber stop codon at position 99 and 201. This observation is not well understood. One interpretation is that, for unknown reasons, the Amber codon was read over and a natural amino acid was placed instead. Since the cells are not coloured, indicating that the chromophore is not bound, the resulting protein appears to be impaired and non-functional.

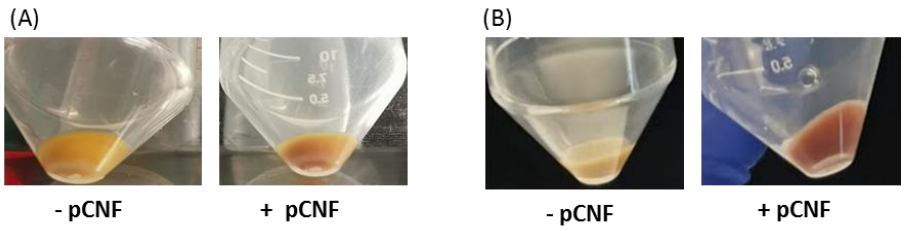

Figure 54. *Cell pellet after IPTG induction of NmHR W99pCNF (with and without feeding pCNF) (A) and the same for W201pCNF (B). The cells have the characteristic purple color only when pCNF is added.*

To verify the correct insertion of pCNF after its addition to the cells, the purified proteins were analyzed by FTIR spectroscopy. The C=N stretching vibration of the cyano group should be visible at about 2230 cm^{-1} [99]. **Figure 55** shows the second derivative of the IR spectra of variants W99pCNF **(panel A)** and W201pCNF **(panel B)** in the region of interest. Both variants show the band at 2230 cm^{-1}, confirming that the C=N is successfully introduced into the proteins. *Nm*HR W99pCNF was measured as a dry (black) and rehydrated (red) sample, showing that the frequency of the cyano group shifts only 2 wavenumbers according to the hydration state. *Nm*HR W201pCNF was measured as a hydrated sample only. For comparison, *Nm*HR wild type has no absorption in this region **(Figure 55, panel C)**.

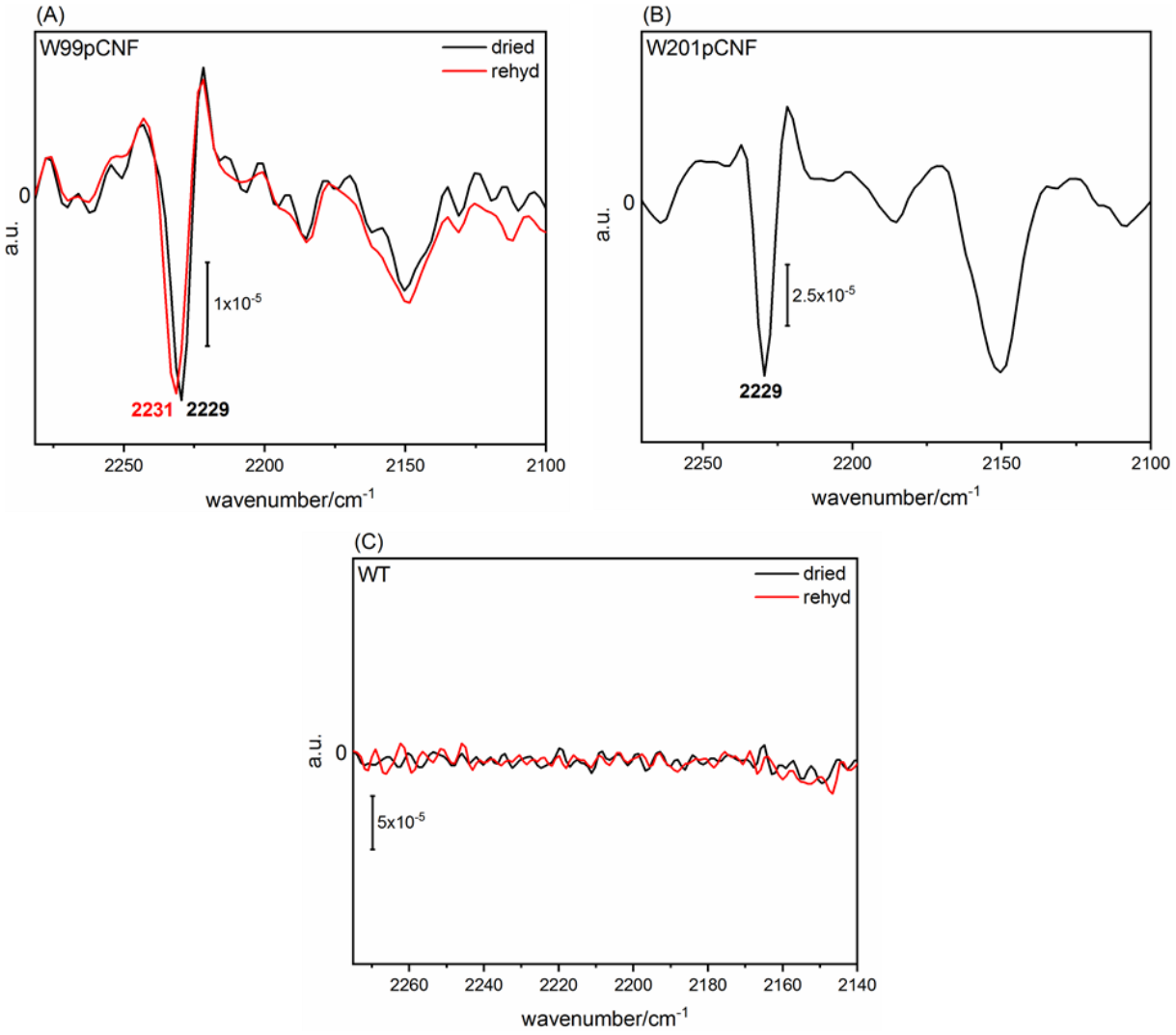

Figure 55. *Second derivative of the absolute spectra in the 2280-2100 cm^{-1} FTIR spectral region of NmHR W99pCNF (A), NmHR W201pCNF (B) and NmHR wild type (C). The negative signal at 2229-2231 cm^{-1} refers to the C=N stretching vibration of the cyano group of pCNF at positions 99 and 201.*

Table 5 shows the maximum absorption of retinal in the UV/Vis spectra of variants W99pCNF and W201pCNF, in 1 M and in 150 mM NaCl, compared to *Nm*HR wild type, *Nm*HR W99F and *Nm*HR W201F. Both pCNF variants show a salt dependence comparable to the phenylalanine substitution.

	Maximum absorption (1 M NaCl)	Maximum absorption (150 mM NaCl)
***Nm*HR wild type**	533 nm	546 nm
***Nm*HR W99F**	529 nm	534 nm
***Nm*HR W99pCNF**	525 nm	532 nm
***Nm*HR W201F**	532 nm	543 nm
***Nm*HR W201pCNF**	536 nm	546 nm

Table 5. *Comparison of the maximum absorption of retinal in the variants NmHR W99pCNF and NmHR W201pCNF with respect to the wild type, NmHR W99F and NmHR W201F, in the presence of two different salt concentrations. All variants show a chloride dependence of the retinal peak in the UV/Vis spectra.*

In addition, flash photolysis of *Nm*HR W99pCNF **(Figure 56, panel A)** shows a similar photoreaction to that of *Nm*HR W99F **(Figure 56, panel B)**, with a slow photocycle. In the case of *Nm*HR W201pCNF **(Figure 56, panel C)** the rise in O_1 and O_2 state accumulates more slowly than in *Nm*HR W201F **(Figure 56, panel D)**, indicating that chloride transfer (O_1 rise) takes longer. As shown previously for *Nm*HR W201F, conformational changes of the protein structure in the variant W201pCNF are also affected (O_2 rise).

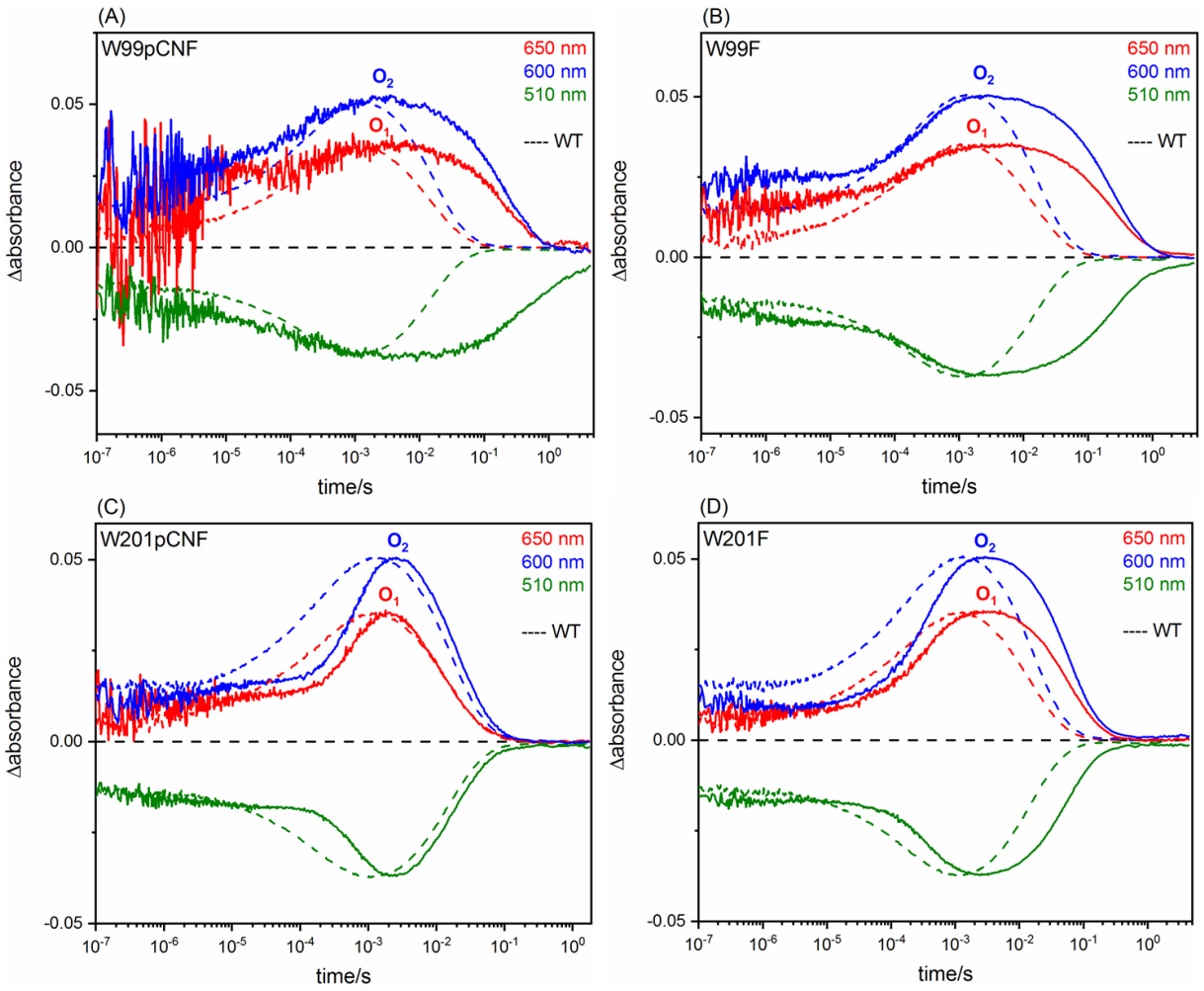

Figure 56. *Photocycle of NmHR W99pCNF (A), NmHR W99F (B), NmHR W201pCNF (C) and NmHR W201F (D) (solid line) compared to wild-type NmHR (dashed line). The photoreaction of the W99pCNF variant shows no major changes compared to W99F variant. The W201pCNF variant shows a faster photocycle compared to W201F variant, but a slower accumulation of the O_2 rise, more pronounced compared to W201F variant, confirming the hypothesis that the substitution of Trp-201 exerts an influence on conformational changes of the protein structure.*

After characterization of the CN-labeled proteins, ultrafast UV/Vis spectroscopy experiments were performed by Dr. Marvin Asido in the group of Prof. Dr. Wachtveitl (Goethe University, Frankfurt) on the variants W99F, W99pCNF, W201F and W201pCNF as well as wild-type *Nm*HR in two different salt concentrations, 1 M versus 150 mM NaCl **(Figure 57, panel A with unlabeled proteins and panel B with labeled proteins)**. The excited state dynamics (ES) of wild-type *Nm*HR is slowed down at low salt concentration, and the formation of the early

photoproduct after retinal isomerization is more pronounced at high salt concentration. In contrast, *Nm*HR W99F and *Nm*HR W99pCNF show no dependence of ES dynamics on NaCl concentration, whereas *Nm*HRW201F and *Nm*HR W201pCNF show a dependence, albeit smaller than in the wild type. These preliminary results suggest that the two tryptophans have individually different effects on the chloride concentration in the early *Nm*HR photoreaction.

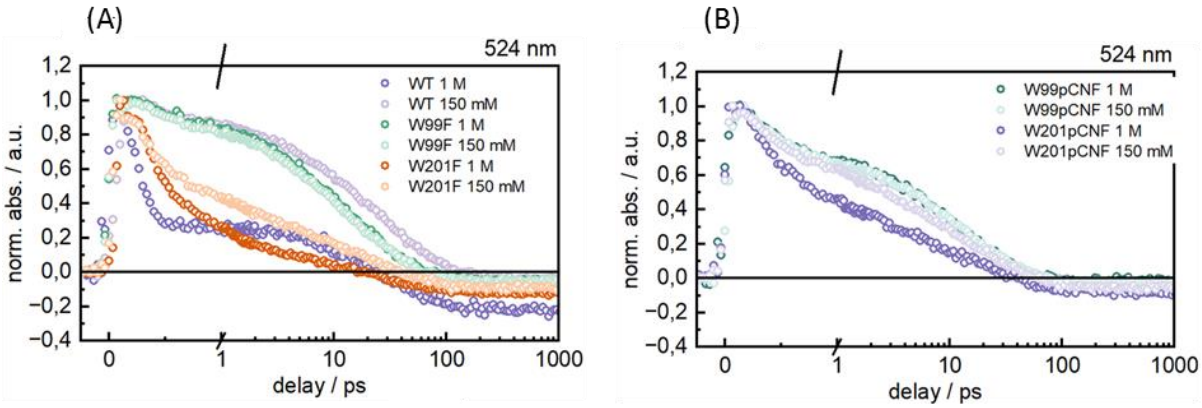

Figure 57. *Ultrafast UV/Vis experiment performed on NmHR wild type, NmHR W99F, NmHR W99pCNF, NmHR W201F and NmHR W201pCNF in 150 mM and 1 M NaCl. Excited state dynamics of NmHR wild type, NmHR W99F and NmHR W201F (A), NmHR W99pCNF and NmHR W201pCNF (B) in high and low salt conditions. The NmHR wild type shows a chloride dependence on excited state dynamics, as do NmHR W201F and NmHR W201pCNF, although to a lesser extent, while the W99F substitution shows no change. Figure courtesy of Dr. Marvin Asido (Goethe University, Frankfurt).*

4.2. *Um*Rh1: *Ustilago maydis* rhodopsin 1

In this project, a characterization of the novel fungal outward proton pump rhodopsin *Um*Rh1 was performed. This protein was expressed for the first time in large quantities in the yeast *Pichia pastoris* (20 mg/L), while previously reported studies were performed in mammalian cells to verify the electrophysiological activity. Therefore, extensive biophysical investigations were necessary to characterize this novel protein. Moreover, a comparison was made between the outward proton pump bacteriorhodopsin (*Hs*BR) and *Um*Rh1 to elucidate the role of the latter. Since very little is known about fungal rhodopsins, the well-known *Hs*BR was used as a model system to investigate similarities and differences between them. Residues known to be important for proton transfer in *Hs*BR are quite conserved in *Um*Rh1, although both proteins are phylogenetically distinct. The DTD motif (Asp-85/Thr-89/Asp-96) of *Hs*BR is replaced by a DTE motif (Asp-118/Thr-122/Glu-129) in *Um*Rh1. Some other residues important for proton ejection on the EC side of *Hs*BR are also quite conserved, as well as residues present in the retinal binding pocket, as shown in **Figure 58** and **Table 6**. The importance of these residues has been investigated by site-directed mutagenesis and subsequent biophysical studies.

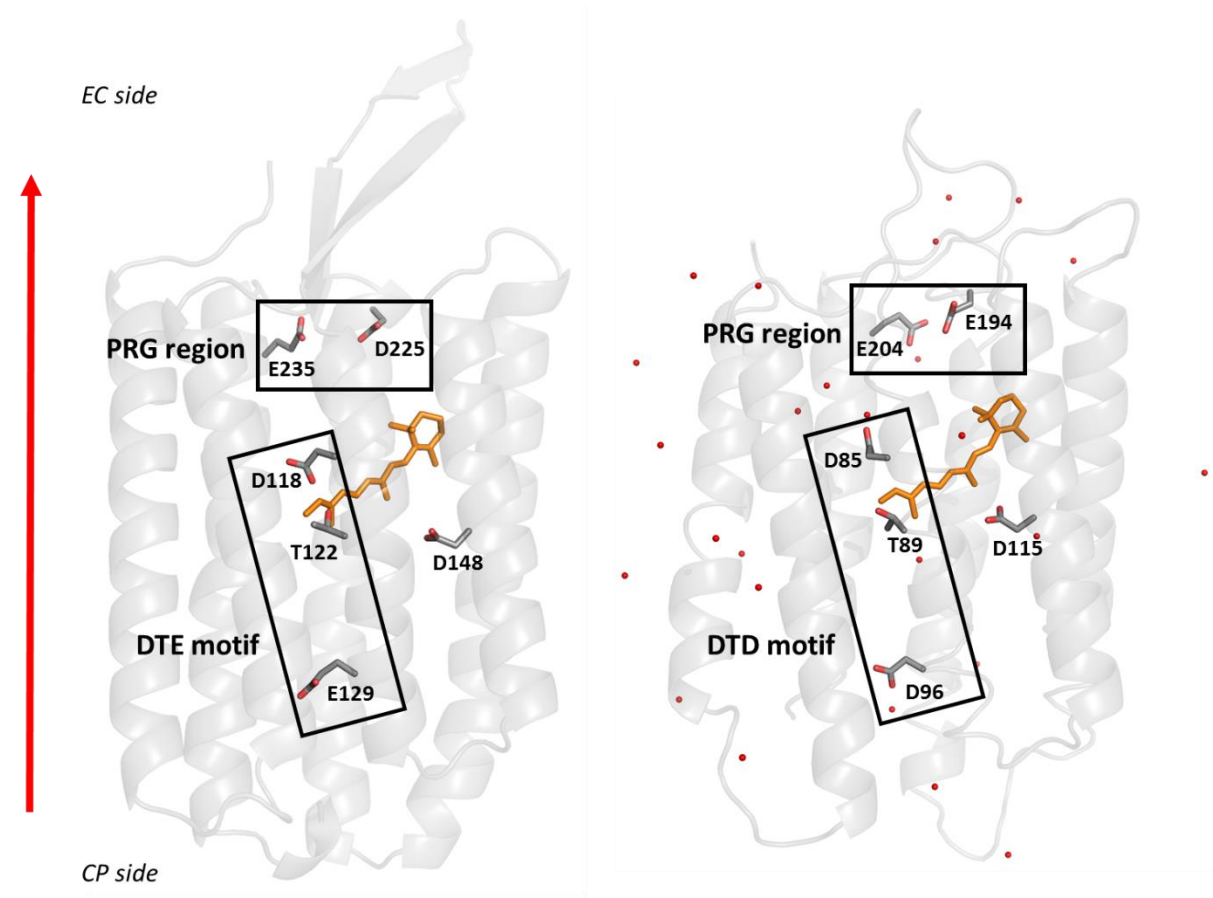

Figure 58. *Structure comparison of UmRh1 (predicted structure) and HsBR (PDB: 1AP9). Conserved residues known to be important for the protonation pathway in HsBR are highlighted. Residues forming the 3-letter motif and the proton releasing group are shown in black rectangles. The direction of proton transport is indicated by the red arrow.*

***Um*Rh1**	**D118**	**T122**	**E129**	D225	E235	D148
***Hs*BR**	**D85**	**T89**	**D96**	E194	E204	D115

Table 6. *Sequence homology between UmRh1 and HsHR. The table shows the amino acids described in this study, in comparison with HsBR. The three-letter motif is highlighted in red.*

This joined project was executed in a team with Jheng-Liang Chen (Freie Universität, Berlin) and Dr. Luiz Schubert (Freie Universität, Berlin) who was involved in the spectroscopic part. A master student, Tim Berneiser was executing experiments on native *Um*Rh1. The individual contributions are indicated.

4.2.1. Steady state and time-resolved UV/Vis spectroscopy of *Um*Rh1 at different pHs

The steady state UV/Vis spectrum of *Um*Rh1 shows a maximum absorption of retinal at 530 nm. In order to understand the pH-dependent behavior described previously[33], a pH titration was carried out, with the result that the protein undergoes a red shift of 5 nm as the pH is lowered **(Figure 59, panel A)**. Using the Henderson-Hasselbach equation, the pKa was found to be around 5 **(Figure 59, panel B)**. This pKa is due to the protonation of an amino acid and will be discussed further in section **4.2.6**. Conversely, the pKa of the Schiff base, calculated at alkaline pH by monitoring the absorbance at 365 nm and 532 nm, was found to be 10, which is lower than that found for *Hs*BR (= 13)[34] **(Appendix Figure S7)**.

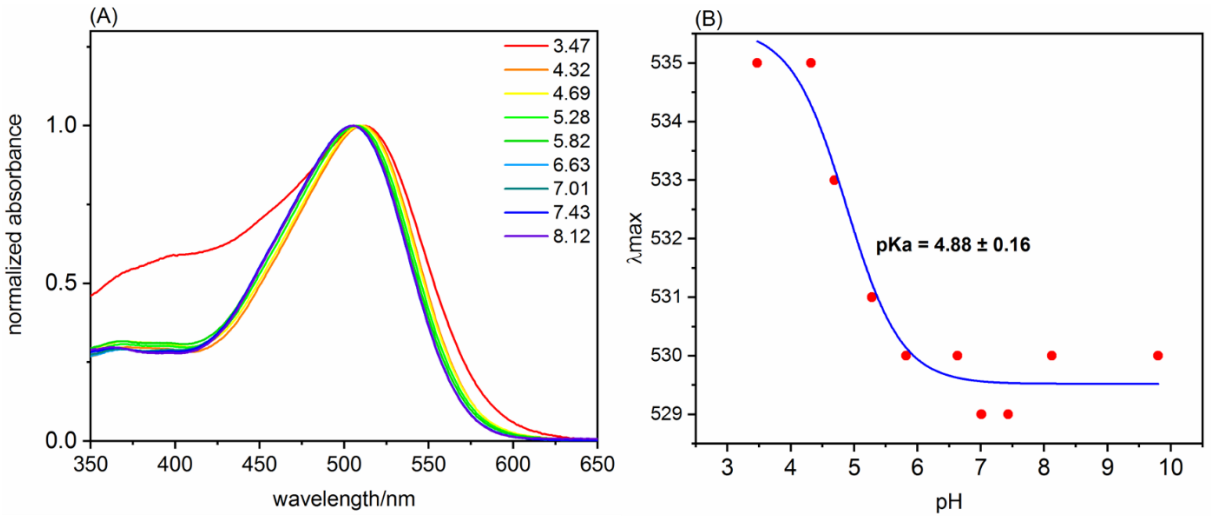

Figure 59. *pH titration in the UV/Vis region of UmRh1 showing the shift of the maximum absorption of the bound retinal (A), pKa of the retinal calculated using the Henderson-Hasselbach equation (B).*

Next, the photoreaction of *Um*Rh1 **(Figure 60, panel A)** was studied using a flash photolysis setup, to evaluate the maximum absorption of each intermediate and their time constants. At neutral pH **(Figure 60, panel B)**, the photocycle of *Um*Rh1 is similar to that of *Hs*BR as follows: After excitation with a green laser (ʎ: 532 nm), the decay of a red-shifted intermediate with respect to the dark state was detected and named K. Next, a blue-shifted intermediate appears at 460 nm (L state), which transitions to a long-lived intermediate, the M state, detected at 400 nm. Interestingly, when the pH is lowered to 5 **(Figure 60, panel C)**, *Um*Rh1 exhibits a faster photocycle with a ground state recovery time constant of 5 ms compared to 40 ms at neutral pH. The O state (620 nm) was detected only at pH 5, but was barely detectable at pH 7.4, while the M state predominated at neutral pH. The decay of the M and O states at acidic pH was found to be faster than in *Hs*BR[34].

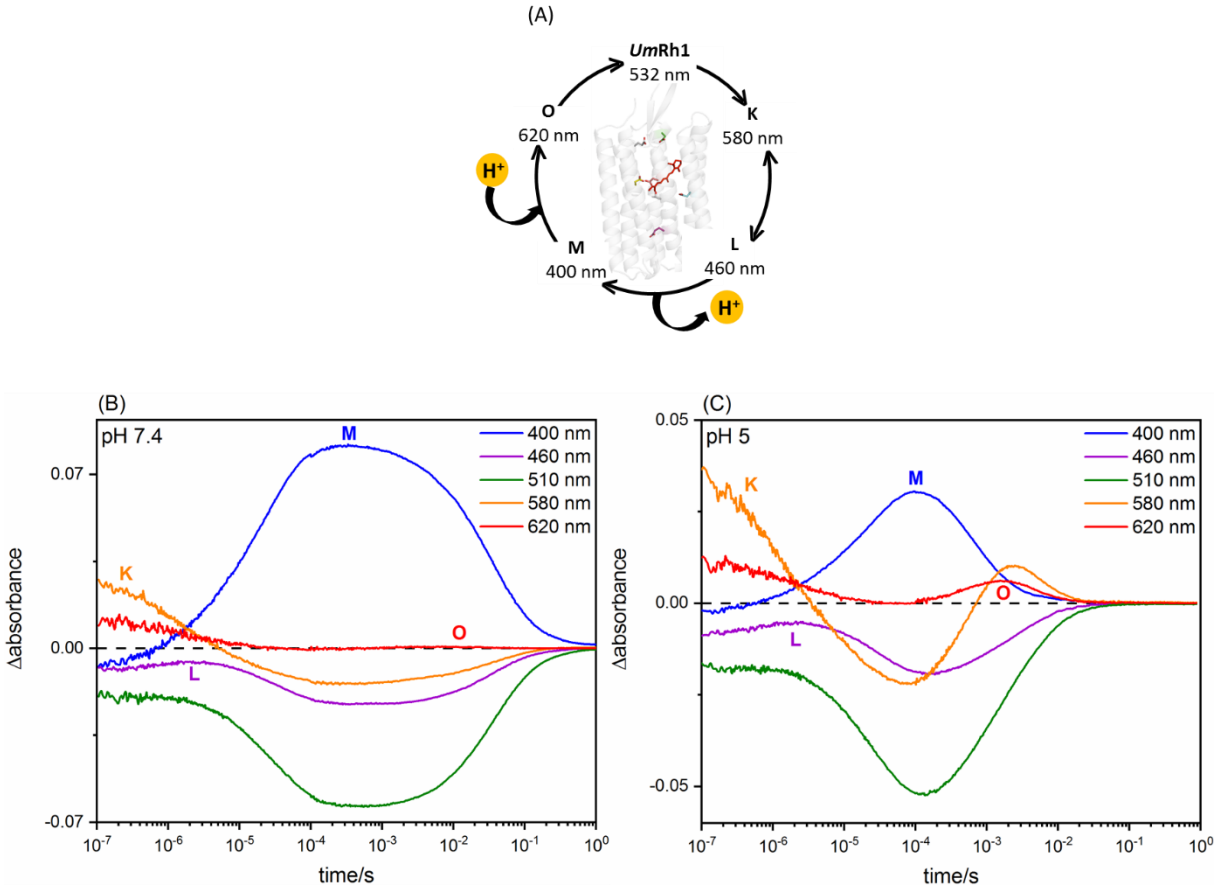

Figure 60. *Photocycle scheme of UmRh1 (A). Photocycle of UmRh1 at pH 7.4 (B) and pH 5 (C). The wavelengths chosen were 400 nm, 460 nm, 510 nm, 580 nm, and 620 nm, which are representative of the M, L, ground state, K, and O states, respectively. The M state is predominant at pH 7.4, while the O state is detected only under acidic*

conditions. The intermediate states and their maximum absorption are shown. The deprotonation of RSB occurs during the rise of the M state and its reprotonation during the decay of the M state.

4.2.2. FTIR spectra of *Um*Rh1 in neutral and acidic conditions

While time-resolved UV/Vis spectroscopy reports on the retinal environment and the protonation state of the Schiff base, FTIR spectroscopy provides additional details on some side chains of amino acids and structural changes of the protein[100]. Since *Um*Rh1 showed a pH-dependent photocycle, the light-induced FTIR difference spectra (difference between the photointermediate and dark states) of *Um*Rh1 were recorded at pH 7.4 and 5 **(Figure 61)**. The band at 1183 cm^{-1} was assigned to the 13-*cis* retinal with protonated Schiff base[101], while the negative band at 1202 cm^{-1} was assigned to the all-*trans* retinal configuration in the dark state. Some bands show differences with pH, such as the band at 1522 cm^{-1}, which is more prominent at pH 5. This signal originates from the O state, an intermediate with a red-shifted absorption compared to the ground state (observed at 1540 cm^{-1}). The positive band at 1568 cm^{-1} was assigned to the M state, which predominates at pH 7.4, as was the small negative band at 1650 cm^{-1} (indicated by the black arrow) of the C=N stretching mode of the retinal Schiff base (RSB). Interestingly, the band at 1668 cm^{-1}, corresponding to the amide I vibration and originating from the protein backbone, is more intense under acidic conditions, suggesting that the protein undergoes larger conformational changes at pH 5 than at neutral pH[34]. Finally, the positive band at 1761 cm^{-1} and the negative band at 1737 cm^{-1} have been assigned to the C=O stretching vibration of either aspartic acid or glutamic acid[79].

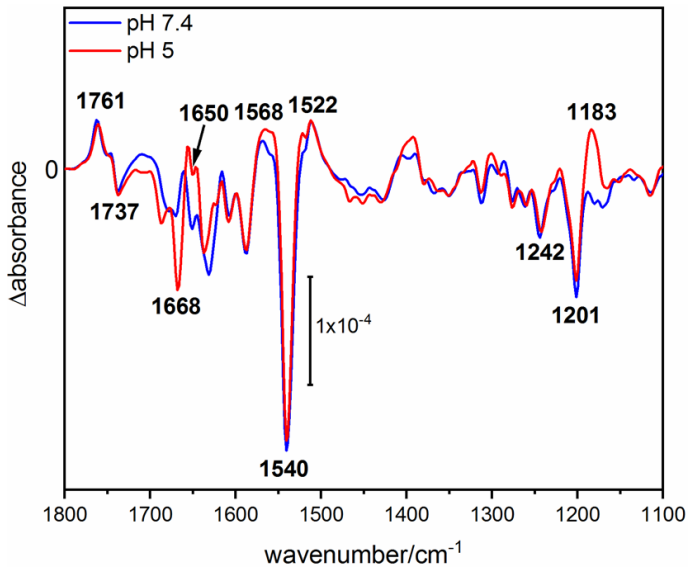

Figure 61. *Light-induced difference FTIR spectra of UmRh1. The spectra at pH 7.4 (blue) and pH 5 (red) were recorded using a green LED (525 nm). The bands discussed in the text are highlighted.*

4.2.3. DTE motif: Asp-118 and its role in proton release

Asp-118 in *Um*Rh1 is part of the DTE motif and is located near the chromophore. In *Hs*BR, the homologue of Asp-118 is Asp-85, the proton acceptor of the PSB **(Figure 58)**. The steady-state FTIR spectrum of *Um*Rh1 shows a positive band at 1761 cm^{-1}, which is in the frequency range of carboxylic acid residues (ν(C=O)) **(Figure 61)**. In *Hs*BR, the protonation of Asp-85, the proton donor to the Schiff base, has been described to show a positive band at exactly the same position[102]. Here the homologue Asp-118 of *Um*Rh1 was studied to see if it has the same function. By an exchange D118E, the positive C=O stretching vibration at 1761 cm^{-1} disappeared in the light-induced difference FTIR, so that this band could be clearly assigned to this Asp **(Figure 62)**. The spectra of *Um*Rh1 wild type and D118E at pH 7.4 are shown in the IR frequency range 1800-1700 cm^{-1}. In the variant, the band at 1761 cm^{-1} shifts to lower frequencies, 1720 cm^{-1}, indicating that the band is due to Asp-118, as suspected, with a role similar to that of Asp-85 in *Hs*BR **(Table 6)**.

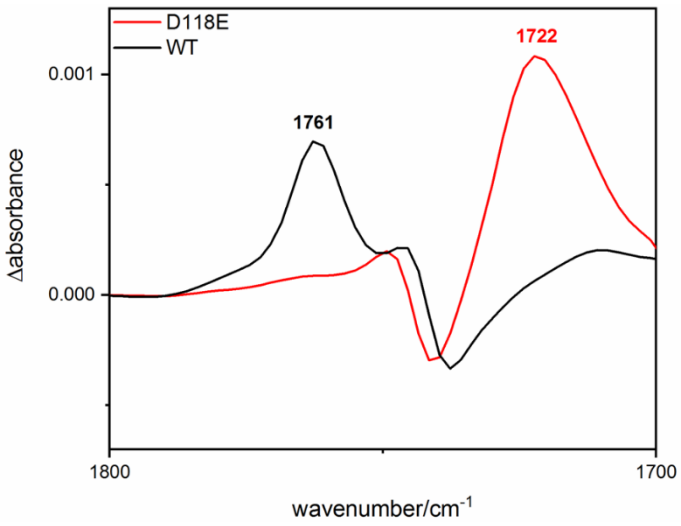

Figure 62. *Light-induced difference FTIR spectra of UmRh1 wild type at pH 7.4 (black) and UmRh1 D118E (red) using a green LED (525 nm), in the indicated region 1800-1700 cm^{-1} of COOH vibrations. The frequency shift indicates that the positive band at 1761 cm^{-1} in the wild type is due to D118. Executed by J-L.Chen (dissertation submitted in February 2025).*

To evaluate the role of Asp-118 for the photoreaction the variant was studied by time-resolved UV/Vis spectroscopy under neutral and acidic conditions. In **Figure 63, panel A** the M state accumulates more rapidly in the mutant at both pHs, similar to what has been described previously also for *Hs*BR D85E [103]. Interestingly, in the variant, the O state is only present in the alkaline environment, in contrast to the wild type, where the O state is only detected at low pH **(Figure 63, panel B)**. This result suggests that although the deprotonation mechanism of the SB is still preserved in the variant, the proton release mechanism in the O state is impaired. The light-induced difference FTIR spectra as well as the flash photolysis of variant D118E were performed by J.-L. Chen (Dissertation submitted in February 2025, FU Berlin).

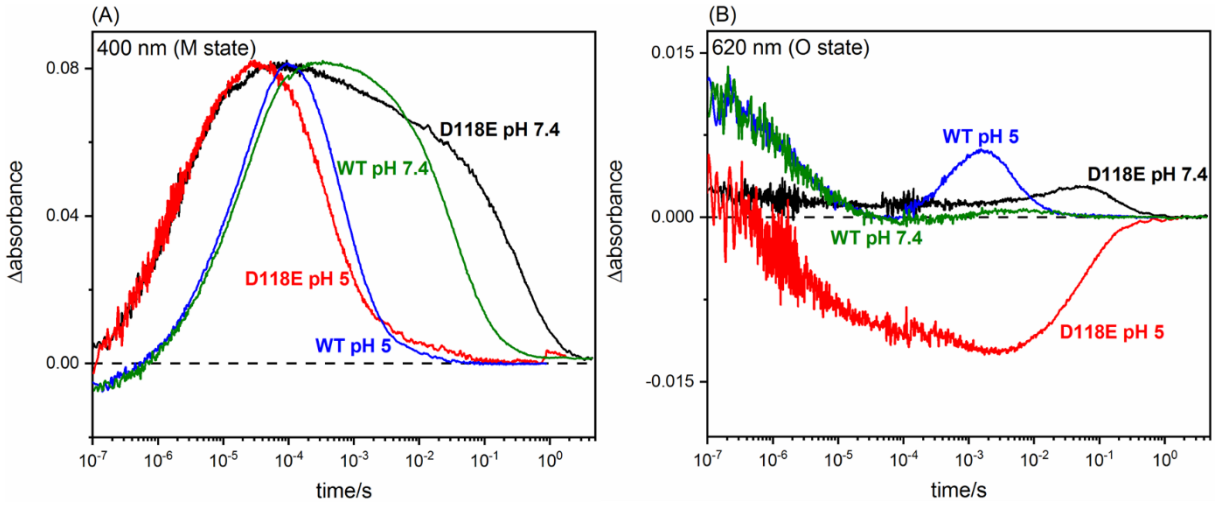

Figure 63. *Comparison of M state kinetics, monitored at 400 nm, between UmRh1 wild type and D118E, at pH 7.4 and pH 5 (A). The M state accumulates more rapidly in the D118E variant than in the wild-type protein. Comparison of O state kinetics, monitored at 620 nm, between UmRh1 wild type and D118E, at pH 7.4 and pH 5 (B). In the D118E variant, the O state is only detected at alkaline pH, the opposite situation for wild-type UmRh1. Executed by J-L. Chen (dissertation submitted in February 2025).*

4.2.4. DTE motif: Glu-129 and its putative role in proton transport

Glu-129, which also belongs to the DTE motif, was investigated in this study **(Figure 58)**. In the range of carboxylic acid residues of the light-induced difference FTIR spectrum of *Um*Rh1 wild type, a negative band was found at 1737 cm^{-1} **(Figure 61)**. Again, *Hs*BR was used for band assignment, as a negative band at 1742 cm^{-1} was described and assigned to Asp-96, the proton donor to the Schiff base[104] (homologous residue to Glu-129), which decreases in intensity at low pH, suggesting that Asp-96 is titrated in *Hs*BR. Interestingly, in *Um*Rh1 wild type, the intensity of the negative band at 1737 cm^{-1} does not decrease when the pH is lowered to 5 **(Figure 61)**. This result provides a preliminary indication that Glu-129 may not be the proton donor for the Schiff base. In addition, the kinetics of the M state, measured at 400 nm, show a linear dependence on pH; the decay slows down with increasing pH **(Figure 64)**. This pH dependence of the M state decay in *Um*Rh1 is similar to that observed for the D96N variant of *Hs*BR[105]. This result, together with the presence of the negative band at 1737 cm^{-1} in the wild-

type spectrum at low pH, suggests that the proton donor to the Schiff base in *Um*Rh1 may not be Glu-129.

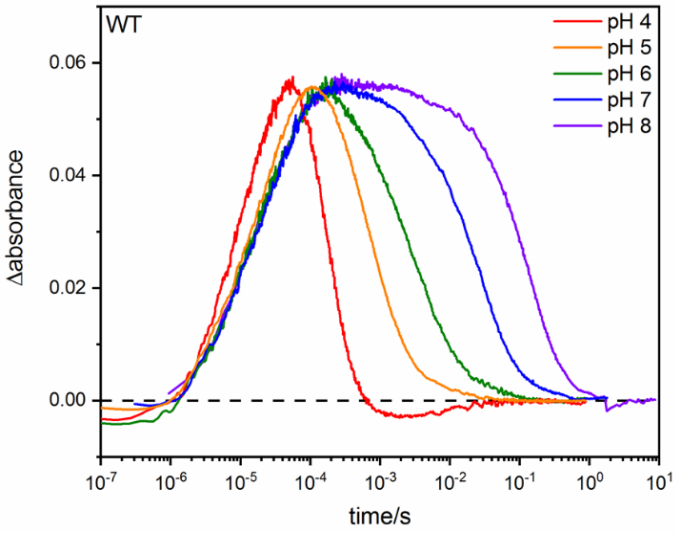

Figure 64. *pH titration of the M state, monitored at 400 nm of UmRh1 wild type using a flash photolysis technique. The decay of the M state slows down with increasing pH.*

To verify this hypothesis, two variants were generated: E129D and E129Q, and the M state kinetics were measured in a pH range from 4 to 8. For both variants, the M state decay shows a linear correlation with pH, comparable to the wild-type protein **(Figure 65, panels A and B)**.

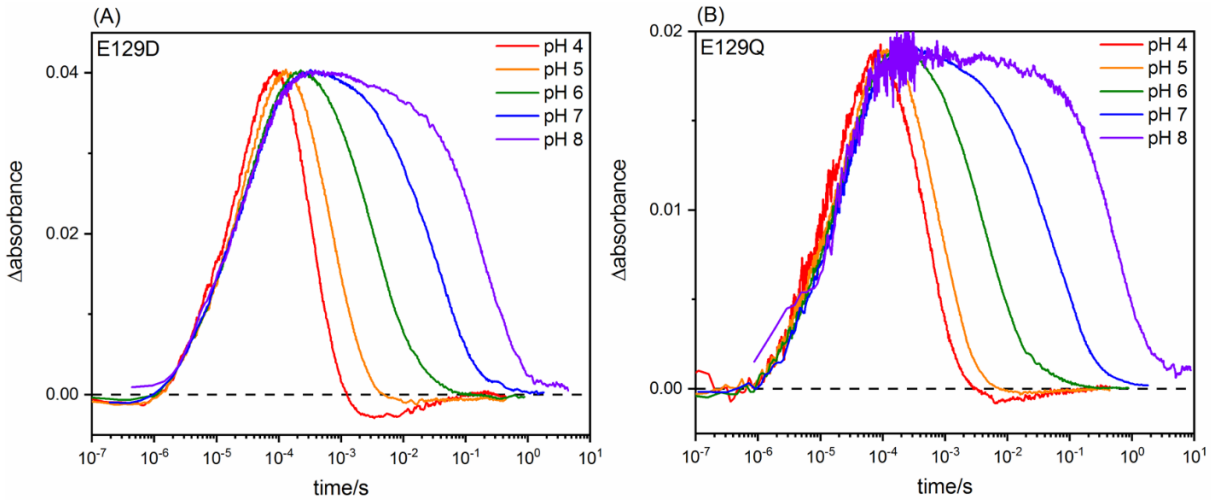

Figure 65. *pH titration of the M state, monitored at 400 nm of UmRh1 E129D (A) and E129Q (B) using a flash photolysis technique. The M decay is slowed down with increasing pH, similar to wild-type UmRh1. pH titration of UmRh1 E129Q was executed by J-L. Chen (dissertation submitted in February 2025).*

When the E129D and E129Q variants are studied by steady-state FTIR spectroscopy, the resulting light-induced difference spectra show the band at 1737 cm^{-1} in both proteins, although with reduced intensity in the case of E129Q **(Figure 66)**. In addition, the spectrum of the E129Q variant shows an additional band at 1697 cm^{-1}, which is in the region of the vibration of the asparagine and glutamine side chains, probably due to the inserted glutamine at position 129. This observation supports the suggestion that Glu-129 is not the proton donor to the SB, but that the proton is taken up directly from the cytoplasmic bulk medium or that another residue has this role.The light-induced difference FTIR spectra and pH titration of the E129Q variant were performed by Jheng-Liang Chen (Freie Universität, Berlin) (Dissertation submitted in February 2025).

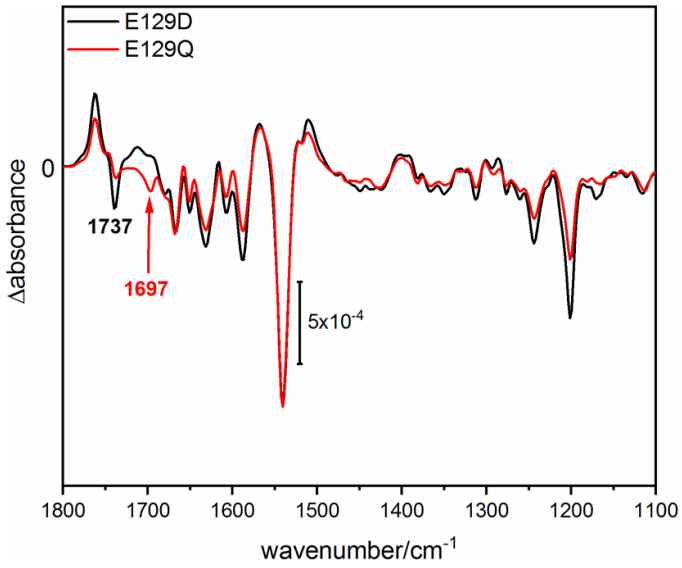

Figure 66. *Light-induced difference FTIR spectra at pH 8.2 of UmRh1 E129D (black) and E129Q (red) using a green LED (525 nm). The monitored band at 1737 cm^{-1} is highlighted. The E129Q spectrum shows an additional band at 1697 cm^{-1}, indicated by a red arrow, due to the inserted glutamine at position 129. Executed by J-L. Chen (dissertation submitted in February 2025).*

4.2.5. Possible interaction of Glu-129 and Asp-148

Since there is still a small residual band at 1737 cm^{-1} for the E129Q mutation, another carboxylic acid residue close to the retinal may contribute to the signal. It was decided to investigate *Um*Rh1 Asp-148, which is close to the retinal, and Glu-129 **(Figure 58)**. Two variants were generated, the D148N variant and the double variant E129Q/D148N **(Figure 67, panels A and B)**. In the variant D148N the band at 1737 cm^{-1} shifts to 1733 cm^{-1} and, surprisingly, the positive counterpart at 1745 cm^{-1} is missing. In addition, a new negative band appears at 1708 cm^{-1}, which can be attributed to the inserted asparagine at position 148. In the double mutant E129Q/D148N, both the positive (1745 cm^{-1}) and negative (1737 cm^{-1}) bands disappear completely and two additional bands appear, one at 1708 cm^{-1} (assignable to asparagine) and one at 1695 cm^{-1}, more likely due to the inserted glutamine at position 129. These changes suggest that the positive/negative bands at 1745 cm^{-1}/1737 cm^{-1} are due to the interaction between Asp-148 and Glu-129. Similar observations are made for *Hs*BR, where Asp-115 (homologous to Asp-148) gives rise to a negative signal that overlaps with the negative band due to Asp-96 (homologous to Glu-129)[106].

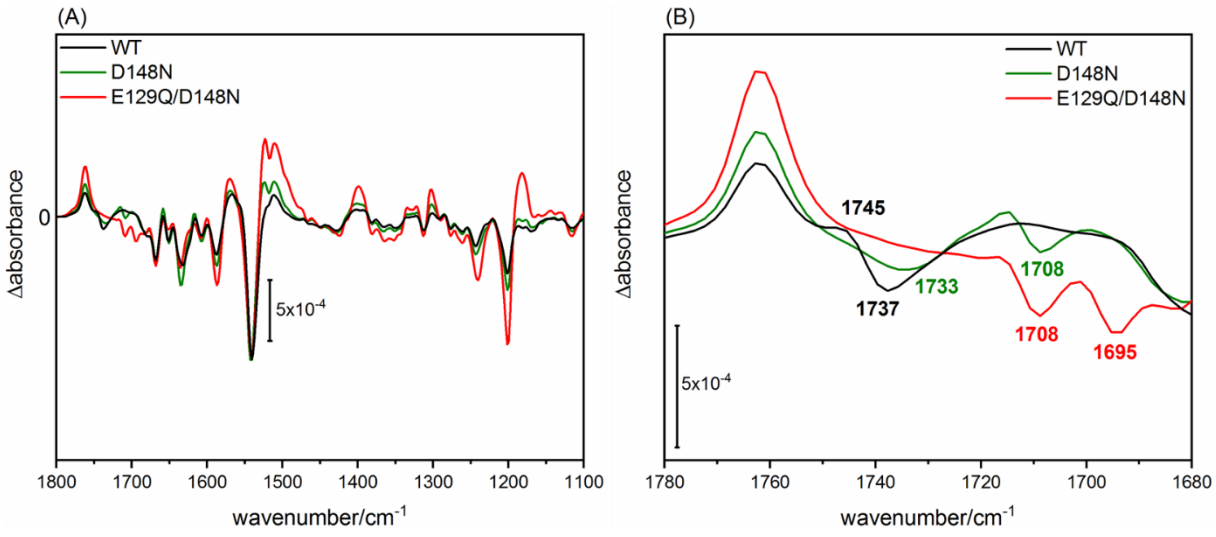

Figure 67. *Light-induced difference FTIR spectra at pH 8.2 of UmRh1 wild type (black), UmRh1 D148N (green) and UmRh1 E129Q/D148N (red) using a green LED (525 nm) (A). Zoom of the FTIR spectral region 1780 cm^{-1} – 1680 cm^{-1} (B). The negative band at 1737 cm^{-1} shifts to 1733 cm^{-1} upon mutation of D148N and both the negative band at 1737 cm^{-1} and its positive counterpart at 1745 cm^{-1} disappear in the double variant. The additional negative*

bands at 1708 cm^{-1} and at 1695 cm^{-1}, are due to the inserted asparagine at positios 148 and glutamine at position 129.

Is Asp-148 the proton donor to the Schiff Base?

To investigate whether Asp-148 is the proton donor for the Schiff base, time-resolved UV/Vis monitoring of the M state was performed on the D148N and E129Q/D148N variants at different pHs **(Figure 68, panels A and B)**. These variants also show a linear correlation between M state and pH, similar to wild-type *Um*Rh1, except for some minor differences in decay at high pH, indicating that it is not the proton donor either.

Taken together, the FTIR and flash photolysis results of the last paragraphs suggest that the band at 1737 cm^{-1} is due to the superposition and contribution of both Asp-148 and Glu-129. However, since both variants still show a pH dependence on the photocycle, both residues do not transfer the proton to the SB and are therefore not the desired proton donors.

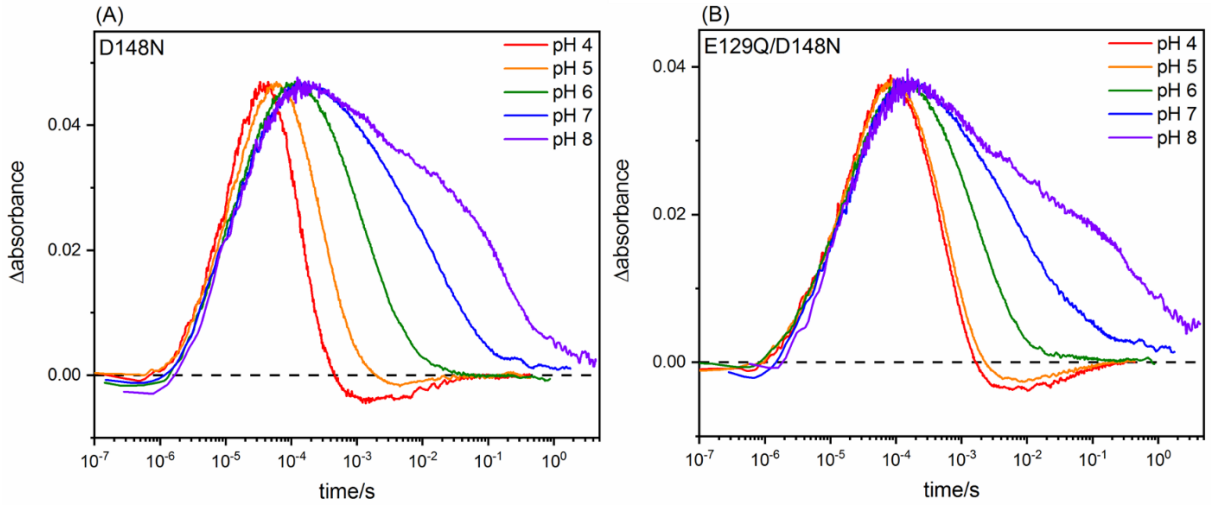

Figure 68. *pH titration of the M state, monitored at 400 nm of UmRh1 D148N (A) and UmRh1 E129Q/D148N (B) using a flash photolysis technique. The M decay is slowed down with increasing pH in the same way as for wild-type UmRh1, but some differences are detected at high pH.*

4.2.6. Proton releasing group: Asp-225 and Glu-235

Next, to further elaborate the proton pathway in *Um*Rh1, the putative proton releasing group (PRG) Asp-225 and Glu-235 on the extracellular side was investigated. Comparing different proton pump rhodopsins, such as the archaeal *Hs*BR and the fungal LR with *Um*Rh1, this region seems to be quite conserved. Asp-225 and Glu-235 in *Um*Rh1 are replaced by Glu-194 and Glu-204 in *Hs*BR and by Asp-248 and Glu-258 in the fungal rhodopsin LR[107], whereas the bacterial outward proton pump proteorhodopsin PRs contain only one carboxylic residue[108], as well as *Psp*R[109] **(Table 7)**.

Proton releasing group region

*Um*Rh1	D225	E235
*Hs*BR	E194	E204
LR	D248	E258
PRs	E142	-
*Psp*R	E188	-

Table 7. *Comparison of the proton releasing group region of different outward proton pumping rhodopsins. UmRh1, HsBR and the fungal LR contain two carboxylic residues, whereas the bacterial proteorhodopsin class and PspR contain only one carboxylic residue.*

First, the D225N variant was generated and analyzed by time-resolved UV/Vis at neutral and acidic pH in comparison to wild-type *Um*Rh1. Although the kinetics of the O state **(Figure 69, panel A)** monitored at 620 nm, are unchanged between the two samples at both pHs, a different situation was found for the M state (monitored at 400 nm) **(Figure 69, panel B)**. At pH 5, both *Um*Rh1 D225N and wild-type *Um*Rh1 show a faster accumulation at 400 nm, whereas at pH 7.4 the variant shows a two-component decay of the M state.

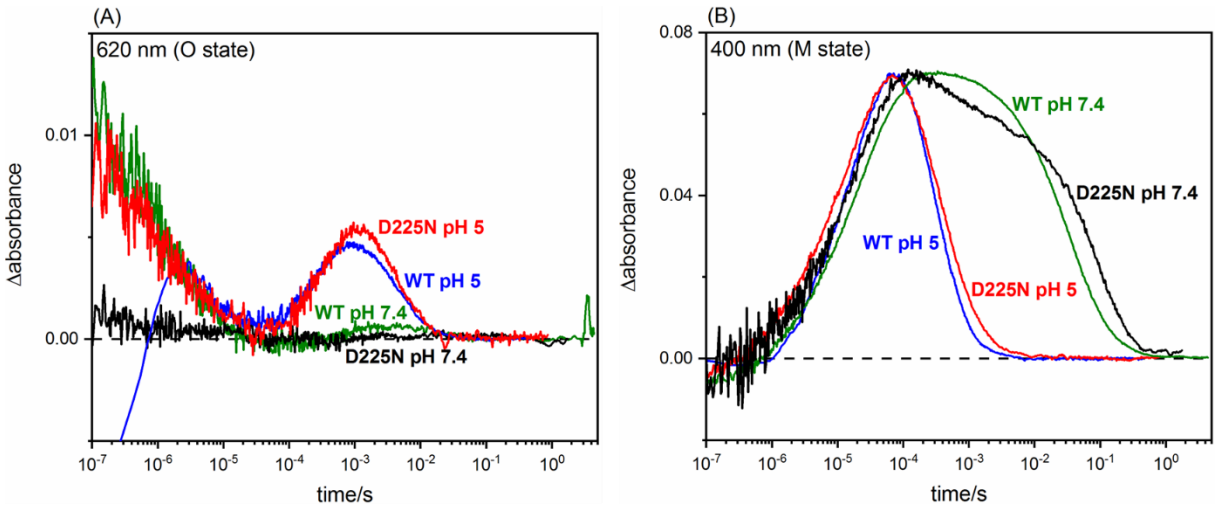

Figure 69. *Comparison of O state kinetics, monitored at 620 nm, between UmRh1 wild type and UmRh1 D225N, at pH 7.4 and pH 5 (A). No differences were detected in the O state traces between the variant and wild-type at either pH. Comparison of M state kinetics, monitored at 400 nm, between UmRh1 wild type and D225N, at pH 7.4 and pH 5 (B). The M state in the D225N variant shows some differences compared to the wild type only at neutral pH.*

Further the pH titration of *Um*Rh1 D225N, monitoring the M state, shows that this different behavior of the M state decay is only present at pH higher than 7 **(Figure 70, panel A)**. Therefore, the decay of the M state at pH 8 was observed at different wavelengths. **Figure 70, panel B** shows the different kinetic traces between 420 nm and 350 nm. Although only one M state was detected between 350 and 370 nm, a second M state appears between 380 and 420 nm.

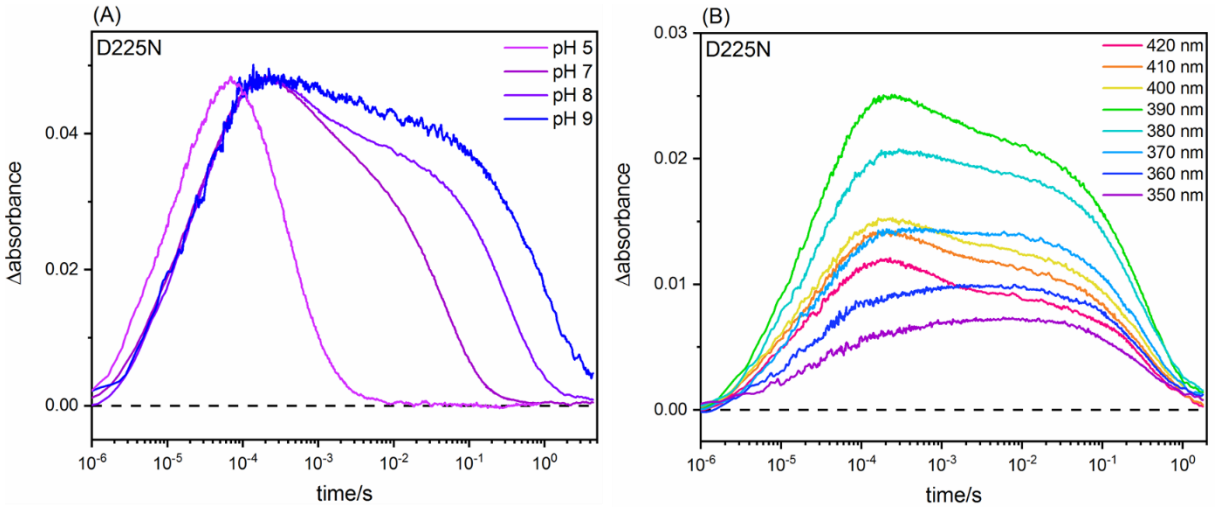

Figure 70. *pH titration of the M state kinetic at 400 nm, performed on UmRh1 D225N (A). Flash photolysis performed on variant D225N at pH 8 measured from 350 nm to 420 nm shows a "second M state" originating from 380 nm to 420 nm (B).*

In *Hs*BR variants of PRG show a slower O decay[36]. This does not seem to be the case in *Um*Rh1 (*vide supra*) **(Figure 69, panel A)**.

In a next step light-induced difference FTIR spectroscopy was used to assign potential bands to the protonation state of Asp-225. For this purpose, two different variants of this position D225N and D225E were analyzed with respect to the wild type at pH 5 **(Figure 71)**. The choice of acidic conditions is due to the fact that the O state accumulates only at low pH. Nevertheless, no differences were found in the light-induced different spectra in the carboxylic acid region (1800-1700 cm^{-1}) compared to the native protein, thus no band could be here assigned due to a change in the protonation state of Asp-225. Similar results have been described for the Glu-194 and Glu-204 variants of *Hs*BR[110].

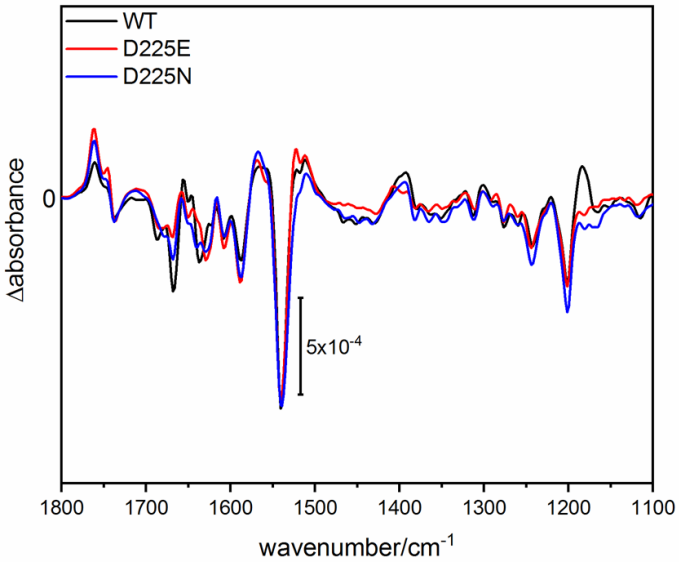

Figure 71. *Light-induced difference FTIR spectra at pH 5 of UmRh1 wild type (black), D225E (red) and D225N (blue), to address structural changes at the potential proton-releasing group, using a green LED (525 nm).*

Surprisingly, functional assays performed by J.-L. Chen, (dissertation submitted February 2025, FU Berlin), on these two variants (*data not shown here*) indicate that both proteins exhibit no pump activity under light, even with conservative substitution of glutamic acid. Interestingly, pH titrations performed by J.-L Chen on D225N and D225E *(data not shown)* show no pH-dependent changes in the maximum absorbance, as previously shown for the wild type **(Figure 59, panel A)**. Therefore, it can be concluded that Asp-225 is responsible for the shift in the UV/Vis spectra at different pHs. In the case of *Um*Rh1 E235Q (homologue of *Hs*BR E204), Chen still reports a shift, but more towards blue absorption at high pH. This suggests a possible interaction of Asp-225 with Glu-235.

4.2.7. Cysteines in *Um*Rh1: Cys-174 and Cys-261

*Um*Rh1 contains two cysteines: Cys-174 near the retinal and Cys-261 on the cytoplasmic side of the membrane **(Figure 72, panel A)**. The S-H stretching vibration of cysteines can be observed in the FTIR spectrum around 2500 cm^{-1}. *Um*Rh1 shows a positive-negative feature at 2565-2557 cm^{-1} **(Figure 72, panel B)**, which is tentatively attributed to a change in the hydrogen

bond of a cysteine residue. To determine which cysteine is the source of the S-H stretching vibration, single point mutations were performed on the two cysteines to the conservative serine, removing the S-H group. **Figure 72, panel C**, shows the output of the steady-state FTIR spectra, at neutral pH, of *Um*Rh1 C174S and *Um*Rh1 C261S in the range of 2650 cm^{-1} to 2450 cm^{-1}. No bands were detected in the C174S variant, whereas in the case of the C261S exchange, the positive-negative band was still present, although the noise level was at the same intensity as the bands as the SH vibration has a low extinction coefficient. To confirm that the bands were not an artifact, the measurement was repeated using an alternative method for FTIR, on BaF_2 window. Here, a dried sample film increases the size of the band, which gives stronger signals **(Appendix Figure S8)**. The result confirmed that the bands at 2565-2557 cm^{-1} were due to Cys-174.

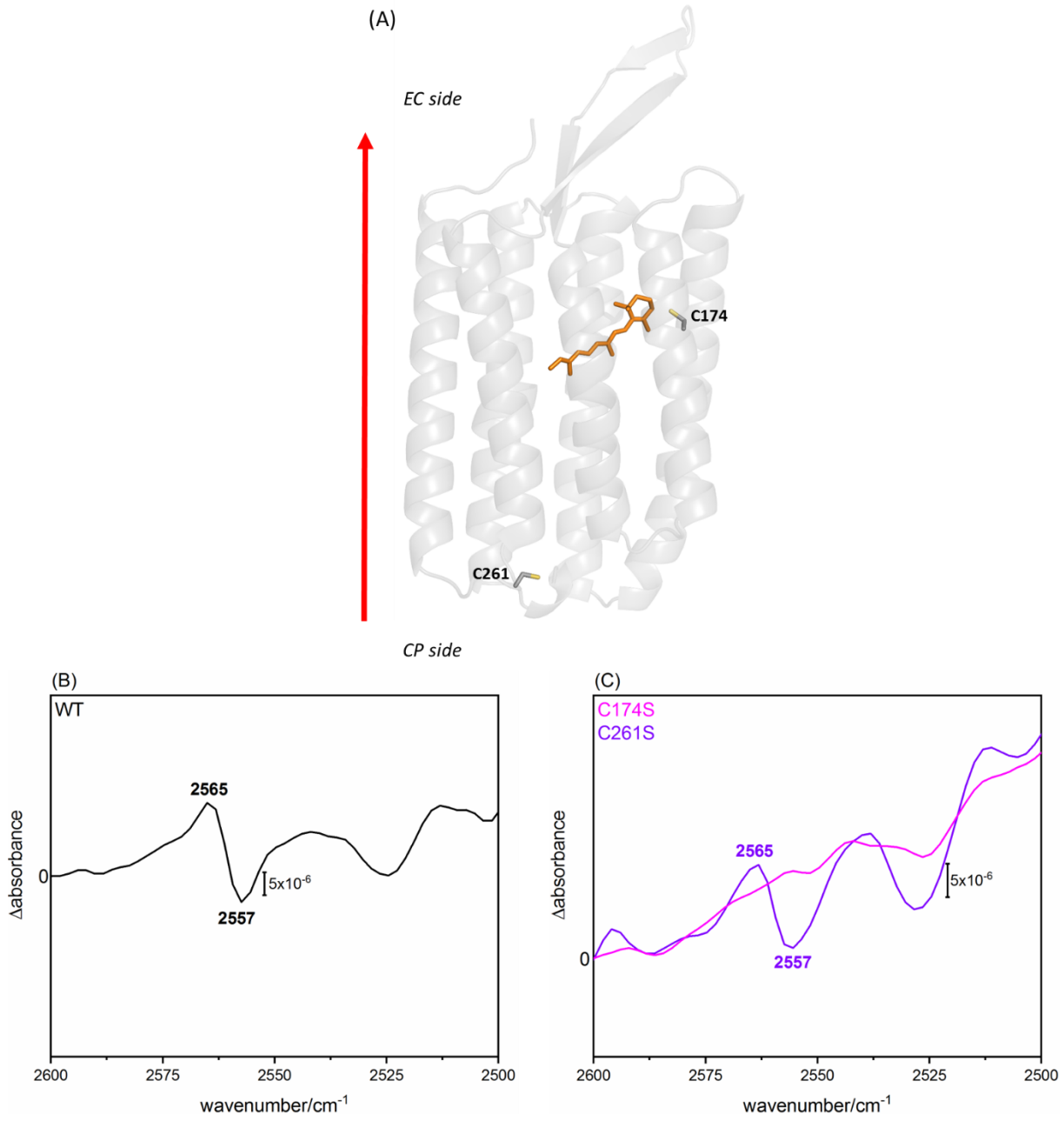

Figure 72. *Predicted structure of UmRh1 with Cys-174 and Cys-261 highlighted (A). Light-induced difference FTIR spectrum of UmRh1 wild type (B), UmRh1 C174S (magenta) and UmRh1 C261S (purple) (C) in the region of the S-H stretching vibrations of cysteine side chains, illuminated by a green LED (λ:525 nm). Although UmRh1 wild type and UmRh1 C261S clearly show a negative/positive peak at 2557/2565 cm^{-1}, UmRh1 C174S shows no band, indicating that Cys-174 is responsible for the H-bond change.*

After the assignment of the SH band, the importance of cysteines in the photoreaction was investigated. Both variants C174S and C261S were investigated by time-resolved UV/Vis spectroscopy at pH 7.4. While *Um*Rh1 C261S shows no major difference from the wild type **(Figure 73, panel A)**, *Um*Rh1 C174S behaves differently in the M state kinetics under alkaline conditions **(Figure 73, panel B)**.

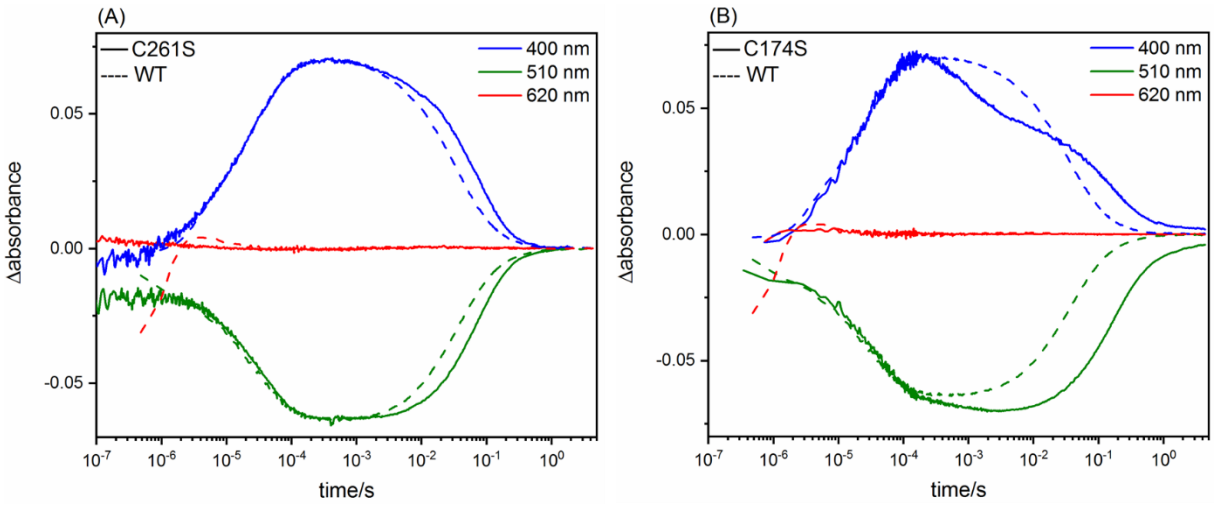

Figure 73. *Flash photolysis experiment performed on UmRh1 C261S (A) and C174S (B) compared to UmRh1 wild type. While UmRh1 C261S shows no differences to the wild type, UmRh1 C174S differs in the M state decay.*

A pH titration of the M state kinetics **(Figure 74, panel A)** indicates that the different behavior of the M state decay in *Um*Rh1 C174S is present only under alkaline conditions. Therefore, the variant was measured at pH 8 by flash photolysis in the wavelength range of 350 nm - 420 nm and the M state decay was monitored showing a "second M state" absorbing from 380 nm to 420 nm **(Figure 74, panel B)**.

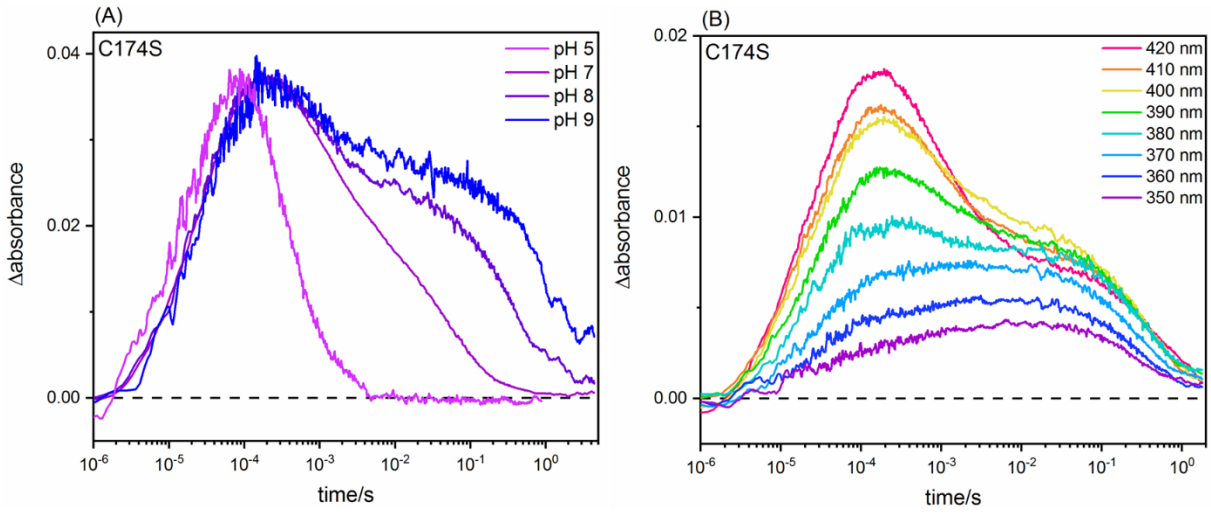

Figure 74. *pH titration of the M state kinetic at 400 nm, performed on UmRh1 C174S (A). Flash photolysis performed on the variant C174S at pH 8, measured from 350 nm to 420 nm (B). C174S shows a "second M state" appearing from 380 nm to 420 nm.*

4.2.8. *Um*Rh1 and pathogenesis

Ustilago maydis is a pathogenic fungus, responsible for corn smut disease in maize plants. *Sabine Panzer et al.* have shown by electrophysiological experiments that *Um*Rh1 has a higher pump activity in the presence of weak organic acids (WOAs), in particular in the presence of the indole-3-acetic acid, and they have speculated that IAA may lead to conformational changes in the protein structure[33]. IAA is a plant auxin which is responsible for plant growth and levels of this WOA are increased in the presence of plant infection. Since IAA has an enhancing effect on *Um*Rh1 pumping, the effect of the auxin on the spectrum and kinetics of *Um*Rh1 was investigated. The UV/Vis spectra of the protein without and with addition of IAA **(Figure 75, panel A)** show no change in the maximum absorption of retinal; the absence of a band at 280 nm is due to saturation of the signal at this wavelength, where IAA absorbs at about 300 nm. To investigate how the photoreaction of *Um*Rh1 is affected by the auxin, time-resolved UV/Vis spectroscopy was performed on *Um*Rh1 in the presence and absence of IAA**.** The pH was monitored before and after the experiment to ensure a stable pH and to exclude any pH effect on the results. **Figure 75, panels B and C** show the kinetics of the M and O states without and with the addition of IAA to the detergent-solubilized *Um*Rh1 and to the *Um*Rh1 reconstituted

in lipid nanodiscs (*Um*Rh1:MSP1D1:DMPC, 1:2:110) sample. The result shows an acceleration of the decay of the M state and the rise of the O state in the presence of IAA, while the other intermediates are not affected[34], thus IAA seems to accelerate the mechanism of reprotonation of the Schiff base, corresponding to the decay of the M state and the effect of the hormone is independent of the protein environment.

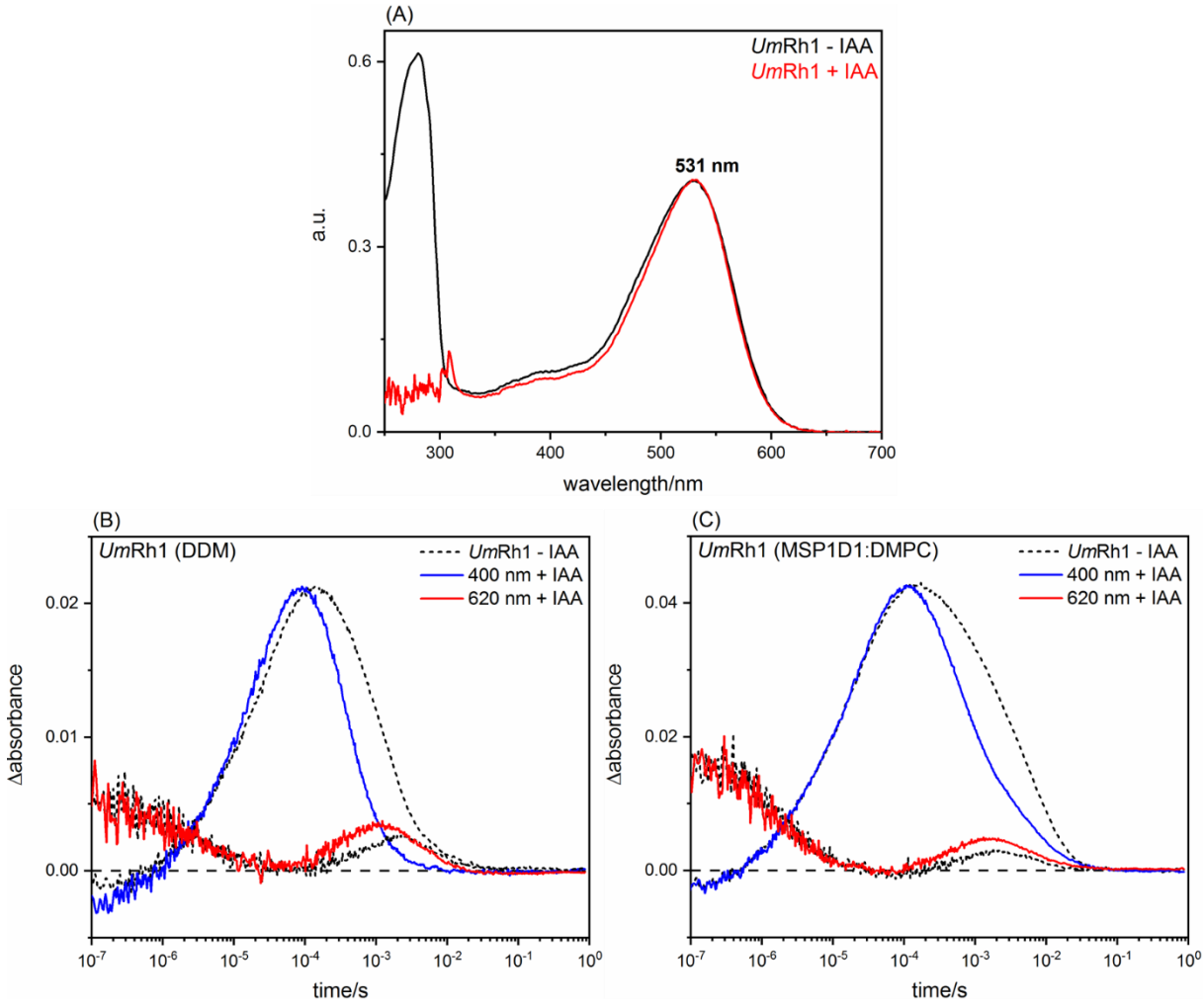

Figure 75. *UV/Vis spectra of DDM-solubilized wild-type UmRh1 in the absence (black) and presence (red) of IAA (A). Kinetic traces at pH 5.5 of DDM-solubilized UmRh1 (B) or in DMPC nanodiscs (C) in the presence (straight line; M in blue and O in red) and absence (dotted line in black for both M and O states) of 20 mM IAA.*

The effect of IAA on the protein was complemented by steady-state FTIR **(Figure 76)**. The black spectrum represents the sample without indole-3-acetic acid and the red spectrum

represents the sample with 4 mM indole-3-acetic acid in buffer, over a spectral region between 1800 and 1100 cm^{-1}. All the characteristic bands of the protein overlap between the two samples, but the characteristic bands of the M and O states show some differences when IAA is applied. For example, the band at 1524 cm^{-1} assigned to the O state is larger in the sample with IAA, whereas the negative feature at 1568 cm^{-1} assigned to the M state is more prominent in the sample without IAA. Interestingly, the band at 1668 cm^{-1} previously assigned to the amide I vibration, reflecting the protein backbone, is more prominent in the IAA sample. This result is in agreement with the flash photolysis experiment showing different kinetics and here the difference in abundance of the two states. Again, it can be speculated that IAA may lead to conformational changes in the secondary structure of the protein, expressed in the difference in the amide I feature.

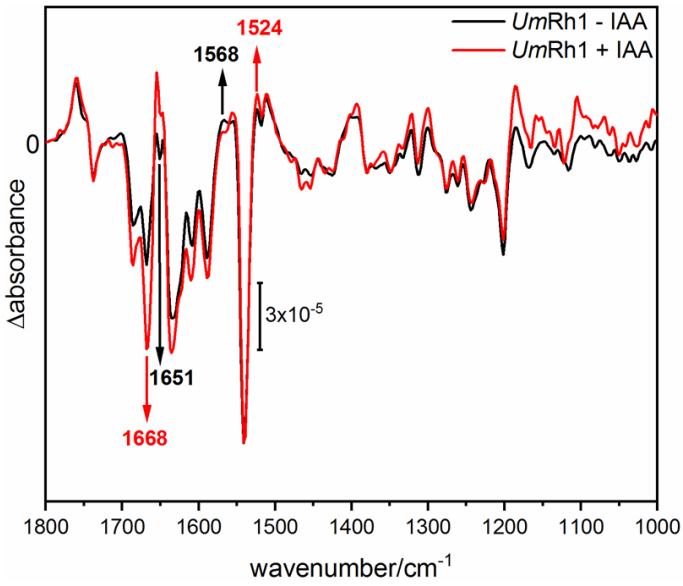

Figure 76. *Light-induced difference FTIR spectra of UmRh1 at pH 5.5 in the absence (black) and in presence (red) of 4 mM IAA using a green LED (525 nm). The bands which exhibit changes upon absence and addition of IAA are depicted with a black and red arrow respectively.*

4.2.9. IAA effect on *Um*Rh1 variants

To better understand the effect of IAA on *Um*Rh1, variants were included in the investigation by adding the plant hormone IAA. It may be of interest to mention that the IAA response here

is similar to that of azide and cyanate on *Hs*BR, specifically on the acceleration of M state decay. The exchange of the carboxyl group with an asparagine in *Hs*BR D96N leads to a slowing down of the reprotonation of the Schiff base, visible during the M decay[111]. Azide was described here to be able to restore the function of the proton donor to the SB in the variant. For this reason, the kinetics of M decay and O rise upon addition with IAA in the *Um*Rh1 E129Q (comparable to *Hs*BR D96N) and other variants (further down) were investigated and compared to the wild-type *Um*Rh1. The decay and rise of the M and O states in E129Q, without and with introduction of IAA seem to be analogous to the *Um*Rh1 wild type, with an acceleration of the M decay in the case of E129Q with IAA, as well as the O rise **(Figure 77, panels A and B)**.

In addition, *Um*Rh1 contains a long cytoplasmic domain at the proton entrance that is unique among fungal rhodopsins. To investigate whether this domain is responsible for the IAA effect on Schiff base reprotonation, this part is deleted in *Um*Rh1 1-271 and examined by flash photolysis. **Figure 77, panel C**, shows for this deletion variant the same behavior as for the wild type, excluding the C-terminus as the cause of the IAA effect.

The next step was to show whether the other, proton-releasing side of *Um*Rh1 was responsible for the IAA phenomenon. Therefore, time-resolved UV/Vis experiments were performed on variants D225E and D225N **(Figure 77, panels D and E)** (see also Chapter **4.2.6**). Again, the response to IAA is almost indistinguishable from that of the wild-type protein.

Another interesting feature of *Um*Rh1 examined in this study is an extracellular extended BC loop, which is a typical feature of fungal rhodopsins and is also located on the proton-releasing side. In LR rhodopsin this extended loop has been discussed and although its role is still unknown, it is thought to be important for protein stabilization[107]. Here, the effect of IAA was also analyzed on *Um*Rh1 in which the BC loop was deleted (variant ΔBC) but it also made no difference in M decay and O rise **(Figure 77, panel F)**.

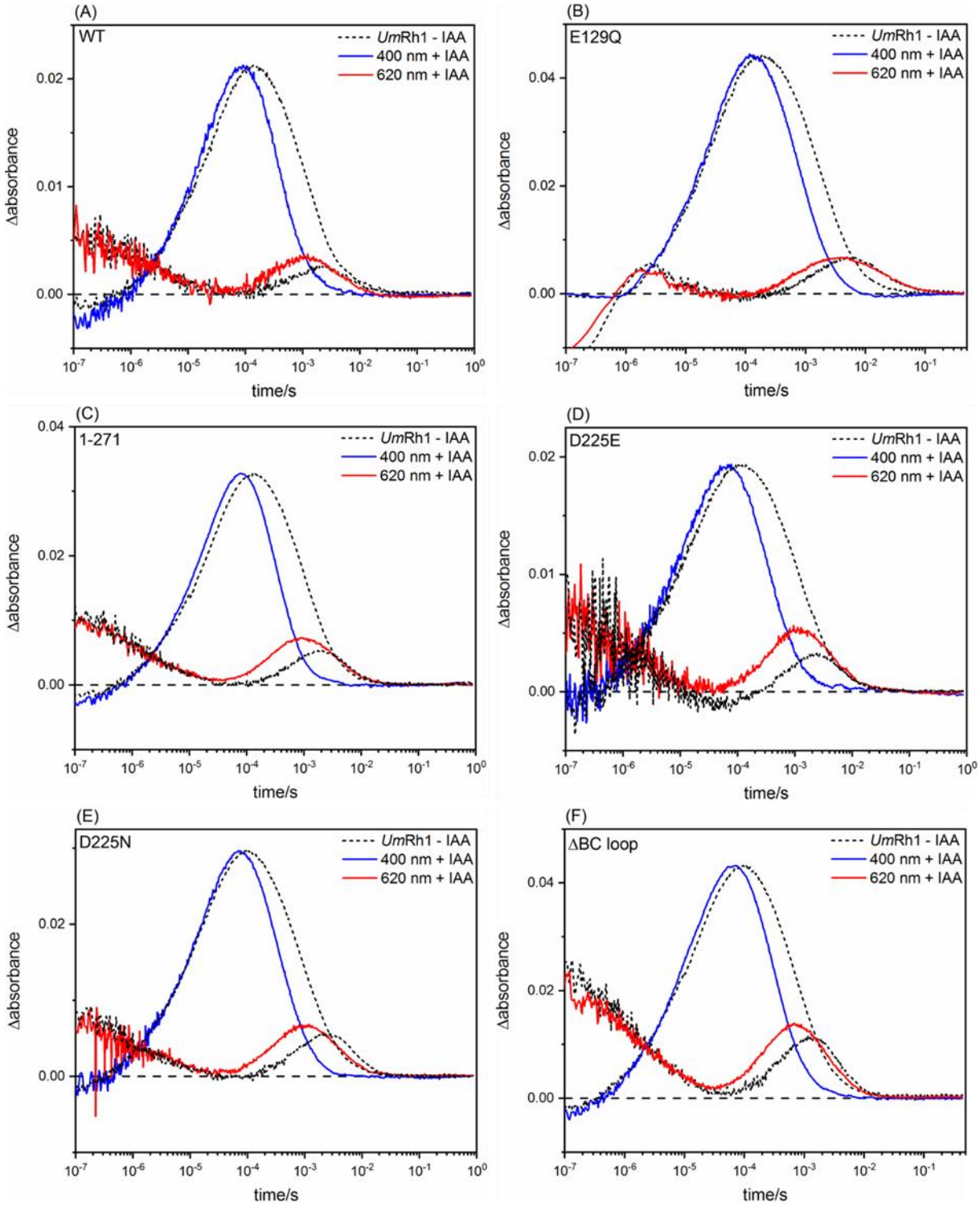

Figure 77. *Kinetic traces at pH 5.5 of UmRh1 wild type (A), UmRh1 E129Q (B), UmRh1 1-271 (C), UmRh1 D225E (D), UmRh1 D225N (E) and UmRh1 ΔBC loop (F) in the presence (straight line; M in blue and O in red) and absence (dotted line in gray for both M and O states) of 20 mM IAA.*

4.3. Agp2: phytochrome from *Agrobacterium fabrum*

This project was done in collaboration with Dr. Anastasia Kraskov and Dr. Johannes von Saß (AG Hildebrandt, Technische Universität, Berlin), Dr. Luisa Herder (AG Scheerer, Charite´ Universitätsmedizin, Berlin) and Dr. Luiz Schubert (Freie Universität, Berlin). The unnatural amino acid p-cyano-phenylalanine was inserted to exchange the residues Phe-192 and Trp-440 **(Figure 78)**, which are involved in the phototransduction of Agp2.

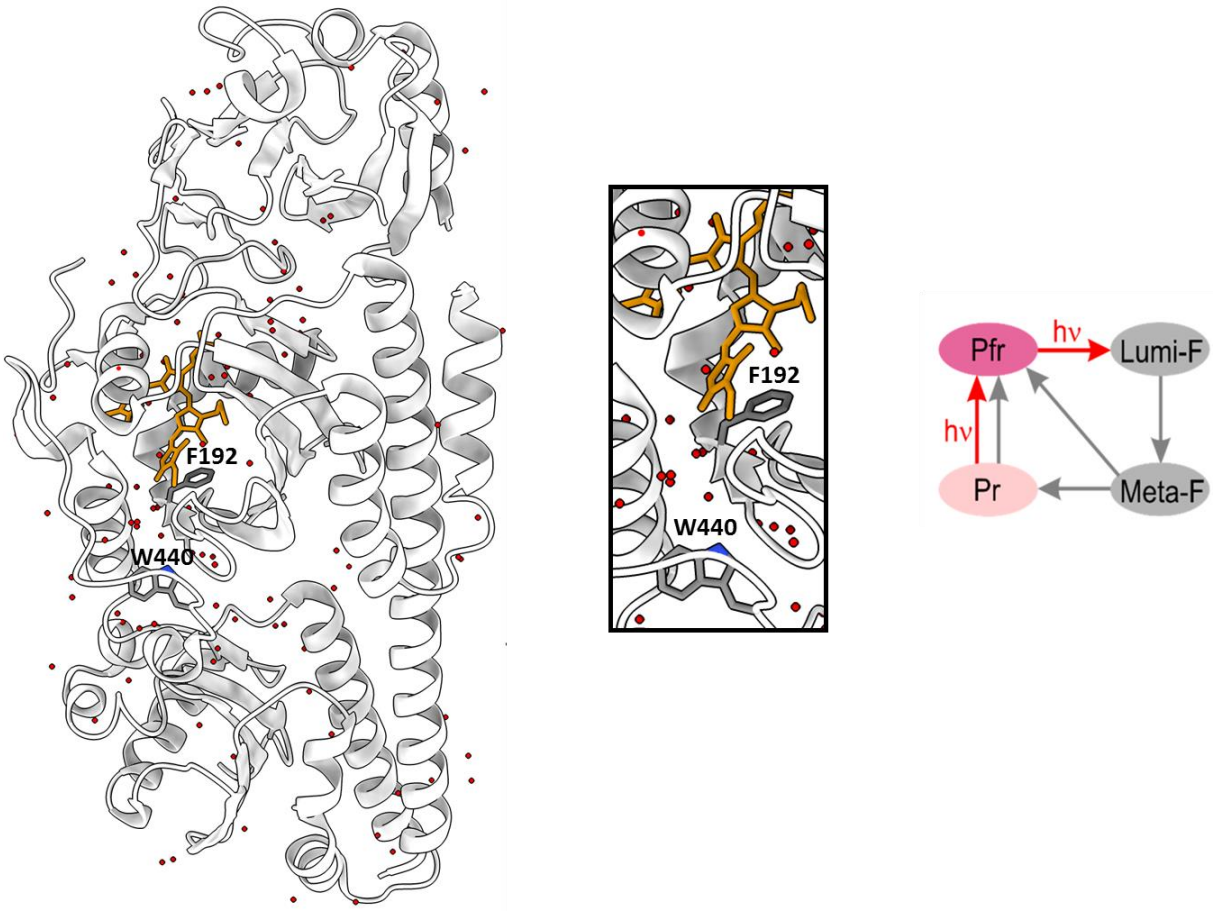

Figure 78. *Structure of the chain A of photosensory core module (PCM) of a bathy phytochrome from Agrobacterium fabrum in the Pfr state (PDB: 6G1Y) (left). The residues discussed in this work are highlighted. The chromophore (biliverdin) is shown in orange and the water molecules are shown as red spheres. Photocycle scheme of Agp2 (right) modified from Ref.*[112].

4.3.1. UV/Vis and FTIR spectra of Agp2-PCM

The UV/Vis spectra of Agp2-PCM, the truncated form of Agp2 lacking the His kinase and the response regulator (RR), show a far/far-red absorption called the Q band and a blue-shifted absorption called the Soret band[113]. In the dark, the Q-band is located at 755 nm, and after illumination with a red LED (780 nm), the peak shifts to 715 nm **(Figure 79)**. This shift indicates that the chromophore, biliverdin, is deprotonated in Pr[114].

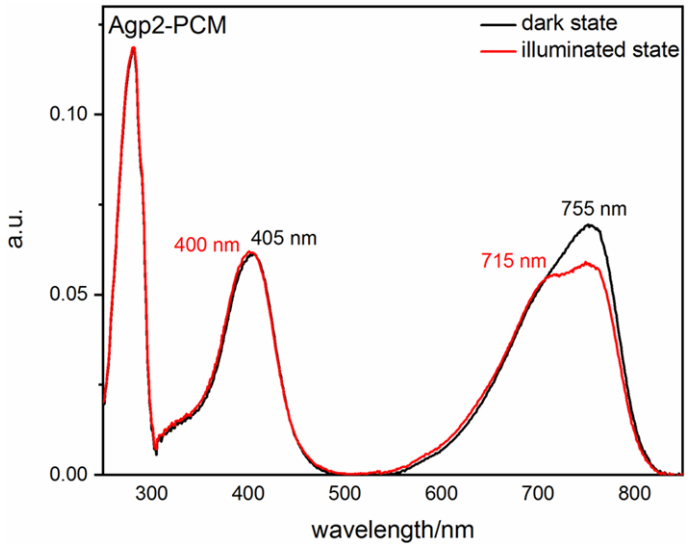

Figure 79. *UV/Vis spectra of Agp2-PCM in the dark (black) and after illumination with a red LED (780 nm) (red). The Q band shifts from 755 nm to 715 nm and the Soret band shifts from 405 nm to 400 nm after illumination.*

During the photocycle, the biliverdin and the protein undergo structural changes that can be monitored by light-induced difference FTIR spectroscopy. The FTIR spectrum of Agp2-PCM (Pr minus Pfr) is shown in **Figure 80**. The negative band at 1750 cm^{-1} is due to deprotonation of the propionic side chain of ring C (propC) of the chromophore in Pfr. The fact that a small positive counterpart is present at 1758 cm^{-1} is due to a small part of propC still protonated, probably due to differeces in sample preparation for IR here, compared to that reported in the literature. The positive band at 1709 cm^{-1} indicates the C=O stretching vibration of ring D in Pr, while C=O stretching modes of rings D and A are observed at 1697 cm^{-1}. The region 1680-1600 cm^{-1} is the amide I region where structural changes of the protein can be observed. During Pfr to Pr photoconversion a secondary structure transition from α-helix to β-sheet takes place. The

formation of β-hairpin and β-sheet in Pr are assigned to 1641 cm^{-1} and 1622 cm^{-1}, respectively, although the degradation of the coiled loop is shown as a negative band at 1631 cm^{-1}[1115].

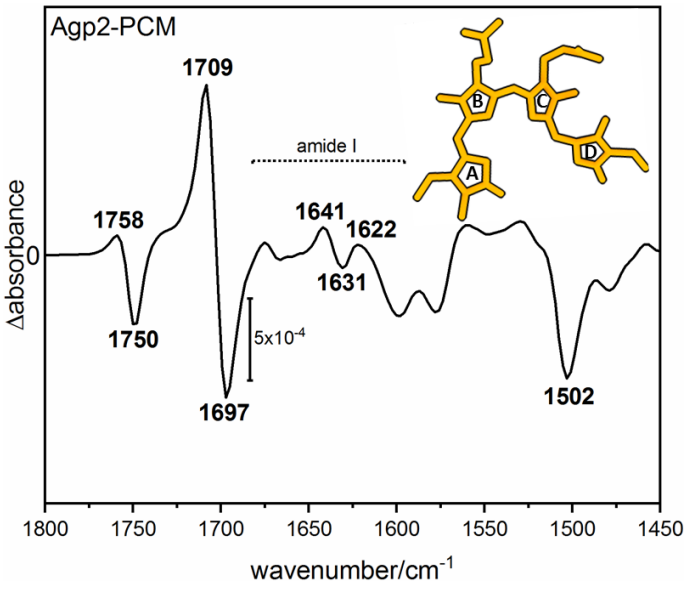

Figure 80. *Light-induced different FTIR spectrum of Agp2-PCM at pH 7.5. The amide I region is highlighted. The structure of the chromophore is shown in orange (top right).*

4.3.2. Insertion of p-cyano-phenylalanine on position Phe-192 of Agp2-PCM

The transition from Meta-F to Pr is a fundamental step and of relevant importance. *Kraskov et al.* have shown that residues such as Phe-192, Tyr-165, and Trp-440 located near the biliverdin undergo displacements from the dark state position[112]. The movement of these amino acids represents a conformational switch for the α-helix to β-sheet conversion. This process is essential for the subsequent deprotonation of ring C (propC) of the chromophore, which causes a change in the local electric field[116]. Therefore, reporter groups such as the unnatural amino acid p-cyano-phenylalanine, which is sensitive to the local electric field, can help to understand this process in more detail. One of the candidates for the insertion of the non-canonical amino acid was Phe-192 (construct kindly provided by Dr. Johannes von Saß, AG Hildebrandt, Technische Universität, Berlin). To verify that the insertion of pCNF at position 192 was successful, a test expression of 10 ml was performed. The SDS gel shown in **Figure 81** shows

the full-length protein band at 56 KDa only in the sample where pCNF was added to the cell culture.

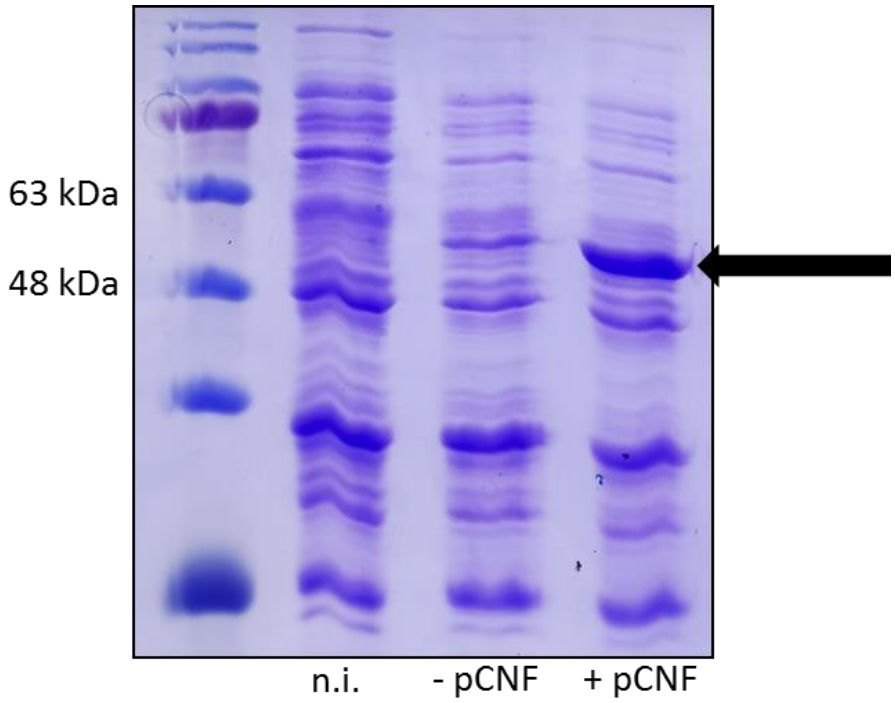

Figure 81. *SDS gel of Agp2 F192TAG from 10 ml culture in absence of IPTG (not induced = n.i.), in the absence of pCNF (-pCNF) and after addition of pCNF (+pCNF). The band at 56 kDa corresponds to the full-length protein and is shown with the black arrow.*

The UV/Vis spectrum of Agp2 F192pCNF shows some small differences compared to Agp2-PCM **(Figure 82, panels A and B)**. The Q-band in the dark state is at 750 nm (Agp2-PCM: 755 nm) and upon illumination it shifts to 710 nm (Agp2-PCM: 715 nm). However, the peak position and shift upon illumination are indicative of the correct photoreactivity of Agp2 F192pCNF.

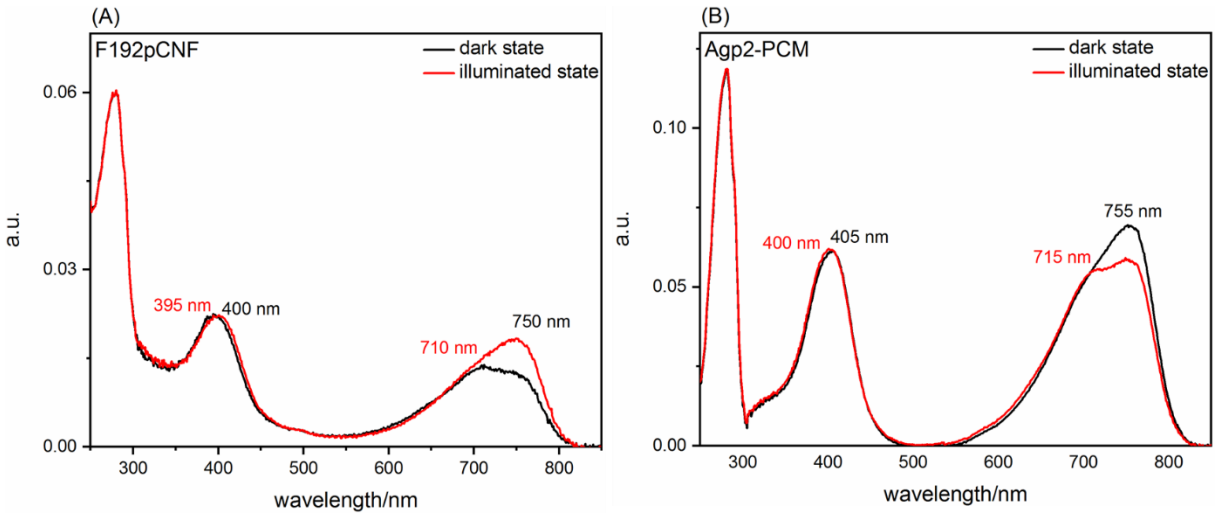

Figure 82. *UV/Vis spectra of Agp2 F192pCNF (A) and Agp2-PCM (B) in the dark (black) and after illumination with a red LED (780 nm) (red). In Agp2 F192pCNF the Q band shifts from 750 nm to 710 nm and the Soret band shifts from 400 nm to 395 nm after illumination.*

To test whether the correct amino acid is inserted at position 192, the C=N stretching vibration of the cyano group was probed by FTIR, as shown in **Figure 83**, in the zoomed region 2245-2215 cm^{-1}. The positive absorption at 2228 cm^{-1} is characteristic of the C=N stretching vibration and confirms the correct introduction of the UAA.

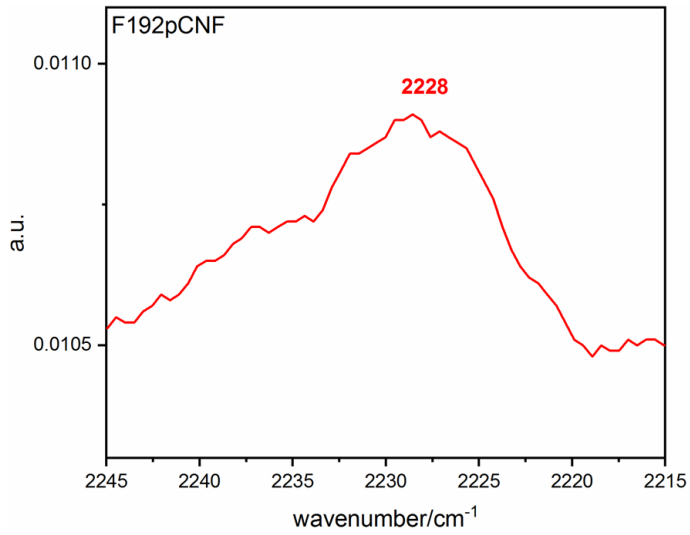

Figure 83. *Absolute spectrum of Agp2 F192pCNF in the FTIR region 2245-2215 cm^{-1}. The positive signal at 2228 cm^{-1} corresponds to the C=N stretching vibration of the cyano group of the pCNF at position 192.*

The light-induced difference FTIR spectrum of Agp2 F192pCNF compared to Agp2-PCM **(Figure 84, panels A and B)** shows all the peculiar bands, but more pronounced in the negative region (Pfr). This is probably due to the fact that the sample was measured as a dry film due to the low starting concentration of the sample, thus slowing down the photocycle. First investigations on this variant are published in *Kraskov et al.*[42].

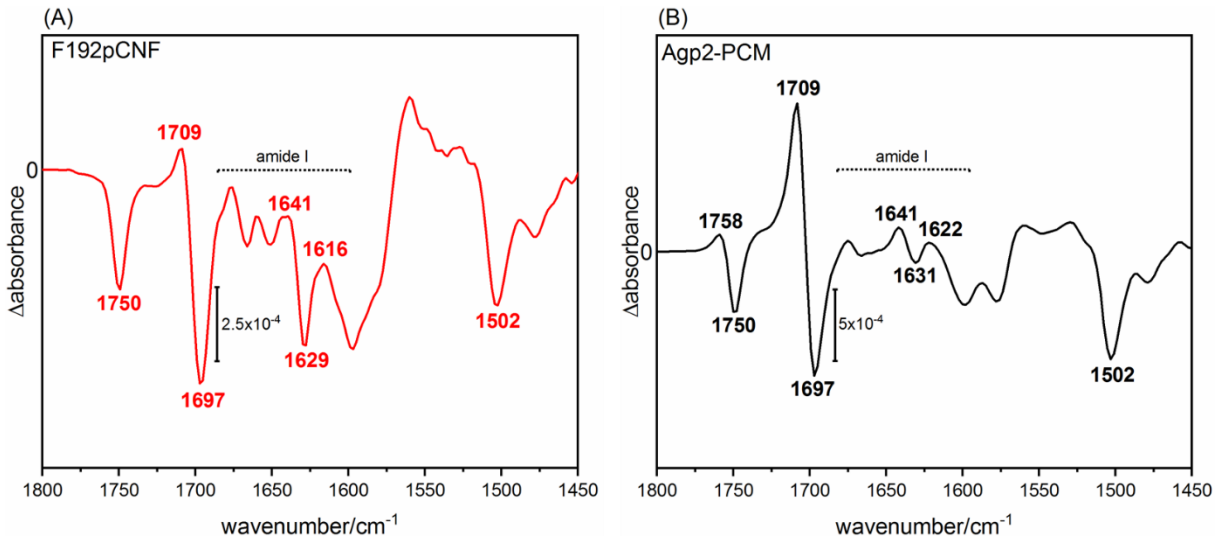

Figure 84. *Light-induced difference FTIR spectrum of Agp2 F192pCNF (A) and Agp2-PCM (B) at pH 7.5 under illumination with a red LED (780 nm) (B). The amide I region is highlighted as well as the indicative bands.*

4.3.3. Insertion of p-cyano-phenylalanine on position Trp-440 of Agp2-PCM

Trp-440, another candidate for the study of electric field variation, is highly conserved among phytochromes. Its side chain position is necessary for the subsequent restructuring of the phytochrome-specific peptide segment (tongue) of the chromophore[37] **(Figure 78)**. Since it is a fundamental amino acid, a first exchange with canonical phenylalanine was tested before the introduction of the CN group via pCNF to verify first that the photoconversion is still functional

with a Phe at that position. The UV/Vis spectrum of Agp2 W440F shows the peak shift from the far red (745 nm) of the Q band to the red absorption (710 nm) upon light, although slightly blue-shifted in comparison to Agp2-PCM, as well as the Soret bands **(Figure 85, panels A and B)**, although there is a mixture of Pfr and Pr, suggesting a terminal pathway back to the dark state.

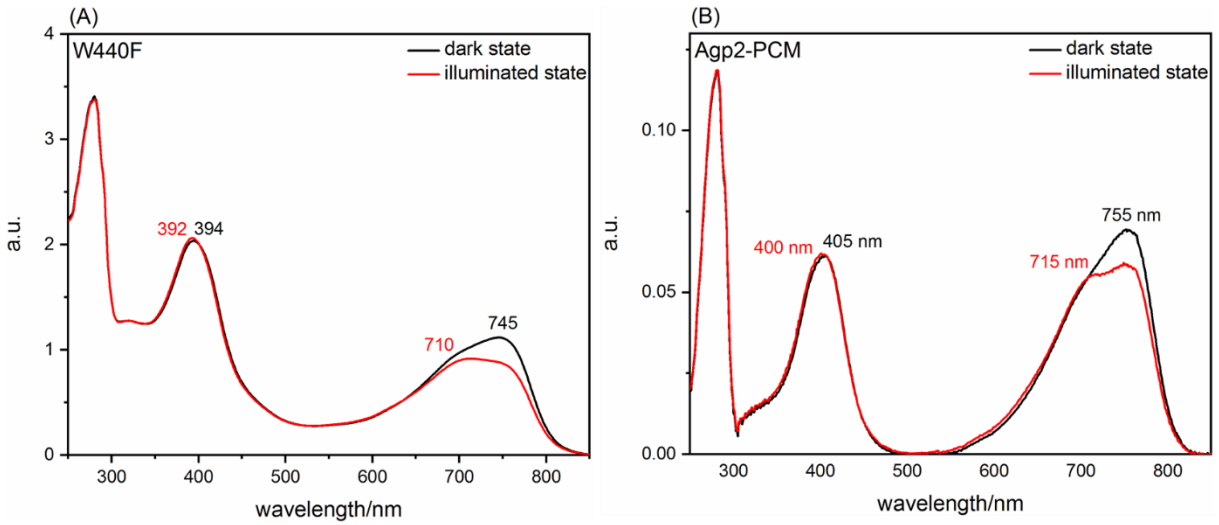

Figure 85. *UV/Vis spectra of Agp2 W440F (A) and Agp2-PCM (B) in the dark (black) and after illumination with a red LED (780 nm) (red (A)). In Agp2 W440F the Q band shifts from 745 nm to 710 nm and the Soret band shifts from 394 nm to 392 nm after illumination.*

The IR difference spectrum shows no change compared to Agp2-PCM in respect of the unfolding of the coiled loop and the formation of β-structures in the amide I region **(Figure 86 panels A and B)**.

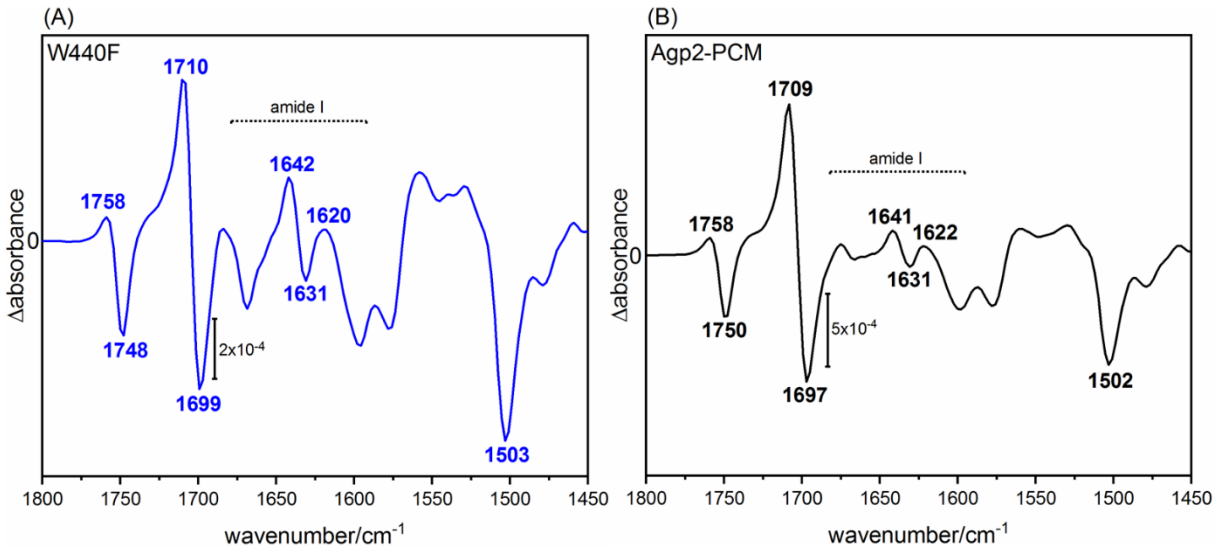

Figure 86. *Light-induced difference FTIR spectrum of Agp2 W440F (A) and Agp2-PCM (B) at pH 7.5 after illumination with a red LED (780 nm) (B). The amide I region is highlighted as well as the peculiar bands.*

Since the substitution of Trp-440 with phenylalanine has no significant effect on the Agp2 photoreaction, Trp-440 was further exchanged with p-cyano-phenylalanine. The SDS gel shows the full-length protein band at 56 kDa, but a large portion is represented by the truncated form at 48 kDa **(Figure 87)**. The difference between Agp2 F192pCNF and Agp2 W440pCNF is due to the different *E. coli* strains used to express the protein. Agp2 F192pCNF was carried out in *E. coli* strain C321ΔA(DE3), a particular strain optimized for the insertion of unnatural amino acids, in which all the UAG codons are replaced by UAA and it lacks the RF-1 release factor. On the other hand, Agp2 W440pCNF was made in the *E. coli* strain BL21(DE3); thus, the RF-1 competes with pCNF to terminate the protein at position 440, where the TAG stop codon is present. The choice of using the *E. coli* strain BL21(DE3) instead of C321ΔA(DE3) stems from the fact that no protein expression was detected in the *E. coli* strain C321ΔA(DE3) *(data not shown).*

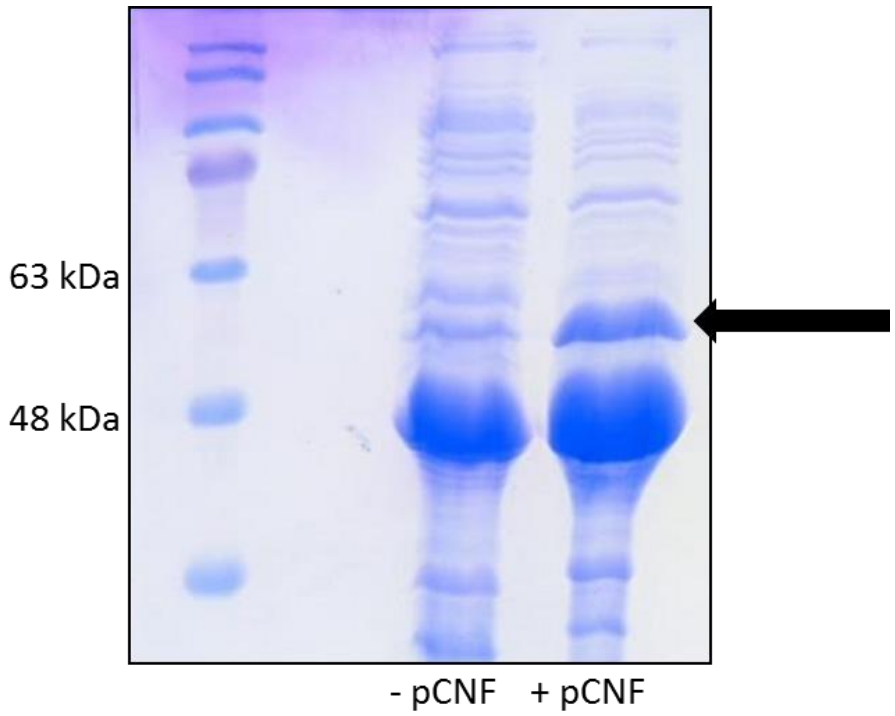

Figure 87. *SDS gel of Agp2 W440TAG from 50 ml expression culture in the absence of pCNF in the media and after addition of pCNF. The band at 56 kDa corresponding to the full-length protein is shown with a black arrow.*

UV/Vis spectrum of Agp2 W440pCNF, compared to Agp2-PCM, shows the peak shift from far red (750 nm) of the Q band to red absorption (695 nm) upon light **(Figure 88, panels A and B)**. This variant also shows a mixture of Pfr and Pr, suggesting a thermal pathway back to the dark state.

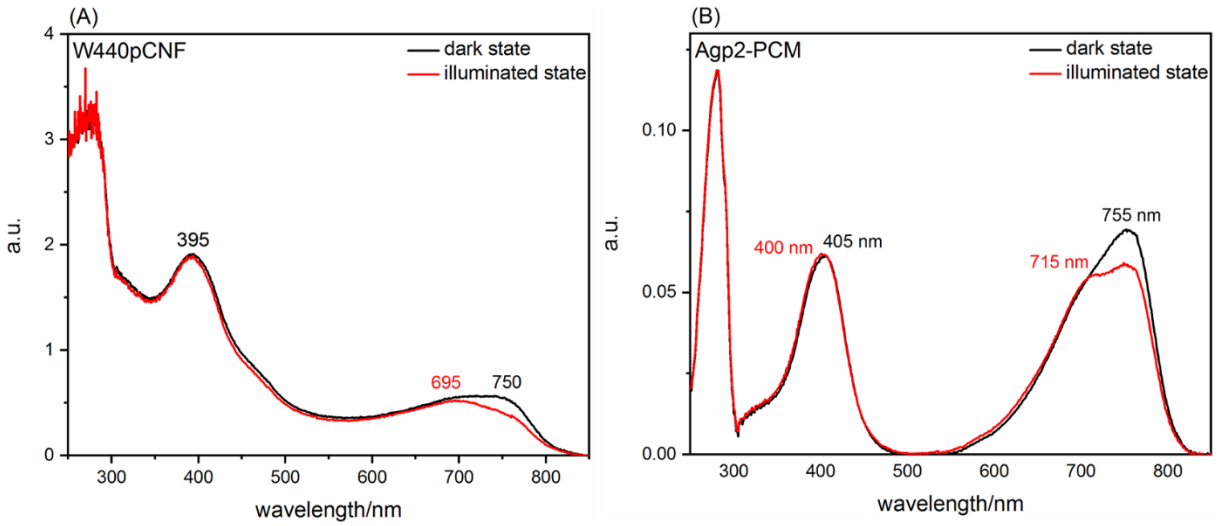

Figure 88. *UV/Vis spectra of Agp2 W440pCNF (A) and Agp2-PCM (B) in the dark (black) and after illumination with a red LED (780 nm) (red). In Agp2 W440pCNF the Q band shifts from 750 nm to 695 nm after illumination.*

Figure 89 shows the second derivative of the absolute spectrum of the C=N stretching vibration of p-cyano-phenylalanine in the IR region of interest. While Agp2 F192pCNF was measured dry due to its low concentration, the absolute spectra of Agp2 W440pCNF are shown in black for the dry sample and in red for the rehydrated sample. Interestingly, the peak shifts by 4 wavenumbers according to the hydration conditions of the sample. This is probably due to the change in H-bonding around the residue. In case of Agp2 F192pCNF the second derivative was not shown due to the low signal-to-noise ratio.

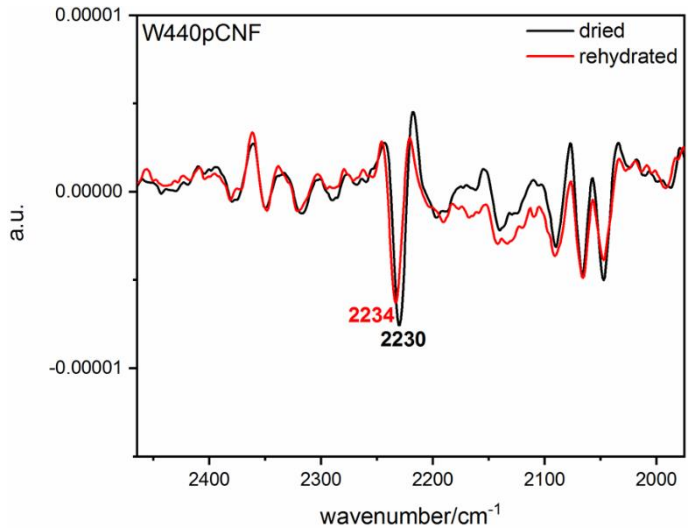

Figure 89. *Second derivative of the absolute spectra of Agp2 W440pCNF in the 2250-1995 cm^{-1} FTIR region. The negative signal at 2230-2234 cm^{-1} corresponds to the C=N stretching vibration of the cyano group of pCNF at position 440 in the dried (black) and rehydrated (red) samples. The frequency of the cyano group shifts according to the hydration state of the sample.*

Figure 90, panels A and B shows the light-induced difference spectrum of the variant, in comparison to Agp2-PCM. As discussed above for Agp2 W440F, there are no major differences in the IR spectrum of Agp2 W440pCNF, especially in the amide I region. These results suggest that upon substitution with phenylalanine and p-cyano-phenylalanine on the highly conserved Trp-440, the photoconversion between Pfr and Pr is still functional, as the secondary structure transition occurring in the PHY domain is not affected, although there is a thermal pathway back to the dark state, as suggested by the UV/Vis spectra.

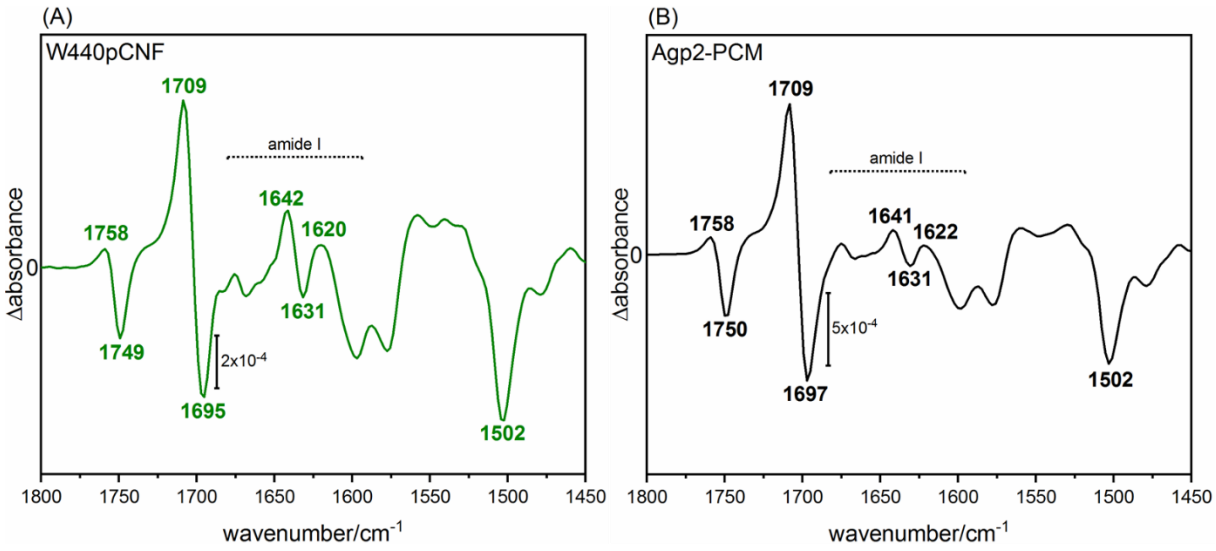

Figure 90. *Light-induced difference FTIR spectrum of Agp2 W440pCNF (A) and Agp2-PCM (B) at pH 7.5 under illumination with a red LED (780 nm). The amide I region is highlighted as well as the peculiar bands.*

5. Discussion

5.1. Motif of different rhodopsins in comparison and their role in the substrate transfer

All rhodopsins contain a three-residue motif that is known to be important for substrate transfer and allows their categorization[117]. In *Hs*BR, the three-residue motif is represented by Asp-85, Thr-89, and Asp-96. The two carboxylic acid residues act as proton acceptor and proton donor of the protonated Schiff base, respectively, and the threonine was found to be important for proton transfer to the SB[118]. *Um*Rh1 has a similar motif, DTE, where the *Hs*BR proton donor to the SB is replaced by Glu-129. The two inward chloride pumps *Nm*HR and *Hs*HR, although they transport the same substrate, have different motifs, NTQ in *Nm*HR and TSA in *Hs*HR, suggesting a divergent evolution. Interestingly, KR2, although it transports the positively charged sodium and in the opposite direction, has a higher sequence similarity to *Nm*HR and a similar motif, NDQ **(Figure 91, panels A and B)**.

(A)

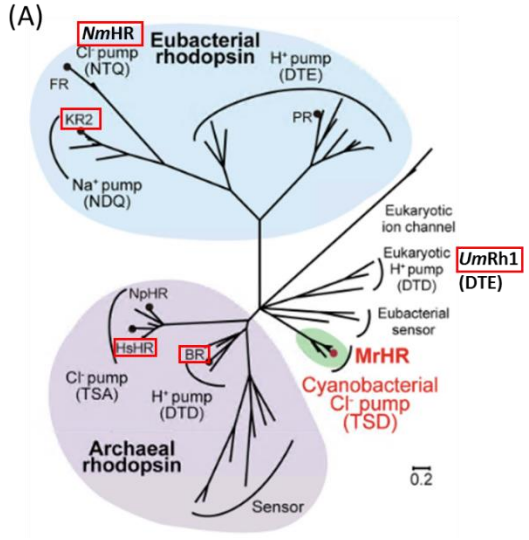

(B)

Rhodopsin	3-residue motif	Function
*Hs*BR	D85/T89/D96	Outward proton pump
*Um*Rh1	D118/T122/E129	Outward proton pump
*Hs*HR	T111/S115/A122	Inward chloride pump
*Nm*HR	N98/T102/Q109	Inward chloride pump
KR2	N112/D116/Q123	Outward sodium pump

Figure 91. *Phylogenetic tree of microbial rhodopsins (A), modified from Ref.*[16]*. 3-residue motif in the rhodopsins described in this work and their function (B).*

One of the main questions that has arisen over the many years of studying different rhodopsins is whether it is possible to convert one type of ion-pumping rhodopsin into another by a single

point mutation on one of the residues of the motif. In *Hs*BR, mutation of Asp-85 to a threonine (as in *Hs*HR) creates an anion-binding site and converts *Hs*BR to a chloride pump[119], however, mutation of Thr-111 in *Hs*HR to an aspartic acid does not convert *Hs*HR to a proton pump[120]. In *Nm*HR, a single point mutation of Thr-102 to an aspartic acid to change the motif from NTQ to NDQ as in KR2 does not result in sodium transfer. In 2016, an inward chloride pump rhodopsin, *Mr*HR **(Figure 91, panel A)**, harboring a TSD motif was converted to an outward proton pump by a single point mutation of Thr-84 to an aspartic acid[16].

Is it possible to convert *Nm*HR into a proton pump like *Hs*BR by mutating Asn-98 with an aspartic acid?

Asn-98, part of the NTQ motif in *Nm*HR, is conserved in the outward sodium pump KR2 but is replaced by a threonine in other halorhodopsins like *Hs*HR and *Np*HR and by an aspartic acid in bacteriorhodopsin (*Hs*BR) **(Figure 91, panel B)**. Asn-112, in KR2, is critical for sodium binding and, together with Asp-116 (Thr-102 in *Nm*HR), opens the conduction pathway for sodium transfer. In KR2 mutation of Asn-112 to an aspartic acid does not abolish the sodium pumping activity[121], but when replaced by an alanine the protein pumps only protons[122]. *Hs*HR, on the other hand, has a threonine at this position (Thr-111), the hydroxyl group on its side chain participates in chloride binding but is not essential[123]. In *Hs*BR, this position is replaced by Asp-85, which is essential for proton pumping and proton translocation, representing the proton acceptor of the protonated Schiff base. Replacing Asp-85 with an asparagine results in no net proton transfer[124].

In the present study, the Asn-98 conserved between *Nm*HR and KR2 was mutated to an *Hs*BR-like aspartic acid. The resulting photocycle was found to be similar to that of *Hs*BR, with the presence of an M state not present in the wild-type protein, indicating deprotonation of the PSB **(Figure 26, panel A)**, although no proton transfer was detected. In *Nm*HR, the Schiff base is protonated throughout the photocycle and its counterion is represented by the chloride itself. Upon replacement with an aspartic acid, N98D becomes the proton acceptor of the PSB in the same way as Asp-85 in *Hs*BR, as shown by pH titration **(Figure 27)** and light-induced differential FTIR spectroscopy, where a new band attributed to the protonation of D98 was found (absent in the wild type) **(Figure 28)**, with a pKa of 4.09. Despite the similarities with

*Hs*BR, *Nm*HR N98D is not able to pump protons or ions as shown in the UV/Vis spectra **(Figure 29)** and in the activity test **(Figure 33)**. Even when the NTQ motif was mutated to DTD, having exactly the same motif as *Hs*BR, no proton transfer was detected (*data not shown*). Thus, it can be speculated that position Asn-98 is fundamental for the chloride pumping pathway. However, when the asparagine Asn-98 was mutated to a glutamine, a conservative substitution, the resulting photocycle was found to be impaired, whereas when mutated to an alanine, the photoreaction **(Figure 30)** and the activity test **(Figure 33)** were found to be similar to the wild type. Crystal structures (performed by K.-L. Lê Công) of *Nm*HR N98A showed the chloride in its binding site, compared to *Nm*HR N98D, which resembles the anion-free form of *Nm*HR wild type, but helix C was found to be slightly bent **(Figure 34)**. Therefore, Asn-98 seems to be more important for the structural stabilization than for the chloride transfer (*manuscript in preparation*).

5.2. Comparison between the two inward chloride pumps *Nm*HR, *Hs*HR and the outward sodium pump KR2

Chloride release reaction to the CP side

Although *Nm*HR and *Hs*HR are both inward chloride pumps, the mechanism of chloride transfer was found to be very different in both uptake and release reactions. The mechanism of chloride release in *Hs*HR is achieved by altering the chloride binding affinity to a specific binding site that ensures vectorial transport[125]. More specifically, previous studies have shown that in *Hs*HR a complex of two arginines and two threonines located on opposite sides of the protein are involved in the process of chloride uptake (Arg-108/Thr-111) and release (Arg-200/Thr-203)[123]. Crystallographic studies by *Mous et al.* have shown that in *Nm*HR chloride release may be achieved by Gln-109 together with Ser-54 and Thr-243, in addition to two water molecules **(Figure 36)**. However, in the present study, when Gln-109 was mutated with an aspartic acid, the chloride release reaction to the CP side was found to be slower but still functional **(Figure 37) (Figure 38)**. Thus, this residue does not seem to be fundamental, which is also supported by *Hosaka et al.* who show that the Q109E and Q109A variants have the same pump activity as

wild-type *Nm*HR[23]. In *Hs*HR, this position is replaced by an alanine (Ala-122) (TSA motif), which has no significant role in the chloride release process.

In the proton pump bacteriorhodopsin, position *Nm*HR Gln-109 corresponds to Asp-96, the proton donor for the Schiff base, and its deprotonation plays a crucial role in opening and closing the cytoplasmic side for the proton uptake reaction[126].

The corresponding residue in KR2, Gln-123, is fundamental for the outward sodium pump mechanism[127]. In KR2, the introduction of a negative charge at position Gln-123, such as an aspartic acid or glutamic acid, prevents KR2 from pumping sodium, instead protons are translocated[127]. Thus, although it is a conserved amino acid, it appears to be fundamental in KR2 but not in *Nm*HR. To conclude, the NTQ motif in *Nm*HR is important but not solely responsible for chloride transfer and ion specificity, as shown by mutation of Asn-98 and Gln-109.

Chloride uptake reaction from the EC side

One finding that suggests a different chloride uptake mechanism between *Nm*HR and *Hs*HR is the presence of an additional α-helix in *Nm*HR on the EC side **(Figure 92, panel A)**, which is absent in archael halorhodopsins. Interestingly, this helix is present in KR2[24] **(Figure 92, panel B)**. This additional feature contains charged amino acids that are thought to be important for the entry of the chloride anion to ensure vectorial transport. Within this work it has been shown that Asn-3, part of the additional α-helix, and Asn-92 show impaired or delayed chloride uptake when a negative charge (e.g. aspartic acid) is introduced at these positions, although the strongest effect was found when Arg-223 was mutated, even with conservative replacement, indicating that it is fundamental for chloride uptake **(Figure 41) (Figure 42)**.

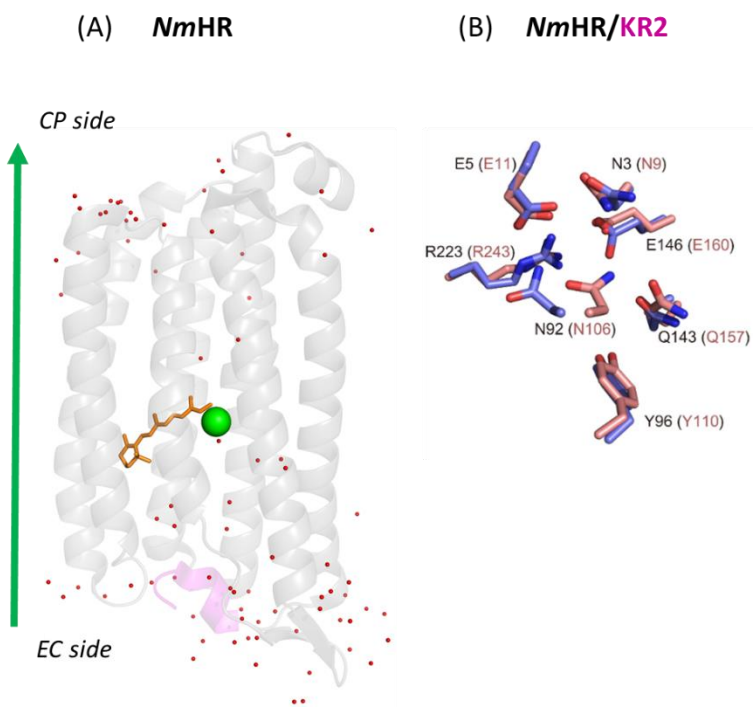

Figure 92. *Structure of the dark state NmHR (PDB: 7O8F). The additional α-helix at the N-terminus is highlighted in magenta. The retinal is shown in orange and the chloride as a green sphere. The direction of chloride transport is represented by the green arrow (A). Comparison of residues located on the additional alpha helix on the EC side between NmHR and KR2 (B). (Figure modified from Ref.*[24]*).*

In *Nm*HR and *Hs*HR there is a conserved amino acid pair consisting of an aspartic acid and an arginine (Asp-231/Arg-95 in *Nm*HR and Asp-238/Arg-108 in *Hs*HR) located in the binding pocket of the retinal **(Figure 93, panels A and B)**. In *Nm*HR, these two residues are involved in the final step of chloride uptake to recharge the dark state. Mutations at Asp-231 and Arg-95 lead to impaired photoreactions, but substitutions of Asp-231 have the most pronounced effect. In the Asp-231 variants, the photocycle shows a strong absorption only for K and L intermediates, i.e. the chloride can be released but not taken up, since the chloride uptake occurs during the decay of O_2 state, even with a conservative substitution such as glutamic acid. *Nm*HR R95A also shows an impaired photoreaction with a long and strong absorption only for K-L and O_1 states, suggesting a pathway back to the K state **(Figure 44)**. Arg-108, in *Hs*HR, is a key residue for chloride uptake and the photocycle and substitutions of Arg-108 lead to striking effects on its photoreaction[123]. However, although these two arginine residues are conserved in

these two chloride pumps their roles are different. While Arg-108 in *Hs*HR is indirectly linked to the chloride through a water network, Arg-95 in *Nm*HR is not[24] **(Figure 93, panels A and B)**. The difference can also be seen in the FTIR spectra. While *Braiman et al.* have shown that in the FTIR spectrum of *Hs*HR, Arg-108 contributes to a change in the H-bonding band at 1695 cm^{-187}, in *Nm*HR a band in the same region (1699 cm^{-1}) is not due to Arg-95, but rather to an amide I mode **(Figure 45) (Figure 46)**. Thus, one can conclude that the role of this pair of charged amino acids, especially Arg-95, is different between the two chloride pumps, showing a divergent evolution.

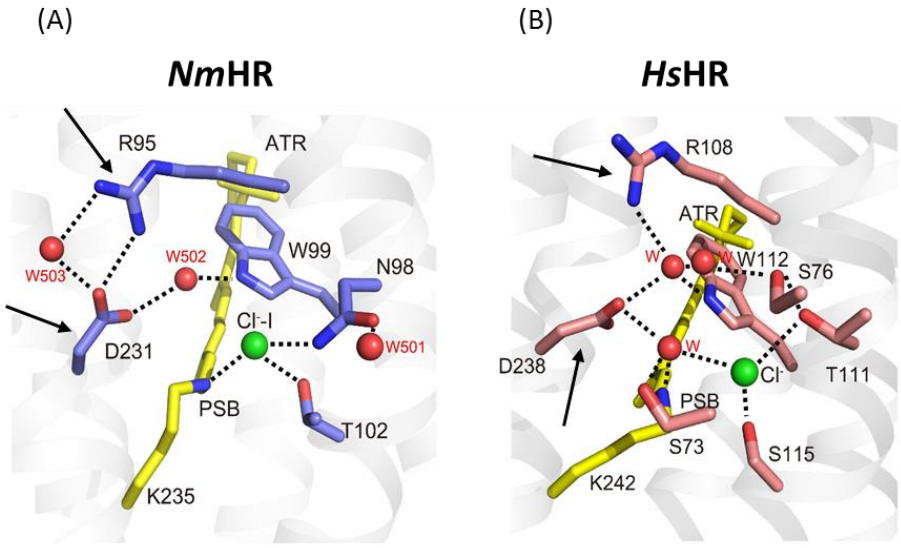

Figure 93. *Comparison of the retinal binding pocket of NmHR (A) and HsHR (B). The charged amino acid pair is conserved between the two halorhodopsins and it is indicated by a black arrow. (D231/R95 in NmHR and D238/R108 in HsHR). (Figure modified from Ref.*[24]*).*

5.3. Comparison between the two outward proton pumps *Um*Rh1 and *Hs*BR

Deprotonation mechanism of the Schiff base

In the present study, a comparison was made between the well-known outward proton pump bacteriorhodopsin (*Hs*BR) and the fungal *Um*Rh1. *Hs*BR shares a high similarity with *Um*Rh1 in residues known to be important for the protonation pathway of the former **(Figure 94)**

(Figure 58). For example, the mechanism of SB deprotonation was found to be similar between the two outward proton pumping rhodopsins. The light-induced difference FTIR spectrum of *Um*Rh1 shows a positive band at 1761 cm^{-1}, which in this work was assigned to Asp-118, representing the proton acceptor of the PSB (Figure 62). Asp-85 in *Hs*BR, which is homologous to Asp-118, shows a positive band in the same frequency range. In addition, the kinetic traces between *Um*Rh1 D118E and *Hs*BR D85E show a faster accumulation of the M state, during which the Schiff base deprotonates (Figure 63). In the case of exchange D85E in bacteriorhodopsin, it has been hypothesized that the acceleration of the M rise is due to the reduced distance between the additional methylene group of the glutamic acid side chain and the SB, which reduces the transition barrier for proton transfer and ultimately the transfer time[102]. Thus, this may also be the case in *Um*Rh1.

Reprotonation mechanism of the Schiff base and proton uptake

While the mechanism of SB deprotonation is similar between *Um*Rh1 and *Hs*BR, a different situation was found for the SB reprotonation mechanism. In *Hs*BR, the reprotonation of the Schiff base takes place in the M to N transition via Asp-96 and a subsequent proton uptake from the cytoplasmic side occurs in the O intermediate[101 105]. Asp-96 shows a negative band in the FTIR spectrum at 1742 cm^{-1}, which loses its intensity under acidic conditions. Furthermore, when Asp-96 is mutated with an asparagine, removing the proton transfer from this amino acid to the deprotonated Schiff base, the band disappears, suggesting that Asp-96 is responsible to the band as it is titrated[104]. In *Um*Rh1, a negative band was also found at 1737 cm^{-1}, but its intensity did not change at low pH (Figure 61). Furthermore, a pH-dependent M state decay was found by time-resolved UV/Vis spectroscopy in both wild-type protein and Glu-129 variants (homologous to Asp-96 in *Hs*BR) **(Figure 94)**, suggesting that the reprotonation reaction does not occur via Glu-129 (Figure 64) (Figure 65). Another conserved residue investigated in this study to elucidate the different mechanism of SB reprotonation was Asp-148. One aspect that motivated the investigation of this residue came from studies carried out on *Hs*BR, where it was shown that the band at 1742 cm^{-1}, previously attributed exclusively to the deprotonation of Asp-96, comes from an overlap of two bilobic bands derived from the proton transfer between two carboxylic residues[128], one at higher frequencies due to Asp-96 and one at lower frequencies due to Asp-115[106]. Asp-115 (Asp-148 in *Um*Rh1) **(Figure 94)** is highly conserved among microbial rhodopsins, although its function is unclear despite its importance

for proton transfer. It seems to be involved in a cluster of intra-helical interactions involving helices C and D (where it is located), maintaining the correct position of Asp-96 and the correct communication between the latter and the Schiff base. The D115A variant shows no reprotonation of the Schiff base via Asp-96[100]. Therefore, the single and double variants *Um*Rh1 D148N and *Um*Rh1 E129Q/D148N were investigated. The light-induced difference FTIR spectra showed that the negative band at 1737 cm^{-1} and its positive counterpart at 1745 cm^{-1} are due to a possible interaction between the two residues, although neither of them represents the donor to the SB, since the *Um*Rh1D148N and E129 variants show a pH-dependent M state **(Figure 67) (Figure 68)**. Most probably the proton is taken up from the cytoplasmic bulk medium. This is not an exceptional case, another recently discovered class of proton pump rhodopsins with a serine or glycine residue at this position (*Hs*BR D96) show a similar reprotonation mechanism, thus lacking an internal proton donor[109].

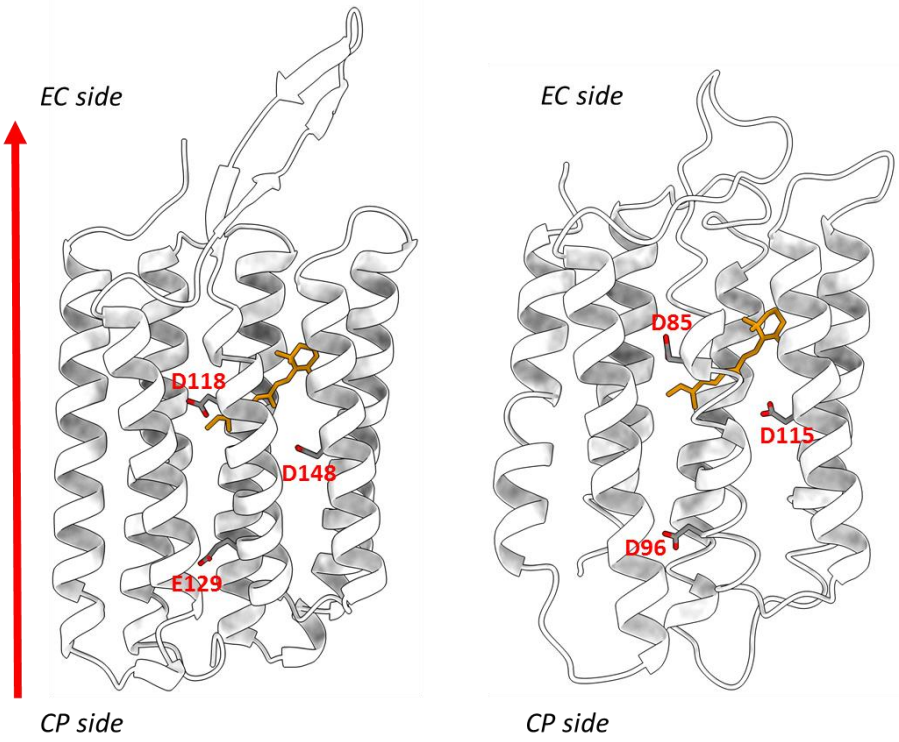

Figure 94. *Structure comparison of UmRh1 (predicted structure) and HsBR (PDB: 1AP9). Conserved residues known to be important for the protonation pathway in HsBR are highlighted.*

Proton release reaction to the EC side

The proton releasing group (PRG) region is quite conserved between *Um*Rh1 and *Hs*BR **(Figure 95)**. In *Hs*BR the proton movement to the EC side initiated by the Schiff base is transferred to the PRG region where Glu-194 (Asp-225 in *Um*Rh1) and Glu-204 (Glu-235 in *Um*Rh1) play a crucial role in the final step of proton release[129]. These two residues are located close to the EC[130] and, in particular, Glu-194 interacts with Asp-85 (proton acceptor of the SB) modulating the pKa of Asp-85 to facilitate its deprotonation in the last step of the photocycle, which is important for the subsequent proton release reaction. Previous studies on the substitution of Glu-194 and Glu-204, in *Hs*BR, with glutamine have shown that the delayed proton release reaction here coincides with the O state, rather than the M state of the native protein via Glu-194 and Glu-204[131]. In *Um*Rh1, substitution of Asp-225 (Glu-194 in *Hs*BR) with an asparagine has no effect on the O state kinetics **(Figure 69)**. However, the M state decay of *Um*Rh1 D225N in the alkaline range (pH 8) shows a second M state **(Figure 70)**. The fact that a second M state is detected in the D225N variant but not in the native protein indicates that proton release may be impaired or delayed. Interestingly, at pH 5, no differences were detected between the variant and the wild type **(Figure 69)**. It appears that at pH 5, the proton release reaction may not occur via Asp-225, but directly from Asp-118, the proton acceptor, or other residues near the SB. The same is seen in *Hs*BR, where at acidic pH Asp-85 releases the proton directly to the EC side[132]. In conclusion, although *Um*Rh1 and *Hs*BR are both outward proton pumps and have a high homology in residues important for proton transfer, they exhibit differences in the mechanism of the proton pathway. One can speculate that this is due to the evolutionary adaptation and the different organism where they are expressed (archaea *versus* fungus), related to the different role they exert.

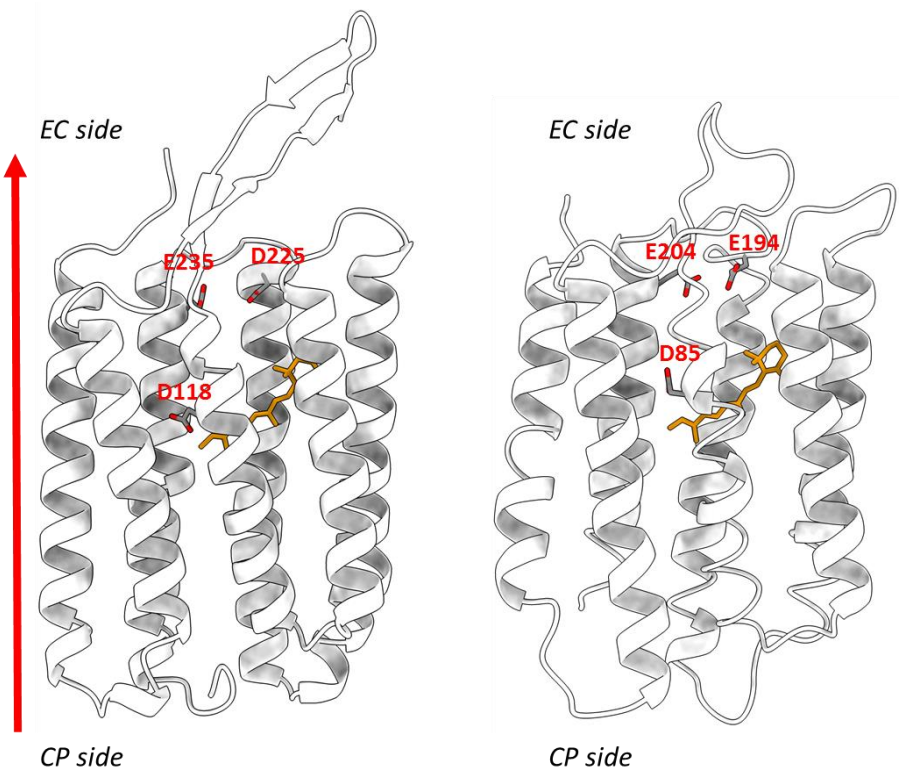

Figure 95. *Structure comparison of UmRh1 (predicted structure) and HsBR (PDB: 1AP9). Conserved residues known to be important for the proton release to the EC side in HsBR are highlighted.*

5.4. Role of *Um*Rh1 in pathogenesis

In this work, an elucidation of the role of *Um*Rh1 in the pathogenesis was studied. *Ustilago maydis* is responsible for corn smut disease in maize plants, giving rise to the development of tumorogenic tissue. Indole-3-acetic acid (IAA) is an auxin, a plant hormone responsible for plant growth and development, which is also produced in the fungus. During plant infection, IAA levels were found to be higher than in non-infected tissues. The biosynthesis of IAA, in the fungus, has tryptophan as precursor and depending on the carbon source synthesis can take different pathways, the most common having as intermediate precursor IPA[133]. In the electrophysiological experiments conducted by *Panzer et al.* the proton pumping activity of *Um*Rh1 was found to be accelerated in the presence of auxins such as IAA (indole-3-acetic acid) and IPA (indole-3-propionic acid), but to a greater extent in the case of the former[33]. In the

present study, the time-resolved flash photolysis experiment detected an acceleration of the M state decay and the O state rise in the presence of IAA, but no differences were detected for the other intermediates, implying that the effect of auxin is limited to the M and O states, in both DDM-solubilized *Um*Rh1 and DMPC nanodisc samples **(Figure 75)**. In *Hs*BR, reprotonation of the Schiff base via Asp-96 occurs during the transition from M state to O state. Since *Um*Rh1 lacks an internal proton donor, a possible effect of IAA may be to accelerate the reprotonation mechanism from the cytoplasm. Previous studies carried out on *Hs*BR have shown a similar effect of azide on the D96N variant (Glu-129 in *Um*Rh1), by restoring the M state decay[134]. Taking this finding into account the E129Q variant was tested in the presence of IAA, but no major differences were found between the sample in the absence and in the presence of IAA **(Figure 77)**. This result is consistent with the finding that *Um*Rh1 Glu-129 is not the proton donor and therefore the effect of IAA on SB reprotonation is independent.

Where does the IAA bind to the protein?

*Um*Rh1 has a long BC loop, which is also present in other fungal rhodopsins such as LR and may be the interaction site for the auxin. But *Um*Rh1 with a truncated BC loop (ΔBC loop) did not show any differences in the M and O states, nor did a variant lacking the C-terminus **(Figure 77)**. Our collaborator on *Um*Rh1, Dr. Ulrich Terpitz, being specialized on electrophysiological experiments on mammalian cells, has speculated that IAA might interact with the proton-releasing group[33], leading to conformational changes in the protein associated with pump increase. Therefore, the D225N and D225E variants were tested, but again no differences were found **(Figure 77)** proofing that the hypothesis most probably is not correct.

However, while IAA has no effect on the maximum absorption of retinal in the UV/Vis spectra of the variants described above, it shows an influence on the maximum absorption of *Um*Rh1 D118E (proton acceptor of the SB), shifting the maximum absorption from 527 nm to 531 nm and thus its pKa **(Appendix Figure S9)**. One may speculate that IAA affects the protonation pathway to the PRG, since it is already known that the proton acceptor of the SB, in this case Asp-118, is responsible for protonating the PRG for the ejection of a proton to the EC side, in the same way as in *Hs*BR[132].

In conclusion, a speculation of the pathogenic mechanism of *Um*Rh1 is that the boosting pump effect of IAA on the reprotonation of Schiff base and the protonation of PRG and subsequent proton release leads to further acidification of the environment, which may represent a signal for plant infection and consequently associated with its role in the pathogenic cycle (*manuscript in preparation*). Although all studies on *Um*Rh1 wild type and variants have been conducted *in vitro* and the native organism may respond differently under certain environmental conditions, it is significant that a plant growth hormone produced by the fungus affects its rhodopsin and may be relevant in the context of tumors.

5.5. Role of cysteines in different rhodopsins

Cysteines are highly involved in catalysis because of their thiol group, which is easily deprotonated, although their abundance in nature is low[135]. In many rhodopsins, cysteines have been found to be important for the photoreaction of the protein, such as in channelrhodopsins. Change of the H-bond of a cysteine side chain can be achieved either with the oxygen atom of the backbone or with an amino acid located on another helix[136]. The S-H stretching vibrations can be monitored by FTIR in the frequency range of 2580-2525 cm^{-1}. *Nm*HR and *Um*Rh1 both show a band in the frequency range of the S-H stretching vibration in steady-state FTIR: 2550 (-) cm^{-1} for *Nm*HR **(Figure 49)** and 2565 (+)/2557 (-) cm^{-1} for *Um*Rh1 **(Figure 72)**. Both proteins contain two cysteines each, and site-directed mutagenesis was used to assign the FTIR band to a specific cysteine. In *Nm*HR, the negative band at 2550 cm^{-1} originates from Cys-105 **(Figure 49)** which is close to the retinal and near the NTQ motif, located between Thr-102 and Gln-109. In *Um*Rh1, a positive/negative band was assigned to a change in the H-bond of Cys-174 **(Figure 72)**, which is also close to the chromophore and seems to be important for the photoreaction since the kinetics of the M state is altered at high pH **(Figure 74)**. Although no potential H-bonding partners of Cys-174 were examined in *Um*Rh1, Cys-105 was found to be deprotonated in *Nm*HR. Its deprotonation coincides with the O state[80], which is the functional state of *Nm*HR since chloride is released and taken up during its lifetime. However, despite mutations in residues adjacent to the cysteine, it was not possible to identify the interaction partner (*data not shown*). One theory is that the protonation occurs at its backbone to induce some local structural changes to allow the chloride transfer, which could be supported by the

fact that conformational changes associated with O_2 rise were found to be slower in the C105S variant **(Figure 48)**; and another theory is that the proton would go to the chloride anion to form HCl to facilitate the chloride passage to the CP side to be released. A debate about the second theory is the evidence that when Cys-105 is replaced by a methionine that cannot deprotonate, the photoreaction is unchanged, indicating that the cysteine is not important for the activity **(Figure 50)**.

5.6. Insertion of the unnatural amino acid pCNF in *Nm*HR and Agp2

The unnatural amino acid p-cyano-phenylalanine can be used as a reporter group for H-bond changes and electrostatics, as the C=N stretching vibration of the cyano group absorbs in an infrared region with no overlap of other protein bands ("transparent window")[99].

Insertion of the unnatural amino acid pCNF in *Nm*HR Trp-99 and Trp-201

In microbial rhodopsins, there are at least two conserved tryptophan residues on the opposite side of the retinal that appear to stabilize the retinal and undergo conformational changes associated with substrate transfer. In *Nm*HR these residues are Trp-99 and Trp-201 which were chosen for the study of electrostatic changes in the retinal region **(Figure 51)**. The motivation for this study in *Nm*HR came from recent publications [100,101] in which the authors have hypothesized that these amino acids here are involved in larger structural changes than in other rhodopsins. Additionally, they are probably required for the first step of chloride transfer. Because of the high conservation of these residues among microbial rhodopsins and their position close to the chromophore, a first exchange with the canonical phenylalanine was tested. *Nm*HR W99F and *Nm*HR W201F showed some differences in the photoreaction, in the former the photocycle was slowed down and in the latter an influence of the substitution on the conformational changes of the protein was detected (monitored as a delay in the rise of the O_2 state), indicating that Trp-201 is important for the conformational changes in *Nm*HR **(Figure 52)**. *Nm*HR W99pCNF and *Nm*HR W201pCNF **(Figure 56)** showed exactly the same behavior in the photoreaction, indicating that the insertion of the unnatural amino acid does not further affect the functionality of the protein, and in addition, all pCNF variants exhibit the absorption band of the C=N stretching vibration in the range of 2229-2231 cm^{-1} **(Figure 55)**. To elucidate

their role in the first step of chloride transfer, we collaborated with J. Wachtveitl's group on ultrafast spectroscopy, a technique capable of elucidating the immediate steps after retinal isomerization. Preliminary results indicate that although *Nm*HR wild type showed an influence of excited state dynamics on NaCl concentration, *Nm*HR W99F and *Nm*HR W99pCNF showed no difference in photoproduct formation at 1 M and 150 mM NaCl, whereas Trp-201 variants showed a dependence, albeit smaller **(Figure 57)**. This may indicate that Trp-99 interacts directly with the chromophore, consistent with the small shift observed in the UV/Vis region, although Trp-201 has an indirect interaction with retinal through conformational changes around the chromophore, consistent with the flash photolysis experiment where slower conformational changes were observed in the variants (*manuscript in preparation*). As mentioned above, p-cyano-phenylalanine is a reporter group that is sensitive to the electrostatic changes observed in the IR region. Therefore, the goal of this aspect of the *N*mHR project is to use ultrafast IR spectroscopy to better elucidate the early changes in the *Nm*HR photocycle.

Insertion of the unnatural amino acid pCNF in Agp2 Trp-440

In bacterial phytochromes, the highly conserved Trp-440 in Agp2 **(Figure 78)** is involved in conformational changes that affect the PHY tongue domain, a phytochrome-specific peptide segment, leading to a secondary structure transition from α-helix in Pfr to β-sheet in Pr[37]. Since this residue is highly conserved in phytochromes, first the exchange with the canonical phenylalanine was performed to ensure that the substitution would not affect the functionality of the protein. The substitution of Trp-440 with the canonical phenylalanine showed a slower conversion between the parent state Pfr and the photoinduced Pr state compared to the wild type **(Figure 85)**, nevertheless all the characteristic bands of the WT protein are also present in the light-induced difference FTIR spectrum of this variant **(Figure 86)**. The subsequently generated pCNF variant Agp2 W440pCNF **(Figure 88) (Figure 90)** showed exactly the same behavior in the photoconversion, indicating that the insertion of the non-natural amino acid does not further impair the functionality of the protein. Furthermore, the pCNF variant exhibits the absorption band of the C=N stretching vibration in the range of 2230-2234 cm^{-1} **(Figure 89)**. Agp2 W440pCNF has been further investigated using Raman, X-ray crystallography and QM/MM by our collaborators (AG Hildebrandt and AG Mroginski TU Berlin, AG Scheerer Charité

Universitätsmedizin Berlin) to elucidate the mechanism of the structural rearrangement during the photocycle (*manuscript in preparation*). Here, it is shown that although Trp-440 is located at the tongue region and not in contact with biliverdin, the W440F and W440pCNF variants exhibit spectral changes associated with the chromophore. Conversely, the analysis of the vibrational Stark effect revealed that processes initiated in the chromophore binding pocket trigger minor structural changes rather distantly in the tongue region, where Trp-440 is located, before major conformational changes occur.

6. Conclusion and Outlook

In this thesis, a comparative study between different rhodopsins was performed to elucidate the differences and similarities between them. In particular, the fungal outward proton pump *Um*Rh1 was compared with the archaeal outward proton pump *Hs*BR, while the bacterial inward chloride pump *Nm*HR was compared with *Hs*BR, the archaeal inward chloride pump *Hs*HR, and the bacterial outward sodium pump KR2. *Hs*BR and *Hs*HR were chosen as model systems because they were the first classes of proton and chloride pumps to be studied and their photoreactivity is well established. Using site-directed mutagenesis and spectroscopic techniques such as time-resolved UV/Vis and steady-state FTIR, an elucidation of the residues involved in chloride and proton transfer was performed, dissecting the entire chloride transfer in *Nm*HR from the first step of chloride movement after retinal isomerization to chloride release and subsequent uptake. Similarly, a dissection of the proton pathway in *Um*Rh1 was carried out and a band assignment in the carboxylic acid region of the FTIR spectra was performed by spectroscopy. As a complement to this study, an extensive literature search of the well-known *Hs*BR, *Hs*HR and KR2 was conducted to support the hypotheses. In addition, a pathogenic role for *Um*Rh1 has been speculated; this protein may be involved in accelerating the reprotonation of the SB and subsequent proton release to the EC side of the protein. Moreover, in the present study, a novel technique was used to study the electrostatic changes around the chromophore in the inward chloride pump halorhodopsin *Nm*HR and in the phytochrome Agp2. Due to the high similarity of its side chain to aromatic residues, pCNF is used to exchange tryptophan, tyrosine or phenylalanine. In this work, the focus was on the exchange of conserved tryptophan residues

close to the chromophore which are known to be important for the photoreaction of *Nm*HR and Agp2 thus exploring the connection between chromophore isomerization and protein structural changes. However, some questions remain open:

What is the role of *Um*Rh1 in pathogenesis?

The auxin IAA has an impact on the kinetics of M and O state in *Um*Rh1, however some debates arise from the mechanism of interaction of the auxin with the protein.

From the observations made here a clear binding site for IAA could not be clearly extracted. Further investigations to elaborate a structural model via X-ray crystallography or cryoEM with and without the auxin would be necessary.

What is the role of cysteine deprotonation or change of H-bonding in the photocycle of *Nm*HR and *Um*Rh1?

This study has shown that both *Nm*HR and *Um*Rh1 contain two cysteines and that the one close to the chromophore is responsible for the deprotonation band in the former and the change in hydrogen bonding in the latter, but no interaction partners were found. Therefore, further mutational studies are needed to identify the proton acceptor and H-bonding partners to elucidate the role of the cysteine side chain in the photocycle of these two rhodopsins.

7. Appendix

DNA sequence pET27b *Nm*HR

CATATGAAAAATATTGAAAGCTTATTTGACTACAGCGCCGGTCAATTCGAATTTAT
CGATCACCTATTGACCATGGGGGTAGGGGTACATTTTGCAGCCTTAATCTTCTTCT
TGTAGTCTCACAATTTGTAGCTCCTAAATATCGTATTGCAACTGCGCTTTCTTGTAT
TGTTATGGTATCTGCAGGGTTGATACTTAACAGCCAGGCGGTCATGTGGACTGAG
CTTATGCGTATGTAGACGGGTCGTACCAGCTTCAAGACCTCACTTTCTCTAACGGA
TACCGTTACGTGAATTGGATGGCGACGATTCCTTGCTTATTGTTACAATTATTGAT
TGTCTTGAATTTGAAAGGCAAAGAATTATTCTCTACTGCAACCTGGTTGATTCTCG
CAGCCTGGGGTATGATCATCACTGGATATGTAGGTCAACTTTATGAGGTTGATGAT
ATAGCTCAATTGATGATATGGGGAGCGGTAAGTACTGCTTTCTTTGTGGTTATGAA
CTGGATTGTAGGGACAAAAATATTCAAGAATCGTGCAACTATGTTAGGTGGAACT
GACTCTACGATTACTAAGGTATTTTGGTTAATGATGTTTGCATGGACGCTATATCC
TATTGCATATCTAGTACCAGCTTTTATGAACAATGCTGATGGTGTGGTATTGAGAC
AATTGTTATTCACCATTGCGGATATTTCTAGTAAAGTGATTTACGGATTGATGATC
ACCTATATCGCCATACAGCAATCTGCTGCTGCTGGATATGTTCCAGCGCAACAAG
CACTAGGGCGTATAGGTATGGACTCTAAAGCAGCCGGCGCTAGCCACCATCACCA
TCACCATCACCATCACCATTGAGGATCC

Amino acid sequence *Nm*HR

MKNIESLFDYSAGQFEFIDHLLTMGVGVHFAALIFFLVVSQFVAPKYRIATALSCIVMV
SAGLILNSQAVMWTDAYAYVDGSYQLQDLTFSNGYRYVNWMATIPCLLLQLLIVLN
LKGKELFSTATWLILAAWGMIITGYVGQLYEVDDIAQLMIWGAVSTAFFVVMNWIV
GTKIFKNRATMLGGTDSTITKVFWLMMFAWTLYPIAYLVPAFMNNADGVVLRQLLF
TIADISSKVIYGLMITYIAIQQSAAAGYVPAQQALGRIGMDSKAAGASHHHHHHHHHH

Primers list *Nm*HR

Name	Forward primer	Reverse primer
Flanking primers	5´- gcCATATGAAAAATAT TGAAAGCTTATTTGACT ACAGC-3´	5´- gcGGATCCTCAATGGTGA TGGTGATGGTGATGGTGAT GGTGGCTAGCGCCGGCTGC TTTAGAGTCCATACCTATAC -3´
D231E: GAT → GAA	5'- G TTA TTC ACC ATT GCG **GAA** ATT TCT AGT AAA GTG TTT AC-3´	5'- GTA AAT CAC TTT ACT AGA AAT **TTC** CGC AAT GGT GAA TAA C-3´
D231N GAT → AAC	5'- G TTA TTC ACC ATT GCG **AAC** ATT TCT AGT AAA GTG ATT TAC	5'- GTA AAT CAC TTT ACT AGA AAT **GTT** CGC AAT GGT GAA TAA C
D231C GAT → TGC	5'- G TTA TTC ACC ATT GCG **TGC** ATT TCT AGT AAA GTG ATT TAC	5'- GTA AAT CAC TTT ACT AGA AAT **GCA** CGC AAT GGT GAA TAA C
R95A: CGT → GCG	5'-C ACT TTC TCT AAC GGA TAC **GCG** TAC GTG AAT TGG ATG GCG-3´	5'-CGC CAT CCA ATT CAC GTA **CGC** GTA TCC GTT AGA GAA AGT G-3´
W99F: TGG → TTT	5'-GA TAC CGT TAC GTG AAT **TTT** ATG GCG ACG ATT CCT TG-3´	5'-CA AGG AAT CGT CGC CAT **AAA** ATT CAC GTA ACG GTA TC-3´
W99TAG: TGG → TAG	5'-GA TAC CGT TAC GTG AAT **TAG** ATG GCG ACG ATT CCT TG-3´	5'-CA AGG AAT CGT CGC CAT **CTA** ATT CAC GTA ACG GTA TC-3´
W201F: TGG → TTT	5'-GG TTA ATG ATG TTT GCA **TTT** ACG CTA TAT CCT ATT GC-3´	5'-GC AAT AGG ATA TAG CGT **AAA** TGC AAA CAT CAT TAA CC-3´

W201TAG: TGG → TAG	5’-GG TTA ATG ATG TTT GCA **TAG** ACG CTA TAT CCT ATT GC-3´	5’-GG TTA ATG ATG TTT GCA **CTA** ACG CTA TAT CCT ATT GC-3´
N98D: AAT → GAT	5’-C GGA TAC CGT TAC GTG **GAT** TGG ATG GCG ACG ATT C-3´	5’-G AAT CGT CGC CAT CCA **ATC** CAC GTA ACG GTA TCC G-3´
N98Q: AAT → CAG	5’-C GGA TAC CGT TAC GTG **CAG** TGG ATG GCG ACG ATT C	5’-G AAT CGT CGC CAT CCA **CTG** CAC GTA ACG GTA TCC G-3´
N98A: AAT → GCG	5’-C GGA TAC CGT TAC GTG **GCG** TGG ATG GCG ACG ATT C	5’-G AAT CGT CGC CAT CCA **CGC** CAC GTA ACG GTA TCC G-3´
N98L AAT → CTG	5’-C GGA TAC CGT TAC GTG **GCG** TGG ATG GCG ACG ATT C	5’-G AAT CGT CGC CAT CCA **CAG** CAC GTA ACG GTA TCC G-3
N98T/T102S AAT → ACC / ACG→TCT	5’-C GGA TAC CGT TAC GTG **ACC** TGG ATG GCG **TCT** ATT CCT TGC TTA TTG TTA C	5’- G TAA CAA TAA GCA AGG AAT **AGA** CGC CAT CCA **GGT** CAC GTA ACG GTA TCC G
T102S ACG→TCT	5´-C GTG AAT TGG ATG GCG **TCT** ATT CCT TGC TTA TTG TTA C-3´	5´-G TAA CAA TAA GCA AGG AAT **AGA** CGC CAT CCA ATT CAC G-3´
T102N ACG→AAC	5´-C GTG AAT TGG ATG GCG **AAC** ATT CCT TGC TTA TTG TTA C-3´	5´-G TAA CAA TAA GCA AGG AAT **GTT** CGC CAT CCA ATT CAC G-3´
Q109D: CAA → GAT	5´-CG ATT CCT TGC TTA TTG TTA **GAT** TTA TTG ATT GTC TTG AAT TTG-3´	5´-CAA ATT CAA GAC AAT CAA TAA **ATC** TAA CAA TAA GCA AGG AAT CG-3´
C55S: TGT → TCT	5’-GCA ACT GCG CTT TCT **TCT**	5’-GC AGA TAC CAT AAC AAT

	ATT GTT ATG GTA TCT GC-3´	**AGA** AGA AAG CGC AGT TGC-3´
C55T: TGT → ACC	5’- GCA ACT GCG CTT TCT **ACC** ATT GTT ATG GTA TCT GC	5’-GCA GAT ACC ATA ACA AT**G GT**A GAA AGC GCA GTT GC
C55A: TGT → GCG	5’-GCA ACT GCG CTT TCT **GCG** ATT GTT ATG GTA TCT GC	5’-GCA GAT ACC ATA ACA AT**C GC**A GAA AGC GCA GTT GC
C105S: TGC → TCT	5´-GATGGCGACGATTCCT**TC T** TTATTGTTACAATTATTG A TTG-3´	5’-CAATCAATAATTGTAACAA TAA **AGA**AGGAATCGTCGCCATC -3´
C105T: TGC → ACC	5’-GAT GGC GAC GAT TCC T**AC C**TT ATT GTT ACA ATT ATT GAT TG	5’-CAA TCA ATA ATT GTA ACA ATA A**GG T**AG GAA TCG TCG CCA TC
C105A: TGC → GCG	5’-GAT GGC GAC GAT TCC T**GC G**TT ATT GTT ACA ATT ATT GAT TG	5’-CAA TCA ATA ATT GTA ACA ATA A**CG C**AG GAA TCG TCG CCA TC
C105M: TGC → ATG	5´-GAT GGC GAC GATT CCT **ATG** TTA TTG TTA CAA TTA TTG ATT G-3´	5’-C AAT CAA TAA TTG TAA CAA TAA **CAT** AGG AAT CGT CGC CAT C-3´
N92Q: AAC → CAG	5’-CAA GAC CTC ACT TTC TCT **CAG** GGA TAC CGT TAC GTG-3´	5’-CAC GTA ACG GTA TCC **CTG** AGA GAA AGT GAG GTC TTG-3´
N92D: AAC → GAT	5’-CAA GAC CTC ACT TTC TCT **GAT** GGA TAC CGT TAC GTG-3´	5’-CAC GTA ACG GTA TCC **ATC** AGA GAA AGT GAG GTC TTG-3´

N92T: AAC → ACC	5’-CAA GAC CTC ACT TTC TCT **ACC** GGA TAC CGT TAC GTG-3´	5’-CAC GTA ACG GTA TCC **GGT** AGA GAA AGT GAG GTC TTG-3´
N92K AAC → AAA	5’-CAA GAC CTC ACT TTC TCT **AAA** GGA TAC CGT TAC GTG-3´	5’-CAC GTA ACG GTA TCC **TTT** AGA GAA AGT GAG GTC TTG-3´
N92C AAC → TGC	5’-CAA GAC CTC ACT TTC TCT **TGC** GGA TAC CGT TAC GTG-3´	5’-CAC GTA ACG GTA TCC **GCA** AGA GAA AGT GAG GTC TTG-3´
N3D: AAT → GAT (flanking primer)	5´-gcCATATGAAA**GAT**ATT GAAAGCTTATTTGACTAC AGC-3´	
N3Q: AAT → CAG (flanking primer)	5´-gc CAT ATG AAA **CAG** ATT GAA AGC TTA TTT GAC TAC AGC-3´	
N3T: AAT → ACC (flanking primer)	5´-gc CAT ATG AAA **ACC** ATT GAA AGC TTA TTT GAC TAC AGC-3´	
N3K: AAT → AAA (flanking primer)	5´- gc CAT ATG AAA **AAA** ATT GAA AGC TTA TTT	

	GAC TAC AGC	
N3C: AAT → TGC (flanking primer)	5´- gc CAT ATG AAA **TGC** ATT GAA AGC TTA TTT GAC TAC AGC	
R223K: AGA → AAA	5´-GCT GAT GGT GTG GTA TTG **AAA** CAA TTG TTA TTC ACC ATT GC-3´	5´-GC AAT GGT GAA TAA CAA TTG **TTT** CAA TAC CAC ACC ATC AGC-3´
R223H: AGA → CAT	5´- GCT GAT GGT GTG GTA TTG **CAT** CAA TTG TTA TTC ACC ATT GC	5´- GC AAT GGT GAA TAA CAA TTG **ATG** CAA TAC CAC ACC ATC AGC
R223Q: AGA → CAG	5´- GCT GAT GGT GTG GTA TTG **CAG** CAA TTG TTA TTC ACC ATT GC	5´- GC AAT GGT GAA TAA CAA TTG **CTG** CAA TAC CAC ACC ATC AGC
P45A: CCT → GCG	5'-GTC TCA CAA TTT GTA GCT **GCG** AAA TAT CGT ATT GCA ACT GCG-3´	5'-CGC AGT TGC AAT ACG ATA TTT **CGC** AGC TAC AAA TTG TGA GAC-3´
K46A: AAA → GCG	5'-CTC ACA ATT TGT AGC TCCT **GCG** TAT CGT ATT GCA ACT GCG-3´	5'-CGC AGT TGC AAT ACG ATA **CGC** AGG AGC TAC AAA TTG TGA G-3´
P104A: CCT → GCG	5´-G AAT TGG ATG GCG ACG ATT **GCG** TGC TTA TTG TTA CAA TTA TTG-3´	5´-CAA TAA TTG TAA CAA TAA GCA **CGC** AAT CGT CGC CAT CCA ATT C-3´
P104G: CCT → GGC	5´-G AAT TGG ATG GCG ACG ATT **GGC** TGC TTA TTG TTA CAA TTA TTG-3´	5´-CAA TAA TTG TAA CAA TAA GCA **GCC** AAT CGT CGC CAT CCA ATT C-3´

P104A/L108C: TTA → TGC	5'- G ACG ATT **GCG** TGC TTA TTG **TGC** CAA TTA TTG ATT GTC TTG-3'	5'- CAA GAC AAT CAA TAA TTG **GCA** CAA TAA GCA **CGC** AAT CGT C -3'
Q68D: CAG → GAT	5´ - GGG TTG ATA CTT AAC AGC **GAT** GCG GTC ATG TGG ACT G - 3'	5´ - C AGT CCA CAT GAC CGC **ATC** GCT GTT AAG TAT CAA CCC – 3´
Q143D : CAA → GAT	5´ - C ACT GGA TAT GTA GGT **GAT** CTT TAT GAG GTT GAT G - 3'	5´ - C ATC AAC CTC ATA AAG **ATC** ACC TAC ATA TCC AGT G - 3'

Special cases:

*Nm*HR N98D/Q109D variant has been performed by using the primers for *Nm*HR Q109D on *Nm*HR N98D plasmid.

*Nm*HR P104A/L108C variant has been performed by using the primers for *Nm*HR L108C on *Nm*HR P104A plasmid.

*Nm*HR N3T/N92T variant has been performed by using the primers for *Nm*HR N92T on *Nm*HR N3T plasmid.

Variants *Nm*HR N3Q, *Nm*HR N3D, *Nm*HR N3T, *Nm*HR N3K and *Nm*HR N3C have been performed using the megaprimer PCR technique, however only the first round of PCR was employed by addition of the forward mutagenesis primer being also the flanking primer and the reverse *Nm*HR flanking primer.

DNA sequence pPIC9K *Um*Rh1

GAATTCATGAACGTCGTATCCGAGCTGCTGAAGCGAGCGGGCAACATGGCCCTCA
GCTCCAACCCCACTGTCGCTGACATCGACATTACTACCCCCGGTTCCGACTGGCTT
TGGGCTGTCTTTTCCGTCATGGCTGCCACTGGACTCGGTACTATGGTGTGGTCACT
CAAGGTGTCGCGTGGTGAGCGAGCCTTCCACTATCTCTCAGCCGCGATTCTCGCTA
CGGCTTCCGTCGCCTACTTTTCGATGGCTTCGGACCTCGGTGCCACCCCAGTCCGC
GTCGAGTTTACCAACTACGGCCCTAACGAAGTCAACGGTCTTCGTCCTACCCGTTC
CATCTGGTACGTTCGTTACATTGACTGGACTGTCACCACCCCTCTCCTGCTCCTCG
AGATCCTGCTTGTTTCTGGTCTCCCCCTCTCGACCGTCTTTATCACCATCTTTTTCG
ATCTTGTCATGATCATCACCGGTCTGATCGGTTCTCTTGTCGAGTCGACCTACAAG
TGGGGTTACTACACCATGGGCTGCGTTGCCATGTTCTATGTCTTCTGGGTCATCTA
TGGCCCTGGTCTCAAATCGGCTTCCCACCTCGGCGCCGACTTTAAGAAGGCCTATC
TCTACTCTTCGCTCGTTCTCACCATCCTTTGGACTCTCTACCCTGTTGCTTGGGGTC
TCGCCGATGGTAGCAACACAATTTCGCCCAACGCAGAGATGATCTTCTATGGTGT
ACTTGACCTGCTTGCCAAGCCTGTCTTCGCGCTCTTCCACCTCTGGTCGCTCCGCC
GATGTAATTACTCTTCGCTCCACCTCAAGAGCGGCAAGTTTTCAGACTACGAGGA
CCTCTCGGGCAACCACTATCGCTCCATGGAGGGCGGCAAGGCCAGCGAAGCTGGT
GTTACCGGAGCTGGGGTCAACGGTGTCGCTACTGGTGTCAACACTACTGGTGCCG
ACGTTACTGGTGCCAACGTCCTCCACCCTGCTCCTCCCACCCAAATGCACACCGTT
ACCCAGCATCATCATCATCATCATGCGGCCGC

Amino acid sequence *Um*Rh1

MNVVSELLKRAGNMALSSNPTVADIDITTPGSDWLWAVFSVMAATGLGTMVWSLK
VSRGERAFHYLSAAILATASVAYFSMASDLGATPVRVEFTNYGPNEVNGLRPTRSIWY
VRYIDWTVTTPLLLLEILLVSGLPLSTVFITIFFDLVMIITGLIGSLVESTYKWGYYTMG
CVAMFYVFWVIYGPGLKSASHLGADFKKAYLYSSLVLTILWTLYPVAWGLADGSNTI
SPNAEMIFYGVLDLLAKPVFALFHLWSLRRCNYSSLHLKSGKFSDYEDLSGNHYRSM
EGGKASEAGVTGAGVNGVATGVNTTGADVTGANVLHPAPPTQMHTVTQHHHHHHA
A

Primers list *Um*Rh1

Name	Forward primer	Reverse primer
Flanking primers	5'-gcGAATTCATGAACGTC GTATCCGAGCTGCTG-3'	5'-gcGCGGCCgcTCAATGATGATG ATGATGATGCTGGGTAAC GGTGTGCATTTGGG-3'
E93Q	5'-CC CCA GTC CGC GTC **CAA** TTT ACC AAC TAC GGC C-3'	5'-G GCC GTA GTT GGT AAA **TTG** GAC GCG GAC TGG GG-3'
E129Q	5'-CCT CTC CTG CTC CTC **CAA** ATC CTG CTT GTT TCT GG-3'	5'-CC AGA AAC AAG CAG GAT **TTG** GAG GAG CAG GAG AGG-3'
C174S	5'-GT TAC TAC ACC ATG GGC **TCT** GTT GCC ATG TTC TAT GTC-3'	5'-GAC ATA GAA CAT GGC AAC **AGA** GCC CAT GGT GTA GTA AC-3'
C174T	5'-GT TAC TAC ACC ATG GGC **ACT** GTT GCC ATG TTC TAT GTC-3'	5'-GAC ATA GAA CAT GGC AAC **AGT** GCC CAT GGT GTA GTA AC-3'
D225N	5'-GCT TGG GGT CTC GCC **AAC** GGT AGC AAC ACA ATT TCG-3'	5'-CGA AAT TGT GTT GCT ACC **GTT** GGC GAG ACC CCA AGC-3'
D118N	5'-C TGG TAC GTT CGT TAC ATT **AAC** TGG ACT GTC ACC ACC C-3'	5'-GG GGT GGT GAC AGT CCA **GTT** AAT GTA ACG AAC GTA CCA G-3'
D118E	5'-C TGG TAC GTT CGT TAC ATT **GAA** TGG ACT GTC ACC ACC C **3'**	5'-GG GGT GGT GAC AGT CCA **TTC** AAT GTA ACG AAC GTA CCA G-3'

C261S	5’-GG TCG CTC CGC CGA **TCT** AAT TAC TCT TCG CTC CAC-3’	5’-GTG GAG CGA AGA GTA ATT **AGA** TCG GCG GAG CGA CC-3’
ΔBC loop	5’-C GGT GCC ACC CCA GTC **AAC GGT CTT CGT CCT ACC CG**-3’	5’-**CG GGT AGG ACG AAG ACC GTT** GAC TGG GGT GGC ACC G-3’
1-271		5’-gcgcggccgcTTAGTGATGGTG ATGGTGATGGTGATGGTGAT GGCCGCTCTTGAGGTGGAGC
E235Q	5’-C ACA ATT TCG CCC AAC GCA **CAA** ATG ATC TTC TAT GGT GTA CTT G-3’	5’-C AAG TAC ACC ATA GAA GAT CAT **TTG** TGC GTT GGG CGA AAT TGT G-3’
D243E	5’-G ATG ATC TTC TAT GGT GTA CTT **GAA** CTG CTT GCC AAG CCT GTC-3’	5’-GAC AGG CTT GGC AAG CAG **TTC** TAC ACC ATA GAA GAT CAT C-3’
D243N	5’-G ATG ATC TTC TAT GGT GTA CTT **AAT** CTG CTT GCC AAG CCT GTC-3’	5’-GAC AGG CTT GGC AAG CAG **ATT** AAG TAC ACC ATA GAA GAT CAT C-3’
D243P	5’-G ATG ATC TTC TAT GGT GTA CTT **CCA** CTG CTT GCC AAG CCT GTC-3’	5’-GAC AGG CTT GGC AAG CAG **TGG** AAG TAC ACC ATA GAA GAT CATC-3’
H254A	5’-CCT GTC TTC GCG CTC TTC **GCT** CTC TGG TCG CTC CGC CG-3’	5’-CG GCG GAG CGA CCA GAG **AGC** GAA GAG CGC GAA GAC AGG-3’
H64A	5’-CGT GGT GAG CGA GCC TTC **GCT** TAT CTC TCA GCC GCG ATT C-3’	5’-G AAT CGC GGC TGA GAG ATA **AGC** GAA GGC TCG CTC ACC ACG-3’

D148N	5’-C GTC TTT ATC ACC ATC TTT TTC **AAT** CTT GTC ATG ATC ATC ACC GG-3’	5’-CC GGT GAT GAT CAT GAC AAG **ATT** GAA AAA GAT GGT GAT AAA GAC G-3’

Special cases:

*Um*Rh1 E129Q/D148N variant has been performed by using the primers for *Um*Rh1 D148N on *Um*Rh1 E129Q plasmid.

DNA sequence pET21b Agp2

CATATGGCATCCACGGACTATCATGTCGACCTGACCAATTGCGACCGCGAACCCA
TTCATATTCCAGGCTATATTCAACCGCATGGCTGCCTTATCGCCTGCGATAACGCC
ATGCGAATGGTGCTGCGGCATTCCGAAAACTGCGGCGAACTGCTGGGACTTGAGG
GCGATCTCAACGGCAGGACCGCCGAGGATGTGCTCGGCAAAAAGCTCGTCCACGA
TCTCCGCAACGCGCTCACCGTCACCGGTAGAACCACGCGCCCCGCCATGCTGCCC
GCAATGGAAACAAGCGACGGCCGCAGCTTCGATATTTCACTCCATCGCTACAAAT
CCACCACCATCATCGAATTCGAGCCCTCGGGCAGCGACGCGCAGCCGCTCGGCAC
GGCGCGCAAGATGGTGGACCGCATCCGCGAAGCCGACAGCGTCGAAAGCCTGAT
CTCCAGAACCACACGCCTGGTAAAGGCGACGCTGGGTTACGACCGGGTGATGATC
TACCGCTTCCAGGAAGACGGCGCCGGCAAGGTCGTGTCGGAGGCCAAGCAGCCC
GAGCTGGAGAGCTTTCTCGGGCAATATTTCCCCGCCAGCGATATTCCACAGCAGG
CTCGCGCACTTTATCTCAAGAACACCTTGCGCATCATCTCCGATGCCAGCGGCACC
CGCATTCCGGTCCTGCCAGCCGTCGATGTCTCCGGTGAGCCGCTCGATCTCTCTTA
CGCGCATTTGCGCAGCGTCTCGCCCATCCATTGCGAATATCTCCGCAATATGGGTG
TTGCCGCCTCCATGTCGATTTCTGTGATTGTCGATGGCGCCCTGTGGGGCCTGATC
GCCTGCCACCATTATTCGCCGCGTGTGCTGAGCATGCCAGTTCGGATCGCTGCGGA
AATGTTCGGGGAATTTTTCTCCATGCATCTGCAGGTTCTGAAGCAGAAGCGCCGCC
TCGACACCATCAACCACGCCCATGCGGCGCTCGACCGGTTTCTGCGGCTGGCCGC
CCATCACGCCAACATTGAAGAACTGCTGGTCGACAGTTTTCAGGATTTTGCCGATC
TGATGCCCTGCGACGGTGTCGGGCTGTGGGTCGGCAACAACTGGCACGGCCATGG
CGCAACGCCACCGCATGATGCCATTCCAAGGCTGGCGCGTTTCGTCGCTTCGGCTT
CGGAAGGCAGGGTCTGGGCAACACACGCCCTGTCGCAGGCCATACCGGAAGCGG
AAATATACGCCGGCACCGCGGCCGGAATGCTTGCTATCCCGCTTTCGCAGGTCAA
GAGCGACTATCTCCTGTTTTTCCGCAAGGAGATCGTGCAGAACCTGAACTGGGCC
GGCAATCCGGAAAAATCCTATGAAACCGGCCCGATGGGCGACCGCCTCACGCCGC
GTAAAAGCTTCGCAATCTGGAAAGAGACCGTTCGCCTGCAGGCACAGCCCTGGTC
GGAAGCCGACCGGGAAATCGCCGAAGCCGCGAGAATCGCGCTTGTCGAAGTGGC
GTTCCACCACAGCGAGCATCACCATCACCATCACTAAGGATCC

Amino acid sequence Agp2

MASTDYHVDLTNCDREPIHIPGYIQPHGCLIACDNAMRMVLRHSENCGELLGLEGDL
NGRTAEDVLGKKLVHDLRNALTVTGRTTRPAMLPAMETSDGRSFDISLHRYKSTTIIE
FEPSGSDAQPLGTARKMVDRIREADSVESLISRTTRLVKATLGYDRVMIYRFQEDGAG
KVVSEAKQPELESFLGQYFPASDIPQQARALYLKNTLRIISDASGTRIPVLPAVDVSGEP
LDLSYAHLRSVSPIHCEYLRNMGVAASMSISVIVDGALWGLIACHHYSPRVLSMPVRI
AAEMFGEFFSMHLQVLKQKRRLDTINHAHAALDRFLRLAAHHANIEELLVDSFQDFA
DLMPCDGVGLWVGNNWHGHGATPPHDAIPRLARFVASASEGRVWATHALSQAIPEA
EIYAGTAAGMLAIPLSQVKSDYLLFFRKEIVQNLNWAGNPEKSYETGPMGDRLTPRKS
FAIWKETVRLQAQPWSEADREIAEAARIALVEVAFHHSEHHHHHH

Primers list Agp2

Name	Forward primer	Reverse primer
W440F: TGG → TTT	5´-C GTG CAG AAC CTG AAC **TTT** GCC GGC AAT CCG G-3´	5´-C CGG ATT GCC GGC **AAA** GTT CAG GTT CTG CAC G-3´
W440TAG: TGG → TAG	5´-C GTG CAG AAC CTG AAC **TAG** GCC GGC AAT CCG G-3´	5´-C CGG ATT GCC GGC **CTA** GTT CAG GTT CTG CAC G-3´
F463TAG: TTC → TAG	5´C ACG CCG CGT AAA AGC **TAG** GCA ATC TGG AAA GAG AC3´	5´GT CTC TTT CCA GAT TGC **CTA** GCT TTT ACG CGG CGT G 3´

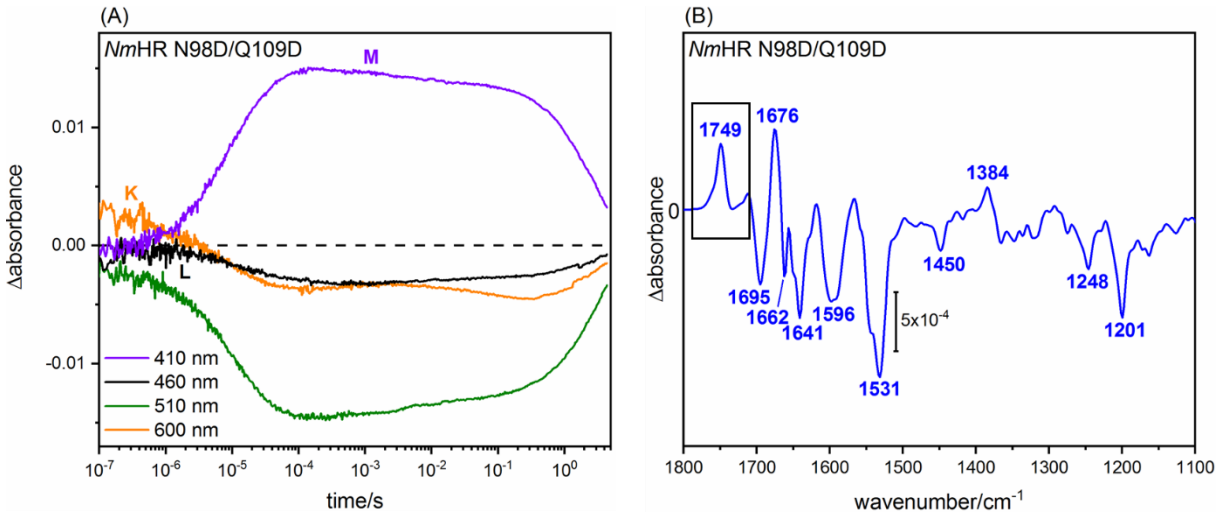

Figure S1. *Flash photolysis of the double variant NmHR N98D/Q109D in 1 M NaCl (A). The kinetics are very similar to the single variant N98D, with the presence of an M state. Light-induced difference FTIR spectrum of NmHR N98D/Q109D using a green LED (λ: 525 nm) (B). The positive peak at 1749 cm^{-1} can be assigned to protonated aspartic acid.*

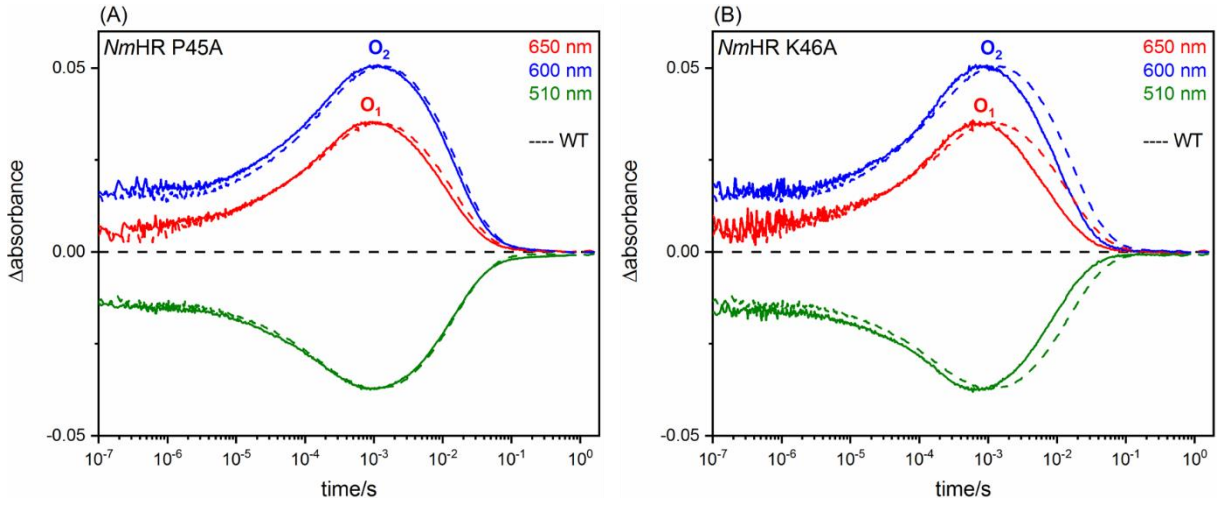

Figure S2. *Photocycle of NmHR P45A (solid line) compared to wild-type NmHR (dashed line) (A). Photocycle of NmHR K46A (solid line) compared to wild-type NmHR (dashed line) (B). Substitution of these residues has no effect on the photoreaction of NmHR.*

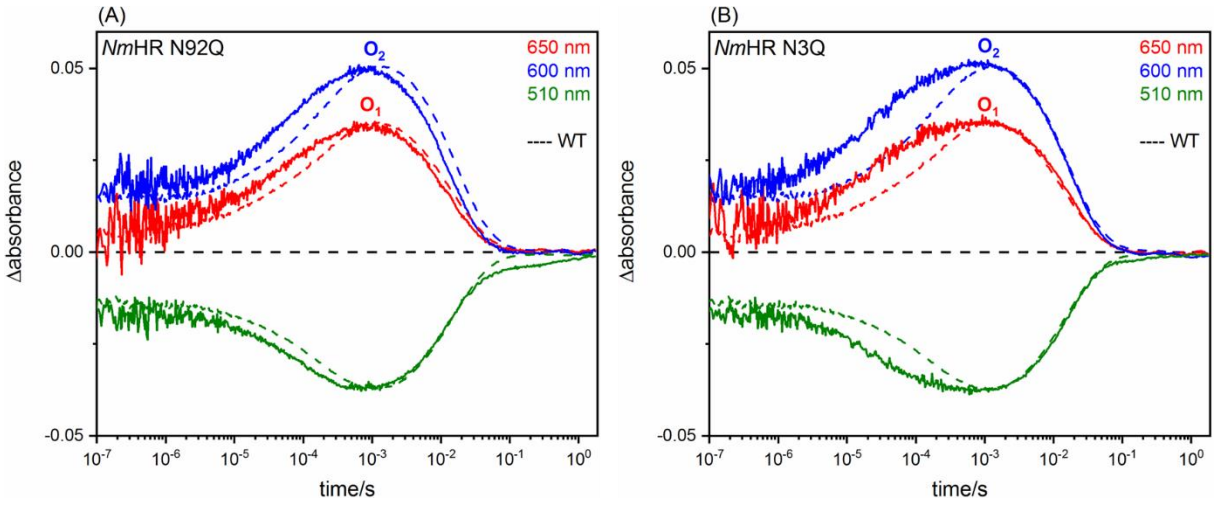

Figure S3. *Photocycle of NmHR N92Q (solid line) compared to wild-type NmHR (dashed line) (A). Photocycle of NmHR N3Q (solid line) compared to wild-type NmHR (dashed line) (B). Substitution of N92 and N3 with a glutamine result in a photocycle similar to that of wild-type NmHR.*

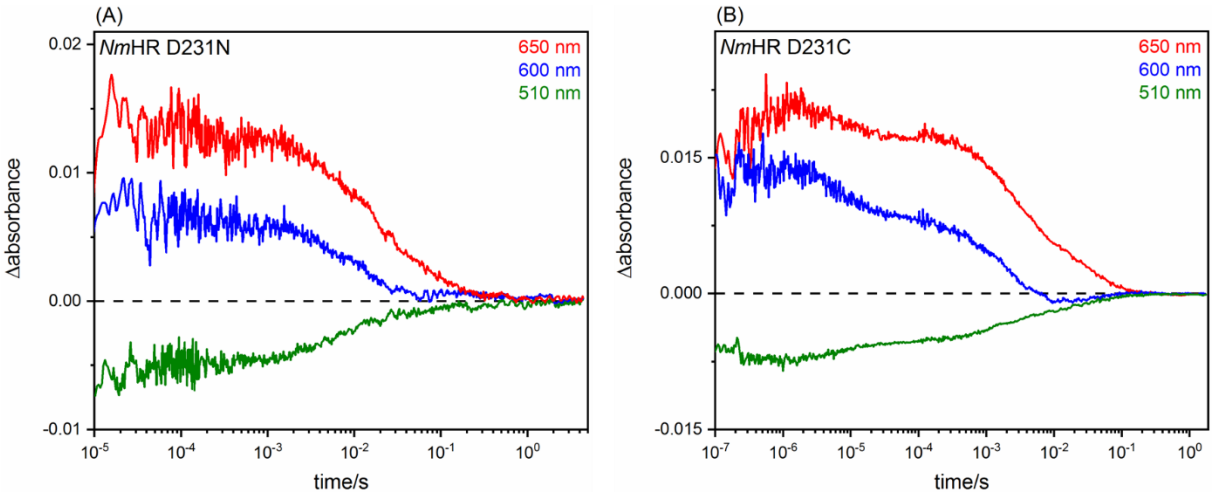

Figure S4. *Substitution of D231 with an asparagine (A) or cysteine (B) results in a strongly impaired photoreaction, similar to the photoreaction of chloride-free NmHR.*

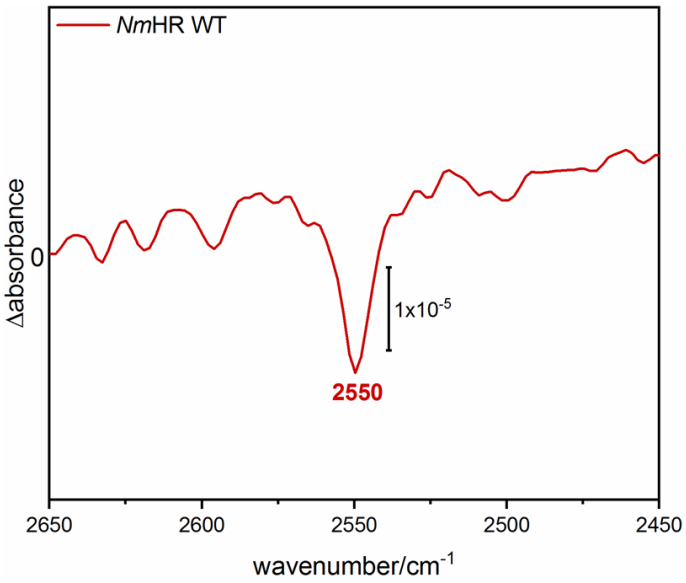

Figure S5. *Light-induced difference FTIR spectrum of NmHR wild type in the region of the S-H stretching vibrations. The negative band at 2550 cm^{-1} is due to the deprotonation of a cysteine side chain.*

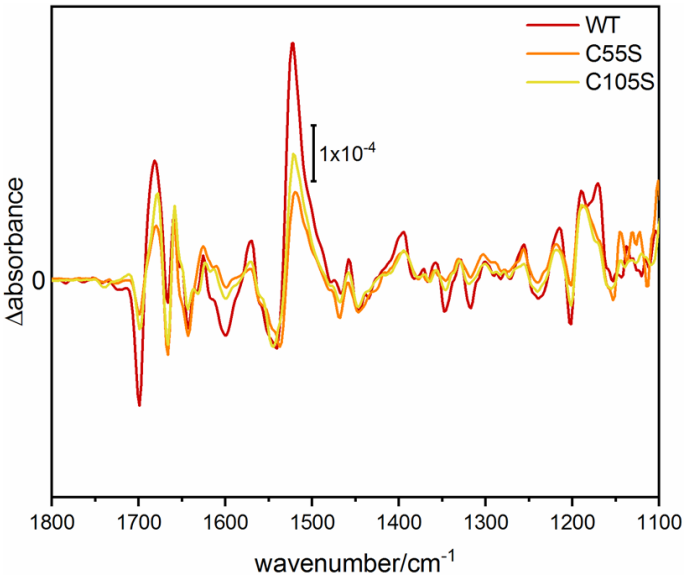

Figure S6. *Light-induced difference FTIR spectrum of NmHR wild type (red), C55S (orange) and C105S (yellow), in the 1800-1100 cm^{-1} region.*

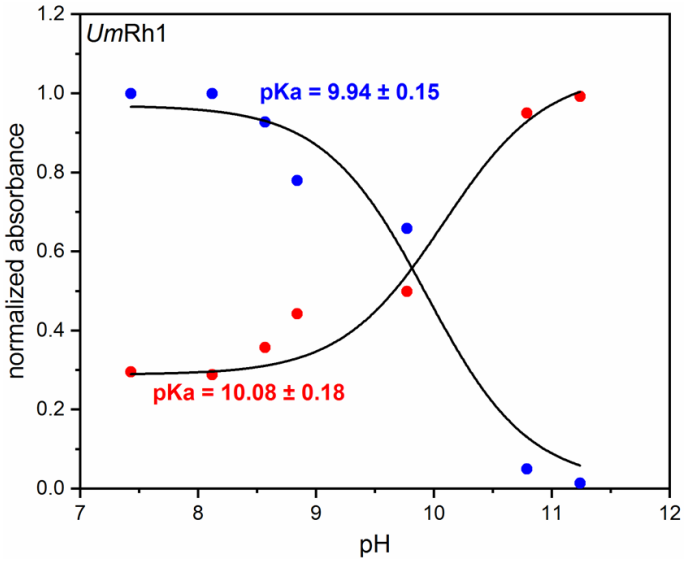

Figure S7. *pKa of the Schiff base in UmRh1, calculated by monitoring the absorbance at 365 nm (blue) and 532 nm (red).*

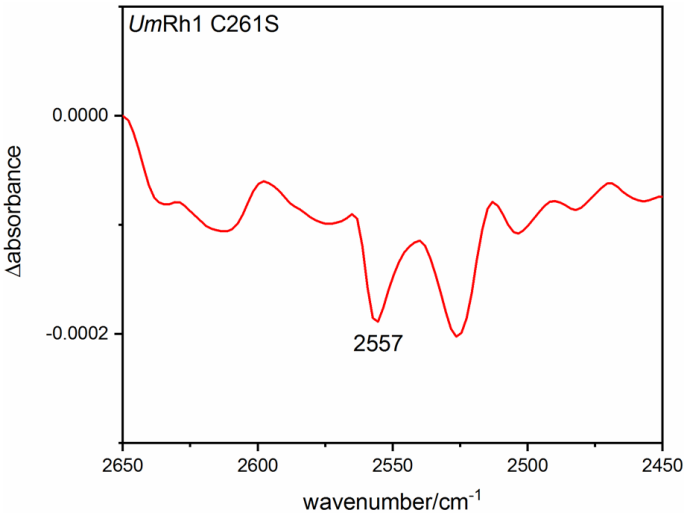

Figure S8. *Light-induced difference FTIR spectrum of UmRh1 C261S in the region of the S-H stretching vibrations measured it as a dry film, in order to increase the signal size for the correct assignment.*

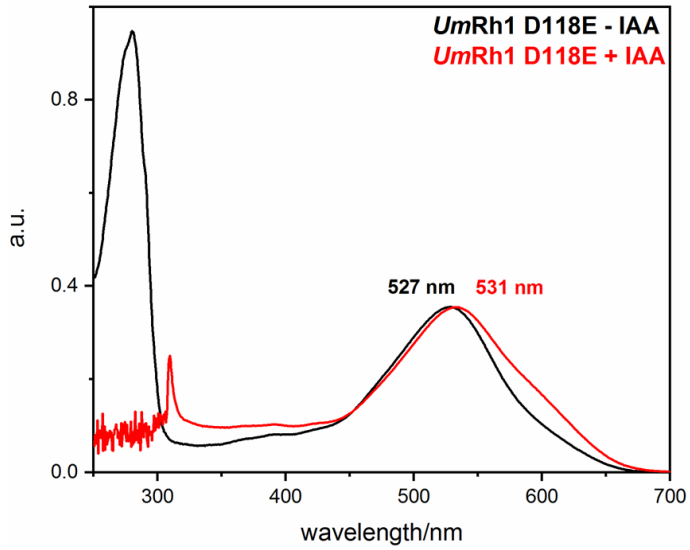

Figure S9. *UV/Vis spectra of UmRh1 D118E variant in the absence (black) and in presence (red) of IAA. The maximum absorption of the retinal shifts from 527 nm to 531 nm upon addition of IAA. The signal at 280 nm is absent in the sample containing IAA because of the saturation of the signal, as IAA has a strong absorption in that region.*

8. References

(1) Kandori, H. Ion-Pumping Microbial Rhodopsins. *Front Mol Biosci* **2015**, *2*, 52. https://doi.org/10.3389/fmolb.2015.00052.

(2) Ernst, O. P.; Lodowski, D. T.; Elstner, M.; Hegemann, P.; Brown, L. S.; Kandori, H. Microbial and Animal Rhodopsins: Structures, Functions, and Molecular Mechanisms. *Chem Rev* **2014**, *114* (1), 126–163. https://doi.org/10.1021/cr4003769.

(3) Kandori, H. Biophysics of Rhodopsins and Optogenetics. *Biophys Rev* **2020**, *12* (2), 355–361. https://doi.org/10.1007/s12551-020-00645-0.

(4) Rozenberg, A.; Inoue, K.; Kandori, H.; Béjà, O. Microbial Rhodopsins: The Last Two Decades. *Annu Rev Microbiol* **2021**, *75*, 427–447. https://doi.org/10.1146/annurev-micro-031721-020452.

(5) Kataoka, C.; Inoue, K.; Katayama, K.; Béjà, O.; Kandori, H. Unique Photochemistry Observed in a New Microbial Rhodopsin. *J Phys Chem Lett* **2019**, *10* (17), 5117–5121. https://doi.org/10.1021/acs.jpclett.9b01957.

(6) Kandori, H. History and Perspectives of Ion-Transporting Rhodopsins. *Adv Exp Med Biol* **2021**, *1293*, 3–19. https://doi.org/10.1007/978-981-15-8763-4_1.

(7) Engelhard, M. Molecular Biology of Microbial Rhodopsins. *Methods Mol Biol* **2022**, *2501*, 53–69. https://doi.org/10.1007/978-1-0716-2329-9_2.

(8) Govorunova, E. G.; Sineshchekov, O. A.; Li, H.; Spudich, J. L. Microbial Rhodopsins: Diversity, Mechanisms, and Optogenetic Applications. *Annu Rev Biochem* **2017**, *86*, 845–872. https://doi.org/10.1146/annurev-biochem-101910-144233.

(9) Ogren, J. I.; Yi, A.; Mamaev, S.; Li, H.; Lugtenburg, J.; DeGrip, W. J.; Spudich, J. L.; Rothschild, K. J. Comparison of the Structural Changes Occurring during the Primary Phototransition of Two Different Channelrhodopsins from *Chlamydomonas* Algae. *Biochemistry* **2015**, *54* (2), 377–388. https://doi.org/10.1021/bi501243y.

(10) Poboży, K.; Poboży, T.; Domański, P.; Derczyński, M.; Konarski, W.; Domańska-Poboża, J. Evolution of Light-Sensitive Proteins in Optogenetic Approaches for Vision Restoration: A Comprehensive Review. *Biomedicines* **2025**, *13* (2), 429. https://doi.org/10.3390/biomedicines13020429.

(11) Kawanabe, A.; Kandori, H. Photoreactions and Structural Changes of Anabaena Sensory Rhodopsin. *Sensors (Basel)* **2009**, *9* (12), 9741–9804. https://doi.org/10.3390/s91209741.

(12) Schreiner, M.; Schlesinger, R.; Heberle, J.; Niemann, H. H. Crystal Structure of Halobacterium Salinarum Halorhodopsin with a Partially Depopulated Primary Chloride-Binding Site. *Acta Crystallogr F Struct Biol Commun* **2016**, *72* (Pt 9), 692–699. https://doi.org/10.1107/S2053230X16012796.

(13) Ihara, K.; Narusawa, A.; Maruyama, K.; Takeguchi, M.; Kouyama, T. A Halorhodopsin-Overproducing Mutant Isolated from an Extremely Haloalkaliphilic Archaeon Natronomonas Pharaonis. *FEBS Lett* **2008**, *582* (19), 2931–2936. https://doi.org/10.1016/j.febslet.2008.07.030.

(14) Engelhard, C.; Chizhov, I.; Siebert, F.; Engelhard, M. Microbial Halorhodopsins: Light-Driven Chloride Pumps. *Chem Rev* **2018**, *118* (21), 10629–10645. https://doi.org/10.1021/acs.chemrev.7b00715.

(15) Neumüller, M.; Jähnig, F. Modeling of Halorhodopsin and Rhodopsin Based on Bacteriorhodopsin. *Proteins* **1996**, *26* (2), 146–156. https://doi.org/10.1002/(SICI)1097-0134(199610)26:2<146::AID-PROT4>3.0.CO;2-E.

(16) Hasemi, T.; Kikukawa, T.; Kamo, N.; Demura, M. Characterization of a Cyanobacterial Chloride-Pumping Rhodopsin and Its Conversion into a Proton Pump. *J Biol Chem* **2016**, *291* (1), 355–362. https://doi.org/10.1074/jbc.M115.688614.

(17) Brown, L. S. Light-Driven Proton Transfers and Proton Transport by Microbial Rhodopsins - A Biophysical Perspective. *Biochim Biophys Acta Biomembr* **2022**, *1864* (5), 183867. https://doi.org/10.1016/j.bbamem.2022.183867.

(18) Singh, M.; Ito, S.; Hososhima, S.; Abe-Yoshizumi, R.; Tsunoda, S. P.; Inoue, K.; Kandori, H. Light-Driven Chloride and Sulfate Pump with Two Different Transport Modes. *J Phys Chem B* **2023**, *127* (32), 7123–7134. https://doi.org/10.1021/acs.jpcb.3c02116.

(19) Astashkin, R.; Kovalev, K.; Bukhdruker, S.; Vaganova, S.; Kuzmin, A.; Alekseev, A.; Balandin, T.; Zabelskii, D.; Gushchin, I.; Royant, A.; Volkov, D.; Bourenkov, G.; Koonin, E.; Engelhard, M.; Bamberg, E.; Gordeliy, V. Structural Insights into Light-Driven Anion Pumping in Cyanobacteria. *Nat Commun* **2022**, *13* (1), 6460. https://doi.org/10.1038/s41467-022-34019-9.

(20) Gordeliy, V.; Kovalev, K.; Bamberg, E.; Rodriguez-Valera, F.; Zinovev, E.; Zabelskii, D.; Alekseev, A.; Rosselli, R.; Gushchin, I.; Okhrimenko, I. Microbial Rhodopsins. *Methods Mol Biol* **2022**, *2501*, 1–52. https://doi.org/10.1007/978-1-0716-2329-9_1.

(21) Yoshizawa, S.; Kumagai, Y.; Kim, H.; Ogura, Y.; Hayashi, T.; Iwasaki, W.; DeLong, E. F.; Kogure, K. Functional Characterization of Flavobacteria Rhodopsins Reveals a Unique Class of Light-Driven Chloride Pump in Bacteria. *Proc. Natl. Acad. Sci. U.S.A.* **2014**, *111* (18), 6732–6737. https://doi.org/10.1073/pnas.1403051111.

(22) Yun, J.-H.; Ohki, M.; Park, J.-H.; Ishimoto, N.; Sato-Tomita, A.; Lee, W.; Jin, Z.; Tame, J. R. H.; Shibayama, N.; Park, S.-Y.; Lee, W. Pumping Mechanism of NM-R3, a Light-Driven Bacterial Chloride Importer in the Rhodopsin Family. *Sci Adv* **2020**, *6* (6), eaay2042. https://doi.org/10.1126/sciadv.aay2042.

(23) Hosaka, T.; Yoshizawa, S.; Nakajima, Y.; Ohsawa, N.; Hato, M.; DeLong, E. F.; Kogure, K.; Yokoyama, S.; Kimura-Someya, T.; Iwasaki, W.; Shirouzu, M. Structural Mechanism for Light-Driven Transport by a New Type of Chloride Ion Pump, Nonlabens Marinus Rhodopsin-3. *Journal of Biological Chemistry* **2016**, *291* (34), 17488–17495. https://doi.org/10.1074/jbc.M116.728220.

(24) Kim, K.; Kwon, S.-K.; Jun, S.-H.; Cha, J. S.; Kim, H.; Lee, W.; Kim, J. F.; Cho, H.-S. Crystal Structure and Functional Characterization of a Light-Driven Chloride Pump Having an NTQ Motif. *Nat Commun* **2016**, *7*, 12677. https://doi.org/10.1038/ncomms12677.

(25) Mous, S.; Gotthard, G.; Ehrenberg, D.; Sen, S.; Weinert, T.; Johnson, P. J. M.; James, D.; Nass, K.; Furrer, A.; Kekilli, D.; Ma, P.; Brünle, S.; Casadei, C. M.; Martiel, I.; Dworkowski, F.; Gashi, D.; Skopintsev, P.; Wranik, M.; Knopp, G.; Panepucci, E.; Panneels, V.; Cirelli, C.; Ozerov, D.; Schertler, G. F. X.; Wang, M.; Milne, C.; Standfuss, J.; Schapiro, I.; Heberle, J.; Nogly, P. Dynamics and Mechanism of a Light-Driven Chloride Pump. *Science* **2022**, *375* (6583), 845–851. https://doi.org/10.1126/science.abj6663.

(26) Mathies, R. A.; Lin, S. W.; Ames, J. B.; Pollard, W. T. From Femtoseconds to Biology: Mechanism of Bacteriorhodopsin's Light-Driven Proton Pump. *Annu Rev Biophys Biophys Chem* **1991**, *20*, 491–518. https://doi.org/10.1146/annurev.bb.20.060191.002423.

(27) Shionoya, T.; Singh, M.; Mizuno, M.; Kandori, H.; Mizutani, Y. Strongly Hydrogen-Bonded Schiff Base and Adjoining Polyene Twisting in the Retinal Chromophore of Schizorhodopsins. *Biochemistry* **2021**, *60* (41), 3050–3057. https://doi.org/10.1021/acs.biochem.1c00529.

(28) Béjà, O.; Aravind, L.; Koonin, E. V.; Suzuki, M. T.; Hadd, A.; Nguyen, L. P.; Jovanovich, S. B.; Gates, C. M.; Feldman, R. A.; Spudich, J. L.; Spudich, E. N.; DeLong, E. F. Bacterial Rhodopsin: Evidence for a New Type of Phototrophy in the Sea. *Science* **2000**, *289* (5486), 1902–1906. https://doi.org/10.1126/science.289.5486.1902.

(29) Okhrimenko, I. S.; Kovalev, K.; Petrovskaya, L. E.; Ilyinsky, N. S.; Alekseev, A. A.; Marin, E.; Rokitskaya, T. I.; Antonenko, Y. N.; Siletsky, S. A.; Popov, P. A.; Zagryadskaya, Y. A.; Soloviov, D. V.; Chizhov, I. V.; Zabelskii, D. V.; Ryzhykau, Y. L.; Vlasov, A. V.; Kuklin, A. I.; Bogorodskiy, A. O.; Mikhailov, A. E.; Sidorov, D. V.; Bukhalovich, S.; Tsybrov, F.; Bukhdruker, S.; Vlasova, A. D.; Borshchevskiy, V. I.; Dolgikh, D. A.; Kirpichnikov, M. P.; Bamberg, E.; Gordeliy, V. I. Mirror Proteorhodopsins. *Commun Chem* **2023**, *6* (1), 88. https://doi.org/10.1038/s42004-023-00884-8.

(30) Schubert, L.; Chen, J.-L.; Fritz, T.; Marxer, F.; Langner, P.; Hoffmann, K.; Gamiz-Hernandez, A. P.; Kaila, V. R. I.; Schlesinger, R.; Heberle, J. Proton Release Reactions in the Inward H+ Pump NsXeR. *J Phys Chem B* **2023**, *127* (39), 8358–8369. https://doi.org/10.1021/acs.jpcb.3c04100.

(31) Waschuk, S. A.; Bezerra, A. G.; Shi, L.; Brown, L. S. Leptosphaeria Rhodopsin: Bacteriorhodopsin-like Proton Pump from a Eukaryote. *Proc Natl Acad Sci U S A* **2005**, *102* (19), 6879–6883. https://doi.org/10.1073/pnas.0409659102.

(32) García-Martínez, J.; Brunk, M.; Avalos, J.; Terpitz, U. The CarO Rhodopsin of the Fungus Fusarium Fujikuroi Is a Light-Driven Proton Pump That Retards Spore Germination. *Sci Rep* **2015**, *5*, 7798. https://doi.org/10.1038/srep07798.

(33) Panzer, S.; Brych, A.; Batschauer, A.; Terpitz, U. Opsin 1 and Opsin 2 of the Corn Smut Fungus Ustilago Maydis Are Green Light-Driven Proton Pumps. *Front Microbiol* **2019**, *10*, 735. https://doi.org/10.3389/fmicb.2019.00735.

(34) La Greca, M.; Chen, J.-L.; Schubert, L.; Kozuch, J.; Berneiser, T.; Terpitz, U.; Heberle, J.; Schlesinger, R. The Photoreaction of the Proton-Pumping Rhodopsin 1 From the Maize Pathogenic Basidiomycete Ustilago Maydis. *Front. Mol. Biosci.* **2022**, *9*, 826990. https://doi.org/10.3389/fmolb.2022.826990.

(35) Balashov, S. P.; Lu, M.; Imasheva, E. S.; Govindjee, R.; Ebrey, T. G.; Othersen, B.; Chen, Y.; Crouch, R. K.; Menick, D. R. The Proton Release Group of Bacteriorhodopsin Controls the Rate of the Final Step of Its Photocycle at Low pH. *Biochemistry* **1999**, *38* (7), 2026–2039. https://doi.org/10.1021/bi981926a.

(36) Dioumaev, A. K.; Brown, L. S.; Needleman, R.; Lanyi, J. K. Fourier Transform Infrared Spectra of a Late Intermediate of the Bacteriorhodopsin Photocycle Suggest Transient Protonation of Asp-212. *Biochemistry* **1999**, *38* (31), 10070–10078. https://doi.org/10.1021/bi990873+.

(37) Schmidt, A.; Sauthof, L.; Szczepek, M.; Lopez, M. F.; Escobar, F. V.; Qureshi, B. M.; Michael, N.; Buhrke, D.; Stevens, T.; Kwiatkowski, D.; von Stetten, D.; Mroginski, M. A.; Krauß, N.; Lamparter, T.; Hildebrandt, P.; Scheerer, P. Structural Snapshot of a Bacterial Phytochrome in Its Functional Intermediate State. *Nat Commun* **2018**, *9* (1), 4912. https://doi.org/10.1038/s41467-018-07392-7.

(38) Velazquez Escobar, F.; Kneip, C.; Michael, N.; Hildebrandt, T.; Tavraz, N.; Gärtner, W.; Hughes, J.; Friedrich, T.; Scheerer, P.; Mroginski, M. A.; Hildebrandt, P. The Lumi-R Intermediates of Prototypical Phytochromes. *J Phys Chem B* **2020**, *124* (20), 4044–4055. https://doi.org/10.1021/acs.jpcb.0c01059.

(39) Nagano, S.; Scheerer, P.; Zubow, K.; Michael, N.; Inomata, K.; Lamparter, T.; Krauß, N. The Crystal Structures of the N-Terminal Photosensory Core Module of Agrobacterium Phytochrome Agp1 as Parallel and Anti-Parallel Dimers. *J Biol Chem* **2016**, *291* (39), 20674–20691. https://doi.org/10.1074/jbc.M116.739136.

(40) Lamparter, T.; Krauß, N.; Scheerer, P. Phytochromes from Agrobacterium Fabrum. *Photochem Photobiol* **2017**, *93* (3), 642–655. https://doi.org/10.1111/php.12761.

(41) Velázquez Escobar, F.; Buhrke, D.; Michael, N.; Sauthof, L.; Wilkening, S.; Tavraz, N. N.; Salewski, J.; Frankenberg-Dinkel, N.; Mroginski, M. A.; Scheerer, P.; Friedrich, T.; Siebert, F.; Hildebrandt, P. Common Structural Elements in the Chromophore Binding Pocket of the Pfr State of Bathy Phytochromes. *Photochem Photobiol* **2017**, *93* (3), 724–732. https://doi.org/10.1111/php.12742.

(42) Kraskov, A.; von Sass, J.; Nguyen, A. D.; Hoang, T. O.; Buhrke, D.; Katz, S.; Michael, N.; Kozuch, J.; Zebger, I.; Siebert, F.; Scheerer, P.; Mroginski, M. A.; Budisa, N.; Hildebrandt, P. Local Electric Field Changes during the Photoconversion of the Bathy Phytochrome Agp2. *Biochemistry* **2021**, *60* (40), 2967–2977. https://doi.org/10.1021/acs.biochem.1c00426.

(43) Lamparter, T.; Xue, P.; Elkurdi, A.; Kaeser, G.; Sauthof, L.; Scheerer, P.; Krauß, N. Phytochromes in Agrobacterium Fabrum. *Front Plant Sci* **2021**, *12*, 642801. https://doi.org/10.3389/fpls.2021.642801.

(44) Huang, C.-J.; Lin, H.; Yang, X. Industrial Production of Recombinant Therapeutics in Escherichia Coli and Its Recent Advancements. *J Ind Microbiol Biotechnol* **2012**, *39* (3), 383–399. https://doi.org/10.1007/s10295-011-1082-9.

(45) Lozano Terol, G.; Gallego-Jara, J.; Sola Martínez, R. A.; Martínez Vivancos, A.; Cánovas Díaz, M.; de Diego Puente, T. Impact of the Expression System on Recombinant Protein Production in Escherichia Coli BL21. *Front Microbiol* **2021**, *12*, 682001. https://doi.org/10.3389/fmicb.2021.682001.

(46) Rosano, G. L.; Ceccarelli, E. A. Recombinant Protein Expression in Escherichia Coli: Advances and Challenges. *Front Microbiol* **2014**, *5*, 172. https://doi.org/10.3389/fmicb.2014.00172.

(47) Pouresmaeil, M.; Azizi-Dargahlou, S. Factors Involved in Heterologous Expression of Proteins in E. Coli Host. *Arch Microbiol* **2023**, *205* (5), 212. https://doi.org/10.1007/s00203-023-03541-9.

(48) Edelheit, O.; Hanukoglu, A.; Hanukoglu, I. Simple and Efficient Site-Directed Mutagenesis Using Two Single-Primer Reactions in Parallel to Generate Mutants for Protein Structure-Function Studies. *BMC Biotechnol* **2009**, *9* (1), 61. https://doi.org/10.1186/1472-6750-9-61.

(49) Zhang, K.; Yin, X.; Shi, K.; Zhang, S.; Wang, J.; Zhao, S.; Deng, H.; Zhang, C.; Wu, Z.; Li, Y.; Zhou, X.; Deng, W. A High-Efficiency Method for Site-Directed Mutagenesis of Large Plasmids Based on Large DNA Fragment Amplification and Recombinational Ligation. *Sci Rep* **2021**, *11* (1), 10454. https://doi.org/10.1038/s41598-021-89884-z.

(50) Zheng, L. An Efficient One-Step Site-Directed and Site-Saturation Mutagenesis Protocol. *Nucleic Acids Research* **2004**, *32* (14), e115–e115. https://doi.org/10.1093/nar/gnh110.

(51) Bok, J. W.; Keller, N. P. Fast and Easy Method for Construction of Plasmid Vectors Using Modified Quick-Change Mutagenesis. In *Fungal Secondary Metabolism*; Keller, N. P., Turner, G., Eds.; Methods in Molecular Biology; Humana Press: Totowa, NJ, 2012; Vol. 944, pp 163–174. https://doi.org/10.1007/978-1-62703-122-6_11.

(52) Xu, Z.; Colosimo, A.; Gruenert, D. C. Site-Directed Mutagenesis Using the Megaprimer Method. *Methods Mol Biol* **2003**, *235*, 203–207. https://doi.org/10.1385/1-59259-409-3:203.

(53) Schuler, M. A.; Denisov, I. G.; Sligar, S. G. Nanodiscs as a New Tool to Examine Lipid–Protein Interactions. In *Lipid-Protein Interactions*; Kleinschmidt, J. H., Ed.; Methods in Molecular Biology; Humana Press: Totowa, NJ, 2013; Vol. 974, pp 415–433. https://doi.org/10.1007/978-1-62703-275-9_18.

(54) Baserga, F.; Vorkas, A.; Crea, F.; Schubert, L.; Chen, J.-L.; Redlich, A.; La Greca, M.; Storm, J.; Oldemeyer, S.; Hoffmann, K.; Schlesinger, R.; Heberle, J. Membrane Protein Activity Induces Specific Molecular Changes in Nanodiscs Monitored by FTIR Difference Spectroscopy. *Front. Mol. Biosci.* **2022**, *9*, 915328. https://doi.org/10.3389/fmolb.2022.915328.

(55) Pettersen, J. M.; Yang, Y.; Robinson, A. S. Advances in Nanodisc Platforms for Membrane Protein Purification. *Trends in Biotechnology* **2023**, *41* (8), 1041–1054. https://doi.org/10.1016/j.tibtech.2023.02.006.

(56) Lacerda, M. P.; Oh, E. J.; Eckert, C. The Model System Saccharomyces Cerevisiae Versus Emerging Non-Model Yeasts for the Production of Biofuels. *Life (Basel)* **2020**, *10* (11), 299. https://doi.org/10.3390/life10110299.

(57) Tran, A.-M.; Nguyen, T.-T.; Nguyen, C.-T.; Huynh-Thi, X.-M.; Nguyen, C.-T.; Trinh, M.-T.; Tran, L.-T.; Cartwright, S. P.; Bill, R. M.; Tran-Van, H. Pichia Pastoris versus Saccharomyces Cerevisiae: A Case Study on the Recombinant Production of Human Granulocyte-Macrophage Colony-Stimulating Factor. *BMC Res Notes* **2017**, *10* (1), 148. https://doi.org/10.1186/s13104-017-2471-6.

(58) Karbalaei, M.; Rezaee, S. A.; Farsiani, H. Pichia Pastoris: A Highly Successful Expression System for Optimal Synthesis of Heterologous Proteins. *J Cell Physiol* **2020**, *235* (9), 5867–5881. https://doi.org/10.1002/jcp.29583.

(59) Che, Z.; Cao, X.; Chen, G.; Liang, Z. An Effective Combination of Codon Optimization, Gene Dosage, and Process Optimization for High-Level Production of Fibrinolytic Enzyme in Komagataella Phaffii (Pichia Pastoris). *BMC Biotechnol* **2020**, *20* (1), 63. https://doi.org/10.1186/s12896-020-00654-7.

(60) Eskandari, A.; Nezhad, N. G.; Leow, T. C.; Rahman, M. B. A.; Oslan, S. N. Current Achievements, Strategies, Obstacles, and Overcoming the Challenges of the Protein Engineering in Pichia Pastoris Expression System. *World J Microbiol Biotechnol* **2023**, *40* (1), 39. https://doi.org/10.1007/s11274-023-03851-6.

(61) Byrne, B. Pichia Pastoris as an Expression Host for Membrane Protein Structural Biology. *Curr Opin Struct Biol* **2015**, *32*, 9–17. https://doi.org/10.1016/j.sbi.2015.01.005.

(62) Liu, D. R.; Magliery, T. J.; Pastrnak, M.; Schultz, P. G. Engineering a tRNA and Aminoacyl-tRNA Synthetase for the Site-Specific Incorporation of Unnatural Amino Acids into Proteins in Vivo. *Proc Natl Acad Sci U S A* **1997**, *94* (19), 10092–10097. https://doi.org/10.1073/pnas.94.19.10092.

(63) Wals, K.; Ovaa, H. Unnatural Amino Acid Incorporation in E. Coli: Current and Future Applications in the Design of Therapeutic Proteins. *Front Chem* **2014**, *2*, 15. https://doi.org/10.3389/fchem.2014.00015.

(64) Wang, L.; Brock, A.; Herberich, B.; Schultz, P. G. Expanding the Genetic Code of Escherichia Coli. *Science* **2001**, *292* (5516), 498–500. https://doi.org/10.1126/science.1060077.

(65) Young, T. S.; Ahmad, I.; Yin, J. A.; Schultz, P. G. An Enhanced System for Unnatural Amino Acid Mutagenesis in E. Coli. *J Mol Biol* **2010**, *395* (2), 361–374. https://doi.org/10.1016/j.jmb.2009.10.030.

(66) O'Donoghue, P.; Prat, L.; Heinemann, I. U.; Ling, J.; Odoi, K.; Liu, W. R.; Söll, D. Near-Cognate Suppression of Amber, Opal and Quadruplet Codons Competes with Aminoacyl-tRNAPyl for Genetic Code Expansion. *FEBS Lett* **2012**, *586* (21), 3931–3937. https://doi.org/10.1016/j.febslet.2012.09.033.

(67) Chemla, Y.; Ozer, E.; Algov, I.; Alfonta, L. Context Effects of Genetic Code Expansion by Stop Codon Suppression. *Curr Opin Chem Biol* **2018**, *46*, 146–155. https://doi.org/10.1016/j.cbpa.2018.07.012.

(68) Tsukamoto, T.; Yoshizawa, S.; Kikukawa, T.; Demura, M.; Sudo, Y. Implications for the Light-Driven Chloride Ion Transport Mechanism of Nonlabens Marinus Rhodopsin 3 by Its Photochemical Characteristics. *J Phys Chem B* **2017**, *121* (9), 2027–2038. https://doi.org/10.1021/acs.jpcb.6b11101.

(69) Brown, J. Q.; Vishwanath, K.; Palmer, G. M.; Ramanujam, N. Advances in Quantitative UV-Visible Spectroscopy for Clinical and Pre-Clinical Application in Cancer. *Curr Opin Biotechnol* **2009**, *20* (1), 119–131. https://doi.org/10.1016/j.copbio.2009.02.004.

(70) Broser, M. Far-Red Absorbing Rhodopsins, Insights From Heterodimeric Rhodopsin-Cyclases. *Front Mol Biosci* **2021**, *8*, 806922. https://doi.org/10.3389/fmolb.2021.806922.

(71) Soloviov, D.; Borshchevskiy, V.; Chizhov, I. Time-Resolved UV-VIS Spectroscopy of Microbial Rhodopsins. *Methods Mol Biol* **2022**, *2501*, 169–179. https://doi.org/10.1007/978-1-0716-2329-9_8.

(72) Hashimoto, K.; Badarla, V. R.; Kawai, A.; Ideguchi, T. Complementary Vibrational Spectroscopy. *Nat Commun* **2019**, *10* (1), 4411. https://doi.org/10.1038/s41467-019-12442-9.

(73) Hackshaw, K. V.; Miller, J. S.; Aykas, D. P.; Rodriguez-Saona, L. Vibrational Spectroscopy for Identification of Metabolites in Biologic Samples. *Molecules* **2020**, *25* (20), 4725. https://doi.org/10.3390/molecules25204725.

(74) Siebert, F.; Hildebrandt, P. *Vibrational Spectroscopy in Life Science*; Tutorials in biophysics; Wiley-VCH: Weinheim, 2008. https://doi.org/10.1002/9783527621347.

(75) Bellisola, G.; Sorio, C. Infrared Spectroscopy and Microscopy in Cancer Research and Diagnosis. *Am J Cancer Res* **2012**, *2* (1), 1–21.

(76) Pirutin, S. K.; Jia, S.; Yusipovich, A. I.; Shank, M. A.; Parshina, E. Y.; Rubin, A. B. Vibrational Spectroscopy as a Tool for Bioanalytical and Biomonitoring Studies. *Int J Mol Sci* **2023**, *24* (8), 6947. https://doi.org/10.3390/ijms24086947.

(77) Markovich, R. J.; Pidgeon, C. Introduction to Fourier Transform Infrared Spectroscopy and Applications in the Pharmaceutical Sciences. *Pharm Res* **1991**, *8* (6), 663–675. https://doi.org/10.1023/a:1015829412658.

(78) Lorenz-Fonfria, V. A. Infrared Difference Spectroscopy of Proteins: From Bands to Bonds. *Chem Rev* **2020**, *120* (7), 3466–3576. https://doi.org/10.1021/acs.chemrev.9b00449.

(79) Barth, A. Infrared Spectroscopy of Proteins. *Biochim Biophys Acta* **2007**, *1767* (9), 1073–1101. https://doi.org/10.1016/j.bbabio.2007.06.004.

(80) Oldemeyer, S.; La Greca, M.; Langner, P.; Lê Công, K.-L.; Schlesinger, R.; Heberle, J. Nanosecond Transient IR Spectroscopy of Halorhodopsin in Living Cells. *J Am Chem Soc* **2024**, *146* (28), 19118–19127. https://doi.org/10.1021/jacs.4c03891.

(81) Andersen, L. H.; Nielsen, I. B.; Kristensen, M. B.; El Ghazaly, M. O. A.; Haacke, S.; Nielsen, M. B.; Petersen, M. A. Absorption of Schiff-Base Retinal Chromophores in Vacuo. *J Am Chem Soc* **2005**, *127* (35), 12347–12350. https://doi.org/10.1021/ja051638j.

(82) Inoue, K.; Koua, F. H. M.; Kato, Y.; Abe-Yoshizumi, R.; Kandori, H. Spectroscopic Study of a Light-Driven Chloride Ion Pump from Marine Bacteria. *J Phys Chem B* **2014**, *118* (38), 11190–11199. https://doi.org/10.1021/jp507219q.

(83) Tsujimura, M.; Ishikita, H. Identification of Intermediate Conformations in the Photocycle of the Light-Driven Sodium-Pumping Rhodopsin KR2. *J Biol Chem* **2021**, *296*, 100459. https://doi.org/10.1016/j.jbc.2021.100459.

(84) Furutani, Y.; Kandori, H. Hydrogen-Bonding Changes of Internal Water Molecules upon the Actions of Microbial Rhodopsins Studied by FTIR Spectroscopy. *Biochim Biophys Acta* **2014**, *1837* (5), 598–605. https://doi.org/10.1016/j.bbabio.2013.09.004.

(85) Lorenz-Fonfria, V. A.; Saita, M.; Lazarova, T.; Schlesinger, R.; Heberle, J. pH-Sensitive Vibrational Probe Reveals a Cytoplasmic Protonated Cluster in Bacteriorhodopsin. *Proc Natl Acad Sci U S A* **2017**, *114* (51), E10909–E10918. https://doi.org/10.1073/pnas.1707993114.

(86) Zhou, X. E.; Melcher, K.; Xu, H. E. Structure and Activation of Rhodopsin. *Acta Pharmacol Sin* **2012**, *33* (3), 291–299. https://doi.org/10.1038/aps.2011.171.

(87) Braiman, M. S.; Walter, T. J.; Briercheck, D. M. Infrared Spectroscopic Detection of Light-Induced Change in Chloride-Arginine Interaction in Halorhodopsin. *Biochemistry* **1994**, *33* (7), 1629–1635. https://doi.org/10.1021/bi00173a003.

(88) Baenziger, J. E.; Méthot, N. Fourier Transform Infrared and Hydrogen/Deuterium Exchange Reveal an Exchange-Resistant Core of Alpha-Helical Peptide Hydrogens in the Nicotinic Acetylcholine Receptor. *J Biol Chem* **1995**, *270* (49), 29129–29137. https://doi.org/10.1074/jbc.270.49.29129.

(89) Asido, M.; Eberhardt, P.; Kriebel, C. N.; Braun, M.; Glaubitz, C.; Wachtveitl, J. Time-Resolved IR Spectroscopy Reveals Mechanistic Details of Ion Transport in the Sodium Pump Krokinobacter Eikastus Rhodopsin 2. *Phys Chem Chem Phys* **2019**, *21* (8), 4461–4471. https://doi.org/10.1039/c8cp07418f.

(90) Kandori, H.; Maeda, A. FTIR Spectroscopy Reveals Microscopic Structural Changes of the Protein around the Rhodopsin Chromophore upon Photoisomerization. *Biochemistry* **1995**, *34* (43), 14220–14229. https://doi.org/10.1021/bi00043a029.

(91) Petkova, A. T.; Hatanaka, M.; Jaroniec, C. P.; Hu, J. G.; Belenky, M.; Verhoeven, M.; Lugtenburg, J.; Griffin, R. G.; Herzfeld, J. Tryptophan Interactions in Bacteriorhodopsin: A Heteronuclear Solid-State NMR Study. *Biochemistry* **2002**, *41* (7), 2429–2437. https://doi.org/10.1021/bi012127m.

(92) Nagasaka, Y.; Hososhima, S.; Kubo, N.; Nagata, T.; Kandori, H.; Inoue, K.; Yawo, H. Gate-Keeper of Ion Transport-a Highly Conserved Helix-3 Tryptophan in a Channelrhodopsin Chimera, C1C2/ChRWR. *Biophys Physicobiol* **2020**, *17*, 59–70. https://doi.org/10.2142/biophysico.BSJ-2020007.

(93) Otomo, A.; Mizuno, M.; Inoue, K.; Kandori, H.; Mizutani, Y. Protein Dynamics of a Light-Driven Na+ Pump Rhodopsin Probed Using a Tryptophan Residue near the Retinal Chromophore. *Biophys Physicobiol* **2023**, *20* (Supplemental), e201016. https://doi.org/10.2142/biophysico.bppb-v20.s016.

(94) Misra, R.; Das, I.; Dér, A.; Steinbach, G.; Shim, J.; Busse, W.; Jung, K.-H.; Zimányi, L.; Sheves, M. Impact of Protein–Chromophore Interaction on the Retinal Excited State and Photocycle of *Gloeobacter* Rhodopsin: Role of Conserved Tryptophan Residues. *Chem. Sci.* **2023**, *14* (36), 9951–9958. https://doi.org/10.1039/D3SC02961A.

(95) Yun, J.-H.; Li, X.; Yue, J.; Park, J.-H.; Jin, Z.; Li, C.; Hu, H.; Shi, Y.; Pandey, S.; Carbajo, S.; Boutet, S.; Hunter, M. S.; Liang, M.; Sierra, R. G.; Lane, T. J.; Zhou, L.; Weierstall, U.; Zatsepin, N. A.; Ohki, M.; Tame, J. R. H.; Park, S.-Y.; Spence, J. C. H.; Zhang, W.; Schmidt, M.; Lee, W.; Liu, H. Early-Stage Dynamics of Chloride Ion–Pumping Rhodopsin Revealed by a Femtosecond X-Ray Laser. *Proc. Natl. Acad. Sci. U.S.A.* **2021**, *118* (13), e2020486118. https://doi.org/10.1073/pnas.2020486118.

(96) Hosaka, T.; Nomura, T.; Kubo, M.; Nakane, T.; Fangjia, L.; Sekine, S.; Ito, T.; Murayama, K.; Ihara, K.; Ehara, H.; Kashiwagi, K.; Katsura, K.; Akasaka, R.; Hisano, T.; Tanaka, T.; Tanaka, R.; Arima, T.; Yamashita, A.; Sugahara, M.; Naitow, H.; Matsuura, Y.; Yoshizawa, S.; Tono, K.; Owada, S.; Nureki, O.; Kimura-Someya, T.; Iwata, S.; Nango, E.; Shirouzu, M. Conformational Alterations in Unidirectional Ion Transport of a Light-Driven Chloride Pump Revealed Using X-Ray Free Electron Lasers. *Proc. Natl. Acad. Sci. U.S.A.* **2022**, *119* (9), e2117433119. https://doi.org/10.1073/pnas.2117433119.

(97) Nango, E.; Royant, A.; Kubo, M.; Nakane, T.; Wickstrand, C.; Kimura, T.; Tanaka, T.; Tono, K.; Song, C.; Tanaka, R.; Arima, T.; Yamashita, A.; Kobayashi, J.; Hosaka, T.; Mizohata, E.; Nogly, P.; Sugahara, M.; Nam, D.; Nomura, T.; Shimamura, T.; Im, D.; Fujiwara, T.; Yamanaka, Y.; Jeon, B.; Nishizawa, T.; Oda, K.; Fukuda, M.; Andersson, R.; Båth, P.; Dods, R.; Davidsson, J.; Matsuoka, S.; Kawatake, S.; Murata, M.; Nureki, O.; Owada, S.; Kameshima, T.; Hatsui, T.; Joti, Y.; Schertler, G.; Yabashi, M.; Bondar, A.-N.; Standfuss, J.; Neutze, R.; Iwata, S. A Three-Dimensional Movie of Structural Changes in Bacteriorhodopsin. *Science* **2016**, *354* (6319), 1552–1557. https://doi.org/10.1126/science.aah3497.

(98) Tucker, M. J.; Oyola, R.; Gai, F. A Novel Fluorescent Probe for Protein Binding and Folding Studies: P-Cyano-Phenylalanine. *Biopolymers* **2006**, *83* (6), 571–576. https://doi.org/10.1002/bip.20587.

(99) Chaudhari, A. S.; Chatterjee, A.; Domingos, C. A. O.; Andrikopoulos, P. C.; Liu, Y.; Andersson, I.; Schneider, B.; Lórenz-Fonfría, V. A.; Fuertes, G. Genetically Encoded Non-Canonical Amino Acids Reveal Asynchronous Dark Reversion of Chromophore, Backbone, and Side-Chains in EL222. *Protein Sci* **2023**, *32* (4), e4590. https://doi.org/10.1002/pro.4590.

(100) Perálvarez-Marín, A.; Lórenz-Fonfría, V. A.; Bourdelande, J.-L.; Querol, E.; Kandori, H.; Padrós, E. Inter-Helical Hydrogen Bonds Are Essential Elements for Intra-Protein Signal Transduction: The Role of Asp115 in Bacteriorhodopsin Transport Function. *J Mol Biol* **2007**, *368* (3), 666–676. https://doi.org/10.1016/j.jmb.2007.02.021.

(101) Zscherp, C.; Heberle, J. Infrared Difference Spectra of the Intermediates L, M, N, and O of the Bacteriorhodopsin Photoreaction Obtained by Time-Resolved Attenuated Total Reflection Spectroscopy. *J. Phys. Chem. B* **1997**, *101* (49), 10542–10547. https://doi.org/10.1021/jp971047i.

(102) Heberle, J.; Oesterhelt, D.; Dencher, N. A. Decoupling of Photo- and Proton Cycle in the Asp85-->Glu Mutant of Bacteriorhodopsin. *EMBO J* **1993**, *12* (10), 3721–3727. https://doi.org/10.1002/j.1460-2075.1993.tb06049.x.

(103) Richter, H. T.; Needleman, R.; Lanyi, J. K. Perturbed Interaction between Residues 85 and 204 in Tyr-185-->Phe and Asp-85-->Glu Bacteriorhodopsins. *Biophys J* **1996**, *71* (6), 3392–3398. https://doi.org/10.1016/S0006-3495(96)79532-2.

(104) Száraz, S.; Oesterhelt, D.; Ormos, P. pH-Induced Structural Changes in Bacteriorhodopsin Studied by Fourier Transform Infrared Spectroscopy. *Biophys J* **1994**, *67* (4), 1706–1712. https://doi.org/10.1016/S0006-3495(94)80644-7.

(105) Lanyi, J. K. Proton Transfers in the Bacteriorhodopsin Photocycle. *Biochim Biophys Acta* **2006**, *1757* (8), 1012–1018. https://doi.org/10.1016/j.bbabio.2005.11.003.

(106) Sasaki, J.; Lanyi, J. K.; Needleman, R.; Yoshizawa, T.; Maeda, A. Complete Identification of C = O Stretching Vibrational Bands of Protonated Aspartic Acid Residues in the Difference Infrared Spectra of M and N Intermediates versus Bacteriorhodopsin. *Biochemistry* **1994**, *33* (11), 3178–3184. https://doi.org/10.1021/bi00177a006.

(107) Zabelskii, D.; Dmitrieva, N.; Volkov, O.; Shevchenko, V.; Kovalev, K.; Balandin, T.; Soloviov, D.; Astashkin, R.; Zinovev, E.; Alekseev, A.; Round, E.; Polovinkin, V.; Chizhov, I.; Rogachev, A.; Okhrimenko, I.; Borshchevskiy, V.; Chupin, V.; Büldt, G.; Yutin, N.; Bamberg, E.; Koonin, E.; Gordeliy, V. Structure-Based Insights into Evolution of Rhodopsins. *Commun Biol* **2021**, *4* (1), 821. https://doi.org/10.1038/s42003-021-02326-4.

(108) Ran, T.; Ozorowski, G.; Gao, Y.; Sineshchekov, O. A.; Wang, W.; Spudich, J. L.; Luecke, H. Cross-Protomer Interaction with the Photoactive Site in Oligomeric Proteorhodopsin Complexes. *Acta Crystallogr D Biol Crystallogr* **2013**, *69* (Pt 10), 1965–1980. https://doi.org/10.1107/S0907444913017575.

(109) Suzuki, K.; Del Carmen Marín, M.; Konno, M.; Bagherzadeh, R.; Murata, T.; Inoue, K. Structural Characterization of Proton-Pumping Rhodopsin Lacking a Cytoplasmic Proton Donor Residue by X-Ray Crystallography. *J Biol Chem* **2022**, *298* (3), 101722. https://doi.org/10.1016/j.jbc.2022.101722.

(110) Zscherp, C.; Schlesinger, R.; Tittor, J.; Oesterhelt, D.; Heberle, J. In Situ Determination of Transient pKa Changes of Internal Amino Acids of Bacteriorhodopsin by Using Time-Resolved Attenuated Total Reflection Fourier-Transform Infrared Spectroscopy. *Proc Natl Acad Sci U S A* **1999**, *96* (10), 5498–5503. https://doi.org/10.1073/pnas.96.10.5498.

(111) Tittor, J.; Soell, C.; Oesterhelt, D.; Butt, H. J.; Bamberg, E. A Defective Proton Pump, Point-Mutated Bacteriorhodopsin Asp96----Asn Is Fully Reactivated by Azide. *EMBO J* **1989**, *8* (11), 3477–3482. https://doi.org/10.1002/j.1460-2075.1989.tb08512.x.

(112) Kraskov, A.; Nguyen, A. D.; Goerling, J.; Buhrke, D.; Velazquez Escobar, F.; Fernandez Lopez, M.; Michael, N.; Sauthof, L.; Schmidt, A.; Piwowarski, P.; Yang, Y.; Stensitzki, T.; Adam, S.; Bartl, F.; Schapiro, I.; Heyne, K.; Siebert, F.; Scheerer, P.; Mroginski, M. A.; Hildebrandt, P. Intramolecular Proton Transfer Controls Protein Structural Changes in Phytochrome. *Biochemistry* **2020**, *59* (9), 1023–1037. https://doi.org/10.1021/acs.biochem.0c00053.

(113) Falklöf, O.; Durbeej, B. Modeling of Phytochrome Absorption Spectra. *J Comput Chem* **2013**, *34* (16), 1363–1374. https://doi.org/10.1002/jcc.23265.

(114) Zienicke, B.; Molina, I.; Glenz, R.; Singer, P.; Ehmer, D.; Escobar, F. V.; Hildebrandt, P.; Diller, R.; Lamparter, T. Unusual Spectral Properties of Bacteriophytochrome Agp2 Result from a Deprotonation of the Chromophore in the Red-Absorbing Form Pr. *J Biol Chem* **2013**, *288* (44), 31738–31751. https://doi.org/10.1074/jbc.M113.479535.

(115) Fernandez Lopez, M.; Nguyen, A. D.; Velazquez Escobar, F.; González, R.; Michael, N.; Nogacz, Ż.; Piwowarski, P.; Bartl, F.; Siebert, F.; Heise, I.; Scheerer, P.; Gärtner, W.; Mroginski, M. A.; Hildebrandt, P. Role of the Propionic Side Chains for the Photoconversion of Bacterial Phytochromes. *Biochemistry* **2019**, *58* (33), 3504–3519. https://doi.org/10.1021/acs.biochem.9b00526.

(116) López, M. F.; Dahl, M.; Escobar, F. V.; Bonomi, H. R.; Kraskov, A.; Michael, N.; Mroginski, M. A.; Scheerer, P.; Hildebrandt, P. Photoinduced Reaction Mechanisms in Prototypical and Bathy Phytochromes. *Phys Chem Chem Phys* **2022**, *24* (19), 11967–11978. https://doi.org/10.1039/d2cp00020b.

(117) Inoue, K.; Kato, Y.; Kandori, H. Light-Driven Ion-Translocating Rhodopsins in Marine Bacteria. *Trends Microbiol* **2015**, *23* (2), 91–98. https://doi.org/10.1016/j.tim.2014.10.009.

(118) Russell, T. S.; Coleman, M.; Rath, P.; Nilsson, A.; Rothschild, K. J. Threonine-89 Participates in the Active Site of Bacteriorhodopsin: Evidence for a Role in Color Regulation and Schiff Base Proton Transfer. *Biochemistry* **1997**, *36* (24), 7490–7497. https://doi.org/10.1021/bi970287l.

(119) Tittor, J.; Haupts, U.; Haupts, C.; Oesterhelt, D.; Becker, A.; Bamberg, E. Chloride and Proton Transport in Bacteriorhodopsin Mutant D85T: Different Modes of Ion Translocation in a Retinal Protein. *J Mol Biol* **1997**, *271* (3), 405–416. https://doi.org/10.1006/jmbi.1997.1204.

(120) Gmelin, W.; Zeth, K.; Efremov, R.; Heberle, J.; Tittor, J.; Oesterhelt, D. The Crystal Structure of the L1 Intermediate of Halorhodopsin at 1.9 Angstroms Resolution. *Photochem Photobiol* **2007**, *83* (2), 369–377. https://doi.org/10.1562/2006-06-23-RA-947.

(121) Kato, H. E.; Inoue, K.; Abe-Yoshizumi, R.; Kato, Y.; Ono, H.; Konno, M.; Hososhima, S.; Ishizuka, T.; Hoque, M. R.; Kunitomo, H.; Ito, J.; Yoshizawa, S.; Yamashita, K.; Takemoto, M.; Nishizawa, T.; Taniguchi, R.; Kogure, K.; Maturana, A. D.; Iino, Y.; Yawo, H.; Ishitani, R.; Kandori, H.; Nureki, O. Structural Basis for Na(+) Transport Mechanism by a Light-Driven Na(+) Pump. *Nature* **2015**, *521* (7550), 48–53. https://doi.org/10.1038/nature14322.

(122) Abe-Yoshizumi, R.; Inoue, K.; Kato, H. E.; Nureki, O.; Kandori, H. Role of Asn112 in a Light-Driven Sodium Ion-Pumping Rhodopsin. *Biochemistry* **2016**, *55* (41), 5790–5797. https://doi.org/10.1021/acs.biochem.6b00741.

(123) Rüdiger, M.; Oesterhelt, D. Specific Arginine and Threonine Residues Control Anion Binding and Transport in the Light-Driven Chloride Pump Halorhodopsin. *EMBO J* **1997**, *16* (13), 3813–3821. https://doi.org/10.1093/emboj/16.13.3813.

(124) Moltke, S.; Krebs, M. P.; Mollaaghababa, R.; Khorana, H. G.; Heyn, M. P. Intramolecular Charge Transfer in the Bacteriorhodopsin Mutants Asp85-->Asn and Asp212-->Asn: Effects of pH and Anions. *Biophys J* **1995**, *69* (5), 2074–2083. https://doi.org/10.1016/S0006-3495(95)80078-0.

(125) Chizhov, I.; Engelhard, M. Temperature and Halide Dependence of the Photocycle of Halorhodopsin from Natronobacterium Pharaonis. *Biophys J* **2001**, *81* (3), 1600–1612. https://doi.org/10.1016/S0006-3495(01)75814-6.

(126) Wang, T.; Sessions, A. O.; Lunde, C. S.; Rouhani, S.; Glaeser, R. M.; Duan, Y.; Facciotti, M. T. Deprotonation of D96 in Bacteriorhodopsin Opens the Proton Uptake Pathway. *Structure* **2013**, *21* (2), 290–297. https://doi.org/10.1016/j.str.2012.12.018.

(127) Tomida, S.; Ito, S.; Inoue, K.; Kandori, H. Hydrogen-Bonding Network at the Cytoplasmic Region of a Light-Driven Sodium Pump Rhodopsin KR2. *Biochim Biophys Acta Bioenerg* **2018**, *1859* (9), 684–691. https://doi.org/10.1016/j.bbabio.2018.05.017.

(128) Maeda, A.; Sasaki, J.; Shichida, Y.; Yoshizawa, T. Water Structural Changes in the Bacteriorhodopsin Photocycle: Analysis by Fourier Transform Infrared Spectroscopy. *Biochemistry* **1992**, *31* (2), 462–467. https://doi.org/10.1021/bi00117a023.

(129) Ge, X.; Gunner, M. R. Unraveling the Mechanism of Proton Translocation in the Extracellular Half-Channel of Bacteriorhodopsin. *Proteins* **2016**, *84* (5), 639–654. https://doi.org/10.1002/prot.25013.

(130) Brown, L. S.; Sasaki, J.; Kandori, H.; Maeda, A.; Needleman, R.; Lanyi, J. K. Glutamic Acid 204 Is the Terminal Proton Release Group at the Extracellular Surface of Bacteriorhodopsin. *J Biol Chem* **1995**, *270* (45), 27122–27126. https://doi.org/10.1074/jbc.270.45.27122.

(131) Zscherp, C.; Schlesinger, R.; Heberle, J. Time-Resolved FT-IR Spectroscopic Investigation of the pH-Dependent Proton Transfer Reactions in the E194Q Mutant of Bacteriorhodopsin. *Biochem Biophys Res Commun* **2001**, *283* (1), 57–63. https://doi.org/10.1006/bbrc.2001.4730.

(132) Lanyi, J. K. Molecular Mechanism of Ion Transport in Bacteriorhodopsin: Insights from Crystallographic, Spectroscopic, Kinetic, and Mutational Studies. *J. Phys. Chem. B* **2000**, *104* (48), 11441–11448. https://doi.org/10.1021/jp0023718.

(133) Reineke, G.; Heinze, B.; Schirawski, J.; Buettner, H.; Kahmann, R.; Basse, C. W. Indole-3-Acetic Acid (IAA) Biosynthesis in the Smut Fungus Ustilago Maydis and Its Relevance for Increased IAA Levels in Infected Tissue and Host Tumour Formation. *Mol Plant Pathol* **2008**, *9* (3), 339–355. https://doi.org/10.1111/j.1364-3703.2008.00470.x.

(134) Le Coutre, J.; Tittor, J.; Oesterhelt, D.; Gerwert, K. Experimental Evidence for Hydrogen-Bonded Network Proton Transfer in Bacteriorhodopsin Shown by Fourier-Transform Infrared Spectroscopy Using Azide as Catalyst. *Proc Natl Acad Sci U S A* **1995**, *92* (11), 4962–4966. https://doi.org/10.1073/pnas.92.11.4962.

(135) Bartlett, G. J.; Porter, C. T.; Borkakoti, N.; Thornton, J. M. Analysis of Catalytic Residues in Enzyme Active Sites. *J Mol Biol* **2002**, *324* (1), 105–121. https://doi.org/10.1016/s0022-2836(02)01036-7.

(136) Lórenz-Fonfría, V. A.; Muders, V.; Schlesinger, R.; Heberle, J. Changes in the Hydrogen-Bonding Strength of Internal Water Molecules and Cysteine Residues in the Conductive State of Channelrhodopsin-1. *J Chem Phys* **2014**, *141* (22), 22D507. https://doi.org/10.1063/1.4895796.